THE CHARACTERISATION OF CLEAN METAL SURFACES

A THESIS SUBMITTED FOR THE
DEGREE OF DOCTOR OF PHILOSOPHY
IN THE UNIVERSITY OF ASTON IN BIRMINGHAM

John Michael Walls, B.Sc.

Department of Physics
November 1973

ABSTRACT

The most perfectly structured metal surface observed in practice is that of a field evaporated field-ion microscope specimen. This surface has been characterised by adopting various optical analogue techniques. Hence a relationship has been determined between the structure of a single plane on the surface of a field-ion emitter and the geometry of a binary zone plate. By relating the known focussing properties of such a zone plate to those obtained from the projected images of such planes in a field-ion micrograph, it is possible to extract new information regarding the local magnification of the image.

Further to this, it has been shown that the entire system of planes comprising the field-ion imaging surface may be regarded as a moiré pattern formed between overlapping zone plates. The properties of such moiré zone plates are first established in an analysis of the moiré pattern formed between zone plates on a flat surface. When these ideas are applied to the field-ion image it becomes possible to deduce further information regarding the precise topography of the emitter. It has also become possible to simulate differently projected field-ion images by overlapping suitably aberrated zone plates.

Low-energy ion bombardment is an essential preliminary to much surface research as a means of producing chemically clean surfaces. Hence it is important to know the nature and distribution of the resultant lattice damage, and

the extent to which it may be removed by annealing.

The field-ion microscope has been used to investigate such damage because its characterisation lies on the atomic scale. The present study is concerned with the in situ sputtering of tungsten emitters using helium, neon, argon and xenon ions with energies in the range 100eV to 1 keV, together with observations of the effect of annealing. The relevance of these results to surface cleaning schedules is discussed.

CONTENTS

CHAPTER ONE

INTRODUCTION

1.1 Preliminary considerations

The characterisation and attainment of clean metal surfaces is an essential preliminary to all surface research, otherwise the effects of contamination and imperfect topography may have a crucial part to play on the surface chemistry and crystallography of the subsequent experiment.

An ideal model system is provided for the characterisation of a clean metal surface by the field-ion microscope. The field evaporated field-ion emitter possesses a somewhat arbitrary topography, but because the technique is capable of atomic resolution, this topography can be precisely defined. Moreover, the preparation of an atomically clean surface is made almost routine by the process of field evaporation. In addition, the ability of the field-ion microscope to resolve the individual atomic structure of a metal surface combined with the capacity to strip off surface atoms one by one and hence to reveal in detail the structure of the sub-surface regions makes this instrument a powerful tool in surface research.

The present study will show that established techniques in experimental optics can be applied to the characterisation of the detailed atomic structure of the field-ion emitter and its image. By setting up suitable analogue models it is possible to determine new information concerning the detailed topography of the specimen and the processes of image formation.

An investigation into the effects of conventional cleaning techniques will also be described. Here, the field-ion microscope has been used to study the processes occurring at the atomic level during low-energy ion bombardment of tungsten field-ion emitters. The extent to which subsequent lattice disorder is removed by annealing will also be reported.

1.2 Relevant Literature

It is not intended to provide a full account of the various imaging techniques and theory as there are now books available on the topic of field-ion microscopy. Thus it is intended only to give a brief description of the basic principles of the field-ion microscope and the interpretation of its images.

Three books are available on the topic, all are entitled 'Field-ion Microscopy'. The first is a short course edited by Hren and Ranganathan (1968). The other two are written by Müller and Tsong (1969) and Bowkett and Smith (1970). In addition, there are a number of general review articles, the most recent of which Southworth (1970) and Smith D. A. and Smith G.D.W. (1970) provide readable introductions to the subject. A review of the metallurgical aspects has been made by Ralph (1970).

1.3 The basic principles of image formation

The detailed atomic structure of the crystal lattice may be studied indirectly using a variety of techniques. These techniques usually rely on the diffraction of some form of radiation such as X-rays or electrons, by the

regular arrays of atoms present in the crystal. The limit of resolution of the technique is a function of the wavelength of radiation used. The diffraction of electrons, as utilised in the transmission electron microscope, even in its most sophisticated form is only just within reach of distinguishing features occurring on the atomic scale. By using a completely different method of image formation, the field-ion microscope is capable of resolving the position at a single atom (Müller (1960)). Both the field emission microscope and the field-ion microscope can be loosely defined as point projection devices. In the field emission microscope, the image is carried from the specimen to the screen by electrons originating in the specimen itself, whereas in the field-ion microscope the image is conveyed by positive ions formed near to the specimen surface.

Figure 1.1 depicts schematically, the layout of a simple field-ion microscope. The specimen is usually made by electropolishing a sharp point on the end of a piece of wire typically 1cm. long. The radius of the specimen is usually in the region 100Å-1000Å. The specimen is mounted with electrical connection to a H.T. power supply and occasionally with access to an electrical heating circuit. The specimen is mounted in a vacuum system and points in the direction of a fluorescent screen. An imaging gas, conventionally helium, is then leaked into the vacuum chamber to a suitable pressure. The specimen mounting leads not only enables a positive potential to be applied to the specimen, but also provide a heat conduction path to the cryogenic coolant (usually liquid nitrogen).

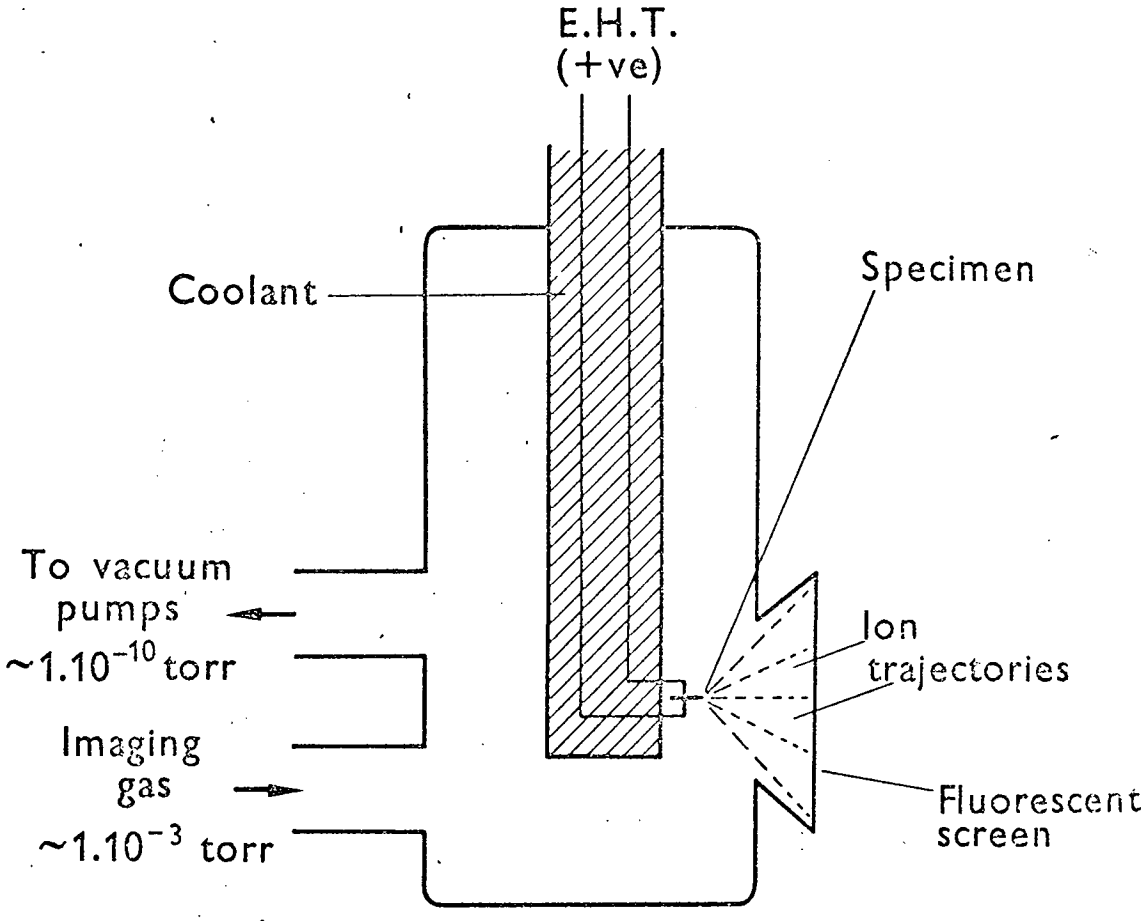

Figure 1.1. A schematic diagram of a simple field-ion microscope. (Courtesy H. N. Southworth).

The extremely sharp curvature of the specimen tip enables an electric field of several volts per Ångström to be generated by applying a potential of a few kilovolts. This field strength attracts imaging gas to the specimen surface by polarisation forces, positive ions are then formed in the viscinity of the specimen and these are repelled and form a projected image of the local field fluctuations existing on the specimen surface when they strike the flat fluorescent screen. In practice, the regions of highest field correspond to the position of protruding atoms on the specimen surface. Hence a pencil beam of ions excites one bright spot on the screen corresponding to each protruding atom on the surface. Thus a direct image of the atomic distribution of the tip surface is produced.

The field-ion emitter is usually approximated to correspond to a hemispherical section taken through an infinite crystal lattice. The intersection of this hemispherical surface produces an interdependantly faceted structure. Drechsler and Wolf (1958) and Müller (1960) have constructed a ball model corresponding to a (011) orientated tip which may be compared with the field-ion image (figure 1.2(a)). When those atoms which protrude most and those that protrude second most are emphasised (by painting them with fluorescent paint and illuminating the model with ultra-violet light), the similarity to the general appearance of a field-ion micrograph is good (figure 1.2(b)). For comparison figure 1.3 is a field-ion micrograph of tungsten.

A considerable advantage of the field-ion microscope

Figure 1.2 (a) A ball model of a (011) orientated tungsten field-ion emitter.

(After Müller (1960)).

Figure 1.2 (b) When those atoms which are protruding most from the emitter surface are emphasised, the model is very similar to a field-ion image.

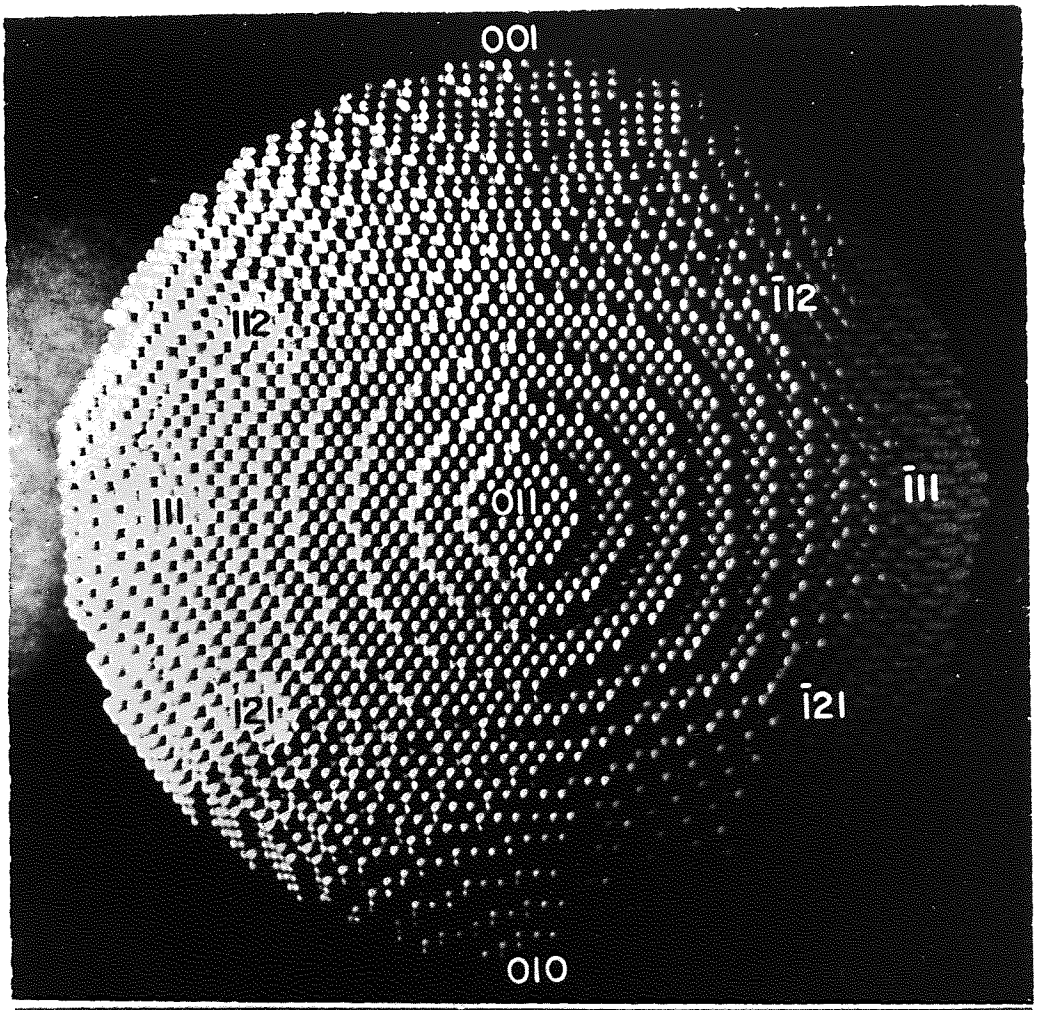
001
112
$\bar{1}12$
111
011
$\bar{1}11$
121
$\bar{1}21$
010

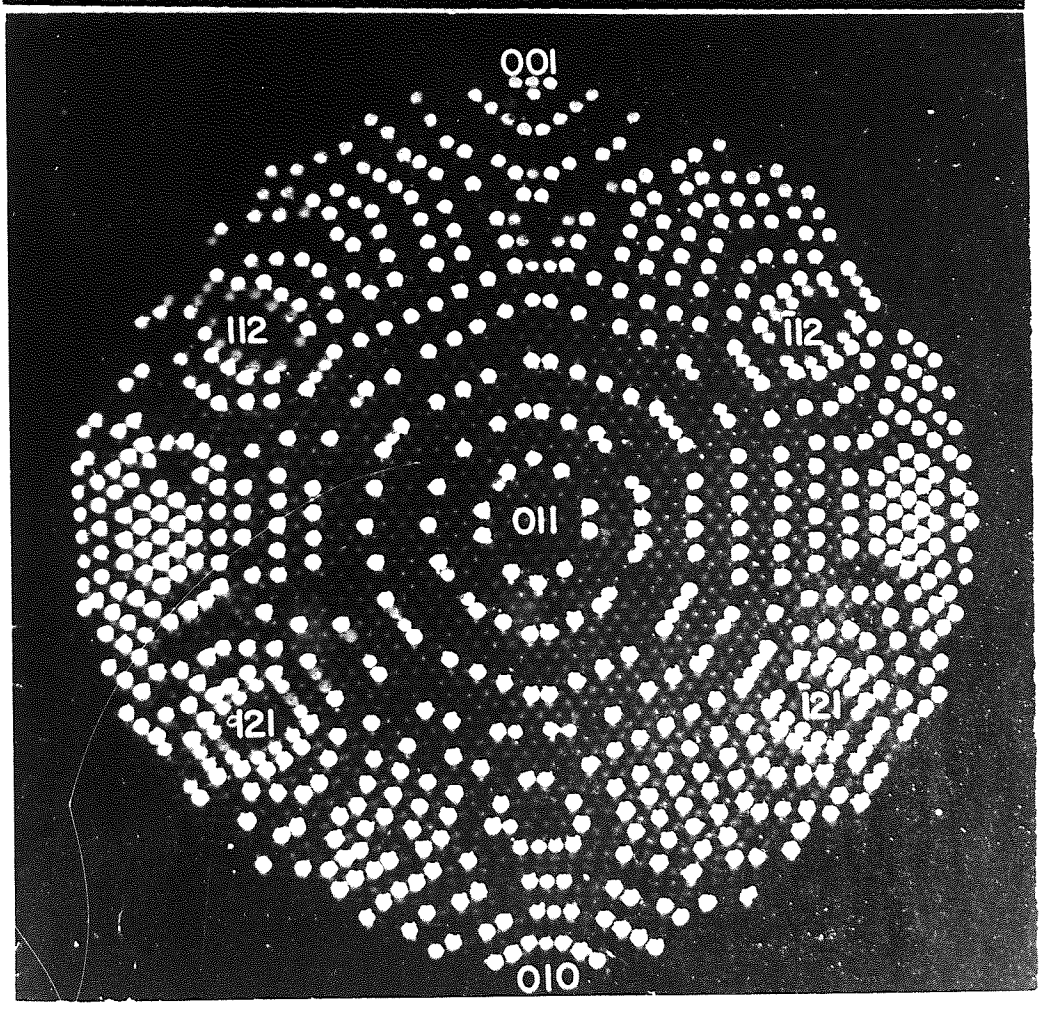
001
112
$\bar{1}12$
011
$\bar{1}21$
121
010

is that of field evaporation. This facility enables an atom by atom dissection of the specimen microstructure to be made by the controlled removal of surface atoms. By increasing the applied voltage to some value above that required for the field ionisation of imaging gas, metal atoms are evaporated (or desorbed) as ions. The process of field evaporation is responsible for the characteristic, almost hemispherical shape of field-ion microscope specimens.

Several factors affect the potential resolution of the microscope. For instance, the imaging gas pressure must be sufficiently low to ensure that the mean free path is high and thus collisions which may deviate the ions from their original trajectories are minimised. However, the most important factor is the velocity of the imaging ion transverse to the electrostatic line of force at the site of field ionisation. Hence the specimen is cooled to a low temperature (usually liquid nitrogen). Thus the incoming gas atom thermally accommodates itself to the specimen temperature via a hopping process (illustrated in figure 1.6) and its lateral momentum is then small. Müller (1960) has obtained an expression for the potential resolution δ assuming the lateral momentum component to be the limiting factor.

$$\delta = \left(\frac{6\times10^{-4}\ Tr}{F}\right)^{\frac{1}{2}} \text{ Å} \qquad \ldots\ldots(1.1)$$

where T is the tip temperature

r is the radius of the specimen

and F is the field strength required for ionisation.

Figure 1.3 A helium field-ion micrograph of tungsten, and below, a schematic diagram illustrating the indexing of field-ion planes.

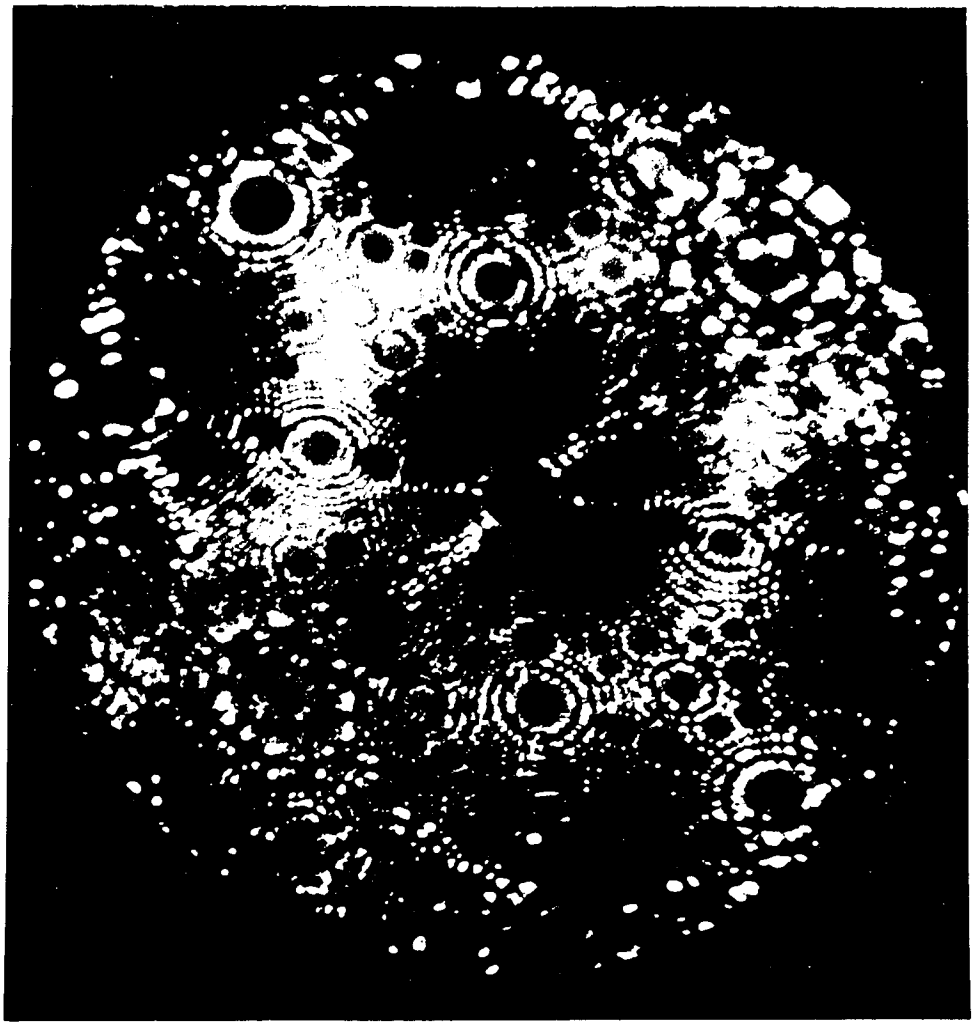

(a)

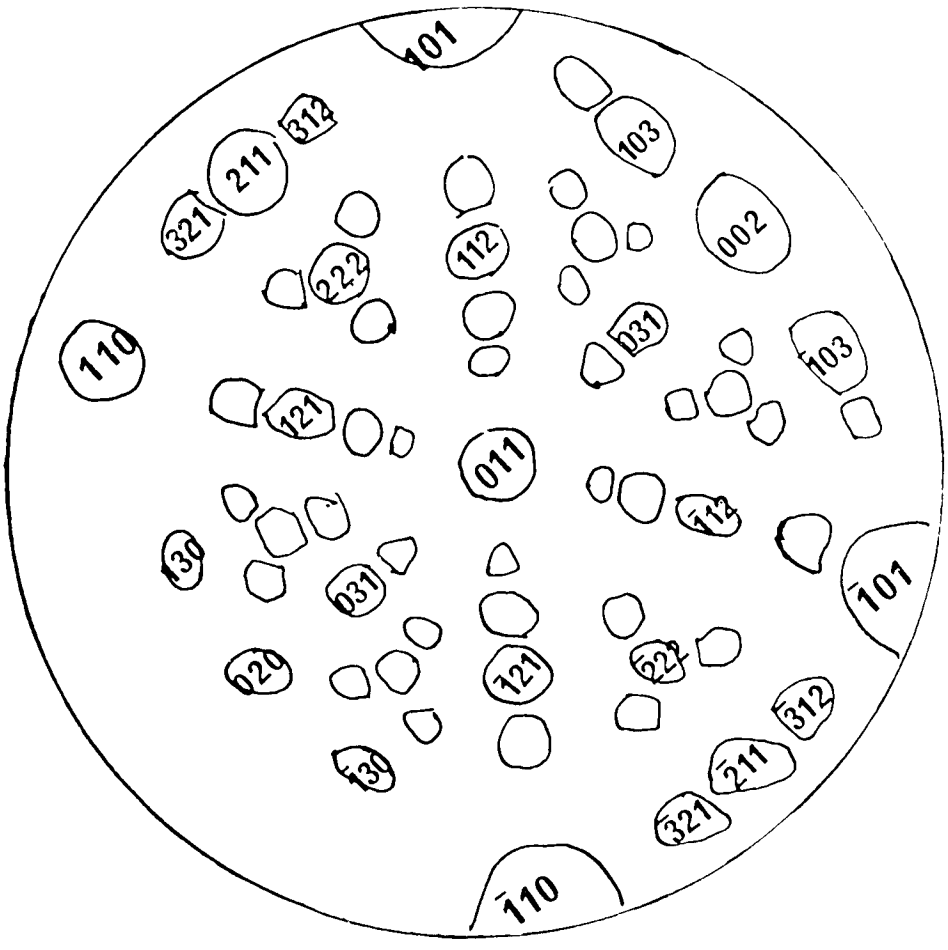
101
103
002
112
222
211
321
312
110
031
103
121
011
112
101
130
031
020
121
22
312
211
321
130
110

(b)

As a general rule, better resolution is obtained with decreasing specimen temperature. The resolution is such that interatomic spacings of 3Å can be resolved. The resolution of the microscope to normal displacements in the specimen atomic structure is much better and G.D.W. Smith (1971) reported a potential resolution of 0.3Å, hence the extreme sensitivity of field-ion images to interstitial atoms. Certainly the resolution of point defects introduced by ion bombardment is possible (see chapter 6).

The important processes of field ionisation and field evaporation will now be discussed. It is not intended to conduct a searching enquiry into these processes, but simply to present a concise picture of the more well established ideas so that in ensuing chapters we can be aware of the processes involved in image formation and the development of the well defined specimen surface topography.

1.3.1. Field ionisation

The theory of field ionisation is at present highly unsatisfactory. Only a synopsis of the classical theory is presented here, but this is sufficient to highlight some of the physical processes involved.

Field ionisation can be considered to be a quantum mechanical tunnelling process (Inghram and Gomer (1954)) whereby an electron is effectively transferred from the thermally accommodated gas atom to the metal. The electron is able to tunnel through a potential barrier which has been narrowed by the high electric field, as illustrated in figure 1.4. The potential energy barrier is further

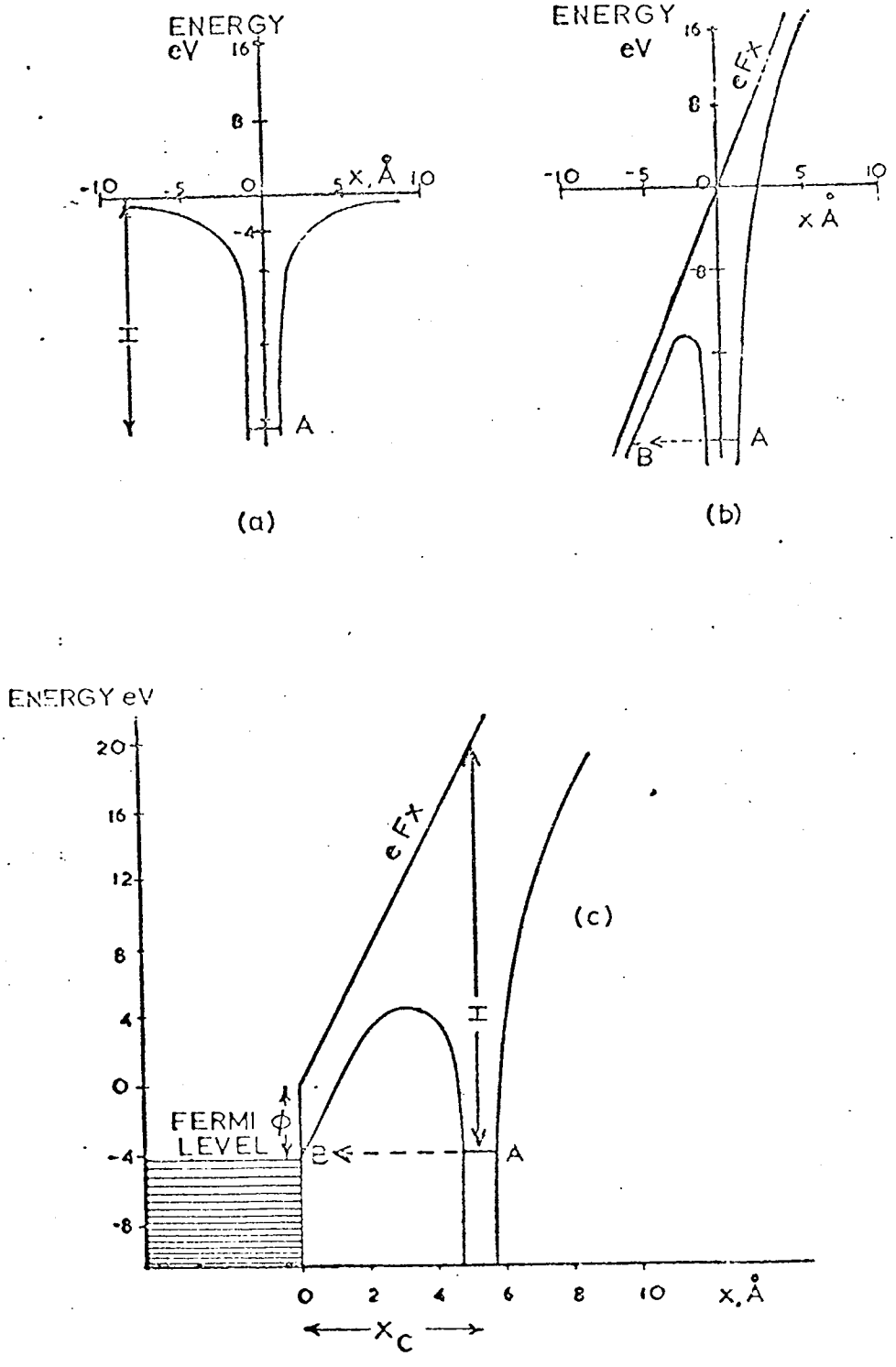

Figure 1.4 (a). Potential energy diagram for an electron in a helium atom as a function of the distance, x, from the nucleus.

(b). The effect on the potential energy curve when the external field is applied. Tunnelling occurs from A to B.

(c). Ionisation at the emitter surface for a helium atom.

(Courtesy H. N. Southworth).

reduced by image forces which attract the electron to the image of the ion-electron dipole, in the conducting surface. Figure 1.4 also shows the gas atom at a critical distance Xc from the emitter surface, it can be seen that if the atom approaches the surface, the electron energy level in the metal must be reduced below the Fermi level in the metal and hence the tunnelling probability must be reduced because of the low number of vacant sites to which the electron may tunnel.

This critical distance for ionisation has been shown by Müller (1960) to be:

$$Xc \simeq \frac{I-\phi}{eF} \qquad \ldots\ldots(1.2)$$

where I is the ionisation energy, ϕ is the work function, F the applied electric field and e is the electronic charge. For helium Xc is typically about 5Å. It has been found that most of the ions are formed in an ionisation zone just outside Xc with a width of only 0.15Å (Tsong and Müller (1964)). Although this rather simple model helps in the understanding of field ionisation, it has several shortcomings. For instance regional brightness (Cranstoun (1972)), the hydrogen promotion effect (Müller (1967)) and gas promoted field desorption have not yet been adequately explained. However, recent discoveries by Müller, McLane and Panitz (1968) and Jason, Burns and Inghram (1965) may point a way to a more fruitful theory. Müller, McLane and Panitz (1968) using the atom probe field-ion microscope have proposed that an apex-adsorbed imaging gas atom is involved in the process, a comparative illustration of the effect of this discovery on field ionisation is shown in figure 1.6. A different

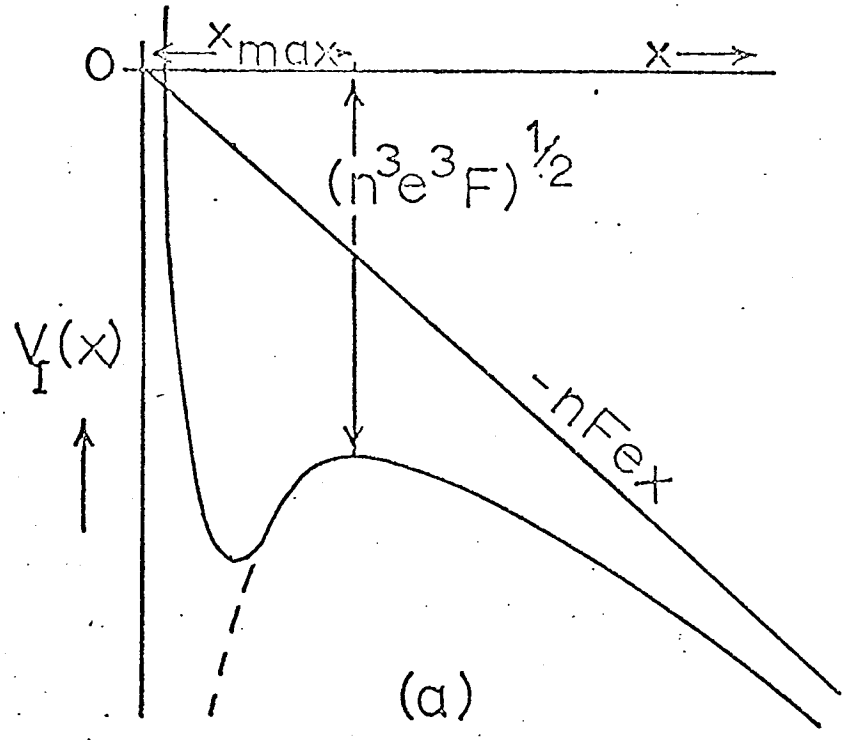

Figure 1.5.(a). Potential energy curve for an ion in the presence of an applied electric field.

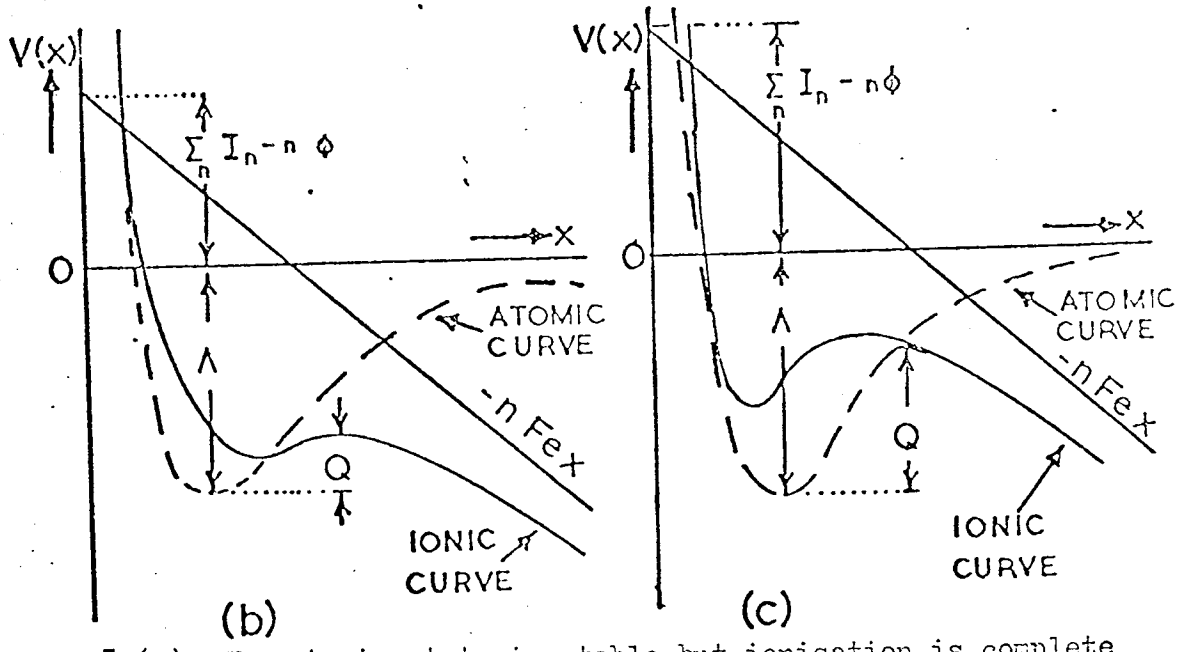

Figure 1.5.(b). The atomic state is stable but ionisation is complete before the maximum in the curve is reached, and evaporation occurs over the Schottky hump. (c). The ionic state is stable and the maximum in the curve corresponds to the point of intersection of the atomic and ionic curves. (Courtesy H. N. Southworth).

approach to the problem has been taken by Forbes (1971) who has examined variations in gas concentration above imaging sites. For a deeper insight into this somewhat controversial topic, Müller (1972) has reviewed current thoughts on the subject.

1.3.2. Field evaporation

If the applied electric field is raised sufficiently above that required to obtain an image, the removal of surface atoms is observed. The process begins at a well defined field, and the rate of removal of atoms increases rapidly with field. The phenomenon is manifested by the collapsing to the centre of the circular facet structure composed of imaged atoms around each surface plane. Continued field evaporation of a newly prepared specimen preferentially removes any topographical irregularities and eventually reveals the characteristic field evaporated end form which is free from adsorbed contamination.

However, although field evaporation enables the sub-structure of a specimen to be revealed, it is also responsible for the main limitation of the technique. The characteristic field Fi for the best imaging conditions for any metal is clearly associated with the best image voltage (B.I.V.) and is dependent primarily on the ionisation energy of the imaging gas. It is clear that for stable field-ion images Fi must be less than the field necessary to field evaporate the specimen Fe, i.e. $Fi<Fe$. If this is not the case imaging conditions cannot be obtained. Recent work, using ultra-high vacuum microscopes and imaging gases with relatively low ionisation energies (such as neon and argon) has enabled

many non-refractory metals to be examined in the field-ion microscope (for example Boyes and Southon (1972)).

In the absence of an applied electric field, the energy Qo required to desorb an atom, as an ion from a surface is given by (Müller (1960)), (Gomer (1961)).

$$Qo = \Lambda + \Sigma nIn - n\phi \qquad .....(1.3)$$

where ΣnIn is the sum of the ionisation energies.

Müller (1960) suggests that field evaporation occurs by direct thermally activated evaporation of an ion over a potential barrier Q which is reduced by Qo, by the applied field. Using this argument the following expression is obtained for the critical field of evaporation:-

$$F = n^{-3}e^{-3}\left[\Lambda + \Sigma nIn - n\phi - kT\ln\frac{t}{t_o}\right]^2 .....(1.4)$$

where n is the charge on the ion, t is the time constant for evaporation and t_o is the reciprocal of the lattice vibration frequency. This expression may then be modified to take into account the double layer which screens the applied field due to a dipole moment ne/q where q is a screening distance. Hence:-

$$F = n^{-3}e^{-3}\left[\Lambda + \Sigma nIn - n\phi + \tfrac{1}{2}(\alpha a-\alpha i)F^2 + \frac{neF}{q} - kT\ln\left(\frac{t}{t_o}\right)\right]^2 \qquad .....(1.5)$$

where αi and αa are the polarisabilities of the ion and atom respectively.

These equations are derived from a study of the atom and ion-potential curves close to the surface of the specimen and the way these curves are modified by the presence of the applied field (see figure 1.5). Other possibilities that have been considered, include tunnelling

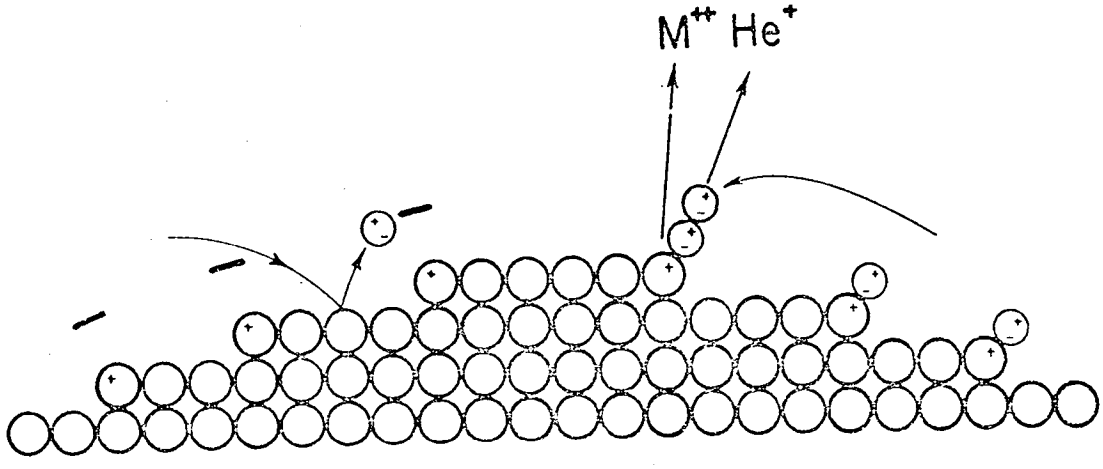

Figure 1.6 Field ionisation on the emitter surface. The model on the left hand side illustrates the conventional view of a freely hopping polarised image gas atom whilst the model on the right hand side shows how the possibility of an apex-adsorbed image gas atom might affect the process. (After Müller (1972).

through the potential barrier especially at low temperature field evaporation. A review of the different approaches that have been made is available (Brandon (1966)), but like field ionisation, the physical understanding of the processes involved is incomplete. More searching articles are available, for instance McKinstry (1972) and Vesely and Ehrlich (1973). Taylor (1970) has also considered the subject in some detail.

1.4 The topography of the field-ion specimen surface

The ball models and the general appearance of the field-ion emitter have already been briefly discussed in section 1.3. Figure 1.2 shows that the locus of the positions of the protruding atoms is polygonal, but approximately circular and corresponds to facets on the ball model where certain crystal planes are parallel to the surface. Thus each set of circular facets corresponds to a crystallographic plane. Further, the step height of each set of circular facets is equal to the interplaner separation of that plane. In the micrograph of tungsten shown in figure 1.3, the various planes are indexed by inspection in a way that is crystallographically consistent. Clearly the prominence of each plane in the field-ion image will depend on its interplanar spacing (Drechsler and Wolf (1958)), (Moore and Ranganathan (1967)), this point is further discussed in chapter 3.

It is possible to show (chapter 3) that the square of the radius of the nth ledge r_n^2 is proportional to n. This provides the basis for an optical analogue that exists between the geometry of a field-ion plane and that of the binary zone plate. This analogue and the new information

it provides are considered in chapter 3.

The entire image can be considered to be an inter-dependent moiré pattern formed by overlapping such binary zone plates (chapter 3), a purely mathematical approach (chapter 4) may then be used to determine the relationship between the individual planes on the field-ion emitter.

Evidence that the hemispherical end form approximation is inadequate has been provided by profiles of field-ion tips obtained using the electron microscope (Norden and Bowkett (1967) and Loberg and Norden (1968)). Fortes 1971(a), 1971(b) has attempted to derive an approximate equation to describe the shape of the profile and concludes that a cubic expression is applicable. Matters are further complicated by the discovery of Hren, Moore and Spink (1972) that the detailed shape of the emitter is sensitive to the rate of field evaporation. They show that high rates of removal of material produces a more hemispherical end form.

1.5 The emitter radius

The most commonly used method of determining the local radius of curvature of a field-ion emitter was first described by Drechsler and Wolf (1958). The method consists of counting the number of net plane rings n between two planes of known angular separation θ in the field-ion micrograph. From figure 1.7 it is clear that if the step height $d(h_1k_1l_1)$ is known, then the local radius of curvature R is given by the formula:-

$$R = \frac{nd}{1 - \cos\theta} \qquad \ldots\ldots(1.6)$$

As an example, consider the local radius of curvature between the planes (002) and (206) on the field-ion micro-

Figure 1.7. The model of the field-ion emitter used to calculate the local radius of curvature, R, by the method of Drechsler and Worf (1958). The number, n, of net plane rings between the centres of two planes $(h_1k_1l_1)$ and $(h_2k_2l_2)$ of known angular separation are counted and R is then found from equation (1.6.).

graph of iridium shown in figure 4.9 in chapter 4. The number of net (002) plane rings between (002) and a position corresponding to the centre of the (206) plane is 15 and the angular separation between the poles of the same planes is 18° 26'. From tables the step height of an (002) plane in iridium is 1.919Å. Hence by substituting in equation (1.6) for n, d and θ, R is found to be 562Å.

Although this method is simple to use, it does contain considerable inaccuracies:-

(1) The phase factors of the two planes are ignored and hence there may be considerable error in the value of n. This is particularly serious when measuring the radius of low radius specimens and in situations where the radius of curvature is to be determined across a small angular separation; in both cases n is likely to be small.

(2) Unless the atoms in the plane $(h_2k_2l_2)$ are fully resolved, it is sometimes difficult to assess which atom positioned on the edge of the first net ring of the plane $(h_2k_2l_2)$ corresponds to the ring through the centre of that plane associated with $(h_1k_1l_1)$ and hence, once more, n is difficult to assess.

These and other problems associated with this method of radius measurement have been considered by Crawford (1973).

Using this method, Drechsler and Wolf (1958) calculated radius values over a number of regions on a tungsten micrograph and found that these values varied by a factor of 4. This has been used extensively as evidence that the emitter profile cannot even be approximately hemispherical. However, other methods of radius determination suggest that such wild variations are incorrect (chapter 4).

In order to circumvent this wide variation in local radius, Drechsler and Wolf (1958) used an "average tip radius" which they defined as:-

$$R_{av} = 33X\ n\ ((011)-(123))\text{Å} \qquad .....(1.7)$$

where n ((011)-(123)) is the number of net rings between the planes (011) and (123) on a tungsten specimen.

Drechsler and Wolf (1958) also pointed out two other methods of radius measurement. The first method involves measuring the applied voltage when imaging a specimen and hence knowing the correct field for the ionisation of a particular image gas, the radius of the specimen can be found. The second method relies on the provision of a fully resolved image where an arc distance d can be measured by counting rings of known interatomic separation within a known subtended angle (between the poles of two planes). Hence from the equation (1.8), R may be obtained

$$d = R\theta \qquad .....(1.8)$$

An alternative and more general method of determining the local radius of curvature from data derived from the micrograph is presented in chapter 4.

1.6 Computer simulation of field-ion images

Moore (1962) was the first to use the "thin shell" model to determine which atoms on the surface of a field-ion emitter would give rise to image points following a general postulate made by Müller (1960) that atoms protruding most from the specimen were imaged. This model led directly to the computer simulation of field-ion images. Computer simulation is of great value to field-ion image interpretation because of the power of the

computer to evaluate quantitatively the effects of simple assumptions about the nature of the field evaporated surface. The 'thin shell' model can also be interpreted in terms of a moiré analogue and this is discussed in chapter 4.

Moore assumed that the field-ion emitter represented an ideal, spherical surface which he defined as consisting of those atoms of an infinite crystal whose centres lie just within a spherical envelope. Moore then suggested that only those atoms which lie within a thin spherical shell of thickness, p, would give rise to image points (illustrated in figure 1.8). Thus by considering a sphere cut by a (100) plane giving approximately circular contours the position of any atom could be referred to an x-y co-ordinate system. The system could be used for both f.c.c. and b.c.c. materials. Moore then assumed that the projection relationship between the three-dimensional lattice and the image plane was orthographic. A typical result of this form of simulation is shown in figure 1.9. The similarity to a real field-ion image is quite good. Further, the relative prominence of the various planes and the number of planes along any one zone are consistent with a real image of equivalent average radius.

Moore and Ranganathan (1967) found the p, the shell thickness, decreased in size with increasing specimen radius. They also considered the development of field-ion planes and found that the appearance of a plane was independent of p but dependent on R; they present a table of planes which ought to be developed at certain specimen radii. An explanation of this phenomenon based on

Figure 1.8. The basis of the "thin shell" model (Moore (1962)), for the interpretation of the field-ion imaging surface. (Brandon (1966)).

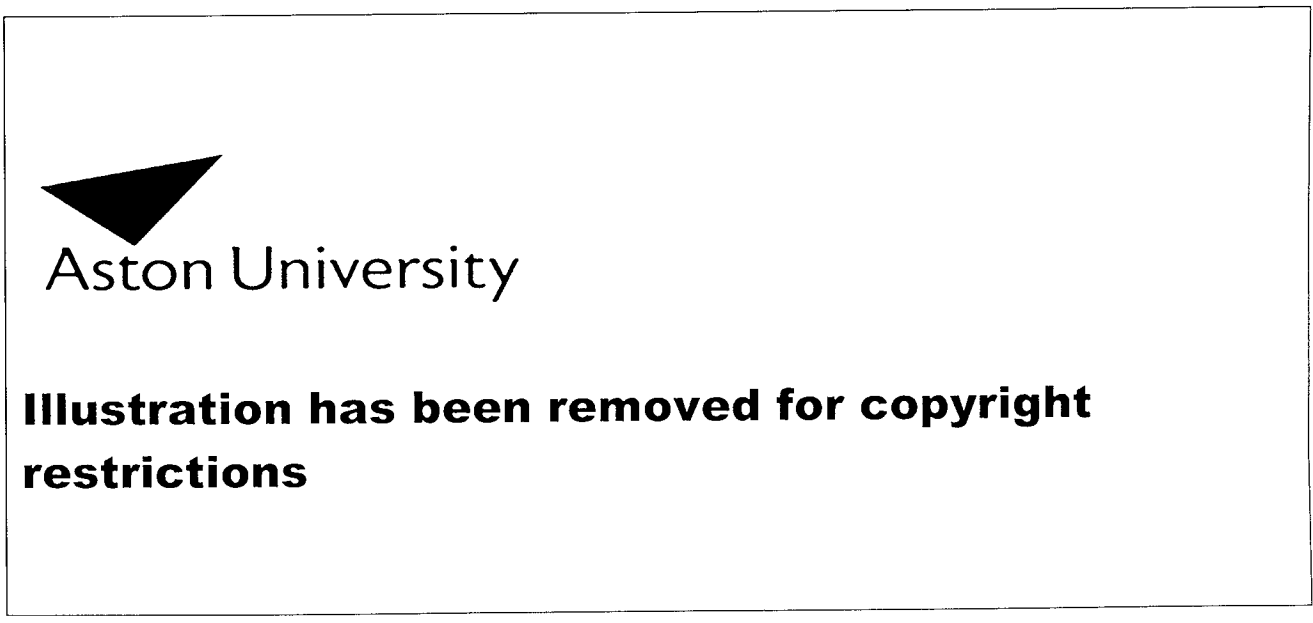

Figure 1.9. A typical example of a computer simulated field-ion image, (Moore (1962)).

moiré theory is given in chapter 3.

Moore (1967(a)) has also extended the computer simulation technique to solid solution alloys by assuming that each alloy species behaves differently to field evaporation (Southworth and Ralph (1969)), but the same with respect to their imaging properties.

The technique has also found importance in the simulation of extended defects, for example Brandon and Perry (1967) and Sanwald and Hren (1968) have managed to simulate dislocation contrast in b.c.c. and f.c.c. lattices. A curious result was obtained by Taylor (1970) investigating the effect of emitter shape on the computed image. Taylor found that Moore's hemispherical assumption was difficult to improve on and found that if the ellipsoidal axes determined from electron micrographs of emitters were used, totally unrealistic images were obtained.

1.7. Experimental details

Unless otherwise stated, all the experiments to be described in subsequent chapters were carried out in a bakeable, stainless steel, ultra-high vacuum (U.H.V.) field-ion microscope. This microscope, which is available commercially from Vacuum Generators Limited, was built around the vacuum system illustrated in figure 1.10. Essentially, the pumping system consists of three separate vacuum pumps; a 40 $l.s.^{-1}$ Mullard ion pump, a liquid nitrogen trapped 2" mercury diffusion pump (backed by a rotary pump) and a 6" titanium sublimation pump. Each of these pumps had an individual function, but all were complementary in action. The ion pump (bakeable) was used to pump the microscope down during bakeout and was

Figure 1.10 A schematic diagram of the ultra-high vacuum system.

Figure 1.11 A schematic diagram of the field-ion microscope head.

A. Specimen support cylinder
B. Copper gripping jaws
C. Inner dewar
D. Outer dewar
E. Radiation shield
F. Insulated electrical conductor
G. Electrical feedthrough
H. Channel plate image intensifier
I. Permanent magnet

n system.

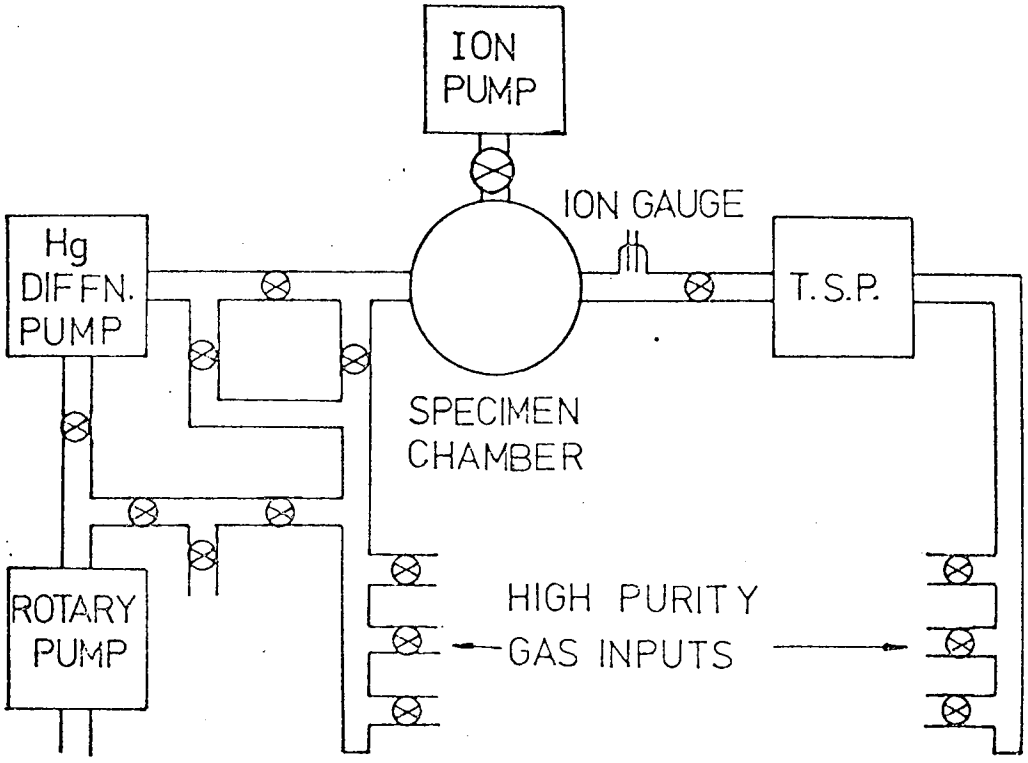

cope head.

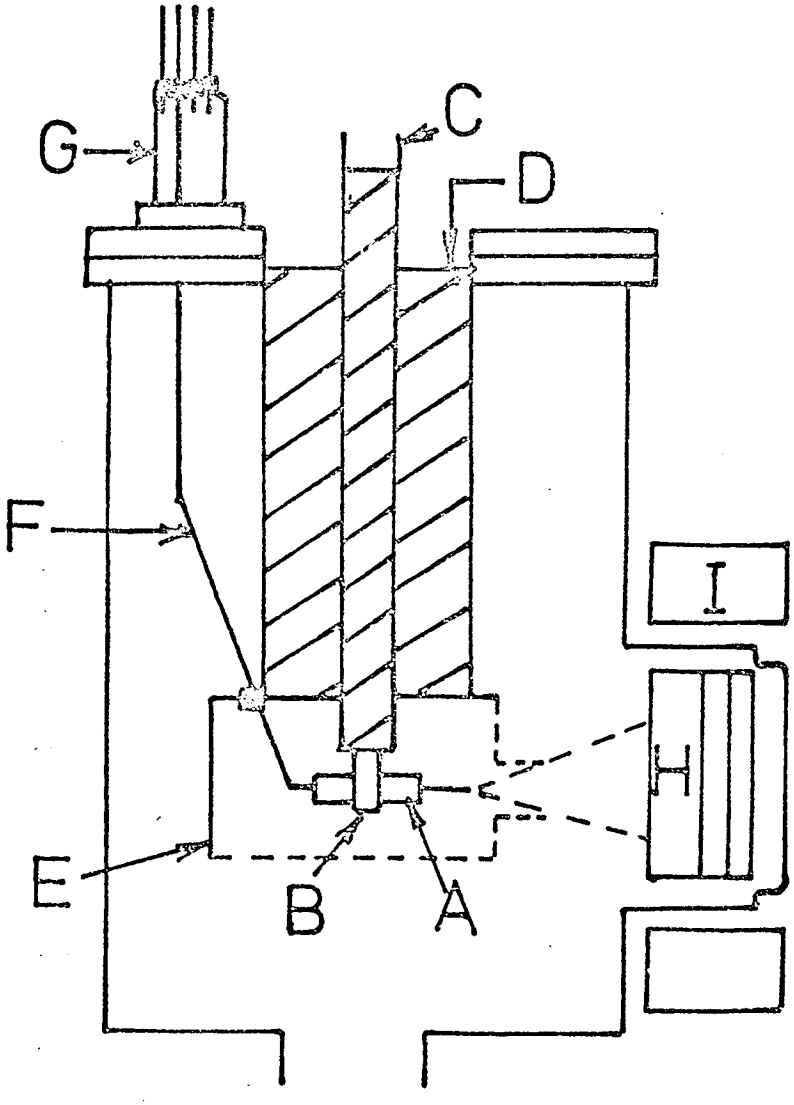

capable of the lowest ultimate pressure. The diffusion pump was used whilst imaging with a continuous flow of some inert gas (the action of the ion pump virtually precludes its use with the noble gases at high pressures). The titanium sublimation pump was situated such that imaging gas could pass through a freshly evaporated titanium layer which removes active contaminent gases, but of course, cannot pump inert gases. Using this system pressures of 5×10^{-10} torr (as measured using a V.I.G. 10 ion gauge) were achieved routinely.

A total of six highly sensitive M06 leak valves (see figure 1.10) controlled the flow of B.O.C. grade X inert or other gases.

The specimen support cylinder was clamped by means of copper jaws (see figure 1.11) which were directly connected to a cryoganic system comprising of an inner and outer dewar which was filled with coolant (usually liquid nitrogen).

The specimen high voltage was supplied by a 30kV Brandenburg power supply equipped with an easily adjustable polarity such that field emission microscopy could also be performed.

The microscope was also fitted with a channel plate converter image intensifier (Turner et al. (1969)) which required two Brandenburg H.T. power supplies to control the image intensity and the focus. An external permanent magnet (approx. 150 gauss) was also required to focus the image. Not only does the use of the channel plate drastically reduce the photographic exposure times to about 10 seconds (at an imaging gas pressure of about

1×10^{-4} Torr), but it also makes practicable the use of gases other than helium for imaging. Hence gases such as neon and argon have been used successfully in situations where a reduced applied electric field has been necessary (Lewis and Gomer (1969), Van Oostrom (1970(a)) and Cranstoun and Pyke (1971)).

Several modifications and improvements have been made to the original design of the field-ion microscope and these have been described in detail by Summers (1973). Modifications made necessary by the inclusion of the ion source and the development of a specimen temperature controller will be described briefly where relevant.

CHAPTER TWO

ZONE PLATES AND MOIRÉ PATTERNS

2.1 Introduction

The purpose of this chapter is to establish the groundwork required in order to draw various optical analogues which are subsequently shown to exist with the surface atomic structure of a clean field-ion emitter. These optical analogues enable new information to be extracted from field-ion micrographs. Almost all the techniques required to perform these analyses are developed in this chapter. Although these techniques are primarily developed for their subsequent use in field-ion microscopy, they also possess importance in certain optical applications such as synthetic holography. Many of the techniques introduced for the mathematical solution of moiré patterns are new and it is felt that these techniques possess a potentially wide applicability.

Initially, the focusing and geometric properties of various types of zone plate are considered. In particular the distinction between the Fresnel zone plate and the binary zone plate is investigated. This is of crucial importance in chapter 3 where it is shown that the image of a single field-ion plane can be considered to be a kind of binary zone plate.

The moiré phenomenon is then introduced. The philosophy and the various mathematical methods of solving problems involving the moiré effect are briefly discussed. Finally two particular moiré patterns are systematically analysed. Both of these moiré patterns are important in the optical analogue interpretation of field-ion micrographs. The first

to be considered is the moiré pattern produced by overlapping zone plates. This situation is shown to be the optical analogue of the field-ion image in chapter 3, the mode of formation of moiré zone plates being similar to the geometric formation of field-ion planes. The second moiré pattern to be examined is that formed by overlapping a zone plate and a grid structure. The grid is analogous to the structure of the crystal lattice and the zone plate corresponds to a projected contoured envelope similar in shape to a field-ion emitter.

Thus in subsequent chapters it is shown that field-ion images may be interpreted in terms of moiré pattern formation and that such an analysis enables new data to be extracted. Conversely, a new insight into the mechanism of field-ion image formation is gained from comparing actual images with those obtained by moiré simulation, using several overlapping zone plates of an appropriate nature. The analysis used relies heavily on the new methods of treatment developed in this chapter.

2.2. Introduction to the zone plate

The zone plate is a familiar pattern in physical optics. It occurs naturally as the interference pattern produced by two coherent wavefronts, or as the hologram of a point object (Rogers (1950)). If the zone plate is fabricated in the form of an optical transparency, with alternative opaque and transparent half-period zones, it behaves somewhat as a lens, (Jenkins and White (1964)). When the transparency is illuminated with a plane wave of monochromatic light, part of the light is diffracted into a converging spherical wave to form a bright focal spot while some of the light

is diffracted into a diverging wave which appears to emanate from a virtual focal spot. The zone plate behaves simultaneously as a positive and negative lens.

There are many different types of zone plate, but the best known type is the Fresnel zone plate which does not occur naturally, but has to be constructed mechanically (for instance, Rogers (1966)) or by computer (Engel and Herziger (1973)). The distinction between the Fresnel and non-Fresnel type of zone plate is not only important in holography, but also in the analogy drawn between the binary zone plate and the field-ion plane (see chapter 3). In this section the various forms of zone plate will be characterised and a method will be developed for calculating the focal length in terms of zone radius and zone separation. These formulae are subsequently important in the interpreation of the moiré pattern produced by overlapping zone plates.

2.2.1 The Fresnel zone plate

The various properties of the Fresnel zone plate have been investigated extensively which is not surprising in view of its many applications. Zone plate theory based on holography has been developed by Horman and Chau (1967). The possibility of utilising its chromatic properties in spectroscopy has stimulated investigation into its imaging properties (Childers and Stone (1969)), particularly resolving power, (Stigliani and Mittra (1967)). More recently investigation has been prompted in its use as a focusing device for vacuum ultraviolet radiation and soft X-rays (Pfeifer, Ferris and Yen (1973)).

2.2.1.1 The geometrical properties of the Fresnel zone plate

The Fresnel (or Soret) zone plate is composed of a series of concentric circles, the radii of which are approximately proportional to the square root of an integer n, where n=0,1,2 and is the number of the ring. Half period zones are formed by making alternate zones completely opaque and transparent as illustrated in figure (2.1(a) and (b)). The Fresnel zone plate then consists of annular zones each of equal area. The general cartesian equation of the Fresnel zone plate is:-

$$x^2 + y^2 = nr_1^2 \qquad \ldots\ldots(2.1)$$

where r_1 is the radius of the first ring.

2.2.1.2. The focal properties of the Fresnel zone plate

A plane wave of monochromatic light when transmitted through the transparent zones interferes constructively at a point on the zone plate axis; this point is termed the focal point and is situated at a distance f from the zone plate, where f is the focal length. The Fresnel zone plate exhibits an infinite series of real (and virtual) focal points at distances $\pm\ ^{f}/_{2P+1}$ where P = 0,1,2...corresponding to the odd order diffraction patterns. The intensity of the point image is a maximum when P=0; this is the condition for the principal focal length. The intensity of successive images then decreases as P increases, the number of observable images depends on the aperture size of the zone plate and the number of zones.

The principal focal length of a Fresnel zone plate is usually given by the formula:-

$$f = \frac{r_n^2}{n\lambda} \qquad \ldots\ldots(2.2)$$

Figure 2.1 (a) A Fresnel zone plate.

(b) A Fresnel zone plate that is $\pi/2$ out of phase to that zone plate illustrated in (a).

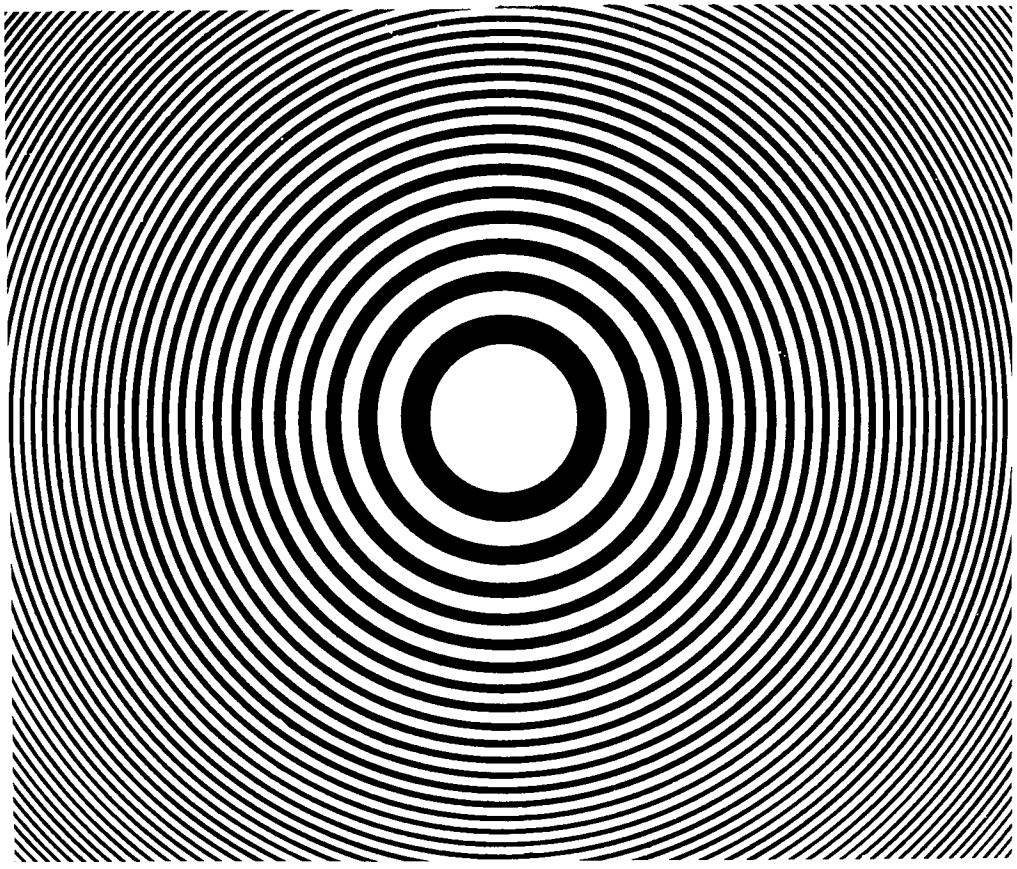

(a)

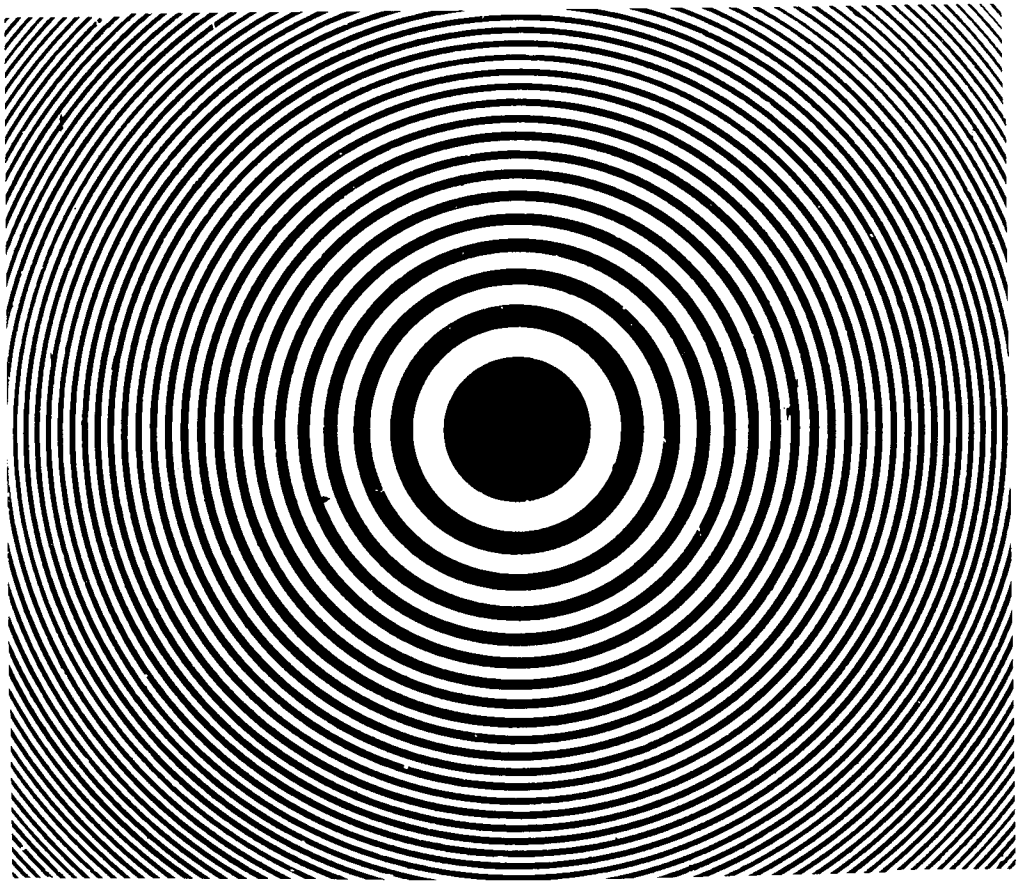

(b)

hase to that

where r_n is the outer circle defining the nth zone. It is also possible to obtain an expression for f in terms of the zone separation and average zone radius (see figure 2.2). This is sometimes more convenient particularly in the interpretation of the moiré pattern formed by the superposition of zone plates, from equation (2.1):

$$r_n^2 = nf\lambda \qquad .....(2.3)$$

and

$$r_{n+1}^2 = (n+1)f\lambda \qquad .....(2.4)$$

where r_{n+1} is the radius of the outer circle defining the (n+1)th zone.

From equations (2.3) and (2.4)

$$r_{n+1}^2 - r_n^2 = f\lambda \qquad .....(2.5)$$

Expanding:

$$(r_{n+1} + r_n)(r_{n+1} - r_n) = f\lambda \qquad .....(2.6)$$

Now, $(r_{n+1} - r_n)$ is the width of the (n+1)th zone, that is, Δr, and $(r_{n+1} + r_n)$ is twice the average radius of that zone, that is, r (see figure 2.2a).

Therefore from (2.5):

$$f = \frac{2r\Delta r}{\lambda} \qquad .....(2.7)$$

2.2.2.3. The phase factor of a Fresnel zone plate

All equations so far encountered for the focal length of a Fresnel zone plate have assumed that in equation (2.1) the factor multiplying r_1^2 is always integral. This is not always the case, for instance compare figure 2.1(a) and figure 2.1(b), each of which depicts a Fresnel zone plate. The central zone of the zone plate shown in figure 2.1(a) is transparent while the zone plate depicted in figure 2.1(b)

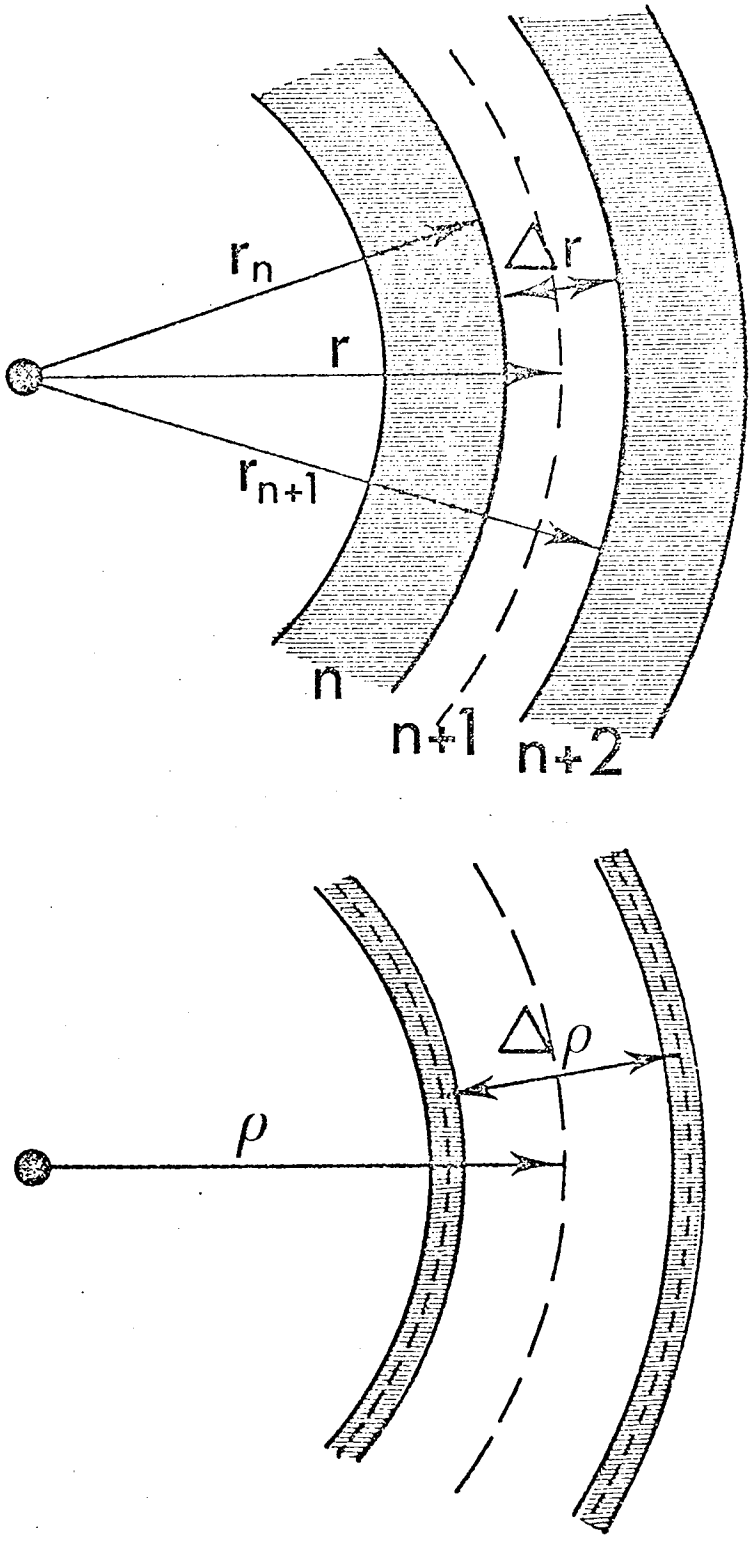

Figure 2.2. (a) Circle radius and zone width for a Fresnel zone plate.
(b) Zone radius and zone separarion for a binary zone plate.

displays an opaque central zone. The phase of these two Fresnel zone plates differs by $\pi/2$. A phase term δ is devised where $0 \leqslant \delta \leqslant 1$ such that equation (2.2) becomes:

$$r_n^2 = (n+\delta)f\lambda \qquad .....(2.8)$$

The question now arises, is the focal length of a zone Fresnel zone plate independent of phase?

Inserting δ into equation (2.3) and (2.4):

$$r_n^2 = (n+\delta)f\lambda \qquad .....(2.9)$$

$$r_{n+1}^2 = (n+1+\delta)f\lambda \qquad .....(2.10)$$

then:

$$r_{n+1}^2 - r_n^2 = f\lambda \qquad .....(2.11)$$

therefore:

$$f = \frac{2r\Delta r}{\lambda} \qquad .....(2.12)$$

Thus the phase factor can take any value between zero and one, corresponding to 180°, but the focal length always remains constant. The phase factor of a Fresnel zone plate is easily measured; a plot of r_n^2 against n gives a straight line which intersects the n axis at between n=0 and n=1. Equation (2.8) also shows that the focal length of the zone plate is given by the gradient of this line.

2.2.2. Other types of zone plate

Rogers (1950) appears to be the first to recognise the existance of a non-Fresnel type of zone plate when investigating the analogy between the zone plate and the hologram. Holographic theory has in turn been used to describe various types of zone plate encountered when mutually coherent spherical and plane wavefronts interfere (Horman and Chau (1967)). Waldman (1966) and more recently Shulman (1970)

have both considered in detail the effects of various transmission amplitude functions, in particular Shulman compares the imaging properties of these zone plate variations.

By definition, the Fresnel zone plate is constructed of annular zones of constant zone area $\pi\lambda f$ and is also characterised by sharply defined radius boundaries at $r_n = (n\lambda f)^{\frac{1}{2}}$. If the amplitude transmittance of a Fresnel zone plate is plotted against radius, a discontinuous square wave function is obtained as illustrated in figure 2.3. Considering real foci only, besides the bright principal focus at f, there also exists higher order foci, located successively at distances equivalent to f/3, f/5, f/7...etc.

Fresnel zone plates are never obtained naturally by the interference of two coherent wavefronts, even when the photography is distortion free. The zone plate produced under these conditions does not possess sharply defined radius boundaries, neither does it possess a series of images. The transmission function of an optically produced zone plate in terms of its radius is an increasing frequency sinusoidal waveform as shown in figure 2.3. (Shulman (1970)). This zone plate, which has been termed a Gabor zone plate, has only one real focus, no higher order foci exist. One rather curious aspect appears if the relative intensities of the principal focal spot of the Fresnel and Gabor zone plates are compared. Although the Gabor zone plate is capable of forming only one image compared with the theoretically infinite number of the Fresnel zone plate; the intensity of the image point of

Figure 2.3 The transmission functions for various types of zone plate

(a) Fresnel zone plate

(b) Binary zone plate

(c) Gabor zone plate

Figure 2.4 A binary zone plate.

ous types of zone plat

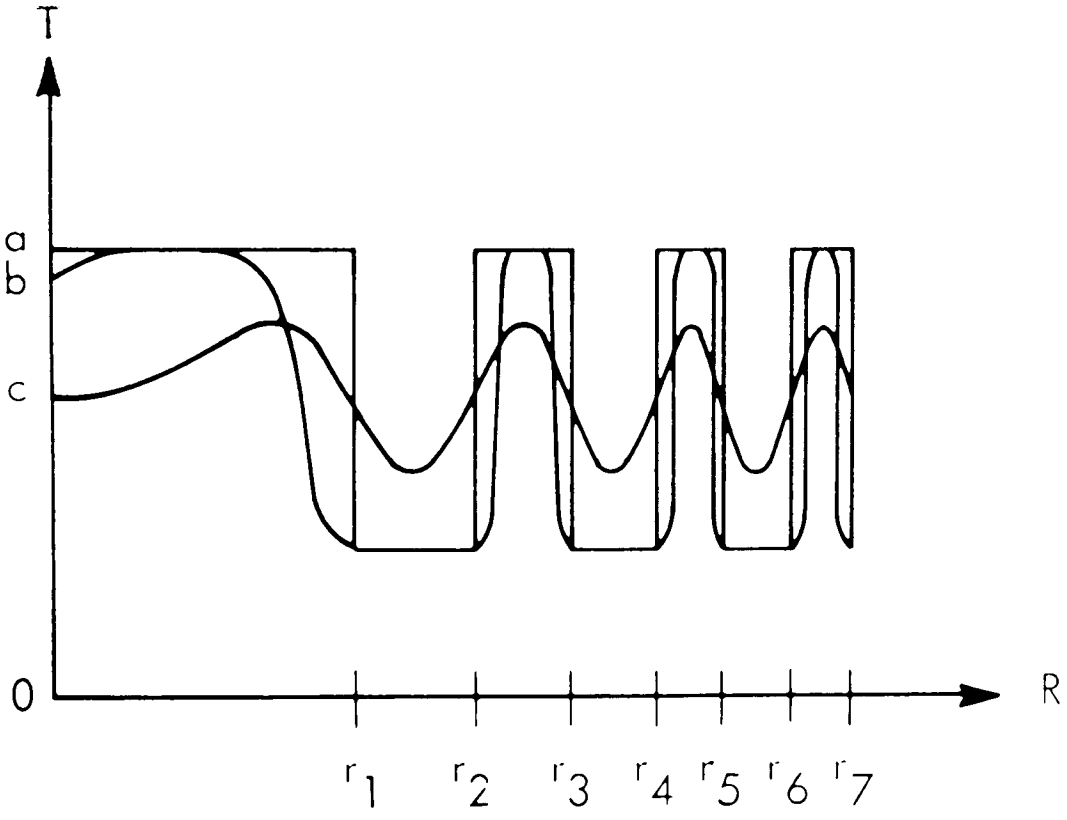

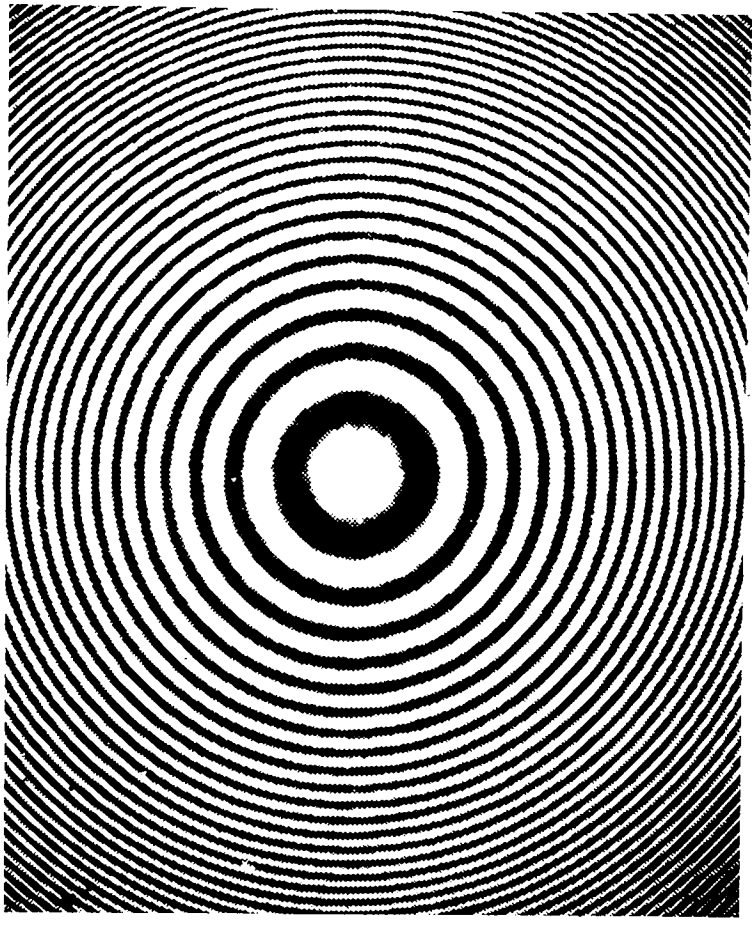

the Gabor zone plate is $(\pi/4)^2$ that of the principal image intensity of the Fresnel zone plate (Horman and Chau (1967)).

Although Gabor zone plate is theoretically feasible in practice it is rather more difficult to obtain. The non-linear nature of the photographic process distorts the contrast of the optically produced zone plate such as to produce a binary (or generalised) zone plate, (Horman and Chau (1967)). The effect of this non-linearity is depicted in figure 2.3, the crests of the sine wave are truncated and the troughs flattened such that an approximately square wave function is produced. Although the contrast of the binary zone plate produces well defined radius boundaries, they do not all occur at $(n\lambda f)^{\frac{1}{2}}$, a point illustrated by figure 2.4. This figure, which is a photograph of an optically produced zone plate, shows that although the area of the full period zones (transparent and opaque) are equal, the area of the half period zones are unequal. The relative sizes of these areas depends on the length of exposure of the photographic plate. The maximum diffraction efficiency at the principal focus was found by Chau (1969(a)) to occur at a density of 0.5. The binary zone plate is also characterised by its imaging behaviour; not only does it produce the principal focal point,but also produces higher order foci located at F/2, f/3, f/4, f/5..., etc. corresponding to both odd and even diffraction terms.

The focal length of a binary zone plate is more difficult to define than the Fresnel zone plate because it does not possess a constant periodicity; r_n is not

necessarily proportional to n. However it is possible to construct an equation similar to equation (2.7) although re-definition of certain dimensions is required. In equation (2.7) the quantity Δr has been defined for a Fresnel zone plate. For the case of a binary zone plate Δr must be replaced by $\Delta\rho$, the zone separation (see figure 2.2(b)), where $\Delta\rho = 2\Delta r$. In order to make the notation consistant r must be replaced by ρ, the average radius of alternate zones.

Hence for other types of zone plate:

$$f = \frac{\rho\Delta\rho}{\lambda} \qquad \text{.....(2.12)}$$

Just as in the case of the Fresnel zone plate it can be shown that the focal length of a binary zone plate is independent of the phase factor. Once again δ can take values $0 \leqslant \delta \leqslant 1$.

There also exists a number of types of zone plate which possess a novel appearance, but which are not directly relevant to the theme of this thesis. Nevertheless these figures are of importance in optics and hence deserve mention in passing. For example, the linear zone plate (figure 2.5(a)) has an action similar to the cylindrical lens. The so called 'quantized' zone plate is illustrated in figure 2.5(b) has been used in character recognition work (Leifer, Rogers and Stephens (1969)). The moiré pattern produced by overlapping two of each of these zone plates consists of a series of moiré linear zone plates or moiré 'quantized' zone plates respectively.

Figure 2.5 (a) The linear zone plate.

(b) The quantized zone plate.

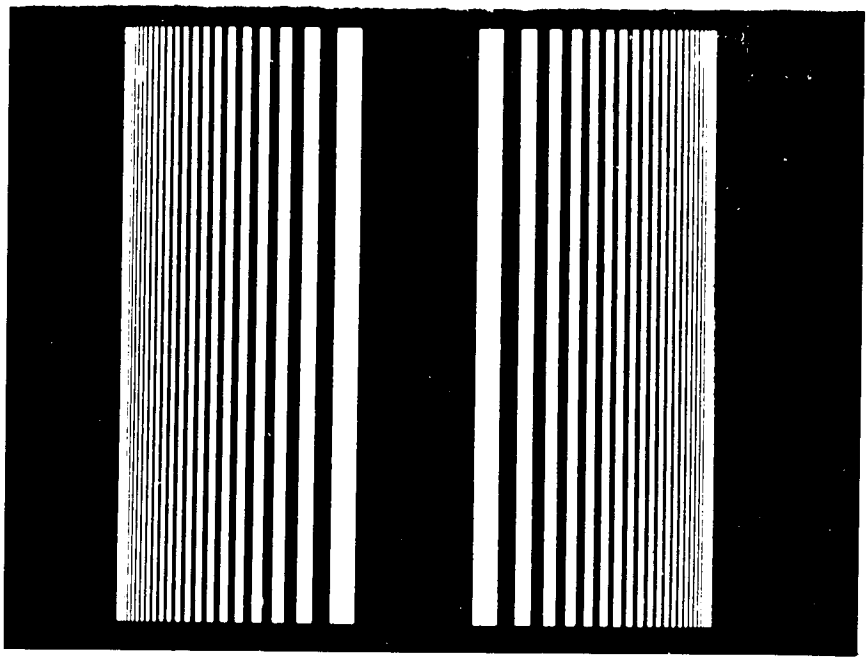

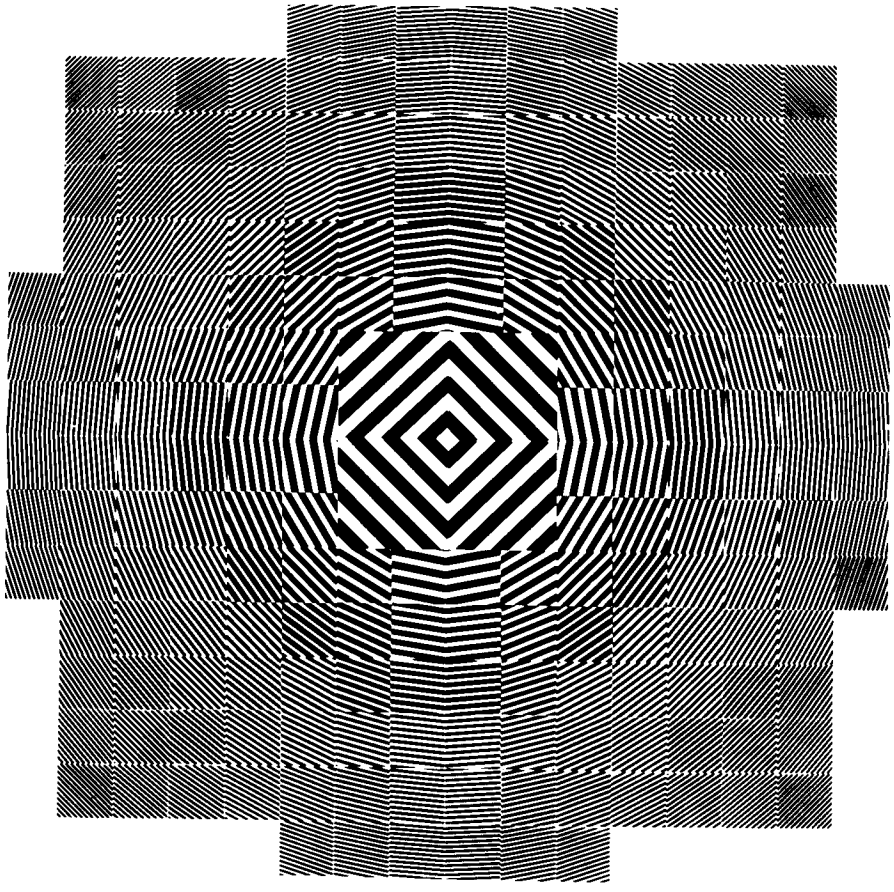

2.3 Introduction to moiré patterns

Moiré patterns are formed whenever two or more periodic structures are superimposed. For the moiré effect to be discernible to the eye, there is a general requirement that these periodic structures should contain alternate solid and open regions. This requirement is often met in everyday life. The word moiré itself, is derived from the French word for "watered" and it is often used in connection with a fabric called moiré silk. This fabric produces a rather pleasing shimmering effect which is due to the moiré pattern caused by overlapping weave.

Unfortunately, the moiré phenomenon is not always so beneficial. For example, the moiré effect has been shown to be a serious drawback to the television transmission of holograms, (Rogers and Leifer (1970)). The previous section drew attention to the zone plate analogy with holography (Rogers (1950)). If a Fresnel zone plate is transmitted onto a television screen, a moiré pattern is formed consisting of a symmetrical array of zone plates formed to each side of the original (see figure 2.6). These moiré zone plates are formed by the interaction between the Fresnel zone plate and the television raster lines, which acts effectively as a fine grating, (this moiré pattern is subsequently analysed in section 2.8.) Thus, when a hologram, which has been transmitted via a television receiver, is reconstructed, "ghost" images appear in positions corresponding to the positions of the moiré zone plates.

Moiré patterns are also a potential hazard and artifact in printing. The periodic array of half tone dots used to print newspaper and magazine illustrations

sometimes interacts with a periodic content within the illustration. Although this effect can be minimised by arranging the angle made by the dots with the offending illustration, many examples can be found particularly in physics journals. For example, figure 2.7 is an illustration which appeared in the literature (Leifer, Walls and Southworth (1973)) and should be compared with figure (2.16) which is the original. The faint zone plates appearing in figure (2.7) and not appearing in figure (2.16) are spurious and are the result of the superimposition of the half tone dot array (which is similar to a grid), on the various zone plates in the original.

The first moiré pattern to be analysed was that formed by the overlap of two diffraction gratings and it was carried out by Lord Rayleigh (1874). In this way he was able to test the quality of his gratings by taking advantage of the huge moiré magnification; a discontinuous moiré pattern implies a defective grating. This technique has since been extended to test replica diffraction gratings and has been investigated in detail by Guild (1956).

The development of moire techniques in engineering has been extensive especially as a precise means of measurement. Moiré patterns are also particularly important in the analysis of strain, this aspect has stimulated a number of reviews, the most notable of which are by Theocaris (1969) and Durelli and Parks (1970). By comparison, the physical interpretation and exploitation of the moiré phenomenon is not quite so advanced. Recently, however popular articles by Oster and Nishijima (1963) and Stecher (1964) appear to have stimulated a greater aware-

Figure 2.6 When a zone plate is transmitted onto a television screen, a series of moiré zone plates are formed. Thus, when a hologram is transmitted onto a television screen, 'ghost' images appear. (After Rogers and Leifer (1970)).

Figure 2.7 Moiré pattern hazards in printing. This figure which has been printed using half tone dots should be compared with the original (figure 2.16). The zone plates appearing in this figure and not appearing in figure 2.17 are spurious and are a result of the superposition of the half tone dot array.

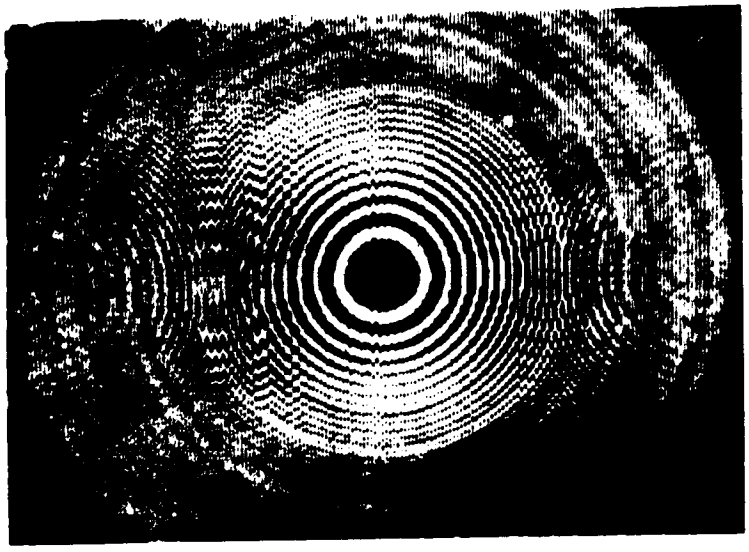

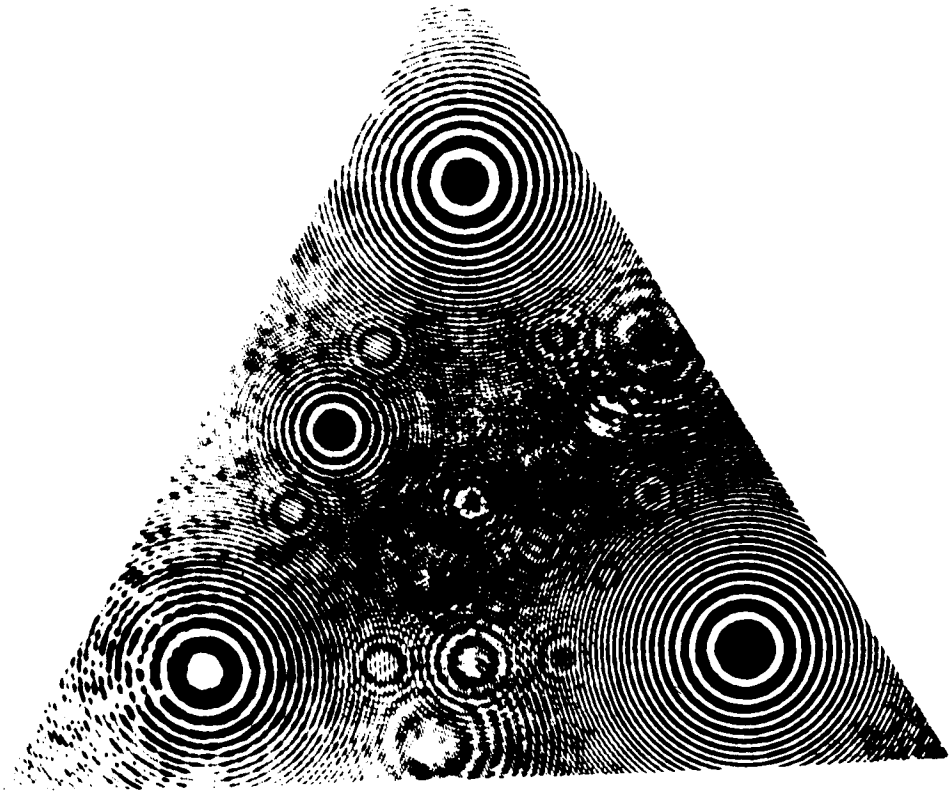

ness of the subject. Fortunately, an important contribution has since been made by Oster, Wasserman and Zwerling (1964) who were able to formulate, in a completely general manner, an indicial representation of the moiré effect enabling a simple mathematical analysis of any moiré pattern, provided the structure of the overlapping figures is known. However, there still remains a large number of physical situations where the moiré analogy has not received a sufficiently thorough investigation.

2.4 The philosophy of moiré patterns

A moiré pattern has been defined by Oster, Wasserman and Zwerling (1964) as the locus of points of intersection of two superimposed figures. The moiré phenomenon has also been variously described as an interference pattern (Durelli and Parks (1967)) and as a diffraction effect (Guild (1956)). The moiré effect is observable if certain criteria are met. The overlapping two dimensional figures must contain some kind of periodicity and must involve alternate transparent and opaque zones. The visual detection of the moiré effect is also facilitated if the physical dimensions of the elements composing the overlapping figures are comparable. However, under the original definition of a moiré pattern, the moiré pattern need not be visible.

Consider the simplest case of the superimposition of equispaced parallel lines (or grating). If the angle θ between the gratings is changed, then as θ increases, the moiré fringes will change and at some point a different fringe system appears to take form. Let us examine this system more closely. Initially, let the two gratings lie

superimposed such that $\theta = 0^{\circ}$ and no moiré effect is apparent. Now rotate one grating with respect to the other; immediately a coarse, dominant moiré pattern appears consisting of straight parallel lines (see figure 2.8(a)). These lines move closer and closer together as θ increases until at $\theta = 45^{\circ}$ the moiré effect is almost indistinguishable due to the uneveness of the fringes and their close proximity. This moiré system continues to fade until $\theta = 180^{\circ}$ and the gratings are exactly superimposed once more. At $\theta = 90^{\circ}$, however, two fringe systems become equivalent although at first sight it is difficult to trace the moiré effect at all (see figure 2.8(b)). As θ increases from 90° to 135°, a new fringe system becomes more dominant and is the mirror image of the first. This system is most readily visually detected when θ is $> 135^{\circ}$. Figure 2.8(c) illustrates this moiré pattern at θ above 150°. This fringe system becomes more and more dominant as the fringe spacing widens until at $\theta = 180^{\circ}$ (or 0°) rhe fringe spacing is infinite. Rotation clockwise ($90^{\circ} > \theta > 0^{\circ}$) results in the first set of moiré fringes and these are known as the subtractive moiré pattern, whereas rotation anticlockwise $180^{\circ} > \theta > 90^{\circ}$ shows the additive moiré pattern. The reasons for this terminology will become clear later when the indicial equation representation method is investigated. The point at which $\theta = 180^{\circ}$ is known as the commutative moiré boundary. Theocaris (1969) has defined the boundary as the region which contains individual rectangles or squares. Hence a second commutative moiré boundary must exist at $\theta = 90^{\circ}$. This boundary is the condition at which the visibility of the

Figure 2.8. Illustrating the concept of a commutative moiré boundary. Θ is the angle between the two gratings.
(a) represents the subtractive moiré effect.

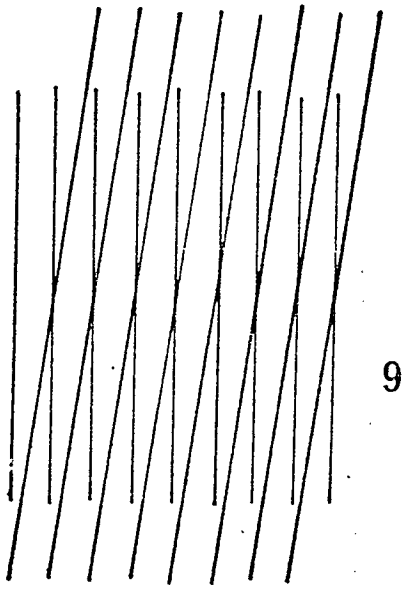

(a)

$90^{\circ} > \theta > 0^{\circ}$

(b) represents the conditions where both the subtractive and the additive moiré conditions are equivalent.

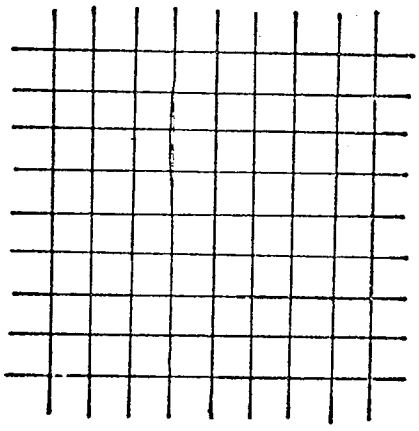

(b)

$\theta = 90^{\circ}$

(c) represents the additive moiré effect.

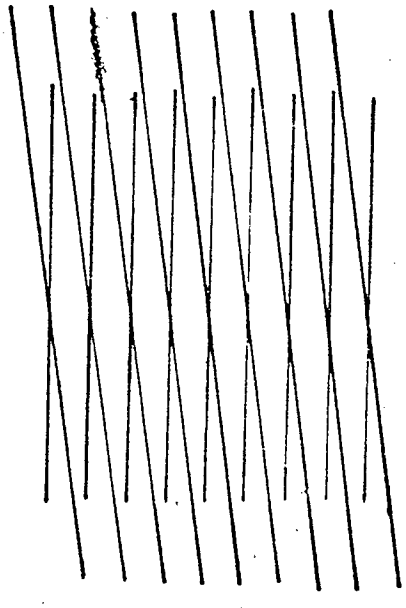

(c)

$180^{\circ} > \theta > 90^{\circ}$

moiré pattern is decided. However both the additive and subtractive moiré patterns extend over the full range of intersecting angles even thought they may not be visually discernible. Indeed, higher order moiré patterns may exist which may never be perceivable whatever the conditions. Hence in the case of some physical analogue situations, care must always be taken not to discard the possibility of certain moiré fringes, just because their visual perception is difficult.

Although a moiré pattern is the locus of points of intersection, visually it may be something quite different. Close inspection of figure (2.8(a)) for instance will reveal that the straight line moiré fringe perceived by the eye is in reality composed of a sawtooth configuration comprising of parts of the two overlapping gratings plus the intersection point. The eye is able to integrate over this configuration, if the interelement spacing is not too coarse, and hence able to conceive the straight line. Obviously, the greater the number of lines the grating possesses per unit area, the less important this sawtooth becomes. Thus as a general rule the greater the number of overlapping elements available the greater the quality (and hence visibility) of the moiré pattern.

Although the eye has relatively little difficulty in picking out the moiré fringe formed by the opaque intersections, this is not the case for the corresponding transparent fringe. Theocaris (1969) has shown that there are good physical reasons for this. The gratings used in figure (2.8) for instance have a transmissivity that is either totally opaque or transparent, there is no

smooth variation incorporating grey tones. Hence when two gratings are overlapped the intersecting points can be made up in three different ways:-

a) opaque element on opaque element

b) opaque element on transparent element

c) transparent element on transparent element

The intersections formed by situations (a) and (b) produce opaque intersections and only (c) produces a transparent intersection. There can be no continuous transparent intersection and hence no completely transparent fringe exists, making their visual detection difficult.

The major importance of the moiré phenomenon is its role as an analogue computer (Oster and Nishijima (1963)). The moiré pattern is able to obtain a solution to the interference between two periodic functions and is then able to visually display it, making it ideal as a teaching aid. Initially, however, the physical system which it is wished to simulate must first be made suitable for moiré. It must be contoured and prepared in order to meet the requirements for a visual moiré pattern. For most physical systems, a natural periodicity exists and its contouring in terms of equal increments of the particular physical dimension in question is not difficult. Oster has prepared many contoured patterns of conical sections by a method of projective geometry. Each element in the pattern corresponds to taking increments of equal height over the conic and then projecting this increment orthogonally into the plane. For instance, a Fresnel zone plate is shown to be the orthographic projection of a parabaloid which is contoured such that each zone corresponds to a fixed

incremental height. This contouring process is not just limited to physical objects, but is equally well applicable to such subjects as electrostatics where equal increments of equipotential may be taken. In the case of field-ion microscope specimens, contours have been taken in order to correspond to successive atomic layers (see chapter 4). This contouring technique can also be applied to light, acoustics, electromagnetic radiation and water waves, to name but a few situations. The moiré pattern analogue technique also has the advantage that it is not only useful in the interpretation of situations involving two physical systems, but also effortlessly produces the solution to any multifunctional problem.

2.5 The mathematical solution of moiré patterns

Many methods exist for the mathematical interpretation of moiré patterns. Several authors have shown that in the case of superimposed parallel grids, a simple geometrical argument can be successful. A vectorial approach has also been invoked for this particular pattern (Rogers (1959)). The most general method, however, for solving the mathematics of moiré patterns is that developed by Oster, Wasserman and Zwerling (1964) and is termed the indicial representation method. One further technique exists whereby the transmissivity of the overlapping figures is considered, this technique has been largely neglected although it could prove the most generally applicable method of all. In this section, these methods are explained and in each case an example is used in order to compare and contrast their relative merits.

2.5.1. The geometric interpretation of moiré patterns

Several authors have followed Lord Rayleigh (1874) in using simple geometry to solve the moiré pattern produced by overlapping two sets of parallel, equispaced straight lines. Notable amonst these authors have been Nishijima and Oster (1964) and Stecher (1964). This method of solution is rather limited in practice because it demands that the moiré pattern must be easily geometrically related to the original overlapping figures. For this reason it has only been used to analyse the pattern produced by overlapping equispaced parallel lines although Nishijima and Oster (1964) have used this technique to describe the moiré pattern involving overlapping figures consisting of parallel lines whose spacing conformed to a Gaussian distribution.

Consider the example of two overlapping gratings inclined at an angle θ. The first grating consists of lines separated by a distance a, the second grating consists of lines separated by a distance b, (where $a \neq b$). From figure 2.9 it can be seen that the moiré pattern consists of equidistant straight lines with spacing d. These fringes are represented by the dotted lines, and make an angle with the b spaced grating of ψ.

It follows directly that:-

$$\sin \psi = \frac{b \sin \theta}{(a^2+b^2-2ab\cos \theta)^{\frac{1}{2}}} \qquad \ldots\ldots(2.13)$$

and

$$d = \frac{ab}{(a^2+b^2-2ab\cos \theta)^{\frac{1}{2}}} \qquad \ldots\ldots(2.14)$$

of course, when a = b

$$d = \frac{a}{2 \sin \theta/2} \qquad \ldots\ldots(2.15)$$

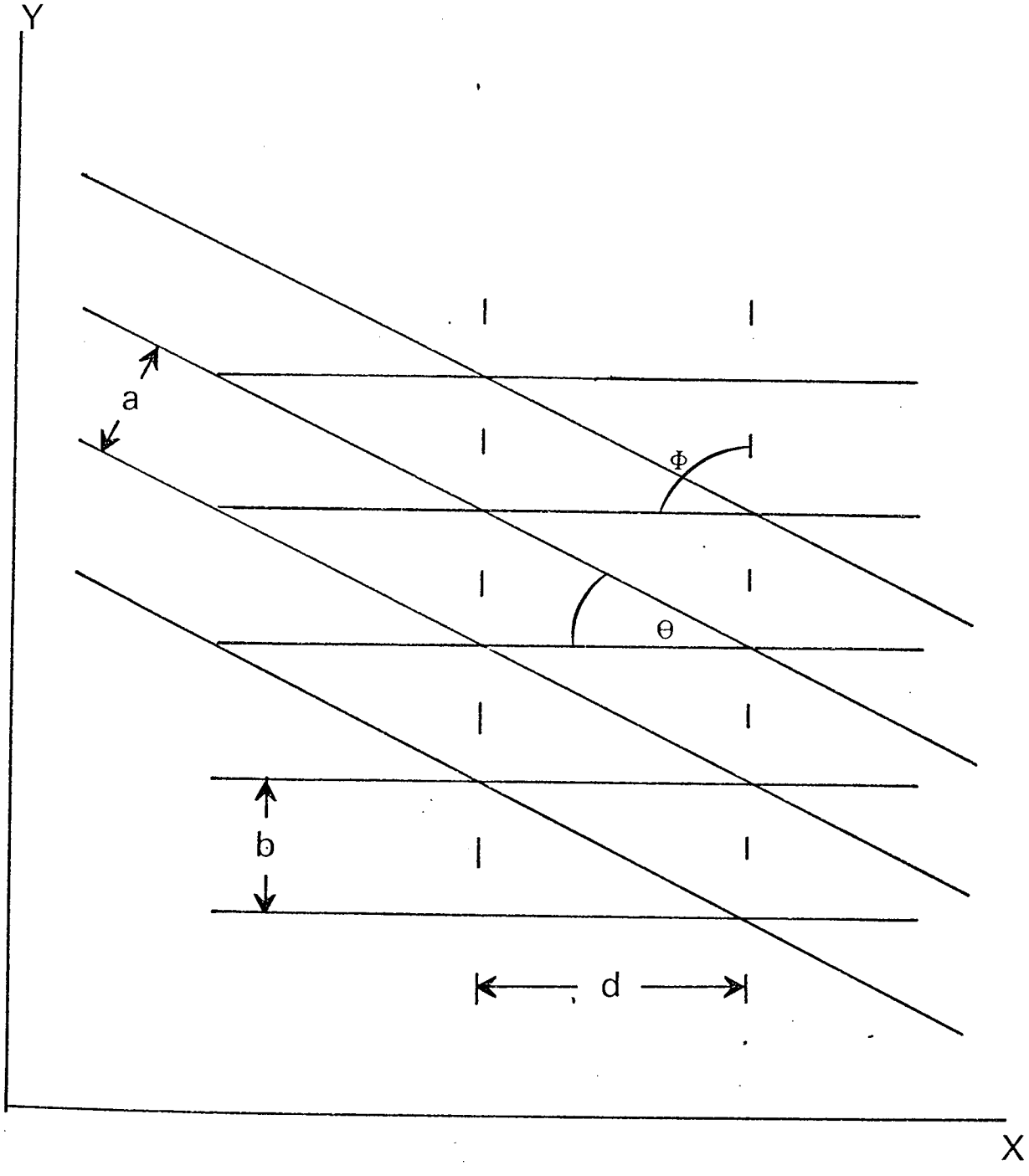

Figure 2.9. A diagram of the moiré pattern produced by overlapping two gratings of spacing a and b respectively. The moiré pattern consists of a grating of spacing equal to d (dotted lines).

2.5.2. The indicial representation method for the analysis of moiré patterns

This method was developed by Oster, Wasserman and Zwerling (1964) and is the most commonly used approach for handling problems concerned with the moiré phenomenon. The method has been slightly modified subsequently by Oster (1964) and Durelli and Parks (1967).

Fundamentally, each set of overlapping figures is considered to be an indexed family of lines or curves. It is found that the resulting moiré fringes are most pronounced when the indices at the intersection satisfy certain criteria. Consider the superposition of two families of curves. The first indexed family of curves is represented by the equation:

$$F(x,y) = \psi(h) \qquad \ldots\ldots(2.16)$$

The second indexed family of curves is likewise represented by the equation:

$$G(x,y) = \phi(k) \qquad \ldots\ldots(2.17)$$

The quantities h and k are indexing parameters running over some subset of real parameters and x and y are the co-ordinates of any point on the figure. The function $F(x,y)$ and $G(x,y)$ determine the geometrical form of the figures, while the functions $\psi(h)$ and $\phi(k)$ determine the spacing of the elements of which the figure is composed. The superposition of the figures represented by equations (2.16) and (2.17) produces a moiré pattern which is a set of curves for which p satisfies the indicial equation:

$$\theta(h,k) = p \qquad \ldots\ldots(2.18)$$

where p runs over some subsets of real integers.

The conditions for the formation of a visible moiré pattern are usually satisfied when $\theta(h,k) = h \pm k$

When the positive sign is taken in equation (2.19), the additive moiré pattern is formed, if the negative sign is taken the result is the subtractive moiré pattern.

However, the most general equation for moiré pattern formation, whether visible or non visible, is of the form:

$$ah \pm bk = p \qquad \text{.....(2.20)}$$

where a and b are rational numbers taking values 0,1,2,3.. etc. (Oster (1964)).

An example of the use of this indicial (or parametric) equation method should indicate how the technique avoids some rather inelegant mathematics. Reconsider the moiré pattern formed by the two gratings superimposed in figure 2.9. The first grating is indexed such that each opaque element is given a value $h=0,\pm1,\pm2,\pm3...$etc., and similarly for the second grating $k=0,\pm1,\pm2,\pm3...$etc. The equation of the first grating then becomes $x = bh$ .....(2.21)

where $F(x) = \frac{x}{b}$ and $\psi(h) = h$.

For the second grating:

$$y = x \cot\theta - \frac{ak}{\sin\theta} \qquad \text{.....(2.22)}$$

where $G(x) = \left(\frac{x\cos\theta - y\sin\theta}{a}\right)$ and $\phi(k) = k$

The moiré fringes represented by the dotted line in figure 2.9 corresponds to the subtractive moiré pattern and is the case satisfied by $a = b = 1$. Thus the indicial equation for this situation is:-

$$h - k = p \qquad \text{.....(2.23)}$$

Substituting for h and k from equations (2.20) and (2.21), the equation for the moiré pattern is:-

$$y = x\left(\frac{b\cos\theta - a}{b\sin\theta}\right) - \frac{pa}{\sin\theta} \qquad \text{.....(2.24)}$$

which can be rewritten as:-

$$y = x \cot \psi - \frac{pd}{\sin\psi} \qquad \ldots\ldots(2.25)$$

Equating corresponding coefficients:-

$$d = \frac{ab}{(a^2+b^2-2ab\cos\theta)^{\frac{1}{2}}} \qquad \ldots\ldots(2.26)$$

and $$\sin\psi = \frac{b\sin\theta}{(a^2+b^2-2ab\cos\theta)^{\frac{1}{2}}} \qquad \ldots\ldots(2.27)$$

If equations (2.26) and (2.27) are now compared with equations (2.13) and (2.14), they will be found to be identical. The indicial equation method has reproduced the result obtained by pure geometric calculation.

The indicial equation technique is invaluable when figures consisting of two dimensional elements are handled. A geometric solution to the moiré pattern formed by these more complicated situations becomes very unwieldy and impractical. The indicial equation approach is especially convenient when interpreting the moiré pattern formed by the overlap of a number of figures. In these cases the indicial equation is simply expanded and takes the form

$$ah \pm bk \pm cl.... = p \qquad \ldots\ldots(2.28)$$

The number of terms on the left hand side of this equation corresponds to the number of figures overlapped. As an example, the reader is referred to section 2.6.6. where the case of three overlapping zone plates is considered.

2.5.3. Transmission function representation method

Theocaris (1969) has described the process of moiré pattern formation as a mechanical interference phenomenon. Herein lies a clue to a new and important technique for the mathematical solution of moiré patterns because it

implies that moiré effect is caused by the mechanical interception of light by the rulings of the figure or the points of intersection. Only the moiré effect produced by the combination of gratings has ever been investigated in this way. Both Theocaris (1969) and Durelli and Parks (1970) have considered this simple case because of its importance in strain analysis. Subsequently, however, the moiré pattern formed by the superposition of zone plates will be considered using this technique (section 2.8).

The central concept of this technique is that any figure can be described in terms of its transmission function. For example the simple grating can be considered to have a transmission function rather like a square wave pattern as illustrated in figure 2.10. The transmittance is either full or zero. However, if we follow Theocaris (1969) and describe this function as a sum of sinusoidal functions then the mathematics become very complicated. Instead, a sine wave approximation is made (Shulman (1970)) such that the transmission function T(x) of the grating (or any other figure) can be described by the expression:-

$$T(x) = \tfrac{1}{2}\left(1 + A \sin \frac{2\pi X}{p}\right) \qquad \text{.....(2.29)}$$

where A is a transmission factor, x is a distance and p is the pitch or wavelength of the particular function used. The numbers $\frac{1}{2}$ and 1 are utilised to preserve the d.c. nature of light. The sine wave approximation is illustrated with the square wave in figure 2.10.

Let us now consider the total transmittance after we have combined any two figures face to face as illustrated in figure 2.11. If incoherent illumination of intensity

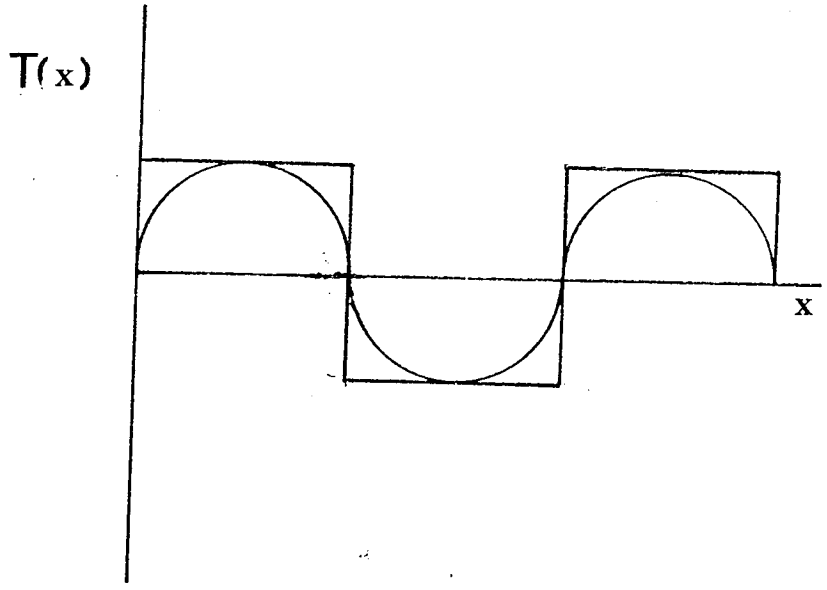

Figure 2.10. The sine wave approximation to a square wave.

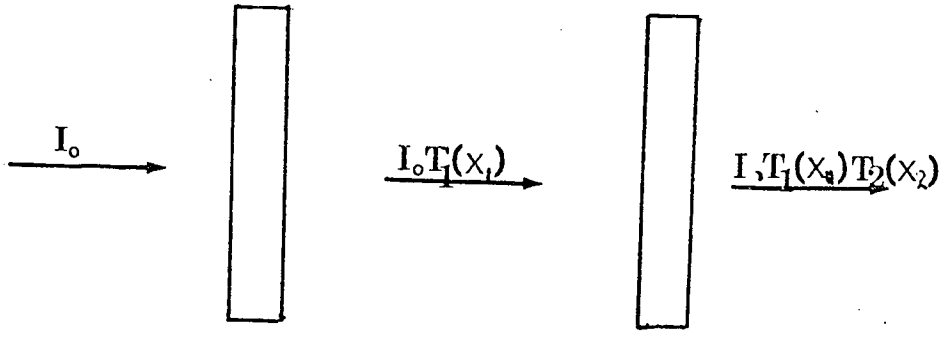

Figure 2.11. The total transmissivity of two overlapped functions. Light of incidence intensity I_o passes through the first system and emerges with intensity $I_oT_1(x_1)$, subsequent passage through a second system modifies the intensity still further to $I_oT_1(x_1)T_2(x_2)$.

I_o is incident on the first face of the first figure, then after the light is transmitted through this first figure the spatial intensity will now not be I_o; but will have altered as a function of the transmission coefficient from I_o to $I_oT_1(x_1)$. Subsequent transmission through the second figure will modify the intensity again such that the final intensity T_1T_2 becomes:-

$$T_1T_2 = I_o[T_1(x_1)][T_2(x_2)] \qquad .....(2.30)$$

An analysis of the right hand side of this equation will then reveal any new periodicities and these will be related to the formation of a moiré pattern.

In order to illustrate this technique, the case considered by Durelli and Parks (1970); the combination of two gratings of unequal pitch will be used. For the detailed mathematics of this case the reader is referred to these authors, but the technique can be illustrated in a diagramatic way. The moiré pattern resulting from the combination of two gratings of unequal pitch is shown in figure 2.12, it consists of a grating with a pitch p_3 much greater than either of the two originals (p_1 and p_2).

Where: $$\frac{1}{p_3} = \frac{1}{p_1} - \frac{1}{p_2} \qquad .....(2.31)$$

This moiré pattern can be understood by reference to figure 2.13. Figure 2.13(a) and figure 2.13(b) represent the sinusoidal approximation of the two gratings, if these are superimposed the interference will produce a transmission function illustrated in figure 2.13(c). The effect is to modify the sine wave by slow modulation of the total transmission function and this corresponds to the observed moiré fringes in figure 2.12. The detailed structure within

Figure 2.12 The moiré pattern produced by superimposing gratings of unequal pitch.

Figure 2.13 The solution of moiré patterns by the transmission function representation method. (a) and (b) represent the sine wave approximation to two gratings of unequal pitch. When these are superimposed the resultant transmission function of the system is represented by (c) and corresponds to the situation illustrated in figure 2.12 (above). (Durelli and Parks (1970).

gratings of

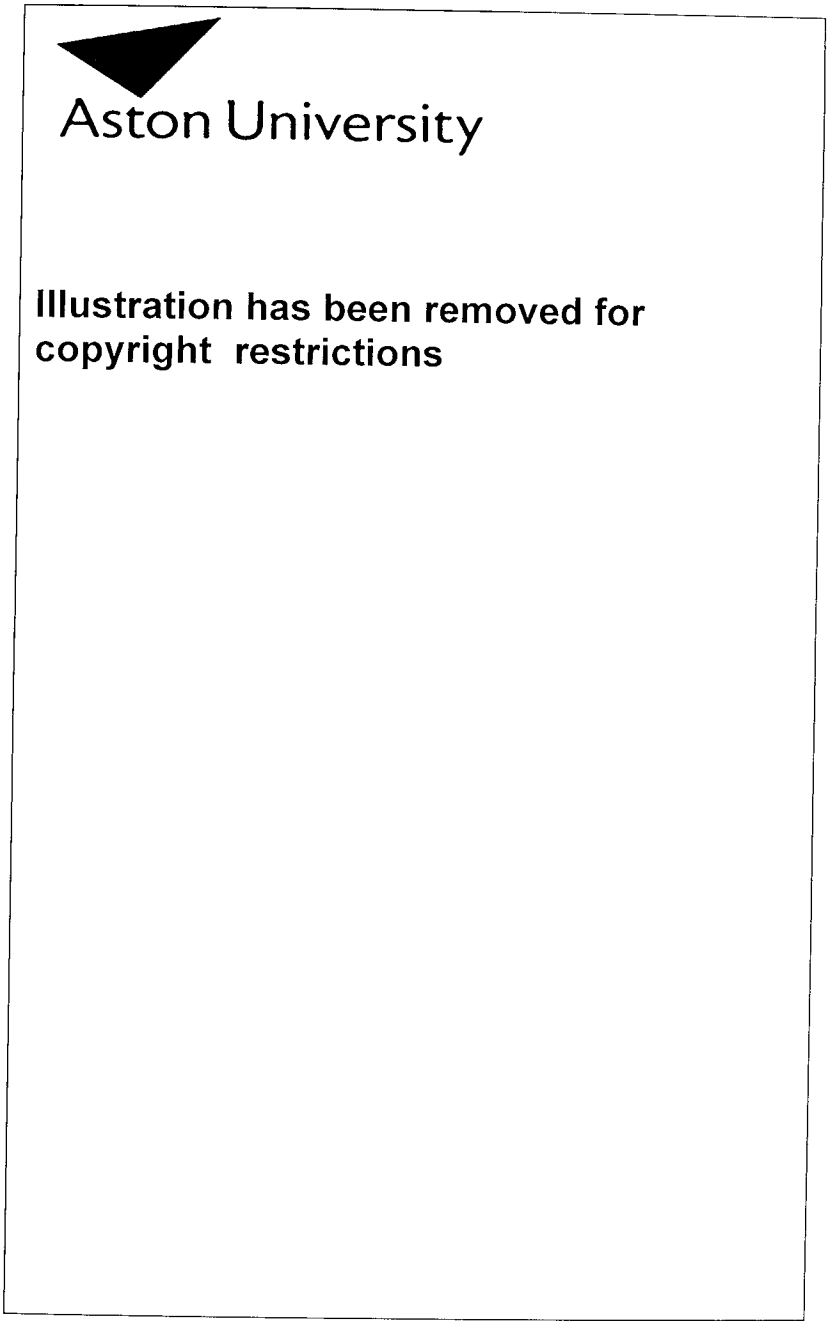

ission
nt the sine
When these
of the system
n illustrated

(a)

(b)

(c)

the general envelope is produced by the various harmonics present. An expression identical to equation (2.30) can be obtained by the geometric approach (Stecher (1964)). A new application of this technique is described later in this chapter.

2.6. The Moiré Pattern Produced by Overlapping Zone Plates*

2.6.1. Introduction

The earliest detailed study of moiré patterns produced by two overlapping zone plates was reported by Oster, Wasserman and Zwerling (1964). This study considered the case of two identical zone plates whose centres were separated by a distance comparable to the diameter of the central zone. Under these conditions the resulting moiré patterns consist of parallel straight lines. Goldfischer (1964) observed that when the separation between the centres of the two zone plates is large compared to the diameter of the central zone, the most prominent moiré pattern consists of many more zone plates which are centred along the line joining the centres of the original zone plates (see figure 2.14). Further studies of this observation have been reported by Moser and co-workers (1964) Oster (1967) and Chau (1969(b)). The analysis has been extended to the general case where the two zone plates have different focal lengths by Chau (1970). The case of three overlapping zone plates has been considered briefly by Moser and co-workers (1964).

In the present work a more systematic analysis of the phenomenon is presented and some new relationships regarding the formation of the moiré patterns are deduced. These are shown to possess a more general applicability.

* Much of the work presented in this section has been published in Optica Acta. (1973) 20 33.

2.6.2. General Analysis

The most general analysis may be obtained by considering the two overlapping zone plates to have not only different focal lengths, but also differing phase factors, δ_1 and δ_2. Thus:-

$$(x-s)^2 + y^2 = (m+\delta_1)r_1^2 \qquad .....(2.32)$$

and

$$x^2 + y^2 = (n+\delta_2)r_2^2 \qquad .....(2.33)$$

represent two zone plates whose centres are separated by a distance, s, the origin of the coordinate axes coinciding with the centre of the zone plate defined by equation (2.33). The principal focal lengths of the two zone plates are given by r_1^2/λ and $r_2^2\lambda$ respectively, where λ is the wavelength of the light used; m,n = 0,1,2,3. .... are positive integers. Assume that $r_1^2 > r_2^2$ and let $r_1^2/r_2^2 = k>1$. $0<\delta_1$ or $\delta_2<1$.

The method used for solving the moiré pattern resulting from the two overlapping figures relies on the use of an indicial equation of the form:-

$$am \pm bn = p \qquad .....(2.34)$$

where m and n are indices defined in equations (2.32) and (2.33). The parameters a and b are non zero positive integers; the resultant p will run over some subsets of the real integers. If we eliminate m and n from equations (2.32), (2.33) and (2.34) we obtain:-

$$\left[x - \left(\frac{as}{a\pm bk}\right)\right]^2 + y^2 = \left(\frac{r_1^2}{a\pm bk}\right)\left[P \mp \left(\frac{1}{a\pm bk}\right)\left(\frac{s^2abk}{r_1^2}\right) + a\delta_1 \pm b\delta_2\right] \qquad .....(2.35)$$

Equation (2.35) has been structured in a similar manner

to equations (2.32) and (2.33) and describes the family of moiré zone plates (henceforth MZP) that form the most prominent part of the moiré pattern. Two separate cases must be considered. The first is where the MZP are situated inbetween the two original zone plates ($0<x<s$) whereupon:-

$$\left[x - \left(\frac{as}{(a+bk)}\right)^2 + y^2 = \left(\frac{r_1^2}{(a+bk)}\right)\left[P - \left(\frac{1}{(a+bk)}\right)\left(\frac{s^2abk}{r_1^2}\right) + a\delta_1 + b\delta_2\right] \quad .....(2.35(a))$$

In figure 2.14 the two original zone plates are shown located at $x=0$ and $x=s$ and it is easy to recognise five MZP formed in between, while a further four are discernible on close examination. The position, prominence and indexing of these MZP are discussed later in the section.

The second case occurs where the MZP lie outside the original zone plates ($x<0$, $s<x$), whereupon:-

$$\left[x - \left(\frac{as}{(a-bk)}\right)\right]^2 + y^2 = \left(\frac{r_1^2}{(a-bk)}\right)\left[P + \left(\frac{1}{(a-bk)}\right)\left(\frac{s^2abk}{r_1^2}\right) + a\delta_1 - b\delta_2\right] \quad .....(2.35(b))$$

In figure 2.14 it is possible to detect a total of four MZP which lie in this region.

2.6.3. The Focal Length of a Moiré Zone Plate

2.6.3.1. MZP within $0<x<s$

From equation (2.35(a)) the focal length, $f_{(a,b)}$ of the MZP defined by a and b is given by:-

$$f_{(a,b)} = \left(\frac{r_1^2}{\lambda}\right)\frac{1}{(a+bk)} \quad .....(2.36)$$

In section 2.6.2. it was stated that for the MZP the parameters a and b must be non zero positive integers. However, it is possible to include the two original zone plates in this notation by allowing a and b to assume the

values (a=1, b=0) and (a=0, b=1). This can be proved by substituting these values of a and b in equation (2.35(a)). In particular, by substituting them into equation (2.36) we find that:-

$$f_{(1,0)} = r_1^2/\lambda \qquad \text{.....(2.37)}$$

and

$$f_{(0,1)} = (\frac{r_1^2}{\lambda})\frac{1}{k} = \frac{r_2^2}{\lambda} \qquad \text{.....(2.38)}$$

These are the values of the focal lengths of the two original zone plates.

From equations (2.36) and (2.37):-

$$f_{(a,b)} = \frac{f_{(1,0)}}{(a+bk)} \qquad \text{.....(2.39)}$$

Substituting the expression for k obtained from equations (2.37) and (2.38), this becomes:-

$$f_{(a,b)} = [\frac{f_{(1,0)}}{a+b(\frac{f_{(1,0)}}{f_{(0,1)}})}] = \frac{f_{(1,0)}\ f_{(0,1)}}{af_{(0,1)}+bf_{(1,0)}} \qquad \text{.....(2.40)}$$

which rearranges to give:-

$$\frac{1}{f_{(a,b)}} = \frac{a}{f_{(1,0)}} + \frac{b}{f_{(0,1)}} \qquad \text{.....(2.41)}$$

Equation (2.41) determines the focal length of the whole series of MZP formed between the two original zone plates by varying the parameters a and b in the indicial equation (2.34). In particular, when a=b=1 the MZP formed is the most prominent one (greatest focal length), and it is interesting to note that equation (2.41) then becomes equivalent to the lens combination formula.

If a and b are given the specific values ($a=a_1$) and ($b=b_1$), equation (2.41) becomes:-

$$\frac{1}{f_{(a_1,b_1)}} = \frac{a_1}{f_{(1,0)}} + \frac{b_1}{f_{(0,1)}} \qquad \text{.....(2.42)}$$

Similarly, when $(a=a_2)$ and $(b=b_2)$:-

$$\frac{1}{f_{(a_2,b_2)}} = \frac{a_2}{f_{(1,0)}} + \frac{b_2}{f_{(0,1)}} \qquad .....(2.43)$$

Now consider the MZP whose parameters have the values $(a=a_3)$and $(b=b_3)$ such that:-

$$a_3 = a_1 + a_2 \qquad .....(2.44)$$

and

$$b_3 = b_1 + b_2 \qquad .....(2.45)$$

then:-

$$\frac{1}{f_{(a_3,b_3)}} = \frac{a_3}{f_{(1,0)}} + \frac{b_3}{f_{(0,1)}} \qquad .....(2.46)$$

Substituting from equation (2.44) and (2.45):-

$$\frac{1}{f_{(a_3,b_3)}} = \frac{a_1+a_2}{f_{(1,0)}} + \frac{b_1+b_2}{f_{(0,1)}} \qquad .....(2.47)$$

rearranging:-

$$\frac{1}{f_{(a_3,b_3)}} = \left(\frac{a_1}{f_{(1,0)}} + \frac{b_1}{f_{(0,1)}}\right) + \left(\frac{a_2}{f_{(1,0)}} + \frac{b_2}{f_{(0,1)}}\right) \qquad .....(2.48)$$

that is:-

$$\frac{1}{f_{(a_3,b_3)}} = \frac{1}{f_{(a_1,b_1)}} + \frac{1}{f_{(a_2,b_2)}} \qquad .....(2.49)$$

Equation (2.49) is an extremely important result because it means that the focal length of any MZP can be calculated directly from the focal lengths of two previous zone plates in the series. It should be noted that $a_1 \neq a_2$ and $b_1 \neq b_2$ simultaneously as (a_1,b_1) and (a_2,b_2) would then define the same zone plate in the series.

When this result is considered in conjuction with that

derived in section 2.6.4.1. (equation (2.60)), it can be seen that two different approaches may be made towards determining the formation of the MZP. These are illustrated in Table 2.1, where, for simplicity, k has been put equal to one. The location of the centres of the MZP is also tabulated here.

In the comprehensive approach the MZP may be considered to be generated by a weighted sum of the two original zone plates. In the sequential approach, on the other hand, the MZP are generated one at a time as the linear sum of the two previous zone plates in the series, which may be either moiré or original, or a combination of the two.

2.6.3.2. M.Z.P. in the region $x<0, s<x$

Following through the above types of analysis for this second situation yields the following result. For the comprehensive approach, the focal length of the MZP whose indices are (a,b) is given by:-

$$\frac{1}{f_{(a,b)}} = \left| \frac{a}{f_{(1,0)}} - \frac{b}{f_{(0,1)}} \right| \qquad \ldots\ldots(2.50)$$

where the modulus notation is introduced in order to keep the focal lengths positive.

The sequential approach developed in section 2.6.3.1. may also be applied to this situation, using equation (2.49).

2.6.4. The Location of a Moiré Zone Plate

2.6.4.1. MZP within $0<x<s$

The distance, $d_{(a,b)}$, of the MZP of indices (a,b) from the original zone plate (0,1), situated at the coordinate origin, is given by:-

$$d_{(a,b)} = \frac{as}{a + bk} \qquad \ldots\ldots(2.51)$$

Table 2.1

Comprehensive and sequential approaches to MZP formation

$(f_{(0,1)} = f_{(1,0)} = f;\ 0<x<S)$

MZP of indices (a,b)	$\frac{1}{f_{(a,b)}}$	Comprehensive approach	Sequential approach	Position
(1,1)	2/f	= 1/f + 1/f	= 1/f + 1/f	s/2
(1,2)	3/f	= 1/f + 2/f	= 1/f + $1/f_{(1,1)}$	s/3
(2,1)	3/f	= 2/f + 1/f	= $1/f_{(1,1)}$ + 1/f	2s/3
(1,3)	4/f	= 1/f + 3/f	= 1/f + $1/f_{(2,1)}$	s/4
(3,1)	4/f	= 3/f + 1/f	= $1/f_{(2,1)}$ + 1/f	3s/4
(2,3)	5/f	= 2/f + 3/f	= $1/f_{(1,2)}$ + $1/f_{(1,1)}$	2s/5
(3,2)	5/f	= 3/f + 2/f	= $1/f_{(1,1)}$ + $1/f_{(2,1)}$	3s/5
etc.	etc.	etc.	etc.	etc.

Therefore its distance from the other original zone plate, (1,0) is:-

$$s - d_{(a,b)} = s - \frac{as}{a + bk} = \frac{bks}{a + bk} \qquad .....(2.52)$$

These distances, $\frac{as}{a+bk}$ and $\frac{bks}{a+bk}$, are the radii, $r_{(0,1)}$ and $r_{(1,0)}$, of the zones of the two original zone plates that overlap at the centre of the MZP, (a,b).

The focal length of a zone plate can be expressed as follows:-

$$f_{(a,b)} = \frac{2r_{(a,b)}\Delta r_{(a,b)}}{\lambda} \qquad .....(2.53)$$

where $r_{(a,b)}$ is the average radius of any zone and $\Delta r_{(a,b)}$ is the width of the same zone.

Therefore, at the centre of the MZP (a,b):

$$r_{(1,0)} = \frac{f_{(1,0)}\lambda}{2\Delta r_{(1,0)}} = \frac{bks}{a + bk} \qquad .....(2.54)$$

whereupon:-

$$\Delta r_{(1,0)} = \frac{f_{(1,0)}\lambda\ (a + bk)}{2bks} \qquad .....(2.55)$$

and

$$r_{(0,1)} = \frac{f_{(0,1)}\lambda}{2\Delta r_{(0,1)}} = \frac{as}{a + bk} \qquad .....(2.56)$$

whereupon:-

$$\Delta r_{(0,1)} = \frac{f_{(0,1)}\lambda(a + bk)}{2\ as} \qquad .....(2.57)$$

Substituting the expression $f_{(1,0)}/k$ for $f_{(0,1)}$ in equation (2.57):-

$$\Delta r_{(0,1)} = \frac{f_{(1,0)}\lambda(a + bk)}{2aks} \qquad .....(2.58)$$

Thus from equations (2.55) and (2.58):-

$$\frac{\Delta r_{(0,1)}}{\Delta r_{(1,0)}} = \frac{b}{a} \qquad .....(2.59)$$

Equation (2.59) shows that the MZP (a,b) is centred at the point where the zone widths of the two original zone plates are in the ratio b:a. In particular the zone widths are equal for the case of the most prominent MZP, (1,1), formed inbetween the two originals.

Using the sequential approach which considers the MZP (a_3,b_3) to be the most prominent zone plate generated by the overlap of two zone plates (a_1,b_1) and (a_2,b_2) we find that an analysis similar to the above yields:-

$$\frac{\Delta r_{(a_1,b_1)}}{\Delta r_{(a_2,b_2)}} = 1 \qquad \ldots\ldots(2.60)$$

This result means that at the centre of any MZP the zone widths of the two directly generating zone plates are equal, and is therefore a general condition for locating the centres of a whole series of MZP. This is a new result and one which leads to further applications in the interpretation of field-ion micrographs (see chapter 3).

THe positions of the MZP that are formed may be found using a graphical construction based on equation (2.59). Figure 2.15 plots zone widths, Δr, against r for two zone plates which, for simplicity, have $\delta_1 = \delta_2 = 1$ and $k = 1$. Strictly, the function of Δr against r is a step function but has been drawn as a continuous curve for clarity and convenience. Also plotted in this figure are integral multiples of Δr. Thus, for example, the position of the MZP, (3,1) is found from the point at which the $3\Delta r_{(0,1)}$ curve intersects the $\Delta r_{(1,0)}$ curve.

Figure 2.15 also reveals a limitation on the number of MZP that may be formed. For example, there can be no MZP whose indices are (9.1) since the relevant Δr curves

Figure 2.14 The moiré pattern formed between two overlapping zone plates for which k=1, but $\delta_1 = \delta_2$. (The zone plates used to produce this illustration are courtesy of H.H.M. Chau).

Figure 2.15 A graphical method for locating the position of a MZP.

Overlapping zone

The zone plates used

tesy of H.H.H. Chan

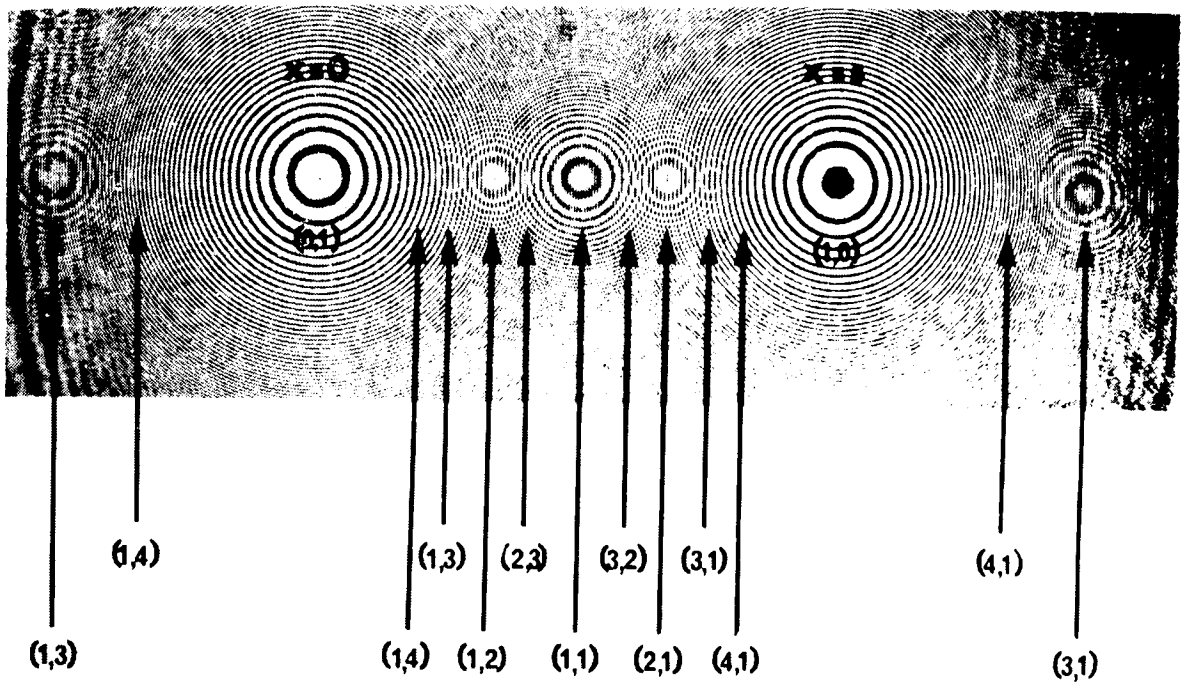

ition of a MZP.

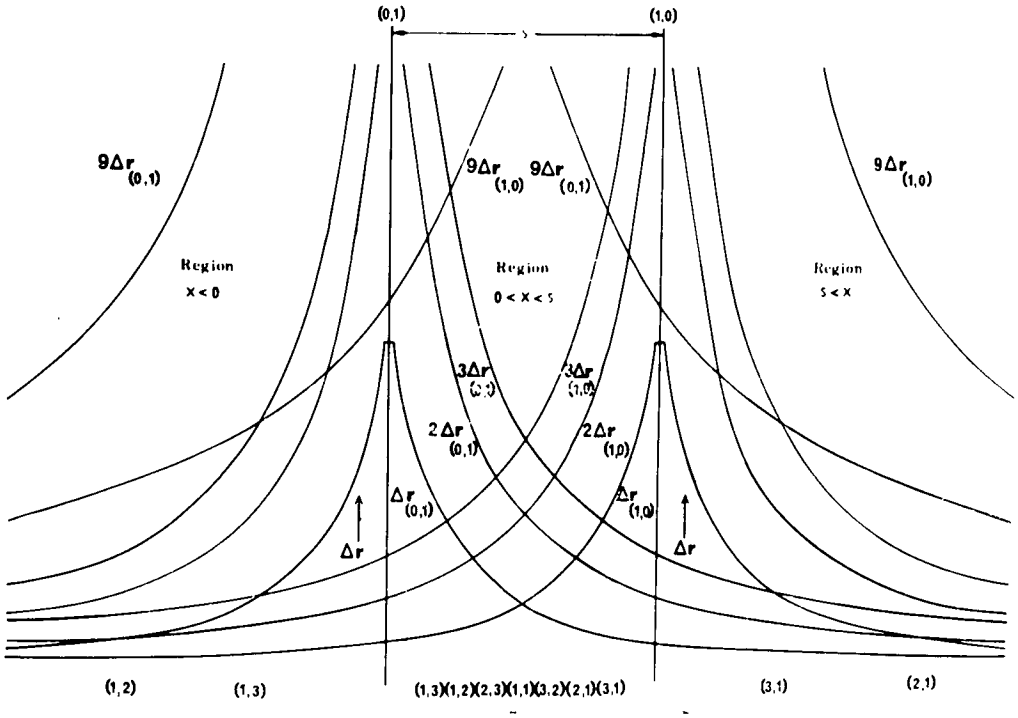

fail to intersect, for the particular values of s and r for which the curves have been drawn. There is a further limitation on the number of MZP that may be detected by the eye: there should, for example be a MZP (5,3) located in between (3,2) and (2,1), but this is not discernible in Figure 2.14. (Note however that Chau (1969(b) has shown that MZP not visible to the eye may still be detected by observing their focussing action using a collimated laser beam).

It is possible to consider the visibility of a MZP in two ways. Firstly, the greater is its ring radius and spacing (and hence focal length), the more prominent it should appear. Thus higher index MZP will be less prominent. Secondly, the greater the number of overlap points forming the rings, the more readily will the MZP be detected. Thus all other parameters being equal, the more zones there are making up the original zone plates, the more readily detected will be the MZP. Again higher index MZP will suffer more on this basis.

The coordinate centre of a MZP of known indices (a,b) is given by $x = as/(a \pm bk)$, enabling a fairly accurate value of k to be obtained from measurements made on the moiré pattern. Thus if a zone plate of known focal length, f_1, is available, then in this way it is quite easy to determine the focal length of an unknown zone plate, $f_2 = f_1/k$, without the need for its direct measurement.

2.6.4.2. MZP in the region $x<0, s<x$

If the comprehensive approach is applied to the MZP formed in the above region it results in an equation identical to equation (2.59). The reason for this may

may be seen from figure 2.15 where Δr has been plotted to either side of the centres of the original zone plates. Thus, for example, the MZP (3,1) formed in $s<x$ is located at the point where the $3\Delta r_{(0,1)}$ curve intersects the $\Delta r_{(1,0)}$ curve in this region, and so on.

As would be expected, the sequential approach again results in an equation identical to equation (2.60).

2.6.5. The phase of a moiré zone plate

2.6.5.1. The phase factor

Unlike its focal length and position, the phase factor, $\delta_{(a,b)}$ of a MZP does depend on the phase factors of the two original zone plates. However, a certain amount of care must be exercised in determining its value. The following expression, taken from equation (2.32), for an original zone plate, contains its periodicity m=0,1,2,3... and phase $0<\delta_1<1$, i.e.:

$$(m + \delta_1) \qquad \text{.....(2.61)}$$

The equivalent expression from, say, equation (2.35(a)), a MZP, is:-

$$\left[P - \frac{1}{(a+bk)} \left(\frac{s^2abk}{r_1^2}\right) + a\delta_1 + b\delta_2\right] \qquad \text{.....(2.62)}$$

but the similarity is deceptive: p is not directly equivalent to m, and hence the remainder of this expression is not equal to $\delta_{(a,b)}$. An illustration should make this clear. Taking the situation where, for simplicity, k=1, $\delta_1=\delta_2=0$ and $s/r_1=10$, then, for the MZP (1,2), the expression (2.62) becomes equal to $[p-66\frac{2}{3}]$. This expression must always be positive, and for the minimum value of p, say p_i, must be <1. Here, therefore, p_i must equal 67, and the phase factor, $\delta_{(1,2)}$ is 1/3. Thus p

takes the values 67, 68, 69...

In general, therefore, the phase factor of the MZP is given by:-

$$\delta_{(a,b)} = \left[Pi - \frac{1}{(a+bk)} \left(\frac{s^2 abk}{r_1^2} \right) + a\delta_1 + b\delta_1 \right] \quad .....(2.63)$$

A further point that must be considered is that this mathematical treatment considers only a series of concentric circles, and does not differentiate between those which enclose opaque areas, and those which enclose transparent areas, as in the actual zone plate. Thus if we consider two series of circles of identical dimensions, in one case the first zone being opaque, and in the other case transparent, then considering these as zone plates we should say that their phase difference was 0.5. However the mathematical analysis would define their phases as being equal.

2.6.5.2. The phase shift

If the moiré pattern formed between two zone plates is observed while the distance between their centres, s, is increased, it is noted that, while the relative positions of the MZP remain the same, within $0<x<s$ the rings forming the MZP are continously decreasing in radius until they collapse to zero at their centre. Thus the phase of the central ring decreases from one to zero, whereupon the next ring becomes the central one, and follows suit.

The total number of rings collapsed when the separation increases from s to s' is given by:-

$$\Delta\sigma = \frac{abk}{(a+bk)r_1^2} \left(s^2 - s'^2 \right) \quad .....(2.64)$$

This quantity, $\Delta\sigma$ is termed the phase shift. Again it must be realised that the analysis refers to the individual rings and hence the numerical value of the phase shift will be twice the number of complete phase cycles of the zone plate.

The rings making up the MZP which are formed outside the two original zone plates increase in radius with increasing s, and a similar procedure to the above may be adopted to determine the appropriate values of phase factor and phase shift for this situation.

2.6.6. Moiré zone plates produced by three overlapping zone plates

2.6.6.1. General analysis

The MZP pattern formed by three overlapping zone plates is shown in figure 2.16(a). The three original zone plates can be represented by:-

$$(x-s)^2 + y^2 = (m+\delta_1)r_1^2 \qquad \ldots\ldots(2.65)$$

$$x^2 + y^2 = (n+\delta_2)r_2^2 \qquad \ldots\ldots(2.66)$$

$$(x-s')^2 + (y-t)^2 = (q+\delta_3)r_3^2 \qquad \ldots\ldots(2.67)$$

their centres being at co-ordinates (s,0), (0,0) and (s',t) respectively (see figure 2.16(b)). The principal focal lengths are given by $\frac{r_1^2}{\lambda}$, $\frac{r_2^2}{\lambda}$ and $\frac{r_3^2}{\lambda}$ respectively; m, n and q = 0,1,2,3,... are positive integers. Assume that $r_1^2 > r_2^2$ and $r_1^2 > r_3^2$ and let $\frac{r_1^2}{r_2^2} = k > 1$ and $\frac{r_1^2}{r_3^2} = k_2 > 1$.

The indicial equation now becomes:-

$$am \pm bn \pm cq = p \qquad \ldots\ldots(2.68)$$

where a, b and c are positive integers.

Figure 2.16 The moiré pattern formed between three overlapping zone plates.

(a) Photograph of the moire pattern.

(b) Co-ordinate diagram.

(c) Indexing of the pattern.

zone

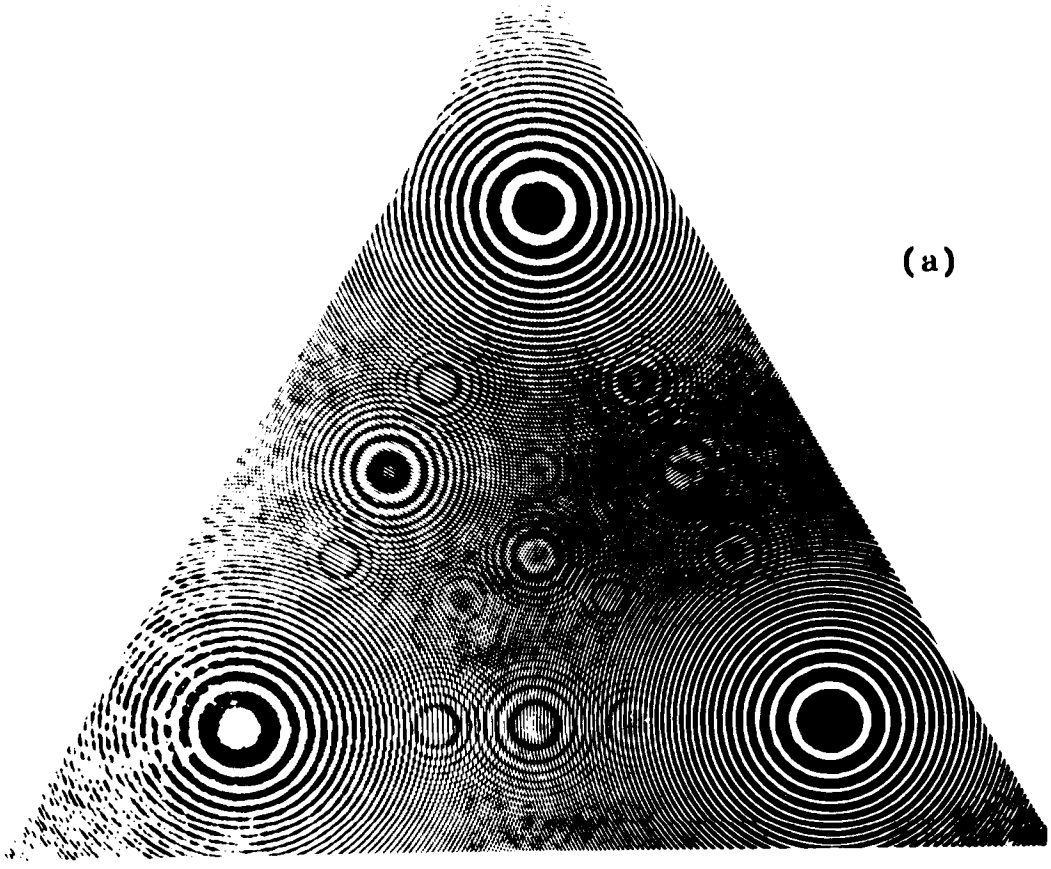

(a)

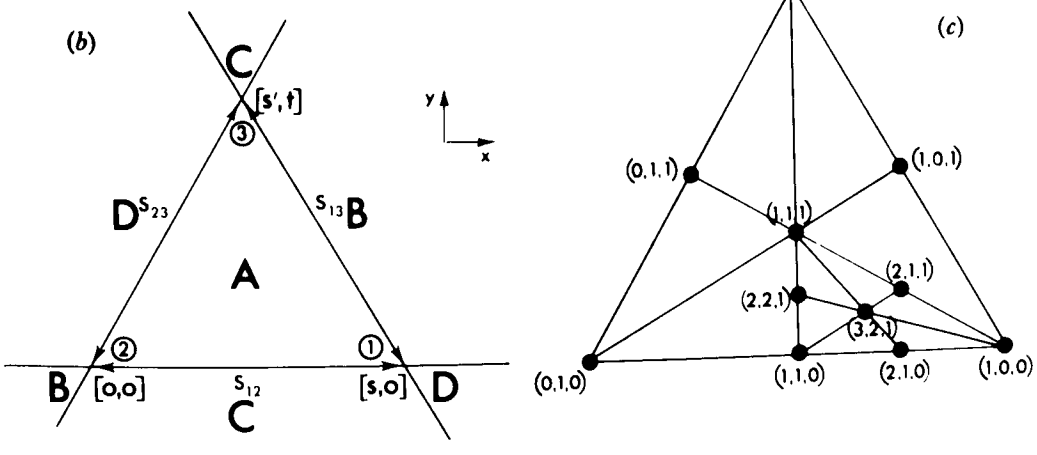
(b)
C
[s',t]
y
x
$D^{S_{23}}$
$S_{13}B$
A
B
[o,o]
S_{12}
[s,o]
D
C
(c)
(0,0,1)
(0,1,1)
(1,0,1)
(1,1,1)
(2,1,1)
(2,2,1)
(3,2,1)
(0,1,0)
(1,1,0)
(2,1,0)
(1,0,0)

Eliminating m, n and q from equations (2.65) and (2.68)

$$\left[x-\frac{(as \pm ck_2 s')}{(a\pm bk_1 \pm ck_2)}\right]^2 + \left[y-\frac{(\pm ck_2 t)}{(a\pm bk_1 \pm ck_2)}\right]^2$$

$$= \frac{r_1^2}{(a\pm bk_1 \pm ck_2)}\left[P\mp \frac{(abk_1 s^2+ack_2(s-s')^2+t^2)\pm bck_1k_2(s'^2+t^2)}{r_1^2(a\pm bk_1\pm ck_2)} + a\delta_1 \pm b\delta_2 \pm c\delta_3\right] \quad .....(2.69)$$

Equation (2.69) represents the family of MZP.

Four separate cases can be considered: firstly and most important, case A, where the MZP are situated within the triangle formed by the lines joining the centres of the three original zone plates, whereupon:-

$$\left[x-\frac{(as+ck_2 s')}{(a+bk_1+ck_2)}\right]^2 + \left[y-\frac{(ck_2 t)}{(a+bk_1+ck_2)}\right]^2$$

$$=\frac{r_1^2}{(a+bk_1+ck_2)}\left[P-\frac{(abk_1 s^2+ack_2((s-s')^2+t^2)+bck_1k_2(s'^2+t^2))}{r_1^2(a+bk_1+ck_2)} + a\delta_1 + b\delta_2 + c\delta_3\right]$$

$$.....(2.70)$$

The remaining three cases, B,C and D are the MZP that lie outside the above mentioned triangle (see figure 2.16(b)) and will not be developed further here.

2.6.6.2. Focal length

From equation (2.70) the focal length $f_{(a,b,c)}$ of the MZP defined by a,b and c is given by:-

$$f_{(a,b,c,)} = \left(\frac{r_1^2}{\lambda}\right)\left(\frac{1}{(a+bk_1+ck_2)}\right) \quad .....(2.71)$$

As before it is possible to include the original zone plates in the notation by allowing a, b and c to assume the values (a=1, b=0, c=0) (a=0, b=1, c=0) and (a=0, b=0, c=1). Then following the method developed in section 2.6.3.1.,

we find that:-

$$\frac{1}{f(a,b,c)} = \frac{a}{f(1,0,0)} + \frac{b}{f(0,1,0)} + \frac{c}{f(0,0,1)} \quad \ldots\ldots(2.72)$$

This represents the comprehensive approach. Using the sequential approach for the MZP (a_4, b_4, c_4) where $a_4=a_1 + a_2 + a_3$, $b_4=b_1 + b_2 + b_3$ and $c_4=c_1 + c_2 + c_3$, it can be shown that:-

$$\frac{1}{f(a_4,b_4,c_4)} = \frac{1}{f(a_1,b_1,c_1)} + \frac{1}{f(a_2,b_2,c_2)} + \frac{1}{f(a_3,b_3,c_3)} \quad \ldots\ldots(2.73)$$

The use of equation (2.72) and (2.73) are illustrated in figure 2.16(c) by considering the MZP (3,2,1). This can be considered as generated by the original 3 zone plates by letting a=3, b=2 and c=1 in equation (2.72) or as generated by MZP's (1,1,0) and (1,1,1) and original zone plate (1,0,0) by letting $a_4=3$, $b_4=2$, $c_4=1$, $a_1=1$, $b_1=1$, $c_1=0$, $a_2=1$, $b_2=1$, $c_2=1$, $a_3=1$, $b_3=0$, and $c_3=0$ in equation (2.73).

It can also be considered as being formed from either MZP's (1,1,1) and (2,1,0) or MZP's (1,1,0) and (2,1,1) or MZP (2,2,1)and original zone plate (1,0,0). This represents an extension of the sequential approach simply by combining two of the three terms on the right hand side of equation (2.73) - there being 3 possible ways of doing this.

This point is perhaps more easily illustrated when considering the most prominent MZP (1,1,1). This can be considered as formed from either the 3 original zone plates, or from 3 possible combinations of an original zone plate and a MZP, namely (1,0,0) and (0,1,1) or

(0,1,0) and (1,0,1) or (0,0,1) and (1,1,0) each MZP of course being formed from the other two originals.

2.6.6.3. Location and phase

From equation (2.70) it can be seen that the co-odinates of the centre of the MZP (a,b,c) within the triangle are:-

$$\left(\frac{as+ck_2s'}{a+bk_1+ck_2} \quad , \quad \frac{ck_2t}{a+bk_1+ck_2}\right)$$

The phase factor of the MZP (a,b,c) within the triangle can also be obtained from equation (2.70) with reference to equation (2.63).

$$\delta_{(a,b,c)} = Pi-\frac{[abk_1s^2+ack_2((s-s')^2+t^2)+bck_1k_2(s'^2+t^2)]}{r_1^2\,(a+bk_1+ck_2)} + a\delta_1 + b\delta_2 + c_3 \qquad .....(2.74)$$

This can be simplified because $\sqrt{((s-s')^2+t^2)}$ is the inter-centre distance between zone plates (1,0,0) and (0,0,1) and $\sqrt{(s'^2+t^2)}$ is the intercentre distance between (0,1,0) and (0,0,1) which we can term S_{13} and S_{23} respectively. To complete the notation we shall term S, the intercentre distance between zone plates (1,0,0) and (0,1,0), S_{12} (see figure 2.16(b)).

$$S_{12} = S \qquad .....(2.75)$$

$$S_{13} = \sqrt{((s-s')^2+t^2)} \qquad .....(2.76)$$

and $$S_{23} = \sqrt{(s'^2+t^2)} \qquad .....(2.77)$$

Therefore:-

$$\delta_{a,b,c,} = Pi-\frac{[abk_1s_{12}^2+ack_2s_{13}^2+bck_1k_2s_{23}^2]}{r_1^2(a+bk_1+ck_2)} + a\delta_1 + b\delta_2 + c\delta_3 \qquad .....(2.78)$$

A more effective method of dealing with these complex

expressions could be to use the extension to the sequential approach discussed in the previous section.

2.6.7. Conclusions

Several new relationships have been put forward regarding the formation of moiré zone plates. These have been enabled by including the original zone plates in the indicial nomenclature used to describe the MZP. Using the established, comprehensive approach, it has been possible to express the focal length of the MZP by an expression similar to the lens combination formula, and to express the position of the MZP in terms of the zone widths of the two original zone plates, the expressions in both cases being weighted by the indices (a,b) of the MZP.

An alternative, sequential, approach has been devised, which allows the MZP to be regarded as generated by the linear combination of two earlier (and in general, moiré) zone plates in the series. In particular this latter approach permits a rather simpler analysis to be made of the much more complex problem of the overlap of three zone plates. Some consideration has been given to the phase of the MZP, and a distinction made between phase factor and phase shift.

The relevance of MZP formation to the technique of synthetic holography has been discussed by Chau (1969(b)). The latter technique involves the superposition of several zone plates (Conger, Long and Parks (1968) and it is apparent that extraneous ghost images could also be formed due to the moiré effect. It is suggested here that there may be further applications in connection with microscopy

and related techniques. For example, zone plates have been used for focusing soft X-radiation (Möllenstedt, Von Grote and Jonsson (1963)) and as correction plates for use with the objective lens in high resolution electron microscopy (Hoppe et al (1969)). It might be possible to use the moiré effect to produce a variable range of zone plates possessing different focal lengths and phase factors.

Probably the most important aspect of this work, however, lies in the interpretation of field-ion micrographs. In chapter 3 using techniques developed in this section it has been possible to interpret the field-ion image in terms of moiré pattern formation. Also a new insight into the mechanism of field-ion image formation has been obtained by simulation, using several overlapping zone plates of an appropriate nature. The analysis used relies heavily on the new methods of treatment developed in this section.

2.7. An analysis of the moiré pattern produced by overlapping zone plates using the transmission function representation technique

In the previous section it was shown that the indicial representation approach may be used to analyse the moiré pattern produced by overlapping zone plates. It would be instructive, however, to briefly reproduce the most important results contained therein by way of the transmission function representation technique which was outlined concisely in subsection (2.5.3.). This will not only serve to demonstrate this new technique, but will also provide new information concerning the moiré pattern

produced by overlapping zone plates.

In subsection (2.5.3.) it was shown that the general sinusoidal approximation for a series of square wave contours is:-

$$T(x) = \tfrac{1}{2}(1 + A \sin \frac{2\pi x}{P} + \delta) \qquad .....(2.79)$$

In this instance the term δ, is introduced to describe the phase of the zone plate. This expression, in fact, accurately describes the transmission function of a Gabor (or sinusoidal) zone plate found to occur in holography. The focal length of the generalised or binary zone plate has been shown in section 2.3 to be given by the expression:-

$$f = \frac{\rho \Delta \rho}{\lambda}$$

Therefore $$\Delta \rho = \frac{f\lambda}{\rho}$$

Substituting $\Delta\rho(=\frac{f\lambda}{\rho})$ for p and ρ for x in equation (2.79), the equation of a zone plate $T_{a_1b_1}$ centred at the co-ordinates S,O in the x,y Cartesian system becomes:-

$$T_1(a_1b_1) = \tfrac{1}{2}(1 + A_1 \sin \frac{2\pi\ \rho^2}{\lambda f_{a_1b_1}} + \delta a_1b_1 \qquad .....(2.80)$$

but $\rho^2 = (x-s)^2 + y^2$

Therefore substituting in equation (2.80) for ρ^2

$$T_1(a_1\ b_1) = \tfrac{1}{2}\ (1 + A_1 \sin \frac{2\pi((x-s)^2+y^2)}{\lambda f_{a_1b_1}} + \delta\, a_1b_1 \qquad .....(2.81)$$

The corresponding equation for a zone plate centred at (x-s), O of focal length $f_{a_2b_2}$ is:-

$$T_2(a_2b_2) = \tfrac{1}{2}\ (1 + A_2 \sin \frac{2\pi(x^2+y^2)}{\lambda f_{a_2b_2}} + \delta\, a_2b_2) \qquad .....(2.82)$$

When the two zone plates are superimposed, face to face, the equation for the total transmissivity of the

system is found by utilising equation (2.29) in subsection 2.5.3. and is equal to:-

$$T_1T_2 = 1/4\ (1 + \frac{A_1 \sin 2\pi(x^2+y^2)}{\lambda f_{a_2b_2}} + \delta_{a_2b_2}$$

$$+ A_1 \frac{\sin 2\pi((x-s)^2+y^2}{\lambda f_{a_1b_1}} + \delta_{a_1b_1} + A_1A_2[\frac{\sin 2\pi(x^2+y^2)}{f_{a_2b_2}} + \delta_{a_2b_2}]$$

$$x\ [\frac{\sin 2\pi(x-s)^2+y^2}{f_{a_1b_1}} + \delta_{a_1b_1}] \qquad .....(2.83)$$

The two first order terms in equation (2.83) reproduce the equations for the original zone plates as described in equations (2.81) and (2.82). The second order term in this equation describes the transmission function of the moiré pattern. The sum and difference modulation terms corresponding to the additive and subtractive moiré pattern may be extracted using the standard trignometric identity:-

$$\sin A \sin B = \tfrac{1}{2}\ (\cos(A-B)-\cos(A+B)) \qquad .....(2.84)$$

The additive moiré pattern corresponds to the case $\frac{1}{2}\cos(A+B)$ while the subtractive moiré pattern is given by $\frac{1}{2}\cos(A-B)$. Taking the case of the additive moiré pattern only.

$$Ta_3b_3 = 1/8(A_1A_2)\cos\frac{2\pi}{\lambda}[\frac{f_{a_2b_2}+f_{a_1b_1}}{f_{a_2b_2}\ f_{a_1b_1}}(x+\frac{f_{a_2b_2}s}{f_{a_1b_1}\ f_{a_2b_2}})^2$$

$$(\frac{-s^2f_{a_2b_2}-1}{(f_{a_1b_1}+f_{a_2b_2})})f_{a_1b_1} + \delta_{a_1b_1} + \delta_{a_2b_2}]$$

$$.....(2.85)$$

Equation (2.85) has been structured in the same way as equations (2.81) and (2.82) so that by comparing coefficients, the moiré pattern is a zone plate whose focal length $f_{a_3b_3}$ is given by the formula:-

$$\frac{1}{f_{a_3b_3}} = \frac{f_{a_1b_1} + f_{a_2b_2}}{f_{a_1b_1}\ f_{a_2b_2}}$$

which rearranges to give:-

$$\frac{1}{f_{a_3b_3}} = \frac{1}{f_{a_1b_1}} + \frac{1}{f_{a_2b_2}} \qquad .....(2.86)$$

This equation is identical to equation (2.49) which was obtained in the previous analysis.

The location of this MZP is also obtained by comparing coefficients and is given by the expression:-

$$\frac{f_{a_2b_2}\, s}{f_{a_1b_1} + f_{a_2b_2}} \qquad .....(2.87)$$

but $f_{a_1b_1}/f_{a_2b_2} = k$ and hence the above expression reduces to $s/_{1+k}$ which is again identical to the location calculated in the previous analysis and corresponds to the case where a=1, b=1, that is the most prominent MZP.

Also contained within equation (2.85) is information concerning the detailed transmissivity of the moiré pattern. This information is important when considering its visibility. In this case the transmissivity of the MZP is $1/8\ A_1A_2$ compared with the value of A1/2 and A2/2 for the original zone plates. This technique is ideal for situations where the particular shape of the transmission function is critical. For instance, in the distinction between the various types of zone plate (see subsection 2.2.3), which is of importance in holography.

2.8. The moiré pattern produced by the superpostion of an equispaced grating on a zone plate.

2.8.1. Introduction

The first observation of the moiré pattern produced between an equispaced grating and a zone plate was made by Oster and Nishijima (1963). Its analysis was conducted by Oster, Wasserman and Zwerling (1964), and subsequently

carried out in more detail by Stecher (1964). The analysis has since received attention by Oster (1967) and Theocaris (1969).

The moiré pattern usually associated with this system consists of a multiple replication of the zone plate arrayed symmetrically about the zone plate in a direction perpendicular to the straight lines composing the grating, (see figure 2.17). Only Stecher (1964) has discovered that by varying the pitch of the grating, a moiré pattern consisting of moiré zone plates (henceforth MZP) of differing focal length may be obtained. Stecher (1964) attempted the analysis of this effect, but no serious, thorough investigation has been made. Stecher (1964) has also made the observation that by overlapping a grid structure with a zone plate, a two dimensional array of moiré zone plates is obtained.

In this chapter a more systematic analysis of the phenomenon is carried out using techniques developed elsewhere (section 2.6). By considering the grid structure to act effectively as two perpendicularly inclined gratings and by using an indicial equation involving three terms, a rigorous mathematical analysis can be performed for the first time.

2.8.2. General Analysis

For the most general case, allow the zone plate to possess a phase factor δ. Hence the equation of a zone plate centred at (0,0)in an x,y co-ordinate system is:-

$$x^2 + y^2 = r_1^2 (m + \delta) \qquad \ldots\ldots(2.88)$$

The equation of an equispaced grating, spacing d, orientated parallel to the y axis is:-

$$x = \pm nd \qquad .....(2.89)$$

The technique used for the solution of the moiré pattern resulting from the overlapping of two figures consisting of two indexed families of curves or lines relies on the use of the indicial equation:-

$$am \pm bn = p$$

However, Theocaris (1969) has shown that in this particular instance the subtractive moiré effect is dominant for positive values of x and the additive moiré effect is dominant for negative values of x. Thus the moiré pattern is symmetric about the y axis. In order to simplify the analysis we shall consider only the additive moiré pattern,but will let the grating take positive and negative values of x, hence preserving the symmetry. The indicial equation now takes the form:-

$$am + bn = p \qquad .....(2.90)$$

If we now eliminate m and n from equations (2.88), (2.89) and (2.90), we obtain:-

$$(x \pm \frac{bk}{2a})^2 + y^2 = \frac{r_1^2}{a}[P + \frac{b^2k^2}{4ar_1^2} + \delta\ ] \qquad .....(2.91)$$

Where the term k is a constant and equal to r_1^2/d. Equation (2.91) has been structured in a similar manner to equation (2.88) and it describes an array of MZP located along the x axis.

Figure 2.18 depicts the moiré pattern formed between a zone plate and a finely spaced grating. A series of MZP are formed some of which replicate the original zone plate,

Figure 2.17 The moiré pattern formed by the superposition of a zone plate and a coarse grating.

Figure 2.18 The moiré pattern formed by overlapping a zone plate and a fine grating.

f a zone

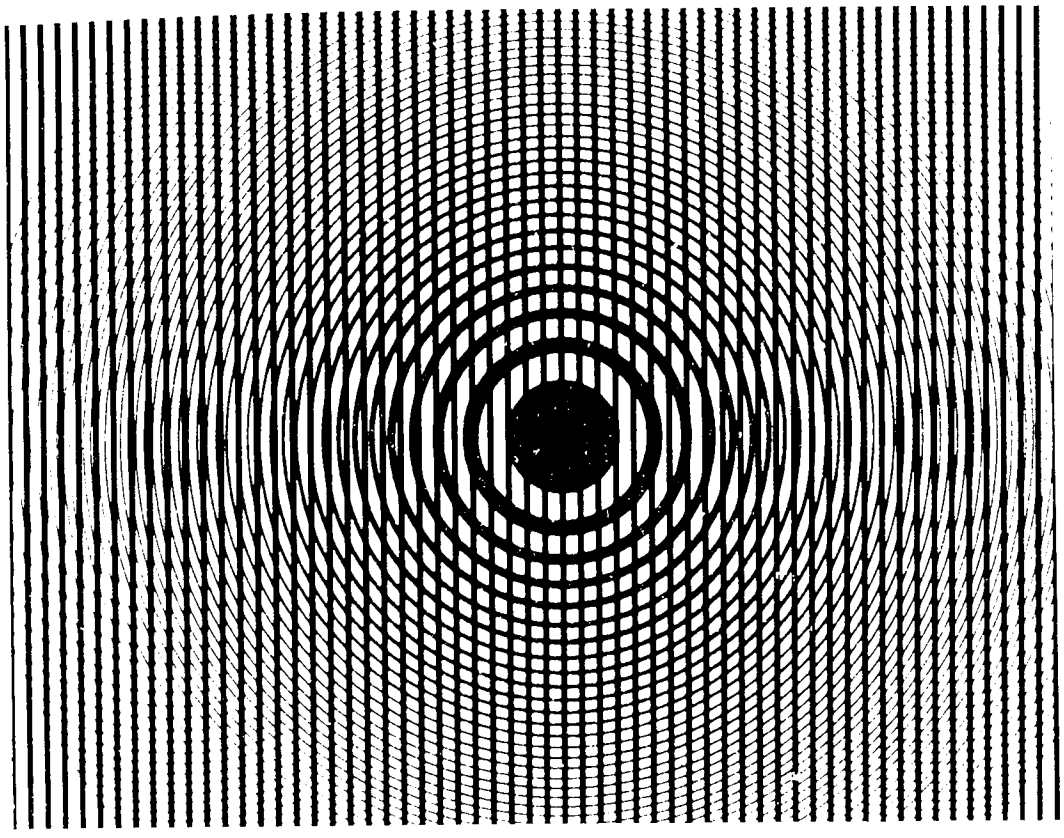

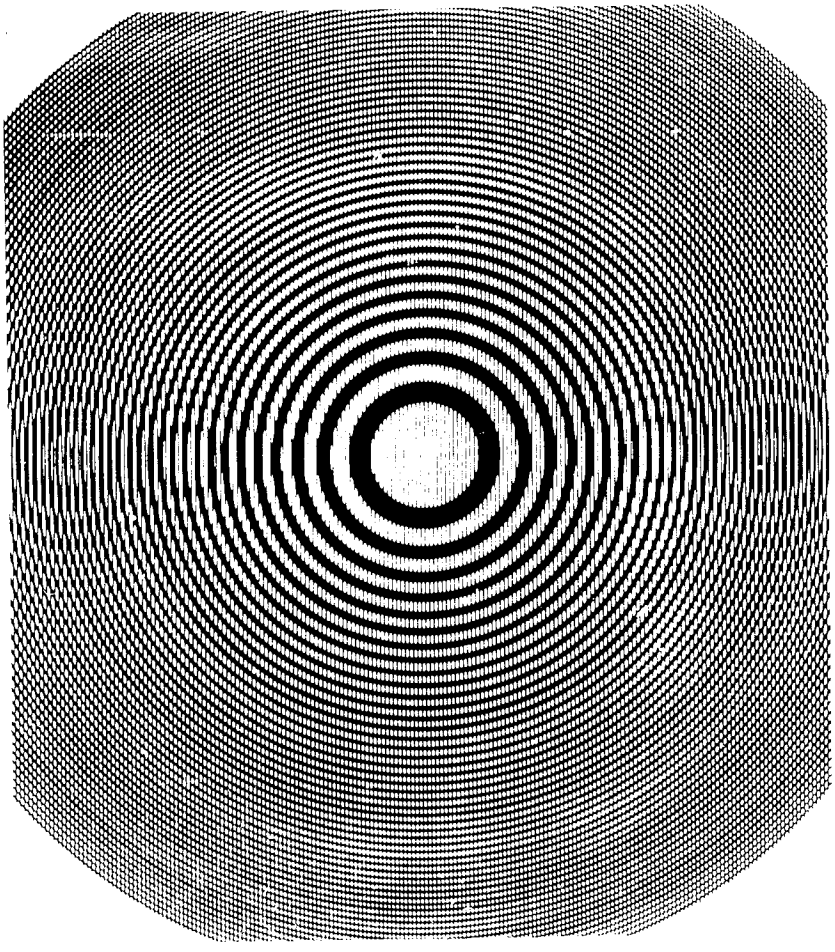

late and

but between each of this type of zone plate MZP's of varying dimensions can be found. The location, prominence and indexing of these MZP will subsequently be discussed in this section.

2.8.3. The focal length of a moiré zone plate

From equation (2.91) the focal length $^{f}(a,b)$ of the MZP as defined by its indices a and b is given by:-

$$^{f}(a,b) = \frac{r_1^2}{a\lambda} \qquad .....(2.92)$$

The original zone plate would take the indices a=1, b=0, in this indicial system. This may be verified by substituting these values into the general equation (2.91). By substituting these values into equation (2.92) we find that:-

$$^{f}(0,1) = \frac{r_1^2}{\lambda} \qquad .....(2.93)$$

This is the value of the focal length of the original zone plate. From equation (2.92) it can be seen that the focal length of an MZP is dependent only on the focal length of the original zone plate and the value of a. It is independent of the grating spacing.

From the equations (2.92) and (2.93):-

$$^{f}(a,b) = \frac{^{f}(1,0)}{a} \qquad .....(2.94)$$

or

$$\frac{1}{^{f}(a,b)} = \frac{a}{^{f}(1,0)} \qquad .....(2.95)$$

Equation (2.95) determines the focal length of the entire series of MZP. For a particular value of a, the focal length will always be the same, The value of b only determines the location of the MZP.

Consider the MZP whose parameters possess the values $(a=a_3)$ and $(b=b_3)$.

Such that $a_3 = a_1 + a_2$ .....(2.96)

and $b_3 = b_1 + b_2$ .....(2.97)

Then $f_{a_3 b_3} = \frac{f_{(1,0)}}{as} = \frac{f_{(1,0)}}{a_1 + a_2}$ .....(2.98)

Hence $\frac{1}{f_{a_3 b_3}} = \frac{1}{f_{a_1 b_1}} + \frac{1}{f_{a_2 b_2}}$ .....(2.99)

Equation (2.99) is an important result and is identical to that obtained for the MZP formed between two overlapping zone plates. However, there is one important difference. The values of b within equation (2.99) are redundant as they have no influence on the focal length of the MZP. Thus equation (2.99) may be generalised further by substituting the parameter b which can take any value.

Thus $\frac{1}{f_{a_3 b}} = \frac{1}{f_{a_1 b}} + \frac{1}{f_{a_2 b}}$ .....(2.100)

The general conclusions drawn appertaining to the similar equation derived for the case of overlapping zone plates are also valid in this instance. Two different approaches may be made in determining the mode of formation of the MZP. These have been investigated in the case of overlapping zone plates in the previous section. In this case, the problem is slightly different. Not only do we have the original zone plate of focal length f, but we have a whole series of MZP of the same focal length occurring whenever a=1. In this case, we must consider the formation of MZP of focal length less than f to be formed by pairs of MZP where a=1 for the comprehensive approach; the sequential approach is unaffected. To clarify this, table 2.2 shows the mode of formation of MZP formed between the original zone plate and the MZP(1,1) which is located at a distance k/2 from (1,0).

Thus in the comprehensive approach, the MZP are considered to be formed by a weighted sum of the two original zone plates. In the sequential mode, the MZP are formed by the linear sum of the two previous prominant MZP in the series.

2.8.4. The location of the moiré zone plate

The distance $d_{(a,b)}$ of the MZP from the original zone plate (1,0), situated at the origin is contained within the general equation (2.91).

$$d_{(a,b)} = \pm \frac{bk}{2a} \qquad .....(2.101)$$

The radius of the original zone plate at the centre of the original zone plate (a,b) must also be $d_{(a,b)}$.

The focal length of a zone plate has been shown to be:-

$$f_{(a,b)} = \frac{2r_{(a,b)}\Delta r_{(a,b)}}{\lambda} \qquad .....(2.102)$$

Hence:

$$f_{(1,0)} = \frac{2r_{(1,0)}\Delta r_{(1,0)}}{\lambda} \qquad .....(2.103)$$

Substituting for $r_{(1,0)}$ from equation (2.101):-

$$f_{(1,0)} = \frac{bk}{a}\frac{\Delta r_{(1,0)}}{\lambda} \qquad .....(2.104)$$

but $k = r_1^2/d$. Therefore $f_{(1,0)} = af_{(a,b)}\frac{\Delta r_{10}}{d}$ .....(2.105)

but $f_{(1,0)} = f_{(a,b)}b$. Hence $\frac{\Delta r_{10}}{d} = \frac{b}{a}$ .....(2.106)

Equation (2.106) shows that the MZP (a,b) is formed when the ratio of the zone separation to the grating spacing is equal to b/a. This confirms and generalises an observation made by Stecher (1964). Here is was observed that at the most prominent MZP ((1,1) in our parametric system) was formed when the zone separation of the zone plate was equal to d. For MZP (1,1) equation (2.106) becomes:

$$\frac{\Delta r_{(1,1)}}{d} = 1 \qquad \ldots\ldots(2.107)$$

This relationship will lead to new applications in the interpretation of field-ion micrographs where a similar relationship exists between the zone widths of two field-ion planes at the centre of a subsiduary plane.

The location of the MZP may also be found using a graphical construction which is based on equation (2.106) and is similar to figure 2.15, used to locate MZP formed between two overlapping zone plates. In figure 2.19 the zone separations Δr are plotted versus x for the original zone plate centred at the co-ordinate origin. This produces the familiar 'hanging curtains' effect. Superimposed on this is the function, grating spacing versus x which is, of course, a straight line parallel to the x co-ordinate. Also plotted in this figure are integral multiples of Δr and d. Hence, for instance the MZP (3,2) is found at the point where the $3\Delta r_{(1,0)}$ curve intersects the 2d straight line.

As before, this figure also reveals the limitations on the number of MZP that are allowed. For instance, in this system, there can be no MZP (1,11) since there can be no intersection point. The number of MZP is also limited by the finite number of zones in the zone plate and the finite pitch of the grating. For example the curve $9\Delta r_{(1,0)}$ fails to intersect the 1d straight line on the figure. The x co-ordinate is a function of the number of zones contained in the zone plate and so for the number of zones allowed for in figure (2.19), the MZP(9,1) is not possible. This MZP would be possible if the grating pitch was increased by a factor of tenfold.

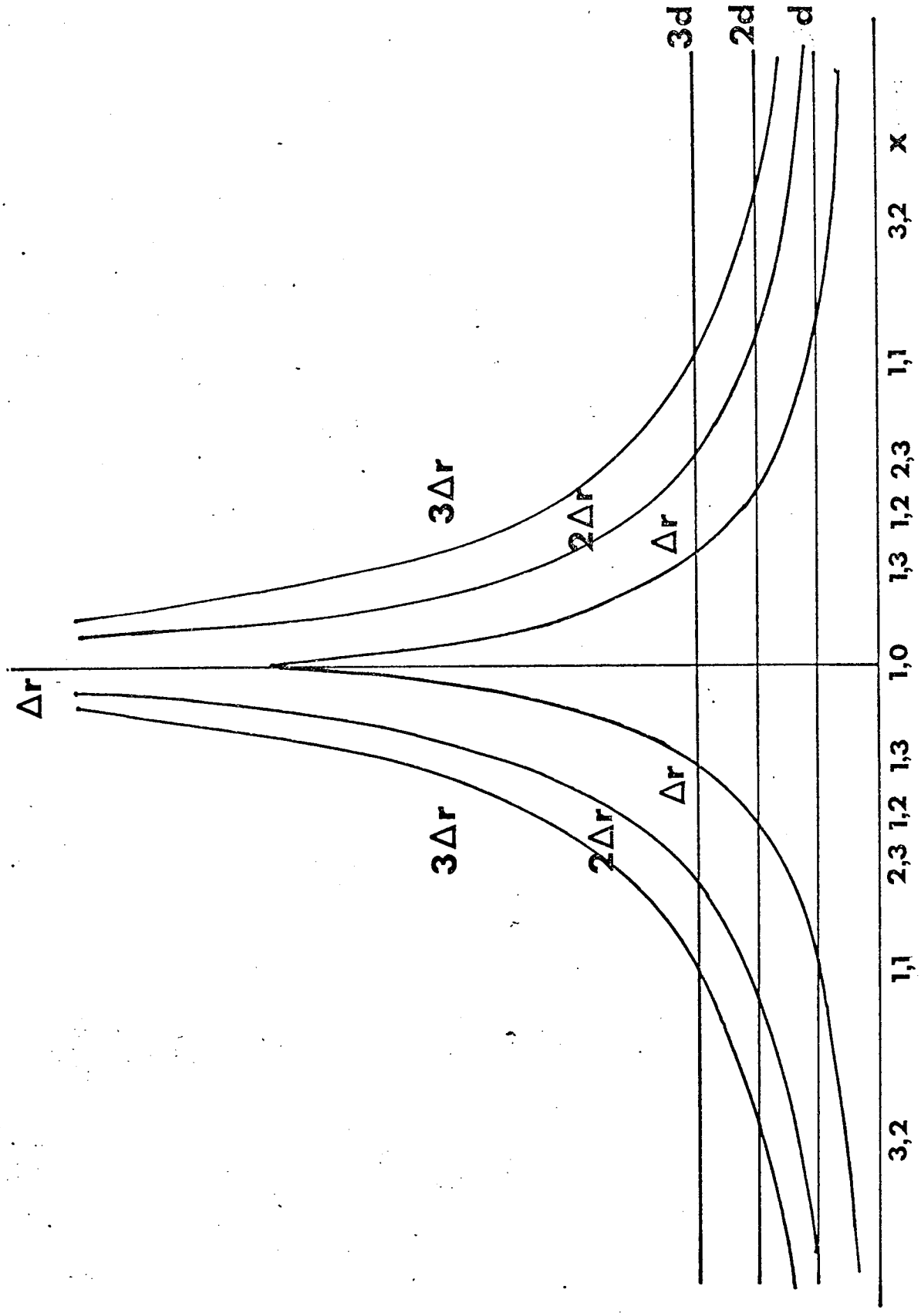

Figure 2.19 A graphical method for locating the position of M.Z.P. formed by superimposing a zone plate with a grating.

This may also provide a useful method of determining the focal length of a zone plate. The co-ordinate centre of a MZP (ab) is given by:-

$$x = \frac{br_1^2}{2ad}$$

Thus if a grating of known pitch d is available, it is quite simple to measure x and knowing a and b, r_1^2 may be calculated. Hence for a particular wavelength λ, the focal length r_1^2/λ can be found.

2.8.5. The phase factor of a moiré zone plate

The phase factor of a MZP has already been defined in section (2.6.5). The phase factor in this system for a particular MZP depends on the location of the MZP (and hence the grating pitch) and the phase factor of the original zone plate. The phase factor of an MZP(a,b) is given by the expression:-

$$\delta_{ab} = \left(\frac{b^2 r_1^2}{4a d^2} + \delta - p_i\right) \qquad \ldots\ldots(2.108)$$

In this case the value of p_i is an integral number such that $(p_i + 1) > \frac{b^2 r_1^2}{4ad^2} + > p_i$. Thus the phase factor ab can only take values $1 \geqslant \delta_{ab} \geqslant 0$.

2.8.6. The moire pattern produced by overlapping a zone plate with a grid structure

2.8.6.1 General analysis

The two dimensional array of MZP formed by this system is illustrated in figure 2.20. The original zone plate is represented by the equation:-

$$x^2 + y^2 = r_1^2(m+\delta) \qquad \ldots\ldots(2.109)$$

The equation of a grid can be broken down into two expressions describing two sets of equispaced gratings orientated

Figure 2.20 The moire pattern formed by the superposition of a zone plate and a grid structure.

n of a zone

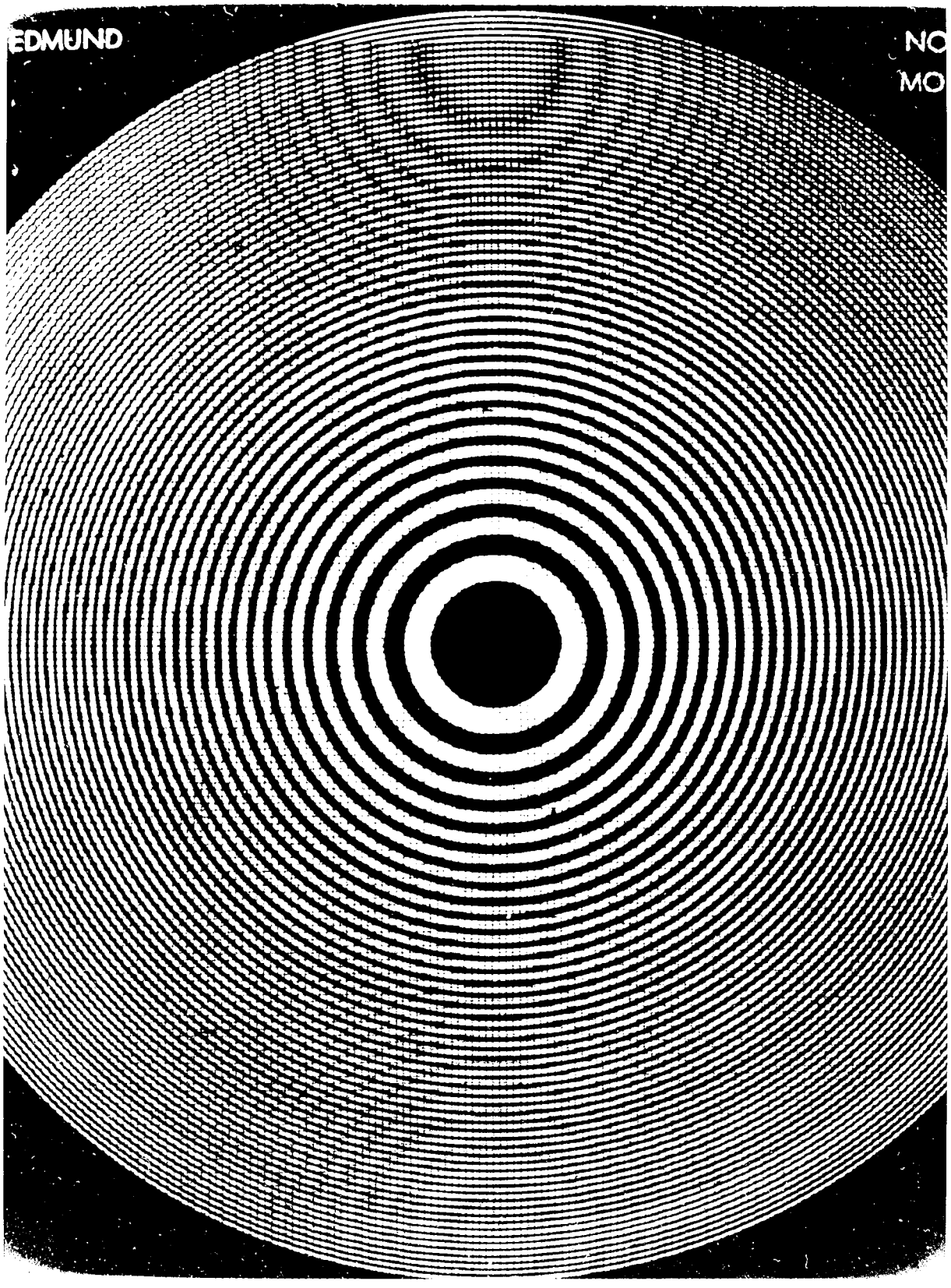

perpendicular to each other. For simplicity we shall consider only the case of a square mesh i.e. when the pitch of the two gratings is equal. Hence the equation of an equispaced grating with spacing d orientated parallel to the y axis is:-

$$x = \pm nd \qquad \text{.....(2.110)}$$

Similarly, the equation of an equispaced grating parallel to the x-axis is:-

$$y = \pm qd \qquad \text{.....(2.111)}$$

The zone plate is situated at the origin of an xy co-ordinate system and its principal focal length is given by r_1^2/λ, m, n and q = 0, 1, 2, 3... are positive integers.

Utilising the indicial equation (ignoring the subtractive moiré effect for reasons outlined earlier).

$$am + bn + cq = p \qquad \text{.....(2.112)}$$

where a, b and c are positive integers.

Eliminating n, n and q from equations (2.109), (2.110), (2.111) and (2.112).

$$(x \pm \frac{bk}{2a})^2 + (y \pm \frac{ck}{2a})^2 = \frac{r_1^2}{a}(p + \frac{k^2}{r_1^2 4a}(b^2+c^2) + \delta) \qquad \text{.....(2.113)}$$

Let us now examine the location and focal length of these MZP.

2.8.6.2. <u>The focal length of a moiré zone plate</u>

Equation (2.113) corresponds to a series of MZP of focal length f_{ab} given by:-

$$f_{(a,b)} = \frac{r_1^2}{a\lambda} \qquad \text{.....(2.114)}$$

As before, the focal length is independent of the grid structure and is solely a function of the focal length of

the original zone plate. Once more, the focal length of the original zone plate corresponds to the case (1,0). Hence following the method used in subsection 2.8.3. we find that for the comprehensive approach:-

$$\frac{1}{f(a,b,c)} = \frac{a}{f(1,0)} \qquad \text{.....(2.115)}$$

For the sequential approach where $a_4 = (a_1 + a_2 + a_3)$ $b_4 = (b_1 + b_2 + b_3)$, and $c_4 = (c_1 + c_2 + c_3)$ it can easily be shown that:-

$$\frac{1}{f(a_4,b,c)} = \frac{1}{f(a_1,b,c)} + \frac{1}{f(a_2,b,c)} + \frac{1}{f(a_3,b,c)} \qquad \text{.....(2.116)}$$

where b and c can take any integral values.

2.8.6.3. <u>The location and phase factor of an MZP</u>

Equation (2.113) shows that the centres of the MZP(a,b) are located at the co-ordinates $(\frac{+bk}{2a})$, $(\frac{+ck}{2a})$. The distance between this point and the origin, corresponds to the radius $r_{(0,1)}$ of the original zone plate & is given by:-

$$r_{(0,1)} = ((\frac{bk}{2a})^2 + (\frac{ck}{2a})^2)^{\frac{1}{2}} \qquad \text{.....(2.117)}$$

Simplifying

$$r_{(0,1)} = \frac{k}{2a}(b^2+c^2)^{\frac{1}{2}} \qquad \text{.....(2.118)}$$

Using the method developed in subsection(2.8.4.) it can be shown that:-

$$\frac{\Delta r_{01}}{d} = \frac{1}{a(b^2+c^2)^{\frac{1}{2}}} \qquad \text{.....(2.119)}$$

That is, at the location of the centre of MZP (a,b,c), the ratio of the zone width of the original zone plate at that point and the grating pitch d is $a(b^2+c^2)^{-\frac{1}{2}}$.

Following the previous analysis, the phase factor of an MZP (a,b,c) is given by the expression:-

$$\delta(a,b,c) = \frac{k^2}{4r_1^2 a}(b^2+c^2) + \delta - p_i \qquad \ldots\ldots(2.120)$$

where $p_i + 1 \geq \frac{k^2}{4r_1^2 a}(b^2+c^2) + \delta \geq p_i$.

2.8.7. Summary and conclusions

This section represents the first systematic investigation of the properties of the moiré patterns formed between a zone plate and a grating and a zone plate and a grid structure. Using techniques developed previously (section 2.6), several new relationships have been put forward regarding the mode of formation of moiré zone plates. In order to generalise the approach to include all types of zone plate, the reader is referred to section 2.2.2.4 where methods have been developed. By the inclusion of the original zone plate into the parametric nomenclature, the sequential and comprehensive approaches formed in section 2.6 to explain the formation of MZP due to the superposition of zone plates, have been extended and modified to explain the formation of MZP in this system.

The relevance of MZP to synthetic holography has been discussed previously and the MZP formed by this method will be important. However the most important application of this study is felt to be in the interpretation of field-ion micrographs. An analogue may be drawn between the zone plate and a single field-ion plane (chapter 3). The zone plate may also represent the projected contours of a shape similar to that of a field-ion emitter. If a zone plate is then overlapped with a grid structure, the resulting

moiré pattern resembles a field-ion micrograph. In this case the grid structure represents the crystal lattice. It is hoped that the present study will lead to a better understanding of the zone width phenomenon at the centre of a (hkl) field-ion plane.

Table 2.2

MZP of indices a,b	$\frac{1}{\hat{f}(a,b)}$	Comprehensive approach	Sequential approach	Position
2,1	2/f	$1/f + 1/f_{11}$	$1/f + 1/f_{11}$	k/4
3,1	3/f	$2/f + 1/f_{11}$	$1/f + 1/f_{(21)}$	k/6
3,2	3/f	$1/f + 2/f_{11}$	$1/f_{11} + 1/f_{21}$	k/3
4,1	4/f	$3/f + 1/f_{11}$	$1/f_{21} + 1/f$	k/8
4,3	4/f	$1/f + 3/f_{11}$	$1/f_{11} + 1/f_{32}$	3k/8
5,2	5/f	$4/f + 1/f_{11}$	$1/f_{21} + 1/f_{31}$	k/5
5,3	5/f	$1/f + 4/f_{11}$	$1/f_{21} + 1/f_{32}$	3k/10

CHAPTER THREE

OPTICAL ANALOGUES OF FIELD-ION MICROSCOPY

3.1. Introduction

This chapter discusses the optical analogues that may be derived between the geometry of a single plane in the field-ion image, and a zone plate, and between the interdependant system of ring structures composing the entire field-ion image, and the moiré pattern formed between overlapping zone plates. Subsequently, the applications of such analogues to the interpretation of field-ion micrographs are discussed.

The zone plate has been dealt with already in chapter 2; only the aspects of fundamental relevance will be briefly reviewed here. It is well known that a zone plate behaves in a similar fashion to a lens in that it brings incident radiation to a focus. Reference to figure 3.1(a) will illustrate the familiar Fresnel zone plate, which consists of alternate black and white circular zones, which, to a first approximation, are of equal area. A more general case is the binary zone plate (Horman and Chau (1967)), shown in figure 3.1(b). Here the series of black zones are not necessarily equal in area to that of the white. The image of a single field-ion plane, figure 3.1(c), possesses a striking similarity to the binary zone plate, and it will be shown that it does indeed possess this zone plate geometry. Hence it is possible to utilise the focussing properties of such images to extract new information from the micrograph. The complicated microscope projection introduces a degree of spherical aberration into the focus and this will be

Figure 3.1 The zone plate analogy with the field-ion plane. This illustration shows the similarity in appearance between :-

(a) A Fresnel zone plate

(b) A binary zone plate

(c) A field-ion plane

(a)

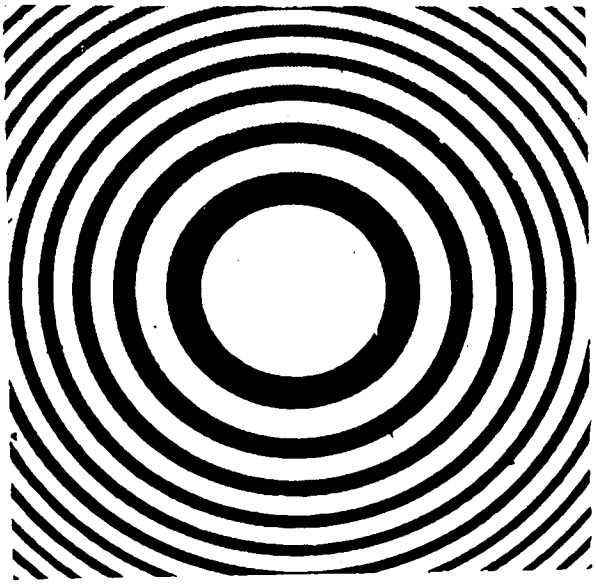

eeld-ion plane. This

rrance between :-

(b)

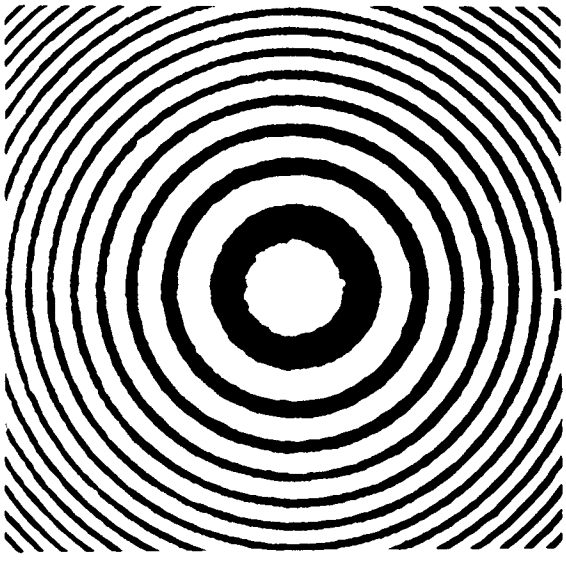

(c)

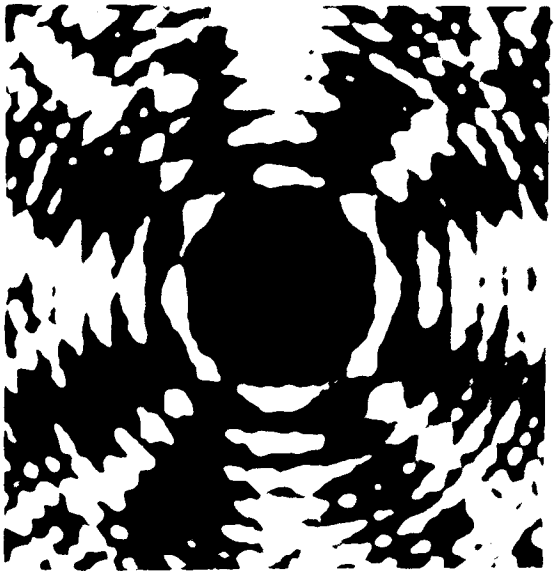

discussed theoretically.

It was shown in chapter 2 that a visible moiré pattern may be formed when two or more periodic structures are overlapped, the loci of the points at which the elements making up each structure overlap will themselves form a pattern which may be apparent to the eye. A zone plate is an example of such a periodic structure, and the moiré pattern produced by the overlap of two zone plates consists of a number of additional zone plates, of different dimensions, centred upon the line joining the centres of the two original zone plates (for a complete analysis see chapter 2). An example of such a moiré pattern is shown in figure 3.16(f) and this should be compared with figure 3.16(a) a region of a field-ion micrograph depicting a number of planes within a zone. Again the similarity is striking, and it will be shown by using techniques developed in chapter 2, that the entire field-ion image may indeed by interpreted in terms of moiré pattern theory. Once more, this analogue enables new kinds of information to be obtained from field-ion micrographs.

3.2. The zone plate analogue†

3.2.1. Zone plates in terms of projection geometry

All types of zone plates may be conceived in terms of projective geometry, these concepts are introduced here and are subsequently used to derive the zone plate

† Part of the work presented in this chapter has been published in J. Appl. Phys. Lett (1973) 23 161.

analogue of a single field-ion plane.

3.2.1.1. The Fresnel zone plate

The exact relationship between the radius, r_n, of the nth ring of a Fresnel zone plate, and its focal length, f, is given by:-

$$r_n^2 = nf\lambda + \frac{n^2\lambda^2}{4} \qquad .....(3.1)$$

Usually $f>>\lambda$ and this may be approximated to:-

$$r_n^2 = nf\lambda \qquad .....(3.2)$$

In terms of projective geometry, equation (3.1) is equivalent to the figure produced when a hyperboloid which has been cut by incremental equally spaced planes at right angles to its axis, is projected in a direction parallel to its axis onto a plane surface. Equation (3.2) on the other hand, is equivalent to a paraboloid treated similarly.

If we now consider a spherical surface cut by a series of parallel planes a distance d apart, (figure 3.2) then the radii of the rings thus defined on its surface may be determined using the Sagitta formula, thus:-

$$r_n^2 = nd(2R - nd) \qquad .....(3.3)$$

where R is the radius of the sphere. This may now be written as:-

$$r_n^2 = 2Rnd - n^2d^2 \qquad .....(3.4)$$

Providing $R>>d$ we may neglect the term n^2d^2 from which it may be seen that the projection of such a figure, perpendicular to the series of parallel planes, is almost as good an approximation to the exact zone plate geometry as is the projected paraboloid viz. $r_n^2 \propto n$.

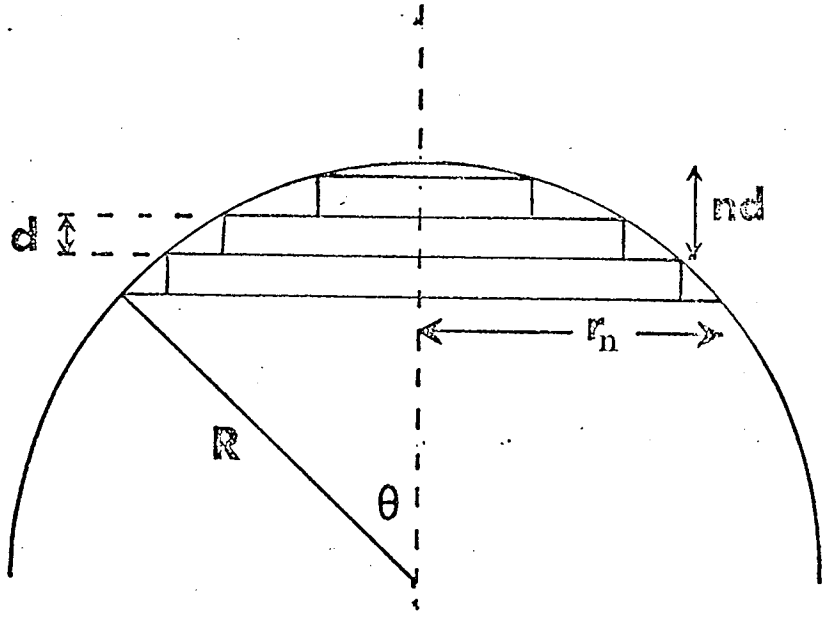

Figure 3.2 A schematic diagram of a field-ion plane used to show that it possesses zone plate geometry, i.e. $r_n^2 \propto n$.

A more general expression for the focal length of a zone plate has been derived in chapter 2 and in the case of the Fresnel zone plate it can be shown that equation (3.2) reduces to:-

$$f = \frac{2r\Delta r}{\lambda} \qquad .....(3.5)$$

where r and Δr are defined by figure 3.3(a). This equation is useful in that it defines the focal length of an annular region, and hence could be applied to a zone plate whose focal length was not constant with distance from the axis (i.e. spherically aberrated). This aspect will be considered in more detail later in this chapter.

3.2.1.2. The binary zone plate

In terms of projective geometry, a binary zone plate may be described as the figure produced when two concentric spheres (i.e. a thin shell) are cut by incrementally spaced planes, and then projected onto a flat surface as before. This is illustrated in figure 3.3(b). We must now replace the quantities r and Δr by ρ and $\Delta\rho$, whereupon the formula for the focal length of an annulus now becomes:-

$$f = \frac{\rho\Delta\rho}{\lambda} \qquad .....(3.6)$$

Comparison of the situation represented by figures 3.3(a) and 3.3(b) shows that for outer spheres of the same radius, R, and planes of the same spacing, d, the binary zone plate will possess twice as many zones for a given value of n. This may be demonstrated by considering the shell thickness in figure 3.3(b) to equal d/2, whereupon the binary zone plate becomes the

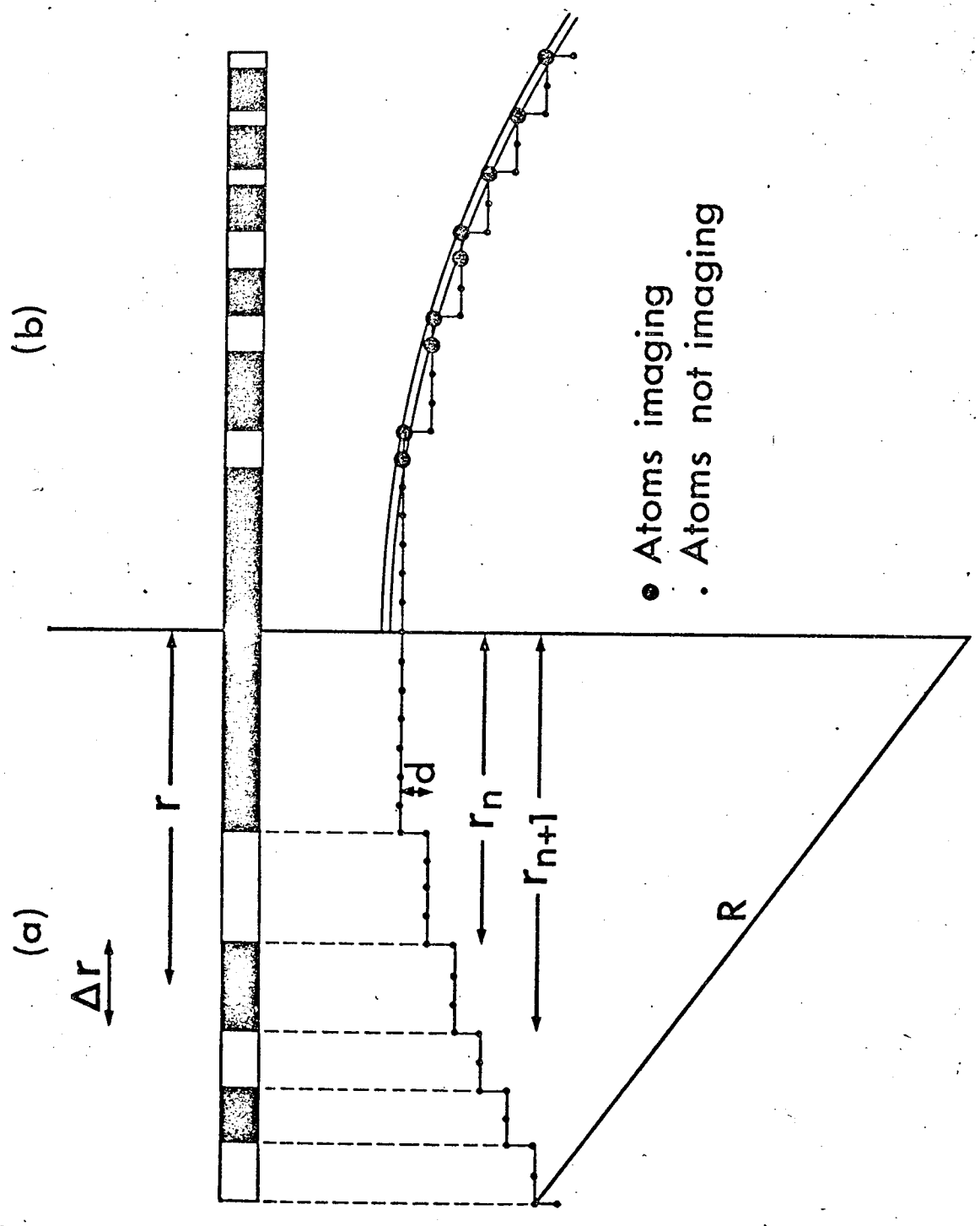

Figure 3.3 The geometry of a single plane on the field-ion surface, (a), showing the stepped atomic structure and the equivalent Fresnel zone plate in orthographic projection with alternate zones appearing black and white, and (b), showing the relative areas imaged and nonimaged, and the equivalent binary zone plate.

special case of a Fresnel zone plate, but with twice as many zones as in figure 3.3(a). It will be seen that by taking this special case of a binary zone plate, we can make subsequent calculations involving binary zone plates that much easier.

3.2.2. The geometry of a field-ion plane

It has been shown by Moore (1962) that the general appearance of the field-ion image may be understood by taking a thin spherical shell through the crystal lattice and by considering that only those atoms which lie within the shell give rise to image points. This model is illustrated for a single plane on the imaging surface by means of figure 3.4(a). Typically the shell thickness would be about one tenth the step height of the plane, and comparison of figure 3.3(b) and 3.4(a) shows that the appearance of such a plane, if projected orthographically as before, is identical to that of the binary zone plate: the imaged atoms form the white zones, and the non-imaged ones the black zones.

We may calculate the focal length of the field-ion zone plate defined in figure 3.4 in the following way. Strictly equation (3.6) should be used since the zone plate is a binary one. However the calculation becomes very much simpler if we instead calculate the special case of this for which the shell thickness equals d/2 i.e. the equivalent Fresnel zone plate (formed by planes whose separation is d/2), as discussed at the end of the previous section and shown in figure 3.4(b). The focal length of the latter is identical to that of the binary zone plate; it is only the total diffracted intensity

at the focal point that is different (Horman and Chau (1967)). (While this latter quantity does itself, in principle, contain information on the zone plate, the field-ion analogy is not sufficiently accurate to justify attempting to use it here).

3.2.3. The focal length of a single field-ion plane

The geometric similarity between the image of a single crystal plane in a field-ion micrograph, and a Fresnel zone plate was first pointed out by Vali and Gordon (1967) and investigated subsequently by Southworth, Leifer and Walls (1973). Since one property of a zone plate is its ability to focus collimated light, Vali and Gordon (1967) have proposed that a suitably magnified field-ion image could be focussed using coherent light, and information extracted from the focal lengths obtained from each plane. However their subsequent analysis is fundamentally incorrect on a number of points.

Figure 3.5(a) shows the stepped atomic structure of a single plane at the apex of a field-ion emitter of radius R. Each parallel atomic plane is a distance, d, apart, and the radii of the rings thus defined on the emitter surface may be determined using the Sagitta formula as before, and hence from equation 3.4:-

$$r_n^2 = 2Rnd \qquad .....(3.7)$$

As Vali and Gordon point out, the condition that $r_n^2 \propto n$ equals that for the construction of a Fresnel zone plate, and the schematic above figure 3.5(a) shows the resulting appearance of such a zone plate with alternate zones made transparent and opaque.

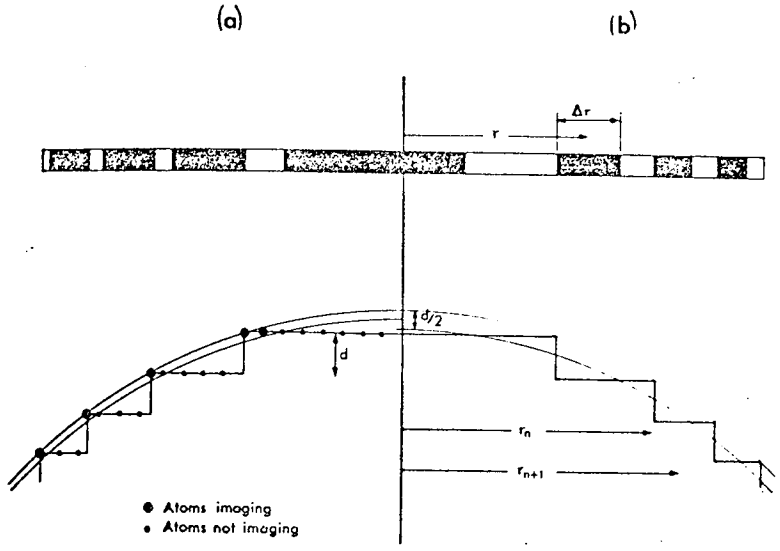

Figure 3.4 (a) The zone plate formed by adopting the 'thin shell' model.

(b) The equivalent Fresnel zone plate formed if we let the shell thickness be d/2.

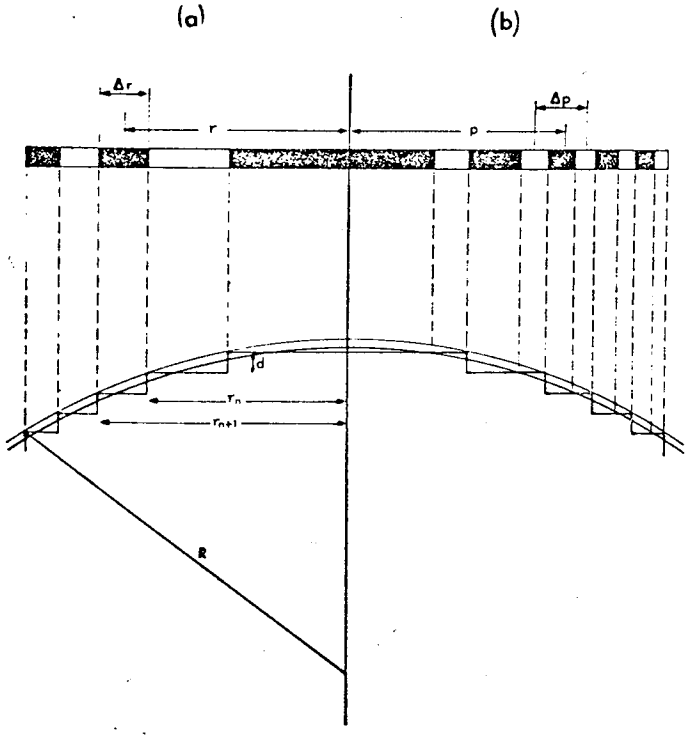

Figure 3.5 (a) The zone plate formed by projecting the stepped structure of the emitter, compared with

(b) The zone plate formed by adopting the thin shell criterion for imaging.

Using equation (3.5) for the focal length, f, of a Fresnel zone plate.

Where:

$$\Delta r = r_{n+1} - r_n \qquad .....(3.8)$$

and

$$r = \frac{r_{n+1} + r_n}{2} \qquad .....(3.9)$$

In this case the focal length of such a zone plate becomes:-

$$f = \frac{2}{\lambda}\left(\frac{r_{n+1} + r_n}{2}\right)(r_{n+1} - r_n) \qquad .....(3.10)$$

$$f = \frac{r_{n+1}^2 - r_n^2}{\lambda} \qquad .....(3.11)$$

Substituting values for r_{n+1}^2 and r_n^2 obtained using equation (3.7) this becomes:-

$$f = \frac{2Rd}{\lambda} \qquad .....(3.12)$$

This expression may be seen to contain information on the emitter radius and the spacing of the atomic planes considered.

Strictly the zone plate considered so far is that obtained by orthogonal projection of the stepped structure of the emitter surface onto the tangent plane at the apex, hence producing unit magnification. In practice magnifications of several million times are produced in the field-ion microscope, since an image of the emitter surface is projected onto a fluorescent screen placed some distance, say T, away. If, following Vali and Gordon, we assume the projection to be a radial (or gnomonic) one, then the zone plate is magnified linearly by a factor T/R, whereupon equation (3.12) becomes:-

$$f = \frac{2T^2 d}{R\lambda} \qquad .....(3.13)$$

This equation is identical to that deduced by Vali and Gordon, ignoring any further (linear) magnification between the image and the transparency used in the focussing experiment.

However this derivation ignores the real nature of the field-ion imaging surface. Moore (1962) has shown that the latter may most readily be illustrated by taking a thin shell through the crystal lattice, and by considering only those atoms which lie within the shell to give rise to image points. This is illustrated in figure 3.5(b). Thus the imaged atoms form the white zones and the non-imaged atoms on the surface the black zones, as shown schematically for an orthogonal projection, above this figure. The resulting kind of zone plate is the binary zone plate, and its focal length may be no longer expressed by the formula used by Vali and Gordon, since the black and white zones are no longer equal in area. Furthermore it is evident that, for a given value of n, the binary zone plate contains twice as many zones as in the Fresnel case. Using the appropriate expression for the focal length of a binary zone plate, equation (3.6), it is possible to show that in the above situation, the corresponding equation to equation 3.13 is:-

$$f = \frac{T^2 d}{r\lambda} \qquad .....(3.14)$$

a factor of 2 different from that of Vali and Gordon.

A further error lies in their assumption of a radial projection. In practice the stereographic projection is a better approximation (Brenner (1962)),

although even this is not exact. If we assume a stereographic projection then the magnification factor, T/R, must be replaced by T/2R, and hence the focal length defined by equation (3.14) becomes a further factor of 4 smaller. If other projection relationships are considered a different correction factor becomes necessary.

Vali and Gordon also made the assumption that the magnification factors for such projections are linear. Actually the factors T/R (for radial) and T/2R (for stereographic) are themselves approximations, and ideally should include some function of θ, the angle that a given point on the emitter surface subtends at the centre. The net effect of this would be to introduce a certain degree of spherical aberration into the zone plate image, since the $r_n^2 \propto n$ relationship is not carried over precisely from the emitter to the image plane. Equation (3.5) is useful here in that in this form it allows the focal length of successive zones to be calculated, and hence the degree of spherical aberration to be evaluated. In practice it turns out that, providing θ is small (as it is for the first few rings around an axially located plane), then the above function of θ is unity and the magnification factors used are good approximations.

However only one plane can lie at the apex of the emitter. The remainder are located around its hemispherical surface, their poles subtending various, and now substantial, angles θ, with the emitter axis. The images of the resulting zone plates will now display

more substantial aberrations since their magnification is no longer linear. Only for the sterographic case do the zones project as circles and even then the latter are not quite concentric, introducing some biased degree of astigmatism into the zone plate. With other projections the aberrations introduced will be more complex. For example figure 3.6 shows the image of a Fresnel zone plate constructed on the surface of a sphere, whose axis makes an angle of 30° with the projection axis, projected (a) radially and (b) stereographically. The aberration is considerably less in the latter case, although still present.

When it is realised that the emitter radius need not be a constant, it becomes apparent that obtaining an exact expression for the focal length of any given zone plate image is not a simple matter, involving as it does, not only T and d, but also local radius and local magnification (the latter being a function of R, θ and the projection relationship). Thus it is not even true that, as stated by Vali and Gordon (1967), images of crystallographically equivalent planes will necessarily exhibit the same focal length. Furthermore their suggestion that the technique could be used to measure interplanar distances at great magnification is not realistic; the uncertainties involved are too great, and in any case such data is already well known from X-ray analysis. Rather, the focussing technique may be used to determine the local image magnification (and hence the projection relationship), providing that the local radius of the emitter, together with the other

Figure 3.6 The appearance of a Fresnel zone plate such as that in figure 3.3, but inclined at an angle of 30° to the emitter axis, projected (a) radially and (b) stereographically.

A

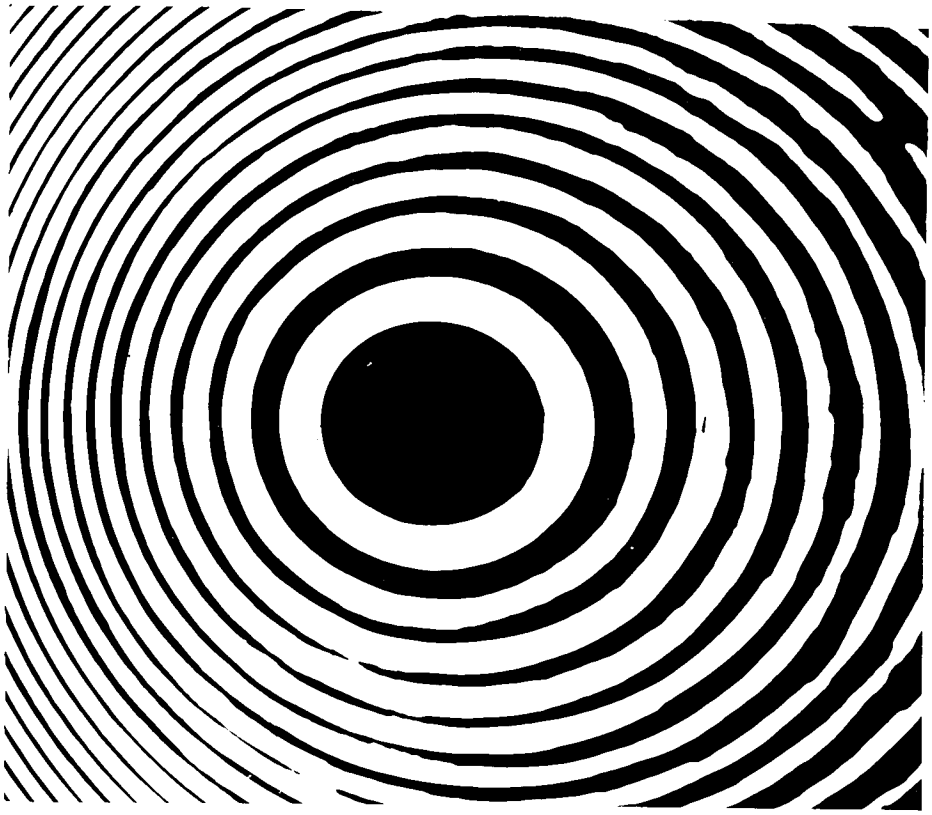

B

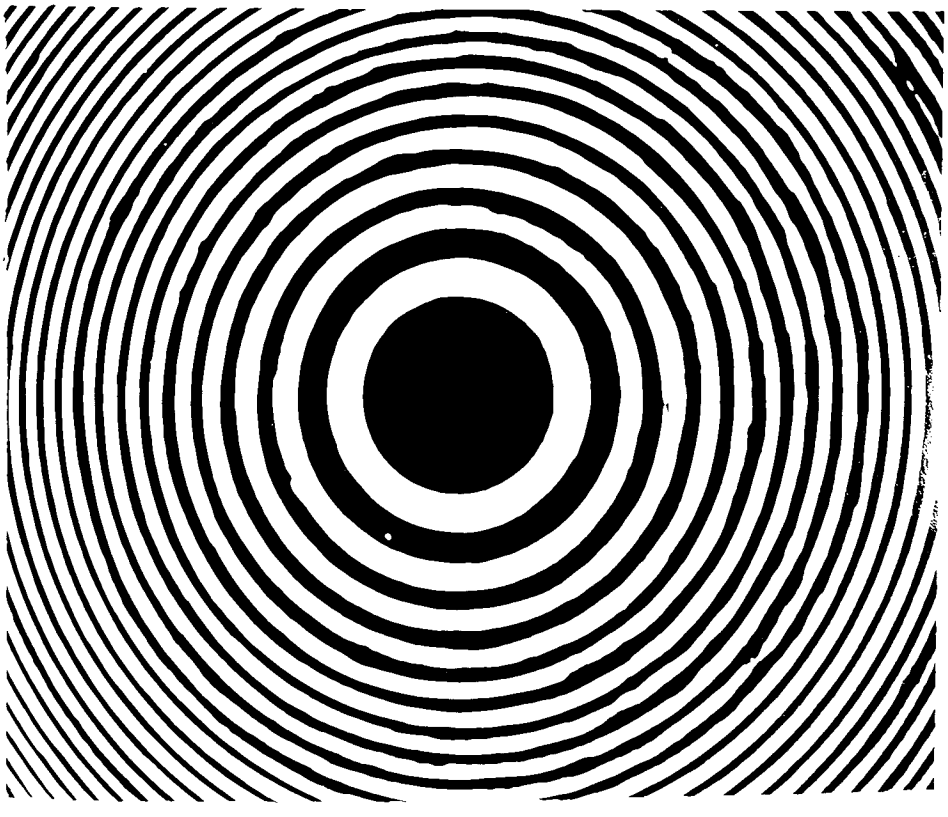

parameters in the expression for the focal length are known. The detailed theory and applications of this technique are described in chapter 5.

3.2.4. The focussing properties of a single field-ion plane

3.2.4.1. The phase factor of a field-ion plane

So far we have implicitly assumed that the field-ion plane is of maximum diameter. In general, field evaporation will have left it at some intermediate size and its centre will lie at a distance δd from the outer sphere where $0 < \delta < 1$. The term δ is the field evaporation phase factor and is discussed in more detail in chapter 4. It is necessary here to show that the focal length of a field-ion plane, as in the case of a zone plate, does not depend on the phase, or in this case the stage of field evaporation of the plane. Numbering the ledges 0,1,2,3,.. it can be seen that:-

$$r_n^2 = 2Rd(n+\delta) \qquad .....(3.15)$$

and similarly:-

$$r_{n+1}^2 = 2Rd(n+1+\delta) \qquad .....(3.16)$$

Substitution of equations (3.15) and (3.16) into equation (3.11) involves the subtraction of the above two terms, the phase factors cancel and we are again left with equation (3.12) for the focal length.

This result is to be expected as conventional zone plates do not necessarily have their zone radii expressed directly by equation (3.1) and it is necessary to include a similar factor δ also referred to as the phase (chapter 2). The Fresnel zone plate shown in figure 3.1(a) does have a phase of zero, but the binary

zone plate shown in figure 3.1(b) does not. Differences in phase do not affect the focal length of either the zone plate or the field-ion plane.

3.2.4.2. The spherical aberration of a projected field-ion plane

Spherical aberration is a term usually used to describe the common observation that lenses do not refract all the incident radiation to a common focal point. The term can also be used to describe the same irregularity displayed by zone plates. In this case, due to some irregularity in the annulus structure, light is not diffracted to a common point on the zone plane axis. The focal length variation along this axis is sometimes referred to as longitudinal spherical aberration. In this section we shall attempt to predict the extent of the longitudinal spherical aberration for a projected field-ion plane in terms of the number of ring n, for a particular value of R. The analysis is performed using the stereographic and the radial projections, both commonly used in the analysis of micrographs. The data derived from the analysis will have a bearing on the usefulness of focussing field-ion micrographs as a means of obtaining information.

a) The spherical aberration of an axially situated field-ion plane projected stereographically

Consider the situation depicted schematically in figure 3.7. A plane lies perpendicular to the emitter axis and is situated so that its pole lies a distance T from the imaging plane. The image consists of a series of concentric rings which correspond to the

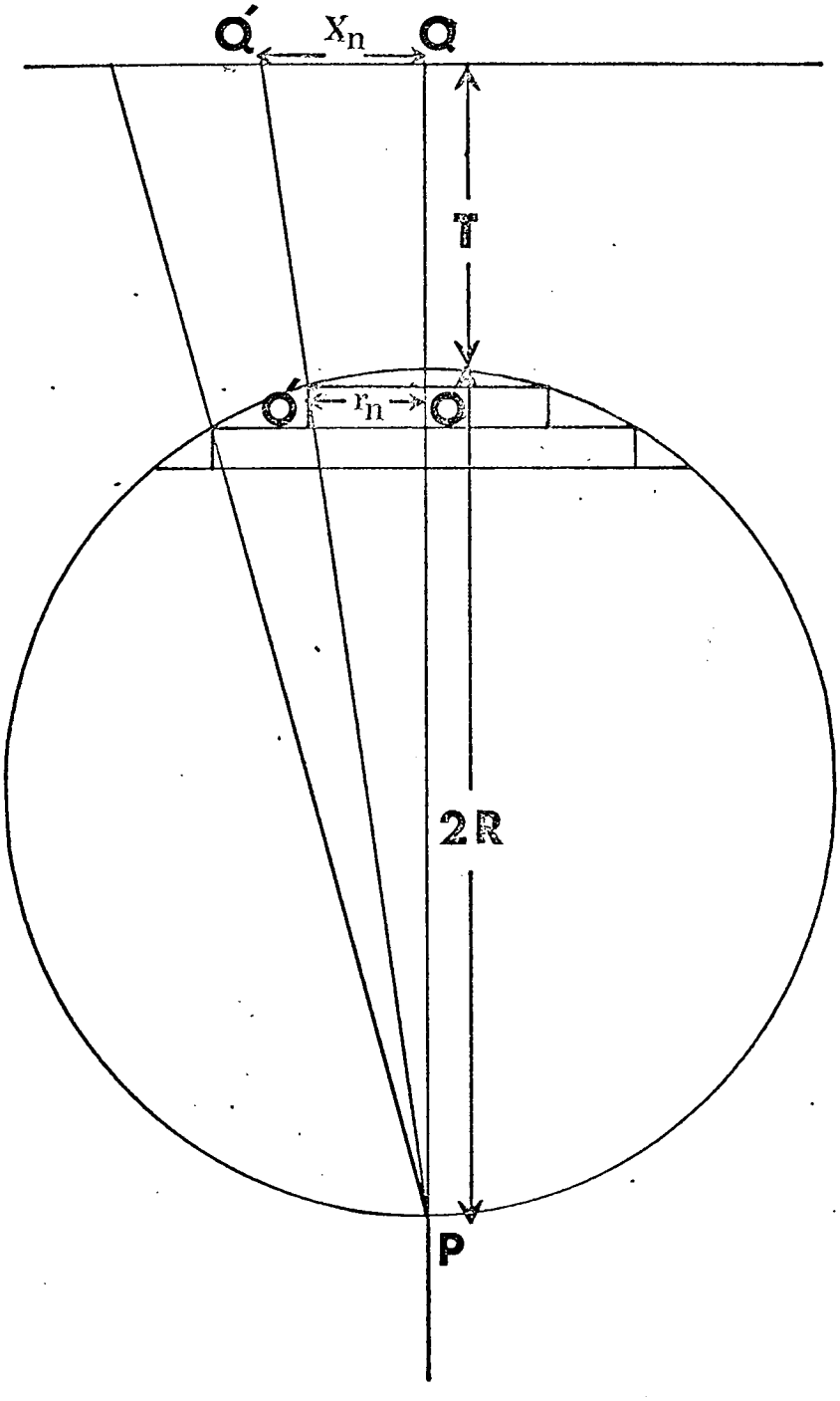

Figure 3.7. The schematic model used to calculate the spherical aberration of a field-ion plane projected stereographically. (Equation 3.22.).

circular facets existing on the specimen surface (assuming that the specimen is hemispherical). It is a property of the stereographic projection that circles project as circles (Phillips(1962)) and hence for this projection the image consists of circular rings. In fact this would also be the case for non-axial planes provided they are projected stereographically. For an axially situated plane, a circular image pattern occurs regardless of projection providing that the projection point is situated on the emitter axis. If the radius of each individual circular facet is r_n (see figure 3.7) then the radius of their magnified images is x_n. Earlier in this chapter it was shown that the field-ion plane in the image was analogous to the binary zone plate. Hence the appropriate equation to determine the focal length of a projected field-ion plane is equation (3.6). This equation is also particularly convenient as it allows the focal length of each annulus comprising the zone plate to be found. Thus the radius of the nth zone in the image ρ is given by the equation:-

$$\rho = \frac{x_n + x_{n+1}}{2} \qquad \ldots\ldots(3.17)$$

The expression for the appropriate zone separation $\Delta\rho$ is:-

$$\Delta\rho = x_{n+1} - x_n \qquad \ldots\ldots(3.18)$$

Let us examine once more, figure 3.7 from the similar triangles $\Delta PQQ'$ and $\Delta POO'$ it can be seen that:-

$$\frac{x_n}{r_n} = \frac{T + 2R}{2R - nd} \qquad \ldots\ldots(3.19)$$

but from equation (3.8) $r_n = \sqrt{(2Rnd)}$, hence substituting

for r_n in equation (3.19) we obtain:-

$$x_n = \frac{T + 2R}{2R - nd}\sqrt{(2Rnd)} \qquad \ldots\ldots(3.20)$$

Similarly, it can be shown that:-

$$x_{n+1} = \frac{T + 2R}{2R - (n+1)d}\sqrt{(2R(n+1)d)} \qquad \ldots\ldots(3.21)$$

Hence by obtaining ρ and $\Delta\rho$ from equations (3.17), (3.18), (3.20) and (3.21), the focal length f is given by the equation:-

$$f = \frac{(T+2R)^2 Rd}{\lambda}\left[\frac{(n+1)}{(2R-(n+1)d)^2} - \frac{n}{(2R-nd)^2}\right] \qquad \ldots\ldots(3.22)$$

Thus for a given lattice spacing d and specimen radius R, this equation enables the percentage change in f to be found as a function of the ring number n. Tungsten is usually (011) orientated and the (011) interplanar spacing is 2.239Å. Typical radius of curvature values for field-ion emitters are 200Å and 500Å. Equation (3.22) has been used to calculate the theoretical percentage change in the focal length as a function of ring number for these two particular values of the local radius of curvature and these are presented graphically in figure 3.8. Immediately it can be seen that the focal length varies almost linearly with ring number and that spherical aberration is reduced with increasing local radius of curvature. For example if the focal length of the 5th annulus is compared with the first then for a specimen of 200Å radius there is almost a $9\frac{1}{2}\%$ change and for a specimen of 500Å radius there is only a $2\frac{1}{2}\%$ change.

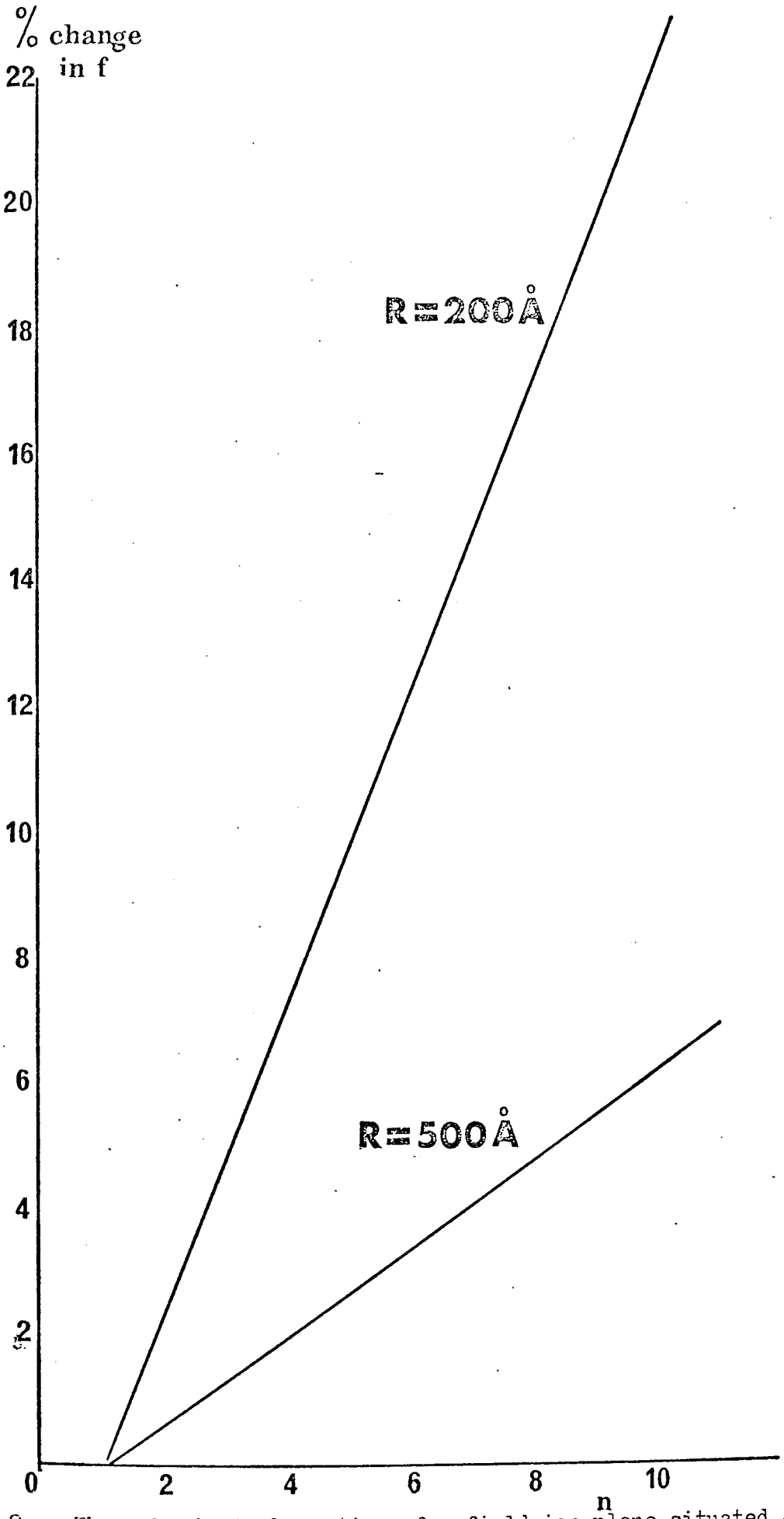

Figure 3.8. The spherical aberration of a field-ion plane situated at the emitter apex, projected stereographically. The percentage change in focal length, f, is plotted as a function of ring number, n.

b) Spherical aberration of an oxially situated field-ion plane projected radially

For a field-ion plane projected radially (i.e. the image corresponds to the situation where the faceted surface structure appears to have been projected from a point on the specimen axis corresponding to the centre of curvature of the specimen (figure 3.9). In this case, by a similar argument to that used above for the stereographic projection, the focal length of a field-ion plane in the image is given by:-

$$f = \frac{(T+R)^2 Rd}{\lambda} \left[\frac{n+1}{(R-(n+1)d)^2} - \frac{n}{(R-nd)^2} \right] \quad .....(3.23)$$

Figure 3.10 depicts the percentage variation in f as a function of ring number n. As before, the results suggest an approximately linear relationship of focal length with ring number. In this case, for instance, the fifth annulus displays a focal length of 20% for a 200Å radius specimen and only about 7% for a 500Å radius specimen.

From these calculations it is clear that the effect of spherical aberration is reduced with increasing emitter radius. Comparing the spherical aberration caused by the two projections considered, it is also clear that in general, the stereographic projection gives the least aberrated images. This is fortunate because of the two, the stereographic projection is a far better approximation to the actual projection operating in the microscope. Indeed, if the projection proposed by Brandon (1964) (see chapter 5) is used then the aberration would be reduced still further. Thus

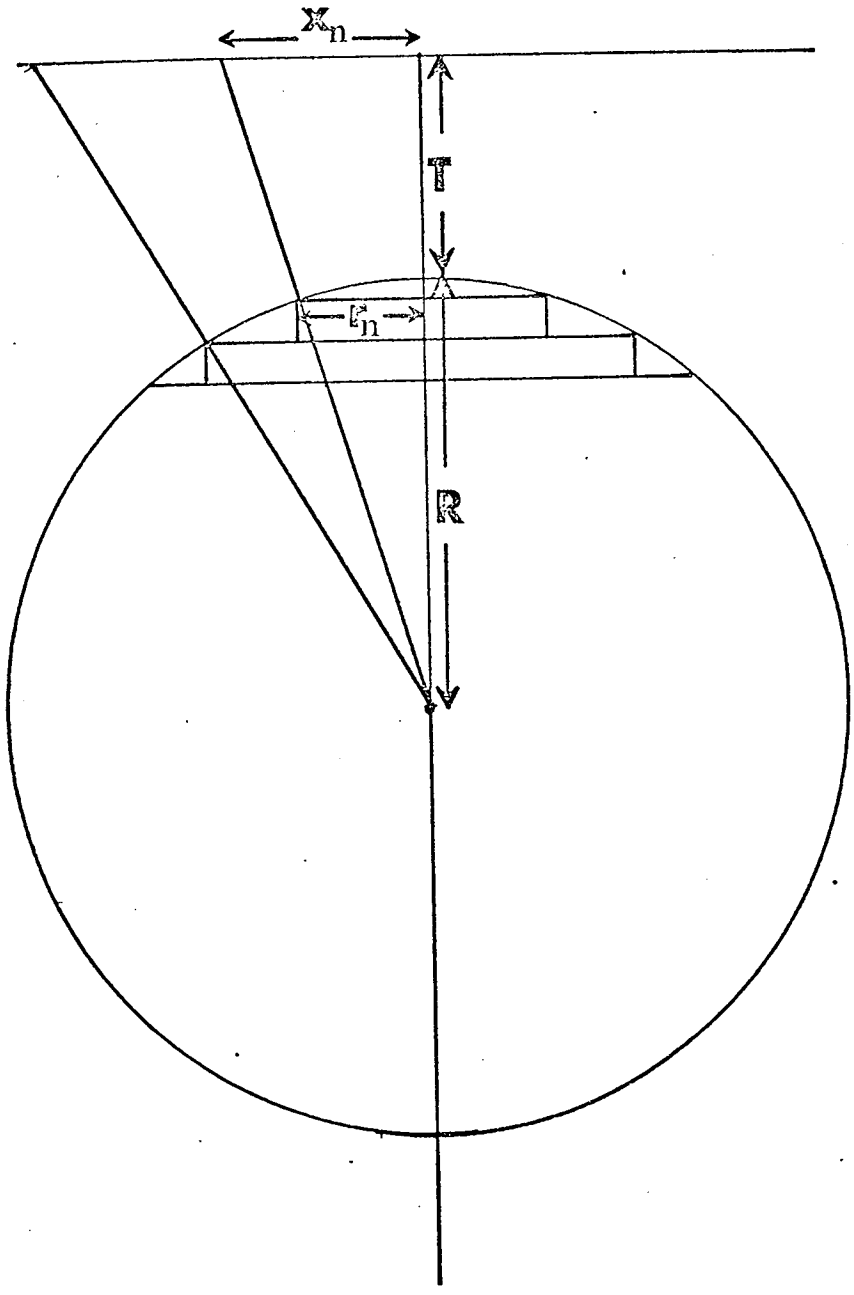

Figure 3.9. The schematic model used to calculate the spherical aberration of a field-ion plane projected radially.

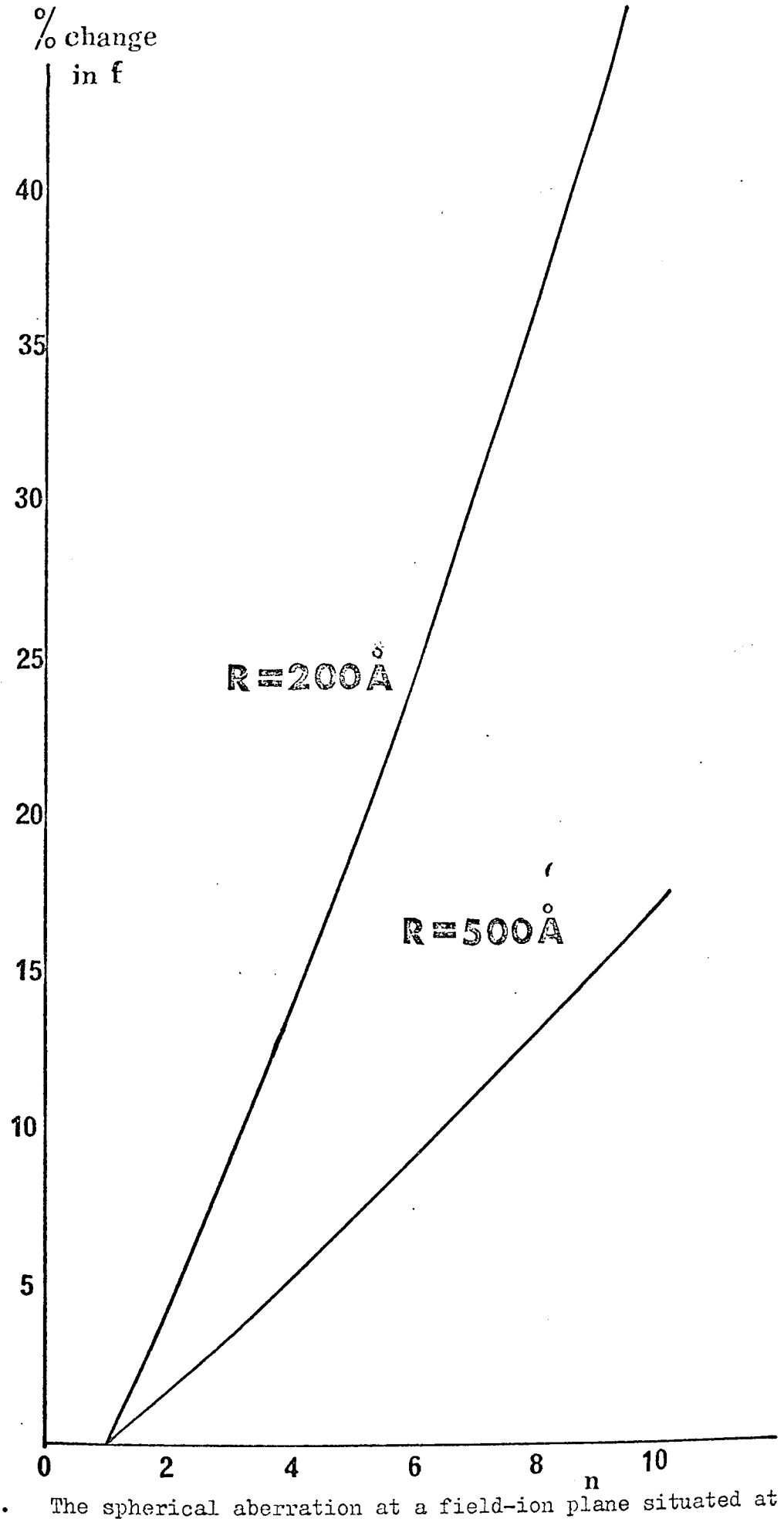

Figure 3.10. The spherical aberration at a field-ion plane situated at the emitter apex projected radially. The percentage change in focal length, f, is plotted as a function of ring number, n.

from these calculations it may be concluded that spherical aberration is not too serious a hazard in obtaining information from field-ion micrographs using the focussing technique as the inaccuracies that they introduce are within the experimental accuracy with which focal lengths may be measured.

Further aberrations arise, however when planes which are inclined at an angle to the axis of the emitter are considered. If the projection is stereographic then the image will still consist of a series of circles, but they will not quite be concentric, introducing some biased degree of astigmatism into the zone plate image, in addition to the spherical aberration. With other projection relationships the images will become aberrated in a much more complex fashion. However when order of magnitude estimages of these aberrations are compared with those which result in practice from variations in the local radius of the emitter, R, it is evident that they also may be ignored.

Hence in order to relate measured focal lengths from field-ion images to the corresponding imaging parameters, it is necessary only to use the appropriate formulae from Table 3.1, having first taken account of any (constant) magnification factor (which must be squared) between the original image, and the subsequent transparency used in the focussing experiment.

TABLE 3.1

PROJECTION	N	FOCAL LENGTH, f
Gnomonic	0	$\frac{2T^2d}{\lambda R}\left(\frac{1}{\cos^4\theta}\right)$
Stereographic	N = 1	$\frac{2T^2d}{\lambda R}\left[\left(\frac{1}{1+\cos\theta}\right)^2\right]$
Brandon	N = 2	$\frac{2T^2d}{\lambda R}\left[\frac{2\cos\theta+1^2}{(2+\cos\theta)^2}\right]$

3.3 The moiré zone plate analogue

3.3.1. A moiré interpretation of the field-ion imaging surface

The similarity between the moiré pattern formed by overlapping zone plates (figure 3.16(f)) and the field-ion image (figure 3.16(a)) was first noted by Oster (1964). It led him to raise the serious question as to whether all the planes which one would identify in the image, actually correspond to crystallographic facets on the imaging surface, or whether the appearance of some might result from some optical moiré effect due to the overlap of more prominent plane images to either side.

As a result of this suggestion a detailed analysis of the atomic configuration on the surface of a field-ion emitter has been undertaken. The conclusion is that if moiré pattern analysis is applied to the overlap of a number of planes on the specimen surface, then the moiré patterns which they would form are identical with the planar structures that are predicted to occur on purely crystallographic grounds. Furthermore the entire imaging surface may be regarded as a complex interdependent moiré pattern. Indeed, rather than implying the existence of spurious imaging effects, the moiré relationship enables new information to be obtained from micrographs since it becomes possible, for the first time, to relate the properties of several planes to one another.

The treatment referred to is a purely mathematical analysis of the interaction of sets of imaged atoms, and in no way involves the concept of a zone plate.

Nevertheless if it can be shown that the same result can be obtained in terms of overlapping zone plates, then there are a number of moiré zone plate relationships which may be used to obtain further information from the image.

Note that, while the single zone plate analogue necessarily deals with the image, involving potentially unknown terms in magnification and projection, the moiré analysis - which deals with relationships, and not with absolute measurements - may be applied directly to the emitter surface. The conclusions apply equally well to the image since there is a one-to-one correspondence between imaging surface and image (see chapter 4).

3.3.2. Moiré zone plates on a flat surface

It is possible to consider a zone plate to be the hologram of a single point (Rogers (1950)), since, if it is illuminated with a collimated laser beam, the 'image' produced is that of a point - the focus†. Hence zone plates are of considerable importance in sythetic holography, and a great deal of attention has been paid to the moiré patterns that are formed as a result of the overlap of such zone plates. A recent re-examination of the problem in chapter 2 has produced a number of new relationships which are directly relevant to the present work.

Principally these are that the zone widths (Δr or $\Delta \rho$) of the original zone plates are equal at the point where

† In the same way one could consider a field-ion micrograph to be the hologram of the projected plane normals of each plane that is imaged on the emitter surface.

the most prominent zone plate in between is formed, and that the reciprocal of the focal length of the latter is the sum of the reciprocals of those of the two original zone plates.

3.3.3. Zone plates on a spherical surface

In all this work it will be convenient to consider the equivalent Fresnel zone plate (figure 3.4(b)) rather than the true binary case: the conclusions to be drawn are identical. Thus figure 3.11 illustrates a zone plate formed on a spherical surface by parallel planes of separation d/2, and whose axis is OP. Our interest lies in the moiré pattern that will be produced when the ring structure which is centred on OP overlaps with another ring structure centred, for example on OQ. The moiré effect at any one point is produced by the overlap of the two periodic structures incident at that point. It follows therefore that in considering the formation of a possible moiré zone plate centred, say, on the point, M, then it is the focal properties at M itself that are relevant.

At M the zone width, $\Delta r'$, is defined as AA'. Strictly AA' is an arc of the sphere, but if we consider it to approximate to a section of the tangential plane at M, then we may use the flat zone plate equation (3.5) where r' now becomes the distance from the axis of the zone plate to the centre of the annulus of width $\Delta r'$. The angle POM is defined as θ_1, and hence AA'P" also equals θ_1. Thus:-

$$AA' = \Delta r' = d/_2 \sin\theta_1 \qquad \ldots\ldots(3.24)$$

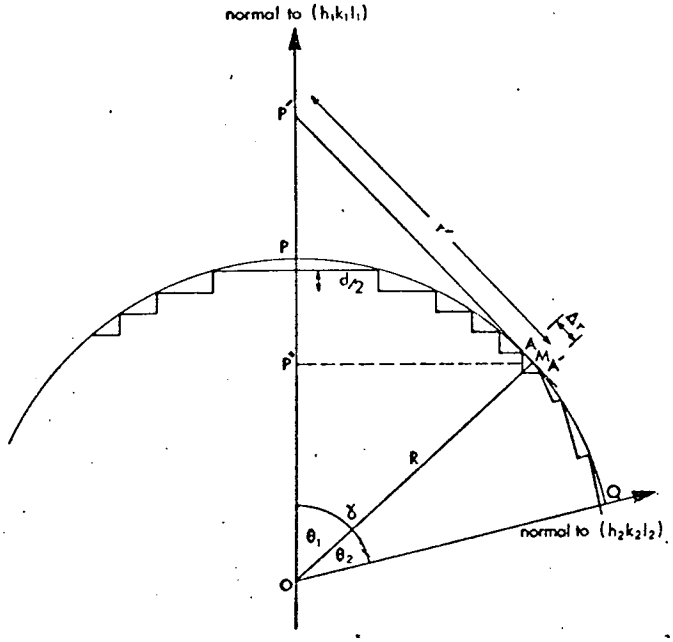

Figure 3.11 The model used to account for the focal length of a zone plate formed on a spherical surface. The focal length is a function of θ.

From the triangle P'OM it can be seen that:-

$$r' = R\tan\theta_1 \qquad .....(3.25)$$

By substituting equations (3.24) and (3.25) into equation (3.5), the focal length, $f(\theta_1)$, of a zone at a point M, subtending an angle θ_1 with the zone plate axis, is given by:-

$$f(\theta_1) = \frac{R\tan\theta_1 d}{\lambda\sin\theta_1}$$

$$= \frac{Rd}{\lambda\cos\theta_1} \qquad .....(3.26)$$

As a check, the focal length at $\theta_1 = 0^\circ$, $f(\theta_1^0)$, is given by:-

$$f(\theta_1^0) = \frac{Rd}{\lambda} \qquad .....(3.27)$$

which is equivalent to equation (3.14), although arrived at differently. It follows therefore that:-

$$f(\theta_1) = \frac{f(\theta_1^0)}{\cos\theta_1} \qquad .....(3.28)$$

3.3.4. Moiré zone plates on a spherical surface

Referring again to figure 3.11, we shall consider two planes on the surface of a field-ion emitter, $(h_1k_1l_1)$, centred upon OP, and $(h_2k_2l_2)$, centred upon OQ, the angle between OP and OQ being γ. OM is the axis of a possible moiré zone plate, and makes angles θ_1 and θ_2 with OP and OQ respectively.

From a purely crystallographic standpoint we expect that there will be a whole range of planar facets lying in the zone between $(h_1k_1l_1)$ and $(h_2k_2l_2)$, whose indices (hkl) are given by the Weiss zone law, viz:-

$$m(h_1k_1l_1) + n(h_2k_2l_2) = (hkl) \qquad .....(3.29)$$

where m, n are positive integers. The interplanar spacing of the plane (hkl) is given by:-

$$d_{(hkl)} = \frac{a}{(h^2 + k^2 + l^2)^{\frac{1}{2}}} \qquad .....(3.30)$$

where a is the lattice parameter of the metal. We are confining our attention here to the case of a cubic crystal, the analysis is later extended to cover hexagonal structures and clearly the analysis can be extended to other cases. It is sufficient merely to consider the most prominent moiré zone plate formed in between the two original ones, since the remainder may then be generated by repeating the analysis between one original and the first moiré zone plate, and so on. Since the prominence of a plane increases with increasing d-spacing (Moore and Ranganathan (1967)), the most prominent (hkl) plane, $(h_3k_3l_3)$ will be that of lowest indices, namely that for which m = n = 1, viz:-

$$(h_1k_1l_1) + (h_2k_2l_2) = (h_3k_3l_3) \qquad .....(3.31)$$

The angle θ_1 which the plane $(h_3k_3l_3)$ makes with, say, $(h_2k_2l_2)$, is given by:-

$$\cos\theta = \frac{h_3h_2 + k_3k_2 + l_3l_2}{(h_3^2 + k_3^2 + l_3^2)^{\frac{1}{2}} (h_2^2 + k_2^2 + l_2^2)^{\frac{1}{2}}} \qquad .....(3.32)$$

The aim is to establish whether the moiré zone plate relationships developed for the flat case, may be extended to the spherical situation, and hence correctly predict that the most prominent moiré zone plate formed at M, should possess identical characteristics to the crystallographic plane $(h_3k_3l_3)$. These characteristics are, (a) its angular location with respect to either one of the originals,

(b) its focal length, or equivalent d-spacing.

(a) Location of the moiré zone plate

We shall use the equal zone widths relationship described in chapter 2 i.e.

$$\Delta r_1' = \Delta r_2' \qquad \text{.....(3.33)}$$

These quantities may be obtained using equation (3.24) and hence:-

$$\frac{d(h_1k_1l_1)}{2 \sin \theta_1} = \frac{d(h_2k_2l_2)}{2 \sin \theta_2} \qquad \text{.....(3.34)}$$

Substituting $\theta_1 = \gamma - \theta_2$, and expanding we find that:-

$$d(h_1k_1l_1) \sin \theta_2 = d(h_2k_2l_2) [\sin\gamma \cos\theta_2 - \cos\gamma \sin\theta] \qquad \text{.....(3.35)}$$

Substituting $(1 - \cos^2\theta_2)^{\frac{1}{2}}$ for $\sin \theta_2$, and $(1 - \cos^2\gamma$ for $\sin \gamma$, and rearranging:-

$$\left\{ \frac{\left[\frac{d(h_1k_1l_1)}{d(h_2k_2l_2)} + \cos \gamma\right]^2}{\left[\frac{d(h_1k_1l_1)}{d(h_2k_2l_2)} + \cos \gamma\right]^2 [1 - \cos^2\gamma]} \right\}^{\frac{1}{2}} = \cos \theta \qquad \text{.....(3.36)}$$

Since

$$\cos \gamma = \frac{h_1h_2 + k_1k_2 + l_1l_2}{(h_1^2 + k_1^2 + l_1^2)^{\frac{1}{2}} (h_2^2 + k_2^2 + l_2^2)^{\frac{1}{2}}} \qquad \text{.....(3.37)}$$

equation (3.36) becomes:-

$$\cos \theta_2 = \frac{h_2(h_1 + h_2) + k_2(k_1 + k_2) + l_2(l_1 + l_2)}{(h_2^2 + k_2^2 + l_2^2)^{\frac{1}{2}} [(h_1 + h_2)^2 + (k_1 + k_2)^2 + (l_1 + l_2)^2]^{\frac{1}{2}}} \qquad \text{.....(3.38)}$$

Hence the moiré zone plate formed at M makes an angle θ_2 with OQ, such that its indices (hkl) must be given by $h=h_1+h_2$, $k=k_1+k_2$, $l=l_1+l_2$, by comparison with equation (3.32). Thus the indices (hkl) derived using the moiré approach do equal the $(h_3k_3l_3)$ of equation (3.31), derived crystallographically.

(b) Focal length of the moiré zone plate

If f_1 is the focal length of the plane $(h_1k_1l_1)$ and f_2 the focal length of the plane $(h_2k_2l_2)$ then at M:

$$f_1(\theta_1) = \frac{Rd_{(h_1k_1l_1)}}{\lambda \cos \theta_1} \qquad .....(3.39)$$

which, using equation (3.30) becomes:

$$f_1(\theta_1) = \frac{Ra}{\lambda \cos \theta_1 \, (h_1^2 + k_1^2 + l_1^2)^{\frac{1}{2}}} \qquad .....(3.40)$$

Similarly

$$f_2(\theta_2) = \frac{Ra}{\lambda \cos \theta_2 \, (h_2^2 + k_2^2 + l_2^2)^{\frac{1}{2}}} \qquad .....(3.41)$$

Knowing that the indices (hkl) of the moiré zone plate are related to $(h_1k_1l_1)$ and $(h_2k_2l_2)$ as described at the end of the previous section, we can evaluate $\cos \theta_1$ and $\cos \theta_2$ using equation (3.32). We use the result obtained earlier in chapter 2 that, for the most prominent zone plate (hkl), formed between $(h_1k_1l_1)$ and $(h_2k_2l_2)$

$$\frac{1}{f_3} = \frac{1}{f_1} + \frac{1}{f_2} \qquad .....(3.42)$$

In terms of a spherical surface this becomes:-

$$\frac{1}{f_3} = \frac{1}{f_1(\theta_1)} + \frac{1}{f_2(\theta_2)} \qquad .....(3.43)$$

Substituting we find that:-

$$\frac{1}{f_3} = \frac{\lambda}{Ra}\left[\frac{(h_1^2+k_1^2+l_1^2)^{\frac{1}{2}}\cos\theta_1 + (h_2^2+k_2^2+l_2^2)^{\frac{1}{2}}\cos\theta_2}{}\right] \quad .....(3.44)$$

Evaluating $\cos\theta_1$ and $\cos\theta_2$ this becomes:-

$$f_3 = \frac{Ra}{\lambda}\,\frac{1}{[(h_1+h_2)^2+(k_1+k_2)^2+(l_1+l_2)^2]^{\frac{1}{2}}} \quad .....(3.45)$$

Hence this refers to a zone plate whose effective d-spacing is given by $\frac{a}{(h_3^2+k_3^2+l_3)^{\frac{1}{2}}}$, which is again that of the crystallographic plane located at M.

3.3.5. The moiré zone plate analogue for hexagonal close packed materials

The angle γ between the normals to the two planes $(h_1k_1i_1l_1)$ and $(h_2k_2i_2l_2)$ for a hexagonal close packed material where c/a represents the ratio of prism height to edge is given by the formula:

$$\cos\gamma = \frac{h_1h_2 + k_1k_2 + \frac{1}{2}(k_1h_2 + h_1k_2) + \frac{3a^2}{4c^2}l_1l_2}{\left\{(h_1^2+h_1k_1+k_1^2)(h_2^2+h_2k_2+k_2^2+\frac{3a^2}{4c^2}l_2^2)\right\}^{\frac{1}{2}}} \quad .....(3.46)$$

The corresponding interplaner spacing is given by:-

$$d_{(hkil)} = \left(\frac{4}{3}\left\{\frac{a^2}{h^2+hk+k^2+3/4\,l\frac{a^2}{c^2}}\right\}\right)^{\frac{1}{2}} \quad .....(3.47)$$

Just as in the case of the cubic lattice we expect a range of planar facets to be formed lying in the zone between $(h_1k_1i_1l_1)$ and $(h_2k_2i_2l_2)$ whose indices are given by the Weiss zone law. Let us again consider only the most prominent moiré zone plate formed in between the two originals. Again, we are able to characterise the moiré zone plate by way of its angular

location and its focal length, both of which should be identical to the equivalent crystallographic plane $(h_3k_3i_3l_3)$.

Following the analysis in section 3.3.4.(a) for the cubic system, the location of the moiré zone plate is controlled by equation (3.33). By substituting appropriate values for cos γ and the interplanar spacing into equation (3.36) we find:-

$$\cos\theta_2 = \frac{h_2(h_1+h_2)+k_2(k_1+k_2)+\frac{1}{2}((k_1+k_2)h_2+(h_1+h_2)k_2)+\frac{3a^2}{4c^2}(l_1+l_2)l_2}{\left\{((h_1+h_2)^2+(h_1+h_2)(k_1+k_2)+(k_1+k_2)^2)(h_2^2+h_2k_2+k_2^2+\frac{3a^2}{4c^2}l_2^2)\right\}^{\frac{1}{2}}} \quad \ldots\ldots(3.48)$$

Thus the moiré zone plate formed at M makes an angle θ_2 with OQ such that its indices are given by $h = h_1+h_2$, $k = k_1+k_2$ and $l = l_1+l_2$ in comparison with equation (3.46). Once again the indices (hkil) derived using the moiré zone plate analogue reproduce the crystallographically derived relationship.

The equivalent interplanar spacing may also be found in a manner identical to that used for the cubic system in equation (3.39) and then substituting in equation (3.35) for the appropriate values of $f_1(\theta_1)$ and $f_2(\theta_2)$, it is possible to show that the focal length f_3 of the most prominent moiré zone plate is:-

$$f_3 = \frac{R}{\lambda}\left[\frac{4a^2}{3(h_1+h_2)^2+(k_1+k_2)^2+(h_1+h_2)^2(k_1+k_2)+\frac{3a^2}{4c^2}(l_1+l_2)^2}\right]^{\frac{1}{2}} \quad \ldots\ldots(3.49)$$

This refers to a zone plate whose effective interplanar spacing is given by $\left(\frac{4}{3}\left\{\frac{a^2}{h_3^2+h_3k_3+k_3^2}+\frac{3}{4}\frac{a^2}{c^2}\right\}\right)^{\frac{1}{2}}$

which again corresponds to the equivalent crystallographic plane located at M.

Although the method has been shown to work for both cubic and hexagonal systems only, the method is quite general and can be shown to work by merely inserting the appropriate values for the interplanar angle and the interplanar spacing.

3.4. The crystallographic development of the field-ion specimen

The position and prominence of field-ion planes has been investigated using iterative computer methods by Moore and Ranganathan (1967), however these factors may be studied more analytically employing the 'hanging curtains' diagram method developed in chapter 2. The method is based on equation (3.33) which states that at the centre of a field-ion plane, the zone widths of the two intersecting planes are equal. Figure 3.12 plots zone widths Δr versus θ (for tungsten, the angle substended by a point on the field-ion surface to the (011) plane). For simplicity, let the phase factors of the two major planes considered by zero, i.e. $\delta_{(011)} = \delta_{(110)}$, although we are only considering the bcc structure (e.g. tungsten), the method is completely general. As before with the moiré zone plate construction, the function of Δr versus θ is a step function, but has been drawn continuous for clarity. Also plotted are the integral multiples(harmonics) of Δr. Thus, for example the position of the plane (132) is found at the point of intersection of the $2\Delta r(110)$ and $\Delta r(011)$ curves. The position of any field-ion plane can be found in

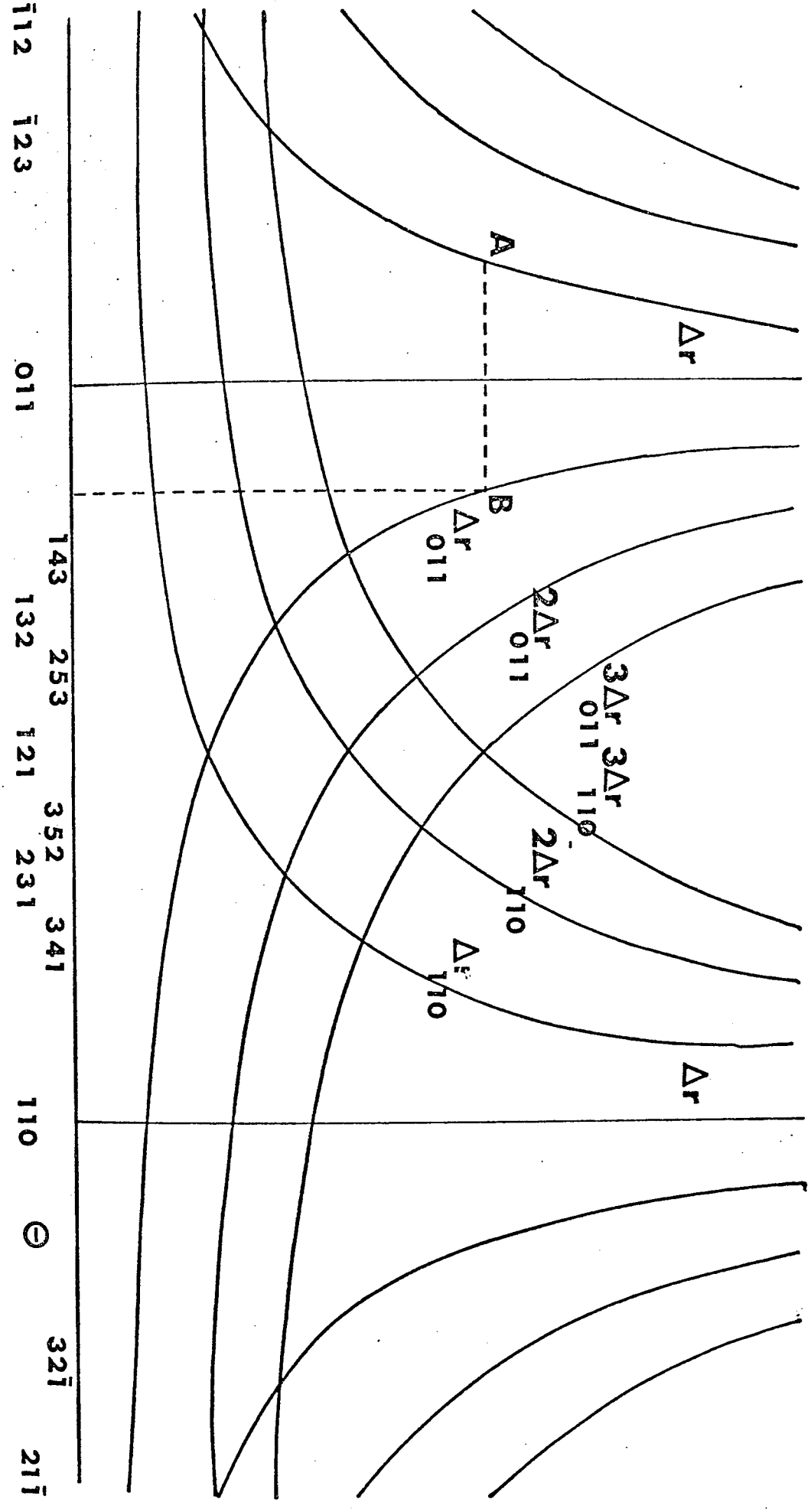

Figure 3.12 A graphical method for locating the position of a field-ion plane.

this manner by finding the intersection of some harmonic of $\Delta r(011)$ with the corresponding harmonic of $\Delta r(110)$. To be completely general, it is possible to overlap the curves of less prominent planes than (011) to obtain the position of other planes, but the use of the major planes in figure 3.12 again leads to clarity.

This figure also reveals the limitation on the number of field-ion planes that may be formed at a given specimen radius. First we must consider more closely the form of the curves in figure 3.12. As these curves are in actual practice stepped functions, the curves possess a plateau symmetric about the Δr axis. The position of this plateau is a function of the specimen radius and hence it is possible that once this is taken into account then some curves cannot intersect and thus the development of the plane they represent is precluded. Thus the plateau of the curves is governed by the radius of the specimen, and it is the position of this plateau which determines the development of a field-ion plane. The position and size of this plateau can be found with respect to Δr and θ by using the following argument. Consider the simple illustration of a single field-ion plane of radius R in figure 3.2. The hemisphere is cut by incremental planes of interplanar spacing d. Consider a point p subtending an angle θ to the centre of curvature O, then (neglecting phase factors) we have from the Saggitta formula:

$$2R - nd = R^2 \sin^2\theta \qquad \ldots\ldots(3.50)$$

but $2Rnd >> n^2d^2$

therefore $2Rnd = R^2\sin^2\theta$ .....(3.51)

Hence $\sin\theta = \sqrt{(\frac{2nd}{R})}$* .....(3.52)

Now, as we are primarily concerned with the step function at the first ring, substituting n=1 into equation (3.52) we find:-

$$\sin\theta = \sqrt{(\frac{2d}{R})} \qquad .....(3.53)$$

This equation determines the angle subtended by the first ring (at maximum size). If this equation is used to plot θ versus R, i.e. the angle subtended by the first ring as a function of specimen radius, a curve illustrated in figure 3.13 is found. Figure 3.13 shows the form of the plot using tungsten (d = 2.239Å) as an example, taking values of R between 100Å and 1200Å. Thus we find that for R = 900Å, the angle θ subtended by the first ring is 4° 3' whereas for R = 100Å, θ = 12° 12'. If the pertinent information is then transferred from figure 3.13 to figure 3.12 the number of possible intersections is reduced, thus reducing the number of possibly developed planes in the field-ion image. An example should make this clear. Consider a field-ion micrograph of tungsten; the specimen radius of curvature is approximately 200Å. From figure 3.13, the first ring of the specimen subtends about 8.5° and the corresponding plateau is drawn AB (dashed lines) onto

* Note that a new method of measuring <u>local</u> radius of curvature can be extracted from this equation. From equation (3.16), $\Delta r = \frac{d}{\sin\theta}$, thus substituting in equation (3.52) we find $R = \frac{2n\Delta r^2}{d}$.

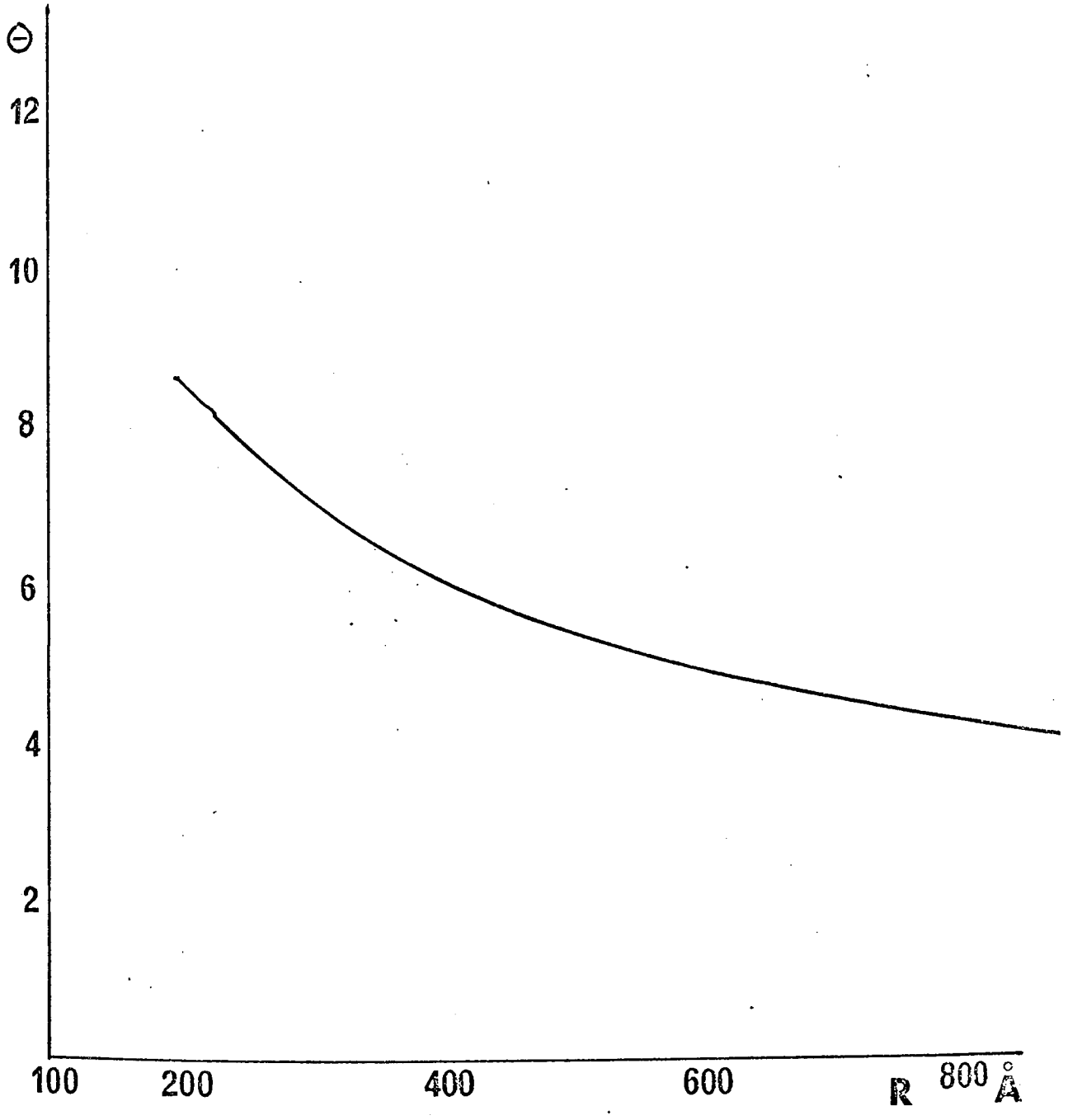

Figure 3.13. The angle subtended by the first ring of a field-ion plane (assuming the plane to have zero phase factor) as a function of the local radius of curvature of the emitter. These results are for the case of tungsten (d = 2.239 Å).

figure 3.12, thus making a $5\Delta r(011) - \Delta r(011)$ intersection impossible, thus a (561) plane cannot exist on the field-ion specimen of radius 200Å. In principle it is possible to predict the exact specimen radius at which a plane will appear in the image.

Although, in principle, a plane will be represented on the specimen surface, it may not be visible. Moore and Ranganathan (1967) imposed a rather artifical condition on the visibility of a plane in a particular zone in the field-ion micrograph suggesting that the plane must be evident on the surface as a flat area representing at least two inter-row distances along the zone. In principle, a plane could be represented by a single row distance, but nevertheless may not be recognisable. Just as in the case of moiré zone plates, the visibility of field-ion planes can be considered in two ways. Firstly, the greater its ring radius (and hence interplanar spacing) the more prominent it should appear. This is the almost trivial conclusion made by Drechsler and Liepack (1965) which is certainly true on the specimen, but may be altered in the image by local magnification effects (see chapter 5). Secondly the greater the number of overlap points (atoms) forming the rings then the more readily it is recognised. Thus the more zones making up the major field-ion planes, the more readily detected will be the vicinal planes. Once again, the higher index planes suffer more on this basis. In general, the higher the intersecting point with relation to the Δr axis in figure 3.12, the less prominent the plane will be.

Hence if it is possible to predict the radius R at which a plane will appear, this may be a means of indicating anomalous behaviour. Hence if the emitter has different radii of curvature (assymetric) or if the specimen contains defects or has been thermally treated then as Moore and Ranganathan point out, these effects may upset the ideal sequence of appearance of planes.

3.5. Moiré simulation of field-ion image projections

3.5.1. Introduction

It has been shown that the complex patterns obtained using the field-ion microscope can be considered as a moiré phenomenon. This interpretation has been extended by relating the moiré patterns produced by overlapping zone considering the formation of moiré zone plates (MZP) on a spherical surface.

A further extension of this approach is possible by considering the projection of the MZP formed on a spherical surface onto a plane surface, and relating the results to the field-ion image projection. Experimentally, this is achieved by first projecting the zone plates and then overlapping the "quasi-zone plates" so produced, to form the moiré patterns.

3.5.2. The production of quasi-zone plates by optical projection

The apparatus required to produce the "quasi-zone plates" (QZP) is illustrated in figure 3.14 and represented schematically in figure 3.15. The zone plate was produced by painting alternate zones on the surface of a 9 inch radius perspex hemisphere such that the separation of

Figure 3.14 A photogtaph of the apparatus used to obtain 'quasi zone plates' which are subsequently used to simulate field-ion micrographs.

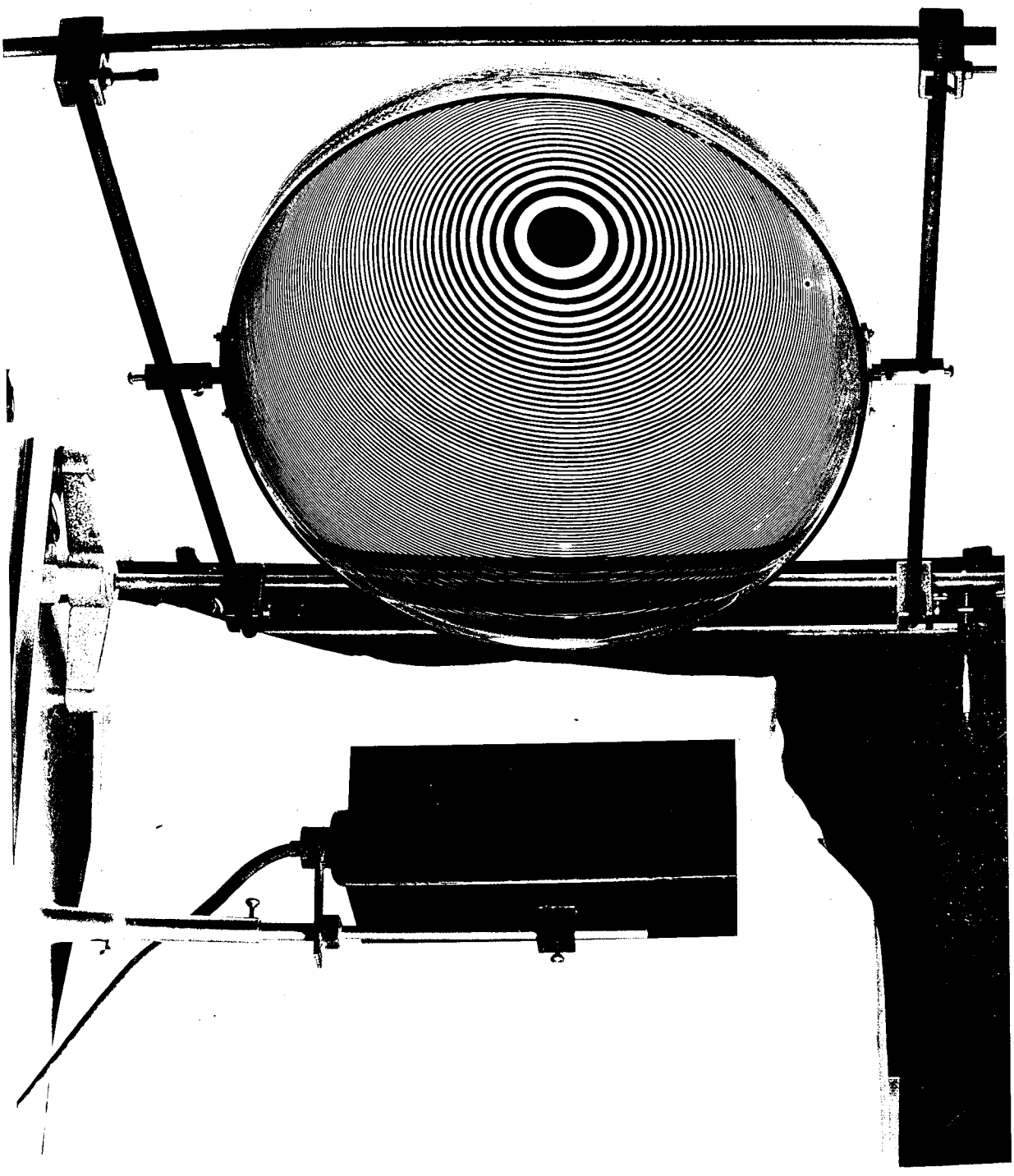

the centres of each transparent zone measured in a direction parallel to TO was a constant 'a' (see figure 3.16). The distance 'a' was 1/10 inch, and the number of transparent zones totalled approximately 85.

The painted hemisphere was then mounted as shown in figures 3.14 and 3.15 in contact with an opal glass projection screen, it being possible to vary the angle θ which the hemisphere made with the symmetrical position (i.e. when T, T' and P are coincident). The light source S was a pointolite lamp which acted effectively as a point source. The distance between O and S was NR where R is the radius of the sphere. S was mounted on an optical bench so that N could be varied. Light from S produced a shadow of the painted hemisphere on the screen, which could be photographed from the other side.

Photographs of the projected shadow were taken on Kodalith ortho film type 3 at values of $N=0,\frac{1}{2},1$ and 2 and at various values of θ. The value $N=\frac{1}{2}$ was used because N=0 proved difficult to photograph and results were not always satisfactory. The values of N=0, 1 and 2, correspond to the gnomonic, stereographic and Brandon (1964) projection respectively. The angles 45° and 55° were chosen to correspond to the angles the (100) plane makes with the (110) and (111) planes respectively for reasons which will become apparent later.

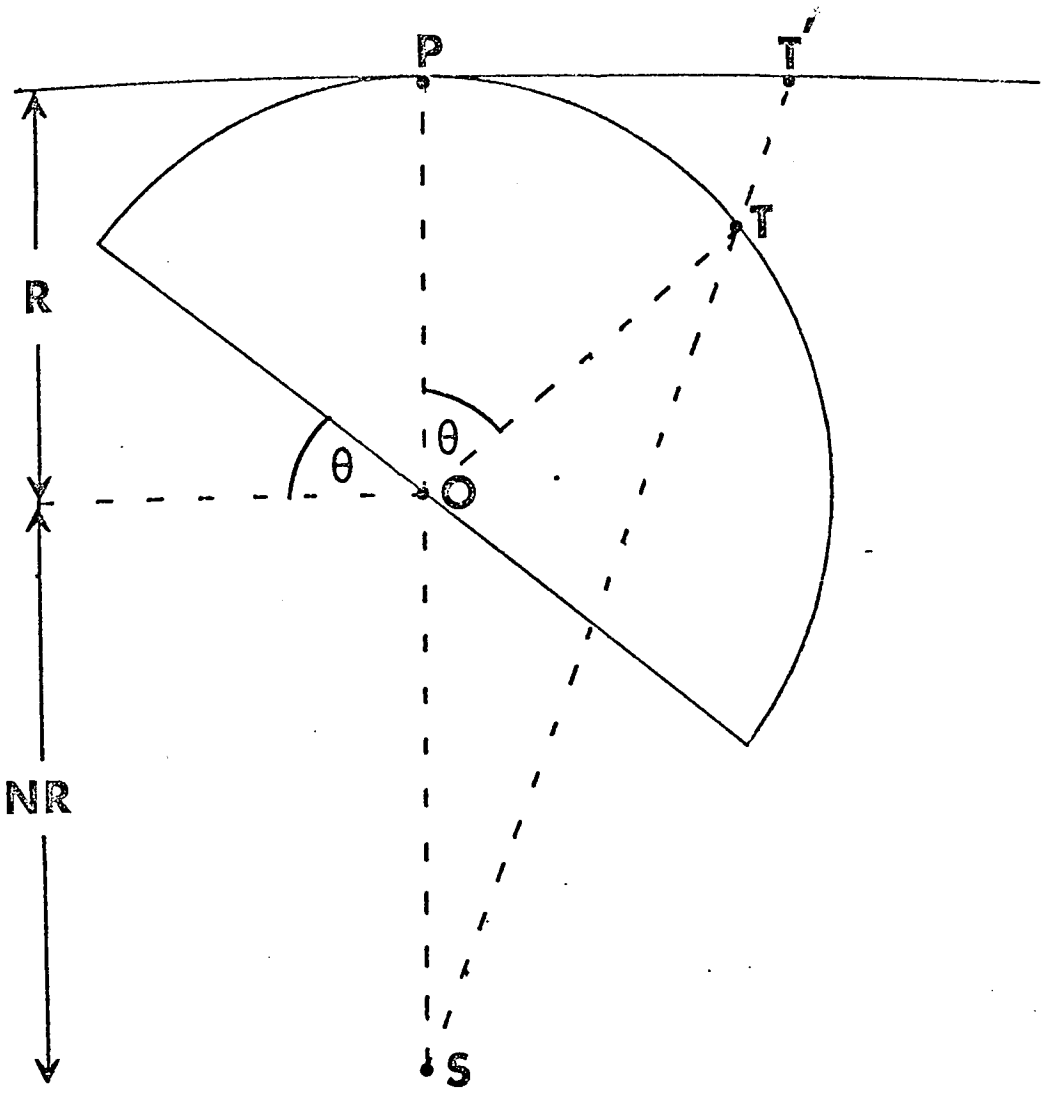

Figure 3.15. A schematic plan of the simulation apparatus.

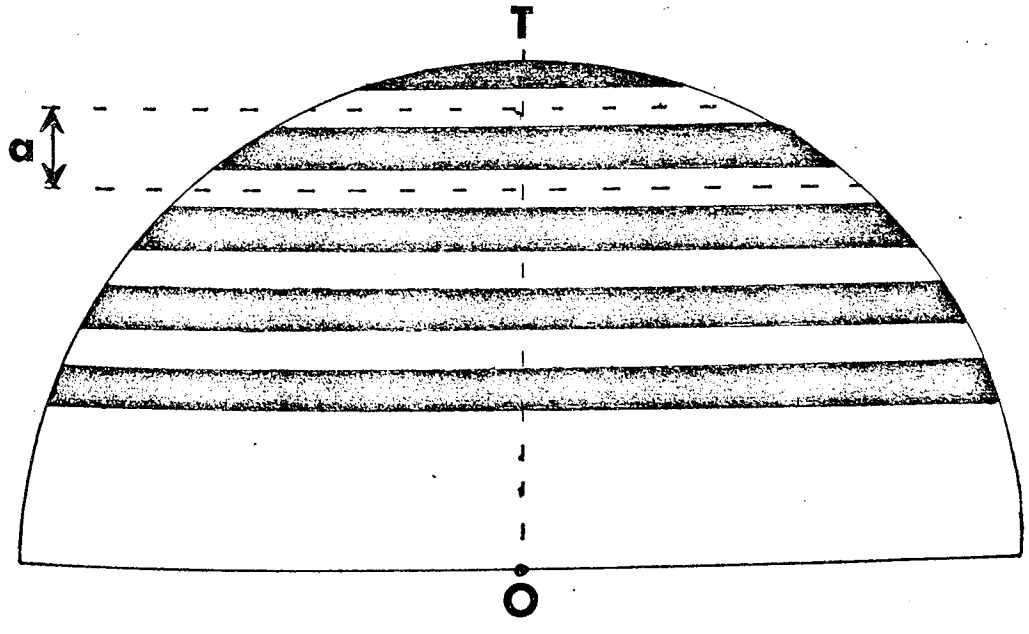

Figure 3.16. A schematic diagram of the zone plate painted on to the perspex hemisphere.

3.5.3. The moiré patterns resulting from the superposition of the quasi-zone plates

(a) Two zone plates

Two QZP with $\theta = 45^{\circ}$ were overlapped for each of the values of $N=0,\frac{1}{2},1$ and 2. The results are illustrated in figure 3.17 (b),(c),(d) and (e) respectively. The four projections illustrated in figure 3.17 can be compared with the two overlapping zone plates illustrated in figure 3.17(f) and also with the region of the field-ion micrograph of (002) orientated iridium shown in figure 3.17(a).

(b) Three zone plates

Three QZP with $\theta = 55^{\circ}$ were also overlapped for each of the values $N=0,\frac{1}{2},1$ and 2. The results are illustrated in figure 3.18(a),(b),(c) and (d). The four projections illustrated in figure 3.18 can this time be compared with the three overlapping Fresnel zone plates shown in figure 3.18(e).

(c) Five zone plates

Four QZP with $\theta = 90^{\circ}$ and one quasi-zone plate with $\theta = 0^{\circ}$ were overlapped for the value of $N=\frac{1}{2}$ and the result is illustrated in figure 3.18(f).

3.5.4. Interpretation

(a) A single zone plate

Several QZP are illustrated in figure 3.19, these correspond to the projections N=0 and N=1 and values of $\theta = 0^{\circ}$, 15° and 30°. Figures 3.17, and 3.18 also show QZP for $N=0,\frac{1}{2},1$ and 2 for various values of θ.

The distortion and spherical aberration of differently projected zone plates and field-ion

Figure 3.17 The moiré pattern formed by overlapping two zone plates.

(a) A region of a field-ion micrograph of iridium.

(b) The moiré pattern formed by two quasi-zone plates produced using the Brandon (N=2) projection.

(c) The moiré pattern formed by superimposing two quasi-zone plates produced using the stereographic, (N=1) projection.

(d) The moiré pattern formed by overlapping two N=$\frac{1}{2}$, quasi-zone plates.

(f) The moiré pattern formed by overlapping two Fresnel zone plates.

(a)
(b) N=2
(c) N=1
(d) N=0.5
(e) N=0

Figure 3.18 The moiré pattern simulation of field-ion micrographs.

(a) By overlapping three radially projected quasi-zone plates.

(b) By overlapping three N=0.5 projected quasi-zone plates.

(c) By overlapping three stereographically projected quasi-zone plates.

(d) By overlapping three Brandon (1964), N=2, projected quasi-zone plates.

(e) The moiré pattern formed by overlapping three Fresnel zone plates.

(f) The moiré pattern simulation of a field-ion micrograph produced by overlapping four N=$\frac{1}{2}$ projected quasi-zone plates.

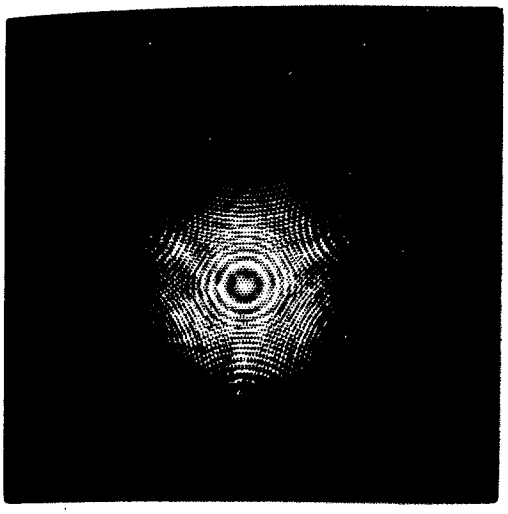

(a) N=0

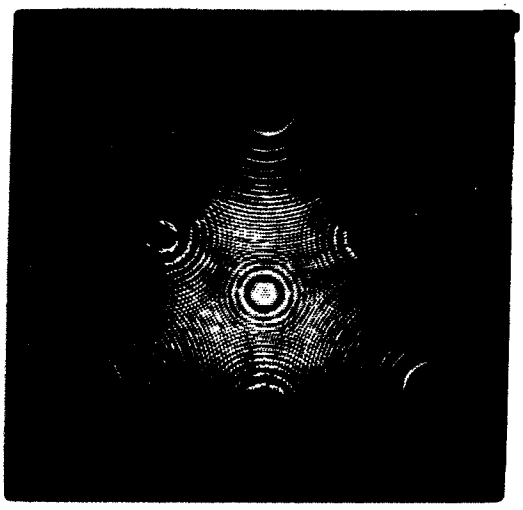

(b) N=0.5

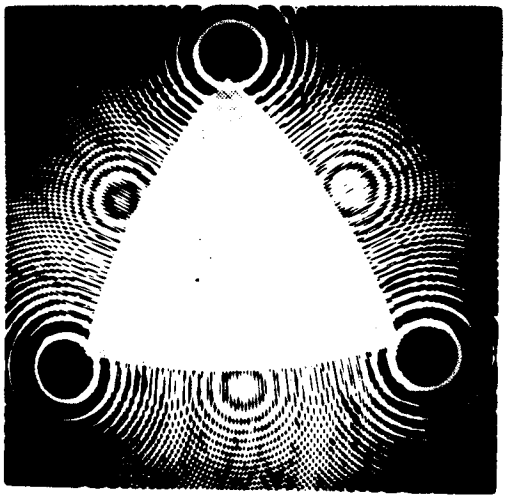

(c) N=1

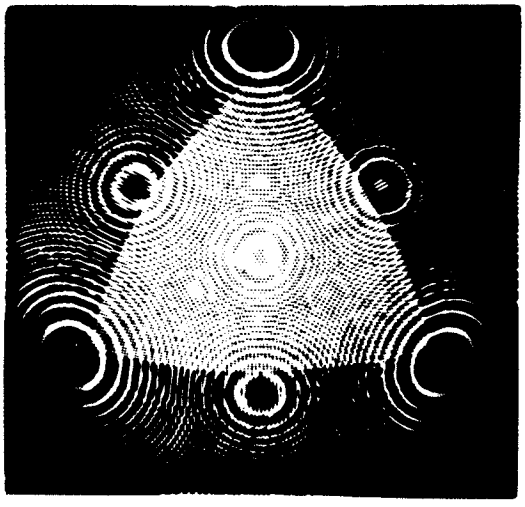

(d) N=2

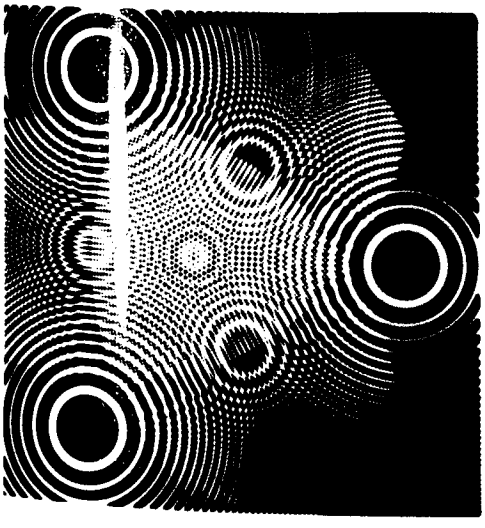

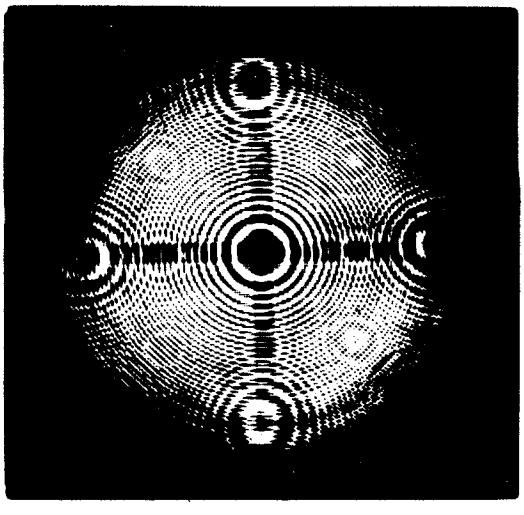

planes has been discussed previously in this chapter and effects due to varying local magnification are dealt with in chapter 5. Comparison of the distortion produced by radial and stereographic projections as illustrated in figure 3.19 reveals that the apparent distortion is greater for the radial projection. In both cases distortion increases with an increasing value of θ.

In the case of the radial projection, at $\theta = 0^{\circ}$, the QZP consists of concentric circles, but as θ increases to 15° and then to 30° the distortion produces non-uniform elliptical shapes. The major axis of these ellipses lies in a direction parallel to a line drawn through the centre of the projection and the centre of the projected QZP. This should be compared with the elliptical figures produced by the Brandon (1964) (N=2) projection, where the major axis lies perpendicular to this same direction.

In the stereographic case (N=1) figure 3.19 shows that at all values of θ, circles project as circles and the QZP still consist of a set of circles. However distortion does occur, but this time in a more subtle fashion. The QZP produced under these circumstances consists of a series of non-concentric circles. The effect increases with increasing θ, and the circle centres are arrayed on the line joining the centre of projection and the centre of the QZP.

It is clear that when $\theta = 0$ for all projections the QZP always consists of concentric circles, this is also known to be the case in field-ion microscopy.

Figure 3. 19 Illustrating the appearance of a quasi-zone plate projected either radially or stereographically. This figure also illustrates the variation of appearance with θ, the angle subtended by the hemisphere to the symmetrical position (see figure 3.15), for values of $= 0^{c}$, 15° and 30°.

RADIAL

STEREOGRAPHIC

0°

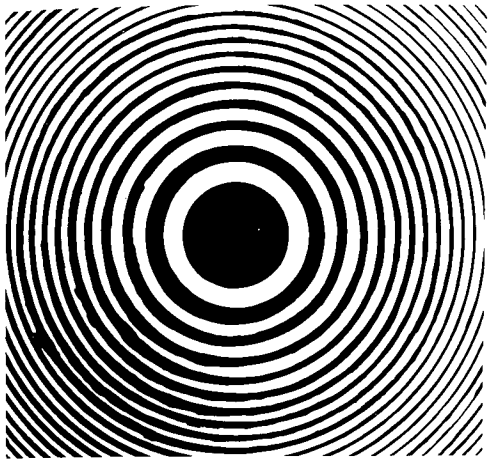

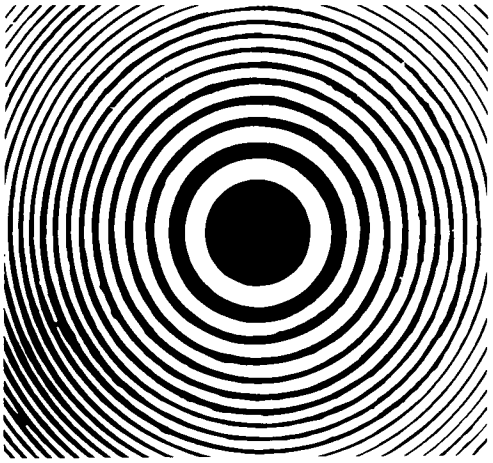

15°

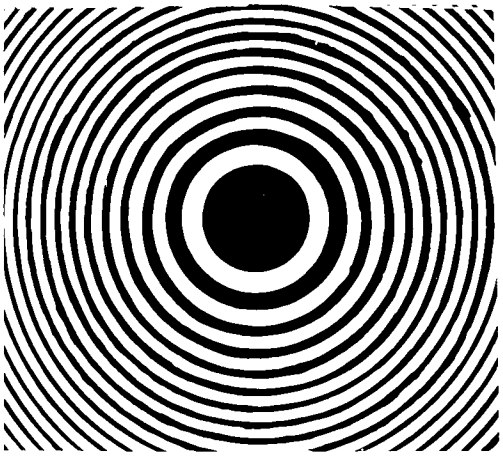

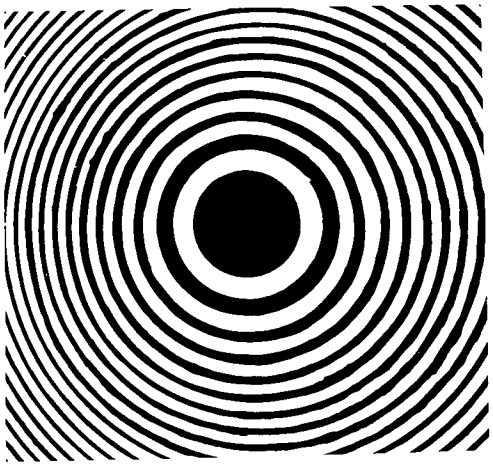

30°

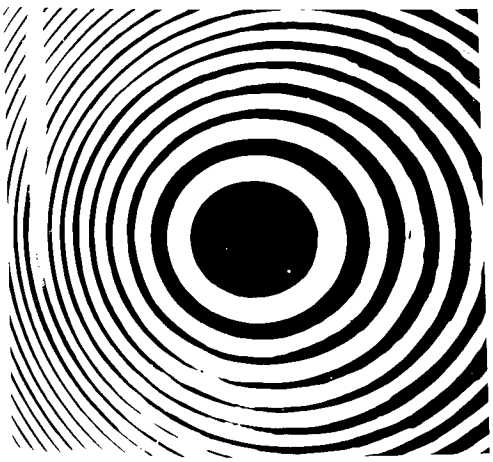

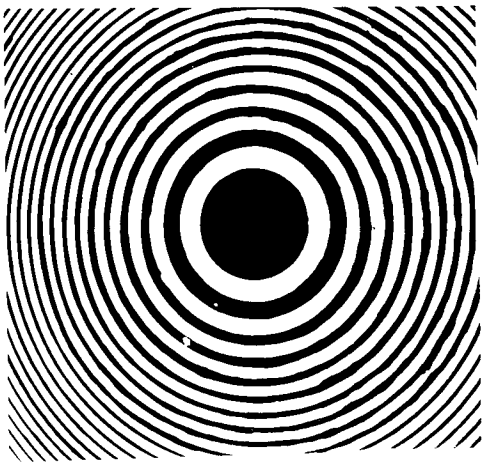

Image distortions corresponding to both the N=0, N=1 N=2 etc., are commonly found in field-ion planes and these are sometimes attributed to specimen assymetry, but clearly the simulations in figure 3.19 show that projection can also produce these effects.

(b) Two zone plates

A sequence of simulations involving the overlap of two QZP together with, for comparison, part of a field-ion micrograph of iridium and the moiré pattern formed by overlapping two conventional Fresnel zone plates are shown in figure 3.17.

The simulations depicted in figure 3.17(b),(c),(d) and (e) are not strictly comparable with a field-ion microscope image of an f.c.c. structure such as that shown in figure 3.17(a). This is because in order to accurately simulate an f.c.c. or b.c.c. structure, two models similar to that illustrated schematically in figure 3.16 are required to conform with crystallographic parity. One model would have twice the 'a' spacing (equivalent to interplanar spacing) of the second model. If only one model is available then simple cubic structures only may be accurately simulated. However it is still possible to obtain information on the effect of projection in the field-ion image by observing the general shape of the QZP and the moiré QZP. In each of the four simulations depicted here, the two original QZP correspond to $\{022\}$ planes situated at an angle $\theta=45^{\circ}$ from the emitter axis, where the plane the apex of the field-ion micrograph (figure 3.17(a)) is an $\{002\}$ plane. The prominence of the various QZP in the simulations do not strictly correspond to the prominence of the field-ion planes

in figure 3.17(a), but would correspond to that of a simple cubic structure.

An overall similarity in appearance can be seen to exist between the patterns shown in figure 3.17. This indicates some consistency in their derivation. In each case the pattern is formed by some type of zone plate be it quasi-, Fresnel or a field-ion plane.

In every case, the "zone lines" between the centres of the "originals" of each pattern is straight, even though the "originals" making up figures 3.17(a),(b), (d) and (e) are non-circular and in figure 3.17(c), non concentric. Also, in each case the central figure situated at $\theta = 0$ (field-ion plane, QZP or MZP) always consists of a series of concentric circles, regardless of projection, even though in some instances the overlapping "originals" are irregularly elliptical. In those cases where the "original" zone plates are elliptical (i.e. figure 3.17(a),(b),(d),(e)) then the moiré zone plates not at the centre are also elliptical. The distortion of the various ellipses increases with increasing values of θ.

The stereographic simulation (figure 3.17(c)) produces a moiré pattern consisting of a series of circular QZP. These QZP are non confocal; the effect increases with increasing θ. All other QZP simulations display elliptical original QZP and moiré QZP. A condition for the formation of elliptical figures is met if $N \neq 1$. If $N > 1$ the ellipses have their major axes perpendicular to the line drawn through the projection centre and the centre of the QZP. Whereas if $N < 1$, the major axes of the ellipses lie parallel to the line.

(c) Three zone plates

The moiré pattern produced by overlapping 3 or 5 QZP or 3 Fresnel zone plates are illustrated in figure 3.18. Figures 3.18(a),(b),(c),(d) are produced by overlapping three QZP where $\theta = 55^{\circ}$. Figure 3.18(e) is the moiré pattern produced by three Fresnel zone plates and figure 3.18(f) is the moiré pattern produced by overlapping 4 QZP ($\theta=90^{\circ}$) and 1 QZP ($\theta=0^{\circ}$).

Once again there is an overall similarity between the simulations, the moiré pattern produced by overlapping 3 Fresnel zone plates and a field-ion micrograph. The original QZP used in this situation are similar to those used in the 2 zone plate case except that θ is now 55°, not 45°., the distortion has thus increased. In the N=0 case (figure 3.18(a)) the ellipsicity of the QZP has made photography difficult. The shapes of the individual QZP are dependant on N in a similar manner to that discussed in the 2 case. Once again, even though 3 QZP are now overlapped, the central moiré QZP is circular. The shapes of the other MZP are in general elliptical (except for the sterographic case) and vary in a fashion discussed previously.

An important point arises from the shapes of the zone lines between the original QZP. For the moiré pattern produced by overlapping zone plates, the zone lines between the original zone plates are straight. In all the moiré simulations all these zone lines are curved just as in field-ion microscopy. What is more interesting is that the amount of curvature depends on projection. Close inspection of figure 3.18 reveals that the curvature increases with increasing N from N=0 to N=2.

3.5.5. Conclusions

Although the present moiré simulations only accurately represent the patterns expected from simple cubic structures, information can still be obtained regarding the shapes of planes and zone lines in the projected image. This information, which has not been obtained by computer simulation, can be obtained as a function of both θ and N. This new insight into the various image distortions introduced by the projection may provide a simple qualitative means of determining which type of projection is operative in different regions of the micrograph. Also planes which appear assymmetric in the image, may not be assymmetric on the specimen surface, but their appearance has merely been distorted in the imaging process. Not only are the shapes of the planes important in determining projection, but now it appears that information is available from the relative curvature of zone lines.

3.6. Discussion

It has been demonstrated that the image of a field-ion plane is geometrically similar to a special kind of zone plate, termed a binary zone plate. Hence it is possible to use the focussing properties of a zone plate to obtain new information from field-ion micrographs. When the local image magnification is taken into account, the focal length of a field-ion plane can be related to its interplanar spacing, d, the emitter-to-screen distance, T, the emitter radius, R, and the projection point as defined by the parameter, N. Chapter 5 discusses the applications of this analysis, and includes variations with θ.

It has also been shown that the entire emitter surface may be regarded as a moiré pattern formed between overlapping zone plates, and it will be interesting to discuss the fundamental reason why this should be so. Basically it stems from the fact that the underlying crystal structure of the specimen may itself be regarded as a moiré pattern. This is shown by figure 3.20, which is a schematic diagram of a crystal structure in two dimensions. Each set of crystal planes, for example (1) and (2), consists of a number of parallel straight lines of periodicity equal to the interplanar spacing. These two sets of straight lines intersect each other at the atom positions, and it is the various patterns that these points of intersection make that define the resultant moiré pattern. Thus, for example, planes such as (3) and (4), shown by the broken lines, may be regarded as moiré patterns formed between (1) and (2). The entire crystal structure is an interdependent moiré pattern. The zone plate configuration which occurs on the emitter surface is formed at the point where each set of crystal planes is tangential to the thin shell described in section 3.2.2. Since each of these plane images is already related to every other by this latter moiré analysis, it will necessarily be related by the overlapping zone plate analysis.

At the same time the overlapping zone plate treatment does give rise to several new relationships in the interpretation of field-ion micrographs, and their application is also discussed. The most

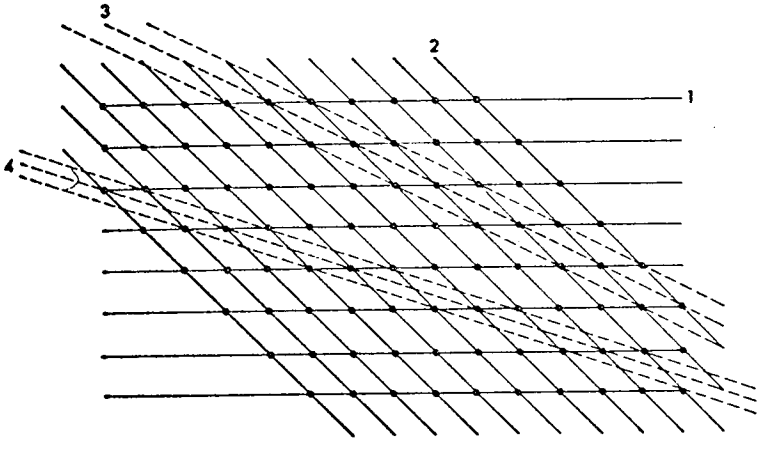

Figure 3.20 The crystal lattice regarded as a moiré pattern.

important new relationship derived in the moiré analysis is that which states that at the centre of any field-ion plane, the effective exposed ledge widths $\Delta\rho$ of any two planes that can be considered to have formed that plane (from the Weiss zone law) are equal. This leads directly to a new conception of how radius affects the appearance or visibility of high index field-ion planes.

A further outcome of this approach is that it is possible to project zone plates formed on a spherical surface onto a plane, using different angular and projection relationships, and then to overlap the aberrated zone plates thus produced. In this way it is possible to simulate the appearance of field-ion images, and the procedure also gives a further insight into the formation of moiré zone plates, this time of a distorted nature.

Indeed the whole discussion of this chapter is of a wider interest than the field-ion situation on its own. In a very general way it demonstrates that it is possible to solve moiré patterns in three dimensions and also that the relationships governing moiré zone plate formation in two dimensions may themselves be extended directly to three. In principle the approach could be used to solve moiré patterns formed over any non-planar surface, given a suitable set of reference coordinates, such as supplied by the crystal lattice in the present example.

CHAPTER FOUR

A MOIRÉ INTERPRETATION OF FIELD-ION MICROSCOPY

4.1 Introduction

A visual moiré pattern may be formed when two periodic structures are overlapped. The loci of the points at which the elements making up each structure overlap, will themselves form a pattern, which may be apparent to the eye. Detection of such moiré patterns is facilitated if the periodic structure is composed of alternately transparent and opaque elements, and if the dimensions of these elements are similar in the two structures.*

These points have been illustrated in the previous chapters. For example in chapter 3, it has been shown that a single field-ion plane is a special kind of zone plate and that the field-ion image may be interpreted as a moiré zone plate phenomenon. The overlap of three zone plates produces a two-dimensional array of moiré zone plates as shown in figure 4.1(a), the formation and properties of such moiré zone plates has been discussed in detail in chapter 2. If figure 4.1(a) is compared with figure 4.1(b) which is the region of a field-ion micrograph of iridium showing several planes, the similarity between these two figures is very striking. It has led Oster (1964) to suggest that the circular regions in field-ion micrographs which are believed to correspond to high index crystallographic planes on the specimen surface, may, instead, be moiré patterns formed by more prominent planes located on either side.

* Part of the work presented in this chapter has been published in Philosophical magazine (1973) 27 915.

Figure 4.1 (a) The moire pattern formed by three overlapping zone plates.

(b) A region of a field-ion micrograph of iridium.

(a)

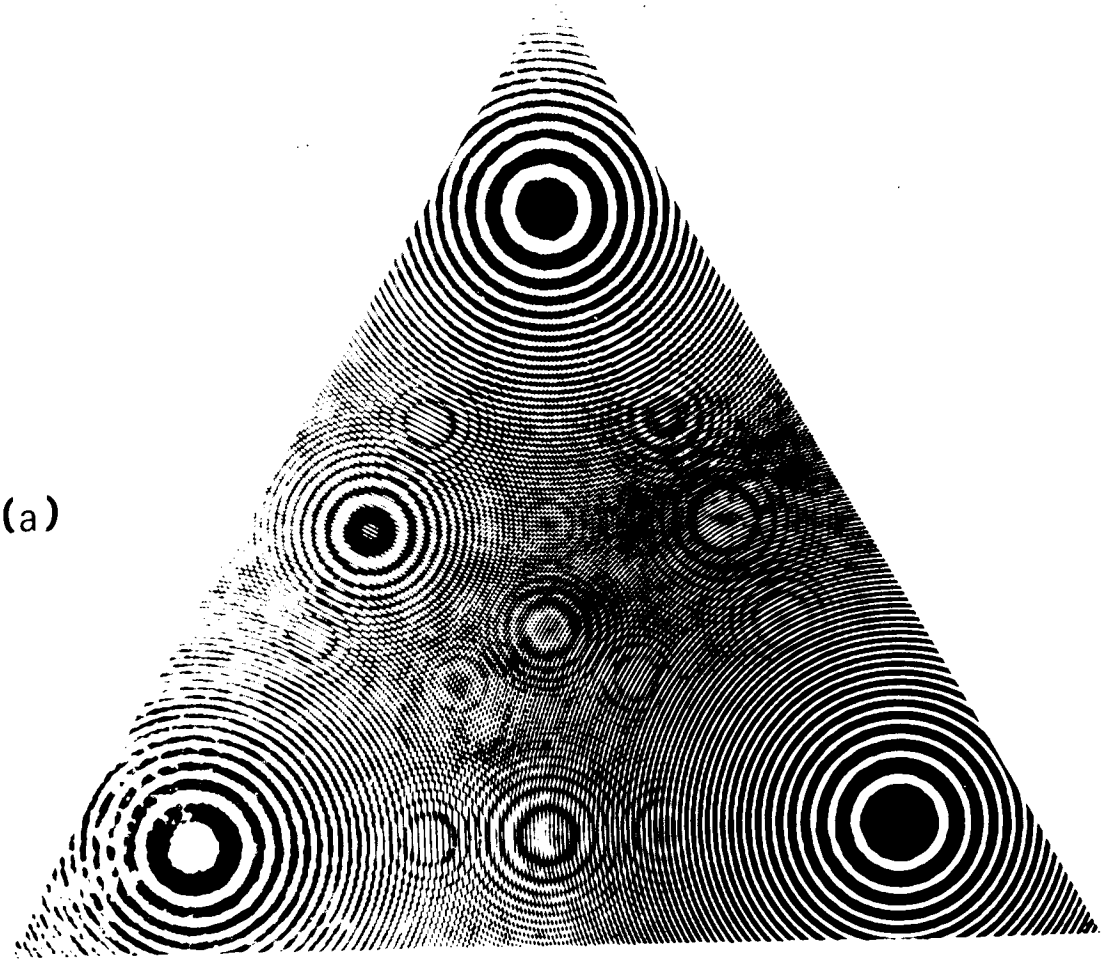

(b)

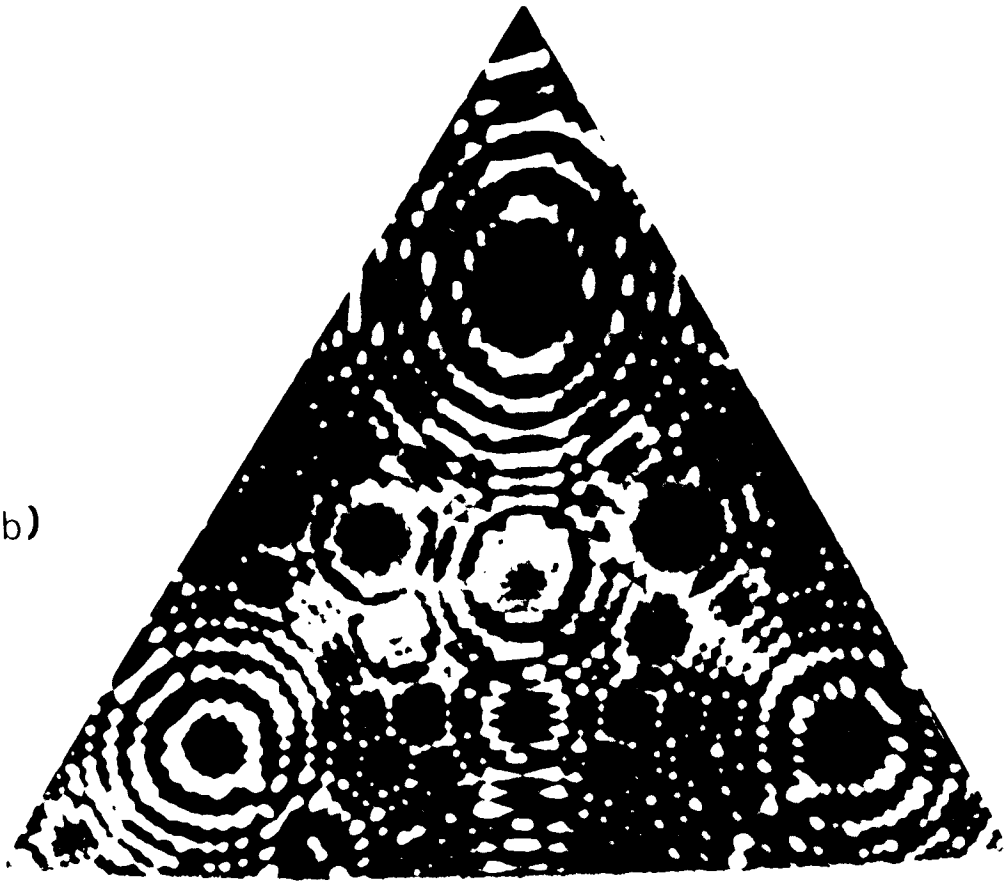

This suggestion carries with it serious implications. While one would probably not doubt that the more prominent ring patterns correspond to genuine low index, facets on the specimen surface, it might be that the less prominent ring patterns, if formed by an optical moiré effect, do not occur in the position, or have the properties of, the higher index planes which they are believed to represent. This would have serious consequences in both the structural and the crystallographic analysis of field-ion micrographs.

It will be demonstrated in this chapter that conventional techniques of moiré pattern analysis may be extended to provide a description of the entire field-ion image. However it turns out that in no case do the position and properties of a plane whose appearance is predicted by the moiré analysis, differ from those expected from a purely crystallographic approach. In addition to demonstrating that the existing interpretation of field-ion micrographs is after all correct, the analysis may be extended to provide new information concerning the detailed shape of the field-ion emitter.

The key to this analysis is the realisation that it is unnecessary to deal directly with the field-ion image, involving as it does an unknown, and possibly variable, projection relationship with the emitter. Instead it is possible to consider the emitter itself, applying straightforward geometric arguments. This is because, in the field-ion situation, the loci of the points at which the elements of the two generating

structures overlap, are the individual atoms. Since there is a one-to-one correspondence between image points and atoms, it is possible to consider the atomic distribution of the emitter surface instead of the image point distribution in the micrograph.

4.2. Moiré analysis

Although the discussion so far has concerned the formation of optical moiré patterns which are discernible to the eye, it is possible to treat the problem of moiré pattern formation in a completely general mathematical fashion.

Consider the moiré pattern to be formed by the overlap of two original periodic structures of the form:-

$$F(x,y) = \Psi(m) \qquad .....(4.1)$$

and

$$G(x,y) = \phi(n) \qquad .....(4.2)$$

respectively, where m and n are indexing parameters running over some subset of the real integers, thus defining the periodicity of the structure, and x, y are the co-ordinates of any point on the structure, with respect to some co-ordinate axes.

When these two structures are overlapped the resultant moiré pattern is a further periodic structure of the form:-

$$H(x,y) = \Theta(p) \qquad .....(4.3)$$

where p is again an indexing parameter. In general the possible values of p are determined by an indicial equation of the form (Oster, Wasserman and Zwerling (1964).

$$\gamma(m,n) = p \qquad .....(4.4)$$

In the present work the general indicial equation (4.4)

may be reduced simply to:-

$$hm + kn = p \qquad \ldots\ldots(4.5)$$

where h, k are the integers 0,1,2,3,... These define a series of moiré patterns, which tend to become less prominent optically with increasing magnitude of h and k.

Equation (4.5) may be extended to:-

$$hm + kn + lq = p \qquad \ldots\ldots(4.6)$$

when the moiré pattern is formed by the overlap of three original periodic structures.

4.3. Geometrical approach

In this section we shall review the distribution of planes on the surface of the field-ion emitter that would be expected from purely geometrical considerations. For simplicity at this stage it will be assumed that this surface is a hemisphere of constant radius, R, and that its crystal structure is cubic.

4.3.1. The formation of a planar facet

Each planar facet occurs where a particular crystallographic plane of atoms lies parallel to the emitter surface, as shown in figure 4.2. If we assume that there is an imaged atom at each point where successive parallel planes intersect the surface, then the image will consist of a series of concentric circles of image points, as shown at the top of the figure. The figure is schematic only, and the true radius of these circles will be related to that of the ledge of atoms giving rise to this image both by the magnification and by the projection relationship.

The prominence of a plane is usually defined in

terms of its interplanar spacing (Moore and Ranganathan (1967)). Thus the lower are its indices, the greater is its interplanar spacing, and the greater will be both the radius and the separation of its rings of image points. However no precise meaning may be attached to this latter statement unless a concept which we shall term the phase factor of the plane is considered.

4.3.2. The phase factor of a plane

The importance of the phase factor in the geometrical interpretation of field-ion micrographs is discussed more thoroughly in section 4.5, together with details of how such information may be obtained using the moiré analysis. Here we shall merely define what is meant by the term phase, and discuss its effect on the numbering of the ledges shown in figure 4.2.

During field evaporation, the radius of the top ledge, r_o, will alter from its maximum value, $r_o \simeq (2Rd)^{\frac{1}{2}}$, at which point its phase equals one, to its minimum value, $r_o = 0$, when the final atom has just been removed. At this point its phase equals zero. In general its radius will be given by $r_o' \simeq (2R\delta d)^{\frac{1}{2}}$ where δd is the distance between the centre of the top ledge and the spherical envelope. Therefore $0 < \delta < 1$. The parameter δ is termed the phase factor of the plane and its value decreases from 1 to 0 as the phase of the top ledge decreases from 1 to 0. Thus the numbering of the ledges begins 0, 1, 2, ... n, and the radius of the nth ledge, $r_n \simeq (2Rd(n + \delta))^{\frac{1}{2}}$.

4.3.3. Distribution of planes over the emitter surface

In order to serve as a basis for comparison with the moiré approach (section 4.4) let us consider the distribution of planes over the emitter surface. Figure 4.3 shows one quadrant of a stereographic projection. Planes lying in the [001] zone, between (100) and (010), may be generated by operation of the Weiss zone law:

$$h(100) + k(010) = (hk0) \qquad .....(4.7)$$

where h and k are positive integers. The interplanar spacing of the (hk0) plane, $d_{(hk0)}$ is given by:-

$$d_{(hk0)} = a/(h^2 + k^2)^{\frac{1}{2}} \qquad .....(4.8)$$

where a is the lattic parameter of the material. (There are restrictions on the values that h and k may take, depending on whether the crystal structure is simple, body-centred or face-centred cubic, but consideration of this point will be delayed until section 4.5). The position of the (hk0) plane may be defined by the angle, θ, that it makes with (100), where:-

$$\cos\theta = \frac{h}{(h^2 + k^2)^{\frac{1}{2}}} \qquad .....(4.9)$$

More generally, we may consider a plane (hkl) which is generated by the operation:-

$$h(100) + k(010) + l(001) = (hkl) \qquad .....(4.10)$$

whose interplanar spacing is given by:-

$$d_{(hkl)} = a/(h^2 + k^2 + l^2)^{\frac{1}{2}} \qquad .....(4.11)$$

and whose position, defined by the angle, θ, which it makes with, say, (001), is given by:-

$$\cos\theta = \frac{l}{(h^2 + k^2 + l^2)^{\frac{1}{2}}} \qquad .....(4.12)$$

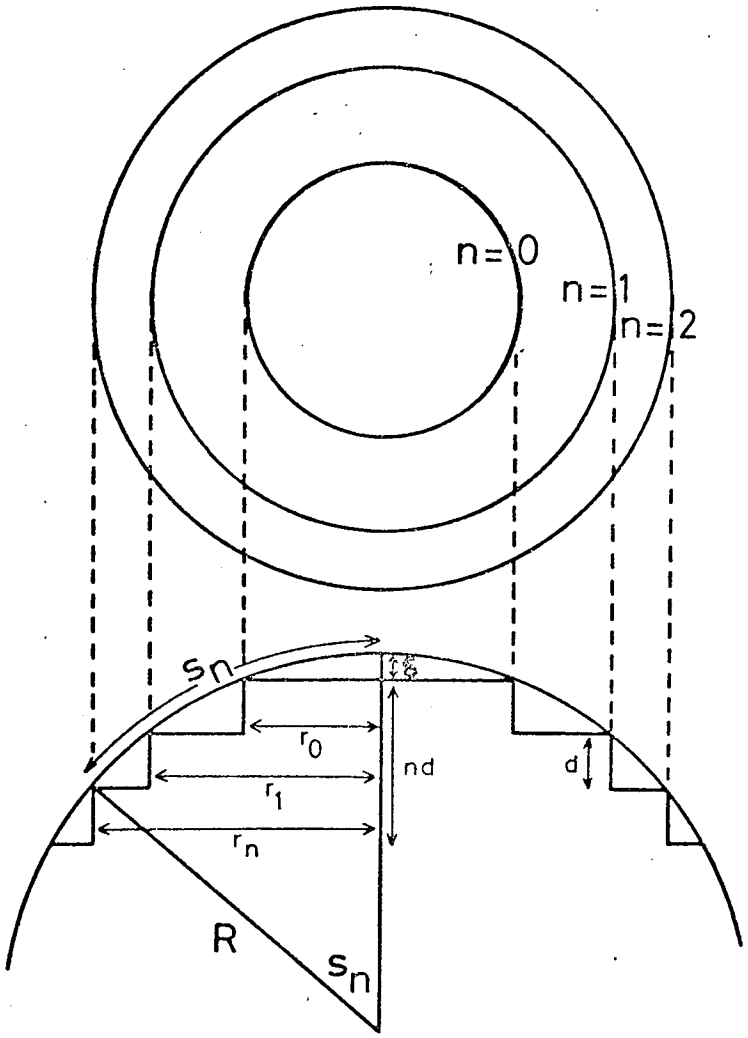

Figure 4. 2. Schematic diagram showing a radial section through a field-ion emitter and the corresponding appearance of the image.

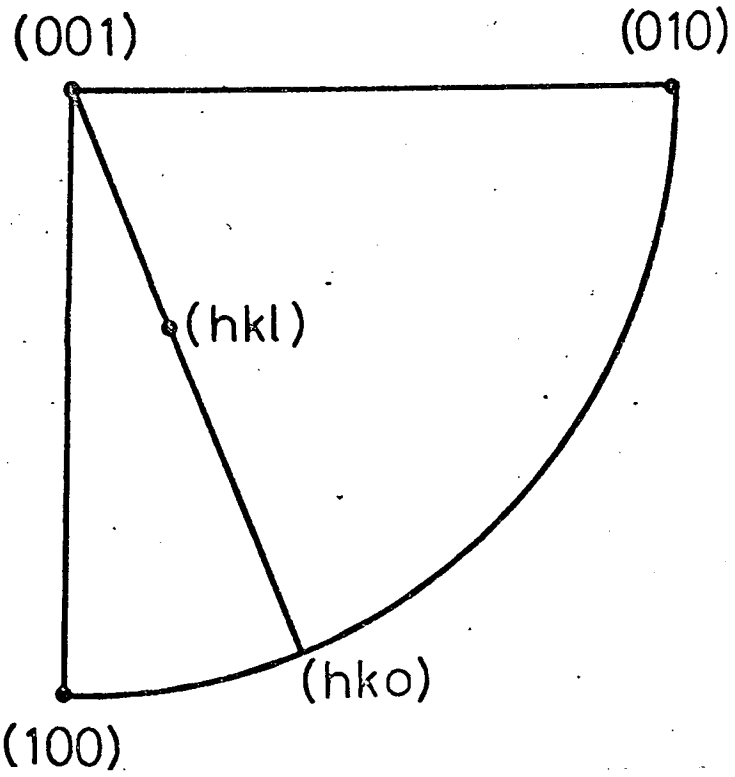

Figure 4. 3. Quadrant of a stereographic projection showing the location of the planes considered in the moire analysis.

Equations (4.9) and (4.12) are of course special cases of the general equation for the angle, θ, between two planes $(h_1k_1l_1)$ and $(h_2k_2l_2)$ viz.

$$\cos\theta = \frac{h_1h_2 + k_1k_2 + l_1l_2}{(h_1^2 + k_1^2 + l_1^2)^{\frac{1}{2}}(h_2^2 + k_2^2 + l_2^2)^{\frac{1}{2}}} \quad \ldots\ldots(4.13)$$

We shall now see how the equations which are quoted in this section compare with those evolved using the moiré analysis.

4.4 Moiré analysis

4.4.1. Overlap of two systems of circles

4.4.1.1. Equation of the original circles

A single plane on the surface of the field-ion emitter will be considered as a series of concentric circles of imaged atoms. When two such systems of circles are overlapped, the imaged atoms which lie at the points of intersection will define the moiré pattern, and this will be shown to consist of further systems of circles. As a starting point we shall consider the two original systems of circles to correspond to the (100) and (010) planes, as shown in figure 4.4. The centres of these circles are separated by a 90° arc, and the circles are numbered 0,1,2,..., m and 0,1,2,...,n respectively.

From figure 4.2 it may be seen that the mth circle of the (100) system, say, will have angular radius s_m, where:-

$$\cos s_m = \frac{R - d_{(100)}(m + \delta_{(100)})}{R} \quad \ldots\ldots(4.14)$$

We may separate out from this equation a factor $A = (1-a\delta_{(100)}/R)$, which contains the phase information, whereupon:-

$$\cos s_m = A - ma/R \qquad .....(4.15)$$

since $d_{(100)} = d_{(010)} = a$, the lattice parameter.

Let x, y be longitude and latitude respectively with respect to the equator, (100) - (010), of any point on the mth circle of the system (100), measuring longitudes from (100), figure 4.5. Then, by the cosine rule for spherical triangles,

$$\cos s_m = \cos x \cos y \qquad .....(4.16)$$

and hence

$$\cos x \cos y = A - ma/R \qquad .....(4.17)$$

is the equation of this circle.

Similarly, the equation of the nth circle of the (010) system is:-

$$\cos (x-90^\circ) \cos y = B - na/R \qquad .....(4.18)$$

where $B = (1 - a\delta_{(010)}/R)$. This reduces to:-

$$\sin x \cos y = B - na/R \qquad .....(4.19)$$

Equations (4.17) and (4.19) correspond to equations (4.1) and (4.2) in the general case.

4.4.1.2. Generation of the moiré pattern

Let h and k be given positive integers. Consider the pairs of circles from the two systems which satisfy the indicial equation (4.5). These will intersect in a set of points (x,y) satisfying equations (4.17), (4.19) and (4.5). Multiplying equations (4.17) and (4.19) by h and k respectively, and then eliminating m and n we get:-

$$\cos y(h \cos x + k \sin x) = h(A-ma/R)+k(B-na/R) \qquad .....(4.20)$$

$$= hA + kB - pa/R \qquad .....(4.21)$$

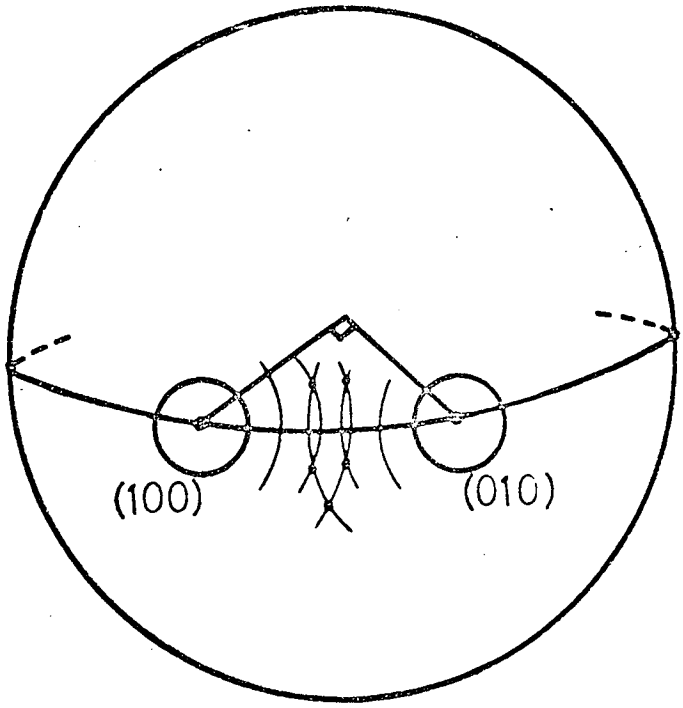

Figure 4.4. Spherical surface showing the overlap of two systems of circles corresponding to the (100) and (010) planes.

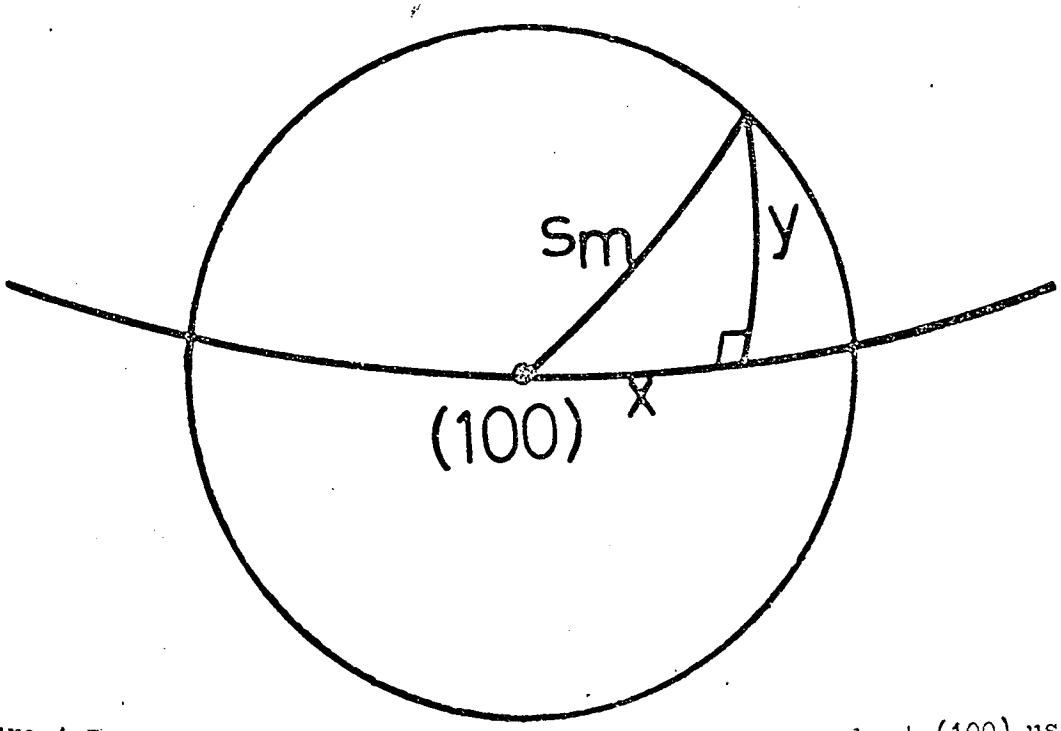

Figure 4.5. Sperical triangle within the mth circle about (100) used to define S_m.

Dividing throughout by $(h^2 + k^2)^{\frac{1}{2}}$

$$\cos y \frac{h}{(h^2 + k^2)^{\frac{1}{2}}} \cos x + \frac{k}{(h^2 + k^2)^{\frac{1}{2}}} \sin x = \frac{hA+kB-pa/R}{(h^2+k^2)^{\frac{1}{2}}} \quad .....(4.22)$$

Define $\theta = \tan^{-1} (k/h)$, as shown in figure 4.6(a). Then equation (4.22) may be written:-

$$\cos y (\cos x \cos \theta + \sin x \sin \theta) = \frac{hA+kB-pa/R}{(h^2+k^2)^{\frac{1}{2}}} \quad .....(4.23)$$

or

$$\cos y \cos (x - \theta) = \frac{hA+kB}{(h^2+k^2)^{\frac{1}{2}}} - \frac{pa}{R(h^2+k^2)^{\frac{1}{2}}} \quad .....(4.24)$$

Comparing equation (4.24) with equations (4.17) or (4.18) we can see that, for each combination of h and k, it defines a moiré pattern consisting of a system of circles of periodicity, p, whose centre is at longitude θ, where θ may be defined by:-

$$\cos \theta = h/(h^2 + k^2)^{\frac{1}{2}} \quad .....(4.25)$$

Equation (4.24) corresponds to the general equation (4.3). It is evident that these systems of circles may be regarded as being generated by planes whose separation $d_{(hk0)}$ (introducing a third parameter, l = 0, for internal consistency) is given by:-

$$d_{(hk0)} = \frac{a}{(h^2 + k^2)^{\frac{1}{2}}} \quad .....(4.26)$$

The expression $(hA + kB)/(h^2 + k^2)^{\frac{1}{2}}$ contains information on the phase of the moiré system of circles, and is discussed further in the section 4.5.

The important result of the above analysis is that equation (4.25) and (4.9), and (4.26) and (4.8) respectively, are identical.

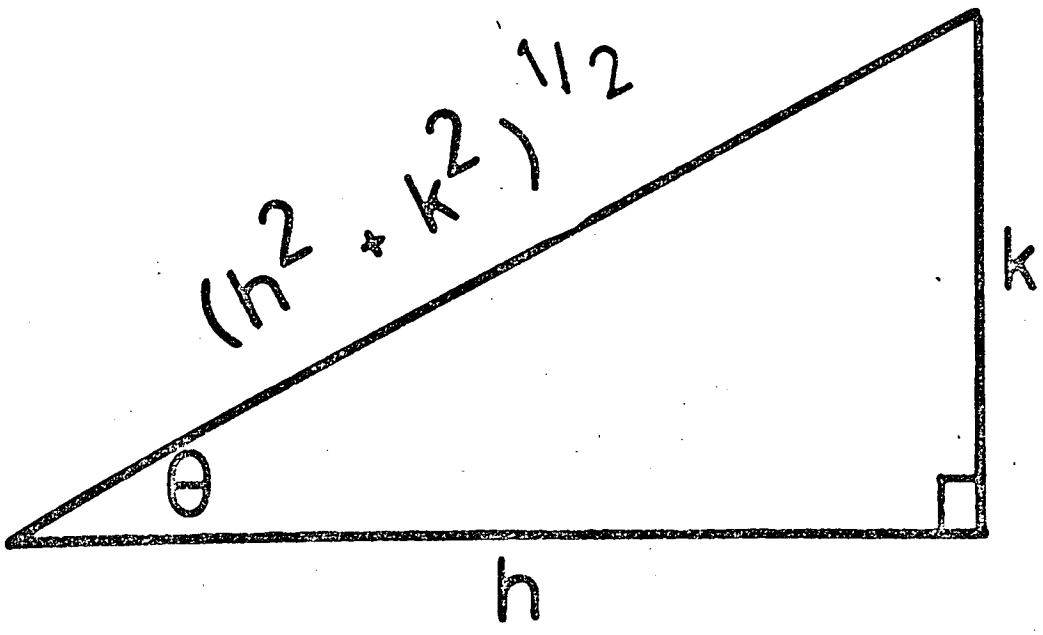

Figure 4.6.(a) Definition of θ in terms of h and k.

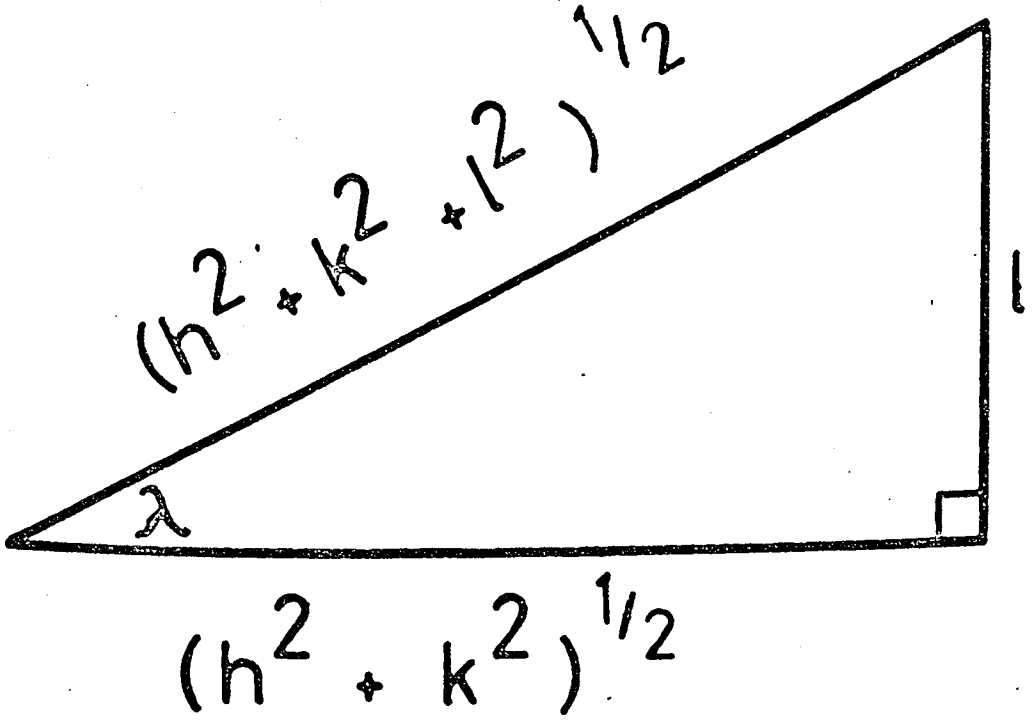

Figure 4.6.(b) Definition of λ in terms of h, k and l.

4.4.2. Overlap of three systems of circles

While the two system case is much the easier to follow, a complete treatment of the field-ion situation necessitates considering the moiré interaction of three systems of circles.

4.4.2.1. Equation of the original circles

To begin with we consider three fundamental families of circles (100), (010) and (001), which are separated by 90° arcs on the sphere, as shown in figure 4.7. As before (100) - (010) is regarded as the equator; (001) is regarded as the pole, and longitudes are measured from (100).

The systems of circles corresponding to (100) and (010) will be represented by equations (4.17) and (4.19), just as before. To find the equation for the (001) case consider figure 4.8. P is a point whose co-ordinates of longitude and latitude are x, y, and which is located on the qth circle around (001). The meridian arc (001) - P is constructed, and is produced to meet the equator (100) - (010) in Q. Then (001)-Q = 90°, P-Q = y and hence:-

$$s_q = (001) - P = 90° - y \qquad .....(4.27)$$

Therefore

$$\cos s_q = \sin y \qquad .....(4.28)$$

By comparison with figure 4.2 it can be seen that:-

$$\cos s_q = C - qa/R \qquad .....(4.29)$$

where $C = (1-a\delta_{(001)}/R)$, and hence

$$\sin y = C - qa/R \qquad .....(4.30)$$

This is the equation for the system of circles corresponding to (001). (x is arbitrary for these circles and so does not enter the equation).

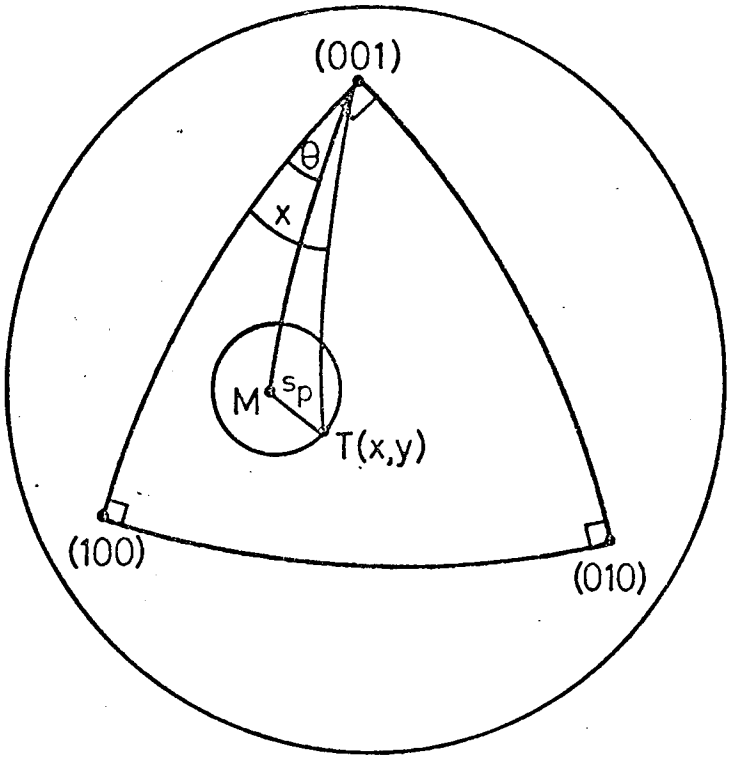

Figure 4.7. Spherical surface showing the parameters involved in the analysis of the overlap of three systems of circles centred on (100), (010) and (001).

Figure 4. 8.

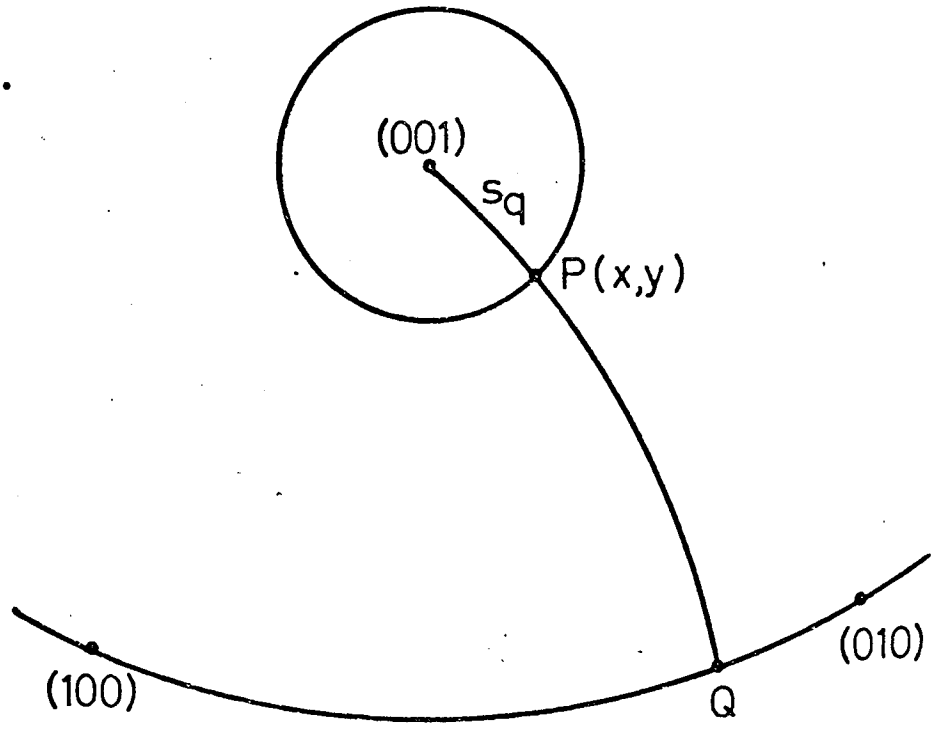

Relationship between a point, P, on the qth circle around (001) and the equatorial line (100) - (010), used to define sq.

It will facilitate the subsequent discussion of the moiré analysis if we pre-empt its conclusions to suppose that the moiré pattern will be found to consist of a family of patterns, each consisting of a system of concentric circles, just as in the two system case. We shall consider one member of this family, corresponding to the specific indexing parameters (hkl), to be centred at a point M, figure 4.7, whose longitude and latitude are θ, λ, respectively. T is a general point (longitude x and latitude y) on one of the circles centred on M and whose angular radius is s_p. M and T are joined to (001) by great circle arcs, so that $M-(001) = \pi/2 - \lambda$ and $T-(001) = \pi/2 - y$.

Applying the cosine rule to the spherical triangle M - T - (001), we get

$$\cos s_p = \cos(\pi/2-\lambda)\cos(\pi/2-y) + \sin(\pi/2-\lambda)\sin(\pi/2-y)\cos(x-\theta) \quad .....(4.31)$$

or

$$\cos s_p = \sin x \sin y + \cos\lambda \cos y \cos(x-\theta) \quad .....(4.32)$$

Equation (4.32) is the x,y equation of this circle.

If we suppose that the system of circles centred on M and of a periodicity represented by a varying parameter p, are generated by the intersection with the sphere of a series of planes of separation $d_{(hkl)}$, then, by comparison with figure 4.2 and equation (4.15) we may write:-

$$\cos s_p = D - \frac{pd_{(hkl)}}{R} \quad .....(4.33)$$

whereupon

$$\cos\lambda\cos(x-\theta)\cos y + \sin\lambda\sin y = D - p\frac{d_{(hkl)}}{R} \quad .....(4.34)$$

is the equation of this system of circles, where D is an expression relating to their phase.

4.4.2.2. Generation of the moiré pattern

Again we define three positive integers, h,k,l. The moiré pattern is found by eliminating m, n and q from the indicial equation (4.6) using equations (4.17), (4.19) and (4.30), whence:-

$$\cos y\,(h\cos x + k\sin x) + l\sin y = hA + kB + lC - {}^{pa}/_{R} \qquad \ldots\ldots(4.34)$$

As before we divide throughout by $(h^2 + k^2)^{\frac{1}{2}}$, and define an angle $\theta = \tan^{-1}(k/h)$ figure 4.6(a), whereupon:-

$$\cos y\cos(x-\theta) + \sin y\left(\frac{h}{(h^2+k^2)^{\frac{1}{2}}}\right) = \frac{hA+kB+lC}{(h^2+k^2)^{\frac{1}{2}}} - \frac{pa}{R(h^2+k^2)^{\frac{1}{2}}} \qquad \ldots\ldots(4.35)$$

Now multiply throughout by $\dfrac{(h^2+k^2)^{\frac{1}{2}}}{(h^2+k^2+l^2)^{\frac{1}{2}}}$ and define an angle $\lambda = \tan^{-1} l/(h^2+k^2)^{\frac{1}{2}}$ figure 4.6(b) whereupon:-

$$\cos\lambda\cos(x-\theta)\cos y + \sin\lambda\sin y = \frac{hA+kB+lC}{(h^2+k^2+l^2)^{\frac{1}{2}}} - \frac{pa}{R(h^2+k^2+l^2)^{\frac{1}{2}}} \qquad \ldots\ldots(4.36)$$

If equation (4.36) is compared with equation (4.34) then it may be seen that, for a given (hkl) the moiré pattern that it describes is indeed a system of circles of periodicity p, centred at longitude θ, latitude λ. Their position may, for example, be defined by the angle $(\pi/2-\lambda)$ between their centre and (001), where from figure 4.6(b):-

$$\cos(\pi/2-\lambda) = \frac{l}{(h^2+k^2+l^2)^{\frac{1}{2}}} \qquad \ldots\ldots(4.37)$$

They are generated by planes whose separation $d_{(hkl)}$ is given by:-

$$d_{(hkl)} = \frac{a}{(h^2+k^2+l^2)^{\frac{1}{2}}} \qquad \ldots\ldots(4.38)$$

and the information concerning their phase is contained in the expression: $\dfrac{hA + kB + lC}{(h^2 + k^2 + l^2)^{\frac{1}{2}}}$

The important result of the above analysis is that equations (4.37) and (4.12) and (4.38) and (4.11) are identical.

4.4.3. Generalised moiré analysis

The above analyses, which consider the formation of moiré patterns from a number of originals by means of a varying range of indices h, k, l, corresponds to the approach to moiré zone plate formation used by Chau (1969(a)), and which we have termed the comprehensive approach. An alternative, sequential, approach, has been developed in chapter 2 which, in the present context, would consider the formation of a moiré system of circles in indices $(h_4k_4l_4)$ as the single consequence of overlapping three systems of circles $(h_1k_1l_1)$, $(h_2k_2l_2)$ $(h_3k_3l_3)$ such that:-

$$h_4 = h_1 + h_2 + h_3 \qquad \text{.....(4.39(a))}$$

$$k_4 = k_1 + k_2 + k_3 \qquad \text{.....(4.39(b))}$$

$$l_4 = l_1 + l_2 + l_3 \qquad \text{.....(4.39(c))}$$

A similar analysis to that developed in section 4.4.2 reveals that the system of circles that forms the resultant moiré pattern is centred at a point which makes an angle θ, with say, $(h_1\ k_1\ l_1)$ such that

$$\cos\theta = \frac{h_1h_4 + k_1k_4 + l_1l_4}{(h_1^2+k_1^2+l_1^2)^{\frac{1}{2}}(h_4^2+k_4^2+l_4^2)^{\frac{1}{2}}} \qquad \text{.....(4.40)}$$

and is generated by planes whose separation is given by:-

$$d_{(h_4k_4l_4)} = \frac{a}{(h_4^2+k_4^2+l_4^2)^{\frac{1}{2}}} \qquad \text{.....(4.41)}$$

Similar to before, equations (4.40) and (4.13) and (4.41) and (4.1) are conjugate.

The importance of this most general treatment is that the identicalities between the geometrical approach (section 4.3) and the moiré approach (section 4.4) will continue to hold even if one considers the formation of moiré patterns between planes which are themselves moiré patterns of the three original (100), (010) and (001) planes. Indeed the distinction of the three original systems is lost, and the whole emitter surface must be considered as an interdependent moiré pattern.

4.5 The phase factor

In the geometrical analysis of field-ion micrographs, the importance of the phase factor of a plane has rarely been recognised. However, neglect of this final fraction of an interplanar spacing can introduce substantial errors into determinations of the emitter radius, using for example, the method due to Drechsler and Wolf (1958). Its appreciation is necessary also in consideration of plane prominence, and can be shown to have a crucial effect on analyses of ledge width effects such as that by Fortes and Ralph (1967).

The method of obtaining the phase information from the moiré analysis itself provides a means of determining the local radius of the emitter. For simplicity the analysis is confined to the case where the moiré plane is formed between only two other planes, all three lying in the same zone, c.f. section 4.4.1.

If we once again consider the two original sets of circles to correspond to (100) and (010), then the angular radii S_m and S_n of their mth and nth circles, respectively are given by an equation similar to (4.14) viz.

$$\cos S_m = \frac{R-d_{(100)}\,(m+\delta_{(100)})}{R} \qquad .....(4.42)$$

$$= A - \frac{ma}{R} \qquad .....(4.43)$$

$$\text{where } A = \frac{R-a\,\delta_{(100)})}{R} \qquad .....(4.44)$$

$$\text{and } \cos S_n = \frac{R-d_{(010)}(m+\delta_{(010)})}{R} \qquad .....(4.45)$$

$$= B - \frac{na}{R} \qquad .....(4.46)$$

$$\text{where } B = \frac{R-a\,\delta_{(010)})}{R} \qquad .....(4.47)$$

The equivalent expression for the moiré plane (hk0) is given by equation (4.24) where s_p is the angular radius of the pth circle, viz.

$$\cos s_p = \frac{hA + kB}{(h^2+k^2)^{\frac{1}{2}}} - \frac{pa}{R(h^2+k^2)^{\frac{1}{2}}} \qquad .....(4.48)$$

However, the similarity between equations (4.43) or (4.45) and equation (4.48) is deceptive. Although, in equation (4.48), the quantity $a/(h^2+k^2)^{\frac{1}{2}}$ <u>is</u> the interplanar spacing of the moiré plane, the parameter p is not directly equivalent to m or n, since while the latter take values 0, 1, 2, 3..., p, which is equal to hm + kn, has an initial value which cannot be zero. Thus an additional operation is needed in order to extract the phase information from this sort of moiré expression (see chapter 2).

The key point to note is that if we extract the quantity $d_{(100)}\ (m + \delta_{(100)})$ from the right hand side of equation (4.42) then for the minimum value of m, $m_{min} = 0$, this expression is equal to $\delta_{(100)}$ times the interplanar spacing of (100), where $0<\delta<1$. To find the corresponding parameter $\delta_{(hkl)}$, which must again obey $0<\delta_{(hkl)}<1$, we must structure the right hand side of equation (4.48) in

a similar way to equation (4.42) and then find the value of $p = p_{min}$. Equation (4.48) is equivalent to:-

$$\cos s_p = \frac{h(R-a\delta_{(100)}) + k(R-a\delta_{(010)}) - pa}{R(h^2 + k^2)^{\frac{1}{2}}} \qquad \ldots\ldots(4.49)$$

$$= \frac{R\left[\frac{h+k}{(h^2+k^2)^{\frac{1}{2}}}\right] - \frac{a}{(h^2+k^2)^{\frac{1}{2}}}\left[h\delta_{(100)} + k\delta_{(010)} + p\right]}{R} \qquad \ldots\ldots(4.50)$$

$$= \frac{R + R\left[\frac{h+k}{(h^2+k^2)^{\frac{1}{2}}} - 1\right] - \frac{a}{(h^2+k^2)^{\frac{1}{2}}}\left[h\delta_{(100)} + k\delta_{(010)} + p\right]}{R} \qquad \ldots\ldots(4.51)$$

which is now in the same form as equation (4.42).

Since $a/(h^2+k^2)^{\frac{1}{2}}$ is the interplanar spacing of the moiré plane (hk0), the quantity:-

$$\frac{R[(h^2+k^2)^{\frac{1}{2}} - (h+k)]}{a} + h\delta_{(100)} + k\delta_{(010)} + p \qquad \ldots\ldots(4.52)$$

is equal to $\delta_{(hk1)}$ when $p = p_{min}$.

A numerical example should make this clear. Let $R = 380$ Å, $h = 3$, $k = 4$ (and therefore $(h^2+k^2)^{\frac{1}{2}} = 5$), $a = 2.0$Å $\delta_{(100)} = 0.2$ $\delta_{(010)} = 0.7$, then expression 4.52 equals:-

$$-380 + [2.7 + p] \qquad \ldots\ldots(4.53)$$

and since $0 < -380 + (2.7 + p_{min}) < 1$, p_{min} must equal 378 (and hence p takes the values 378, 379, 380...) and $\delta_{(hk1)}$, the phase factor of the moiré plane, equals 0.7.

Thus

$$\delta_{(hk1)} = p_{min} + \frac{R[(h^2+k^2)^{\frac{1}{2}} - (h+k)}{a} + h\delta_{(100)} + k\delta_{(010)} \qquad \ldots\ldots(4.54)$$

In principle, therefore, it would be possible to calculate, R, the emitter radius, knowing h, k, a, p_{min}, and by measuring $\delta_{(100)}$, $\delta_{(010)}$ and $\delta_{(hk1)}$ from the

micrograph. The value of p_{min} is calculated from hm + kn, where m and n are the numbers of the circles around (100) and (010) which coincide at any single point on the innermost ring of the plane (hkl).

In practice of course the (100) and (010) planes may not be visible in a given micrograph, and in addition it is not possible to identify, and hence count, values of m and n over more than very short distances. However the analysis may be generalised to the case of a plane $(h_3k_3l_3)$ lying in the zone between two planes $(h_1k_1l_1)$ and $(h_2k_2l_2)$ where $h_3 = h_1 + h_2$, $k_3 = k_1 + k_2$ and $l_3 = l_1 + l_2$, whereupon it may be shown that:-

$$\delta_{(h_3k_3l_3)} = p_{min} + \frac{R}{a}\left[(h_3^2+k_3^2+l_3^2)^{\frac{1}{2}} - (h_1^2+k_1^2+l_1^2)^{\frac{1}{2}} - (h_2^2+k_2^2+l_2^2)^{\frac{1}{2}}\right] + \delta_1 + \delta_2 \qquad .....(4.55)$$

The application of this formula to the determination of field-ion emitter radii is discussed in the next section.

4.6. The moiré method of emitter radius measurement

In this section a method of determining the local radius of curvature of a field-ion emitter based on the previous analysis will be discussed. A comparison will then be made between results obtained using this method and the Drechsler and Wolf method previously discussed.

An equation for R may be obtained by re-arranging equation (4.55). Thus:-

$$R = \frac{a}{\left((h_1^2+k_1^2+l_1^2)^{\frac{1}{2}}+(h_2^2+k_2^2+l_2^2)^{\frac{1}{2}}-(h_3^2+k_3^2+l_3^2)^{\frac{1}{2}}\right)} \times \left[p_{min} + \delta_{h_1k_1l_1} + \delta_{h_2k_2l_2} - \delta_{h_3k_3l_3}\right] \qquad .....(4.56)$$

The radius of curvature R may thus be determined providing information is available regarding the values of p_{min} and the various phase factors. The value of p_{min} may be found directly from the micrograph. It is simply the sum of the number of net plane rings counted from the first ring on $h_1k_1l_1$ and $h_2k_2l_2$ respectively to some atomic position on the first ring on the plane $h_3k_3l_3$. For a completely accurate result the phase factors may be determined by measuring the radius of the rings comprising the field-ion plane r_n (using a travelling microscope), by plotting r_n^2 versus the number of the ring n, where the first ring is n = 1 etc., then the intercept between n = 0 and n = 1 gives the value of the phase factor.

An example should help to clarify the use of the method. Consider the radius of curvature of the region of the emitter between the planes (002) and (204) in figure 4.9. For this situation $h_1k_1l_1$ in equation (4.56) becomes (002) and similarly $h_2k_2l_2$ is (204) and $h_3k_3l_3$ is (206). Phase factor measurements on these three planes gave the following results:-

$\delta_{(002)} = 0.4$, $\delta_{(204)} = 0.3$ and $\delta_{(206)} = 0.9$.

From the micrograph p_{min} can be seen to possess a value equal to (17+6), that is 23. The lattice parameter for iridium a is equal to 3.838Å. Substituting these values into equation (4.56) yields a value for R equal to 595Å.

A rapid method of obtaining an approximate value for R may be obtained by neglecting the phase factors of the three planes involved. In this case equation (4.56) reduces to:-

$$R = \frac{a\, p_{min}}{(h_1^2+k_1^2+l_1^2)^{\frac{1}{2}} + (h_2^2+k_2^2+l_2^2)^{\frac{1}{2}} - (h_3^2+k_3^2+l_3^2)^{\frac{1}{2}}} \qquad (4.57)$$

Using this approximate relationship, the radius of curvature of the same region (002) - (206) - (204) can be quickly calculated and is found to be 600Å.

The moiré method of obtaining the local radius of curvature has several advantages over the Drechsler and Wolf method. The most important advantage is that p_{min} is an integer and hence ring counting is to an actual atom and is completely accurate. Further there is no confusion over which rings one is actually counting; in the Drechsler and Wolf method n may not relate to the step height $dh_1k_1l_1$ unambiguously. The radius of curvature measured by the moiré method is associated with a wider area than that measured by the Drechsler and Wolf method.

Variations in R tend not to be as wild as those sometimes encountered using the Drechsler and Wolf method, (variations of R up to a factor of 4 have been reported on a single micrograph). For the particular example considered here (figure 4.9) variations in radius between 585Å and 772Å were obtained. The corresponding variation in R for Drechsler and Wolf type calculations (phase factors were not taken into account) was between 472Å and 890Å.

Table 4.1 contains local radius of curvature measurements for four regions on the field-ion micrograph of iridium in figure 4.9. Compiled in this table are local radius measurements based on both the accurate and approximate moiré methods and also for each region two Drechsler and Wolf calculations and their average. Although the average value of the two Drechsler and

Figure 4.9 An indexed field-ion micrograph of iridium. (Courtesy E. W. Müller).

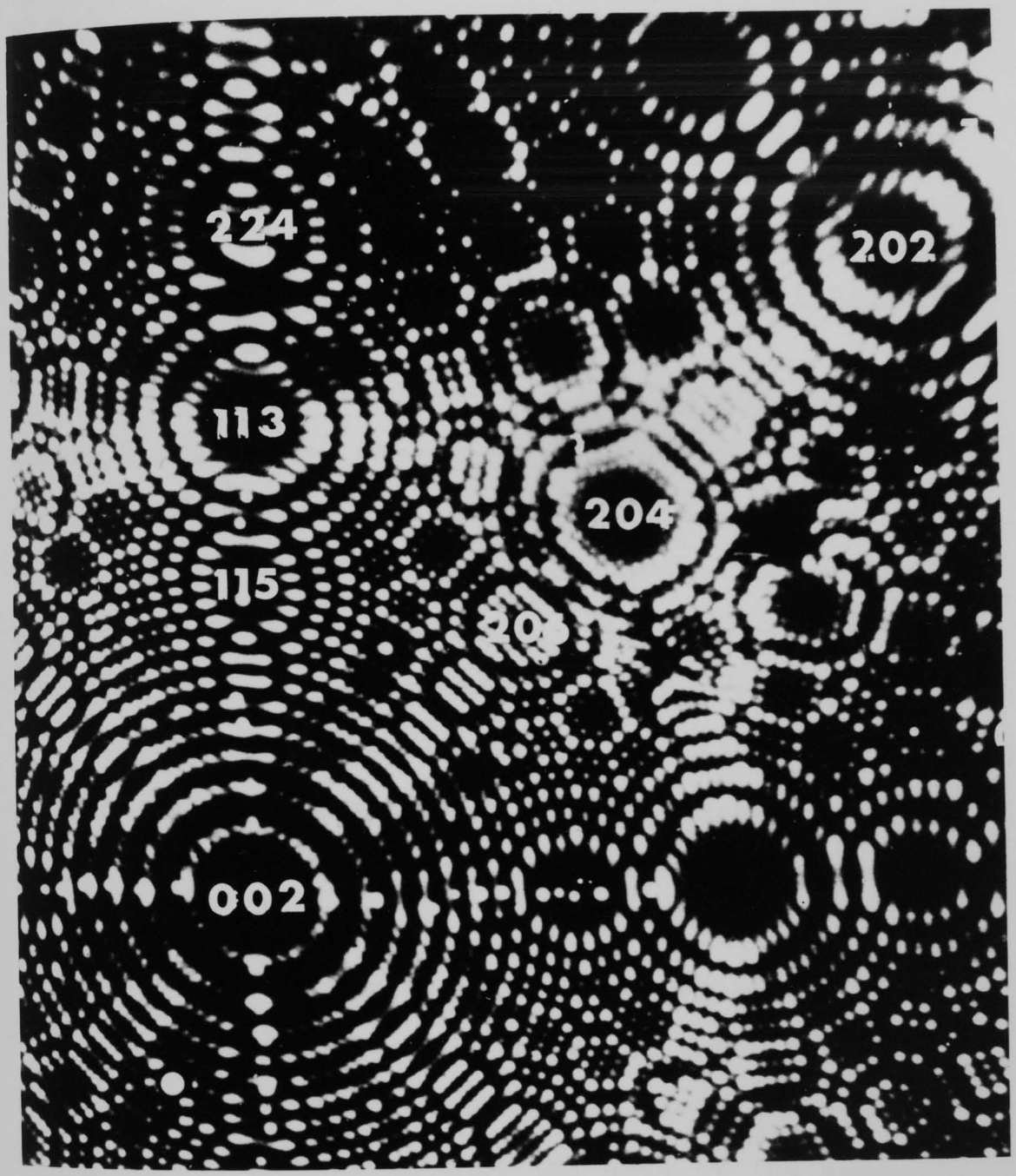
224
202
113
204
115
002

Wolf method calculations is possibly not the best comparison (a weighted average may be better); it can be seen for this example that this value is always within about 15% of the moiré result. The approximate moiré method is best used over a region involving a large value of p_{min}, where the values of the phase factors are relatively insignificant.

4.7 An alternative moiré interpretation of field-ion microscopy

Instead of considering the loci of intersecting points generated by ring structures on the surface of the field-ion emitter, a second moiré interpretation exists which is derived in a similar way to computer simulation of field-ion images. This interpretation was first used by Moore (1967(b)). The crystal lattice is represented by a suitable grid structure and the specimen envelope is represented by a projected contoured hemisphere which corresponds to the 'thin shell' model used in computer simulation (Moore (1962)).

Moore assumed for simplicity an orthographic projection, the sections of the shell intersected by lattice planes are projected into a series of concentric annuli. It can be shown that the area of the annuli corresponding to the image are constant whereas the area of the non-imaged annuli are not.

The grid structure corresponds to the actual crystal structure concerned. The simple cubic structure is illustrated in figure 4.10(a) where the interplanar spacing is d (corresponding to the pitch of the grid in the optical analogue model discussed in chapter 2).

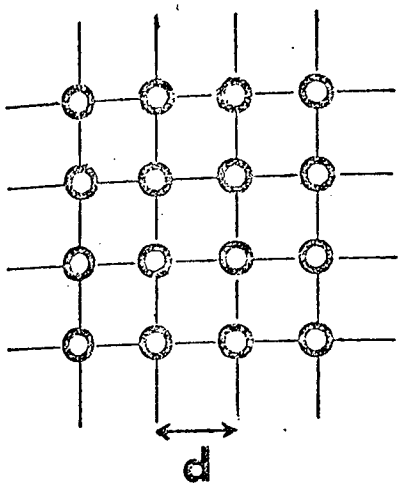

(a) simple cubic structure

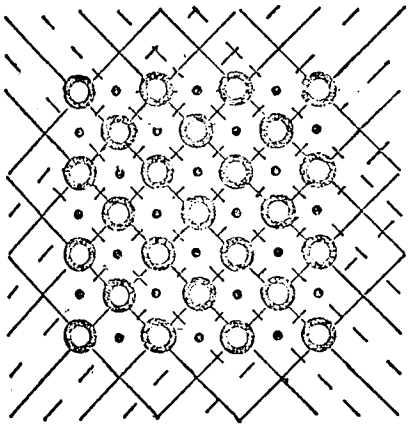

(b) face centred cubic

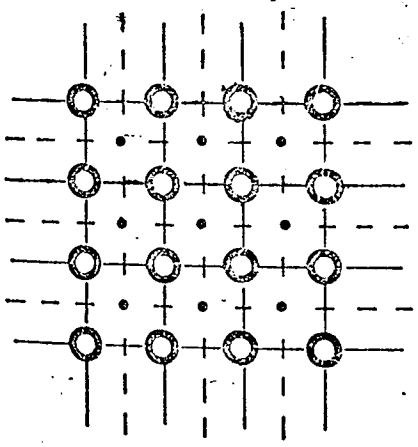

(c) body centred cubic

The position of topmost surface atoms

The position of the atoms in the second atomic layer.

Figure 4.10 The grids corresponding to the various crystal structures used in the moire interpretation of field-ion microscopy involving the superposition of a grid and a zone plate. The solid lines correspond to the grid used to simulate the topmost surface layer and the dotted lines simulate the positions of the atoms below.

The equivalent grid is also drawn in - in solid black lines. For the more complicated structures such as f.c.c. and b.c.c., it is necessary to resort to the use of two gratings which represent the alternate atomic layers of the lattice*. The situation for f.c.c. and b.c.c. are illustrated in figures 4.10(b) and 4.10(c) respectively. In each case two grids are required to represent the alternate layers of atoms. These diagrams allude to the (100) planes of each crystal structure. The grid representing the top layer of atoms is drawn in solid lines in each case, whereas the second layer is represented by a dashed line.

The simulation of a field-ion image for simple cubic structures is simple and is illustrated in figure 2.20 in chapter 2. Moore (1967(b)) has been able to produce the appropriate moiré effect corresponding to the two grid situation by colouring alternate annuli red and green on the transparency and by drawing points on the two intersecting grids one green and one red on the other transparency. Thus light is only able to pass through regions of the same colour and the image appears as a mixture of red and green spots.

Clearly, moiré patterns centred on planes other than (100) are obtainable. Hence a (110) orientated pattern requires two intersecting grids combined with the appropriate set of circular annuli, whereas a (111) orientated pattern would require the intersection of three hexagonal arrays.

* The author is indebted to Dr. A.J.W. Moore for the provision of his unpublished work on this topic.

An optical analogue of this situation exists and has been dealt with in chapter 2. Here, the circular annuli are depicted in the form of a special binary zone plate. If we take the situation where the imaged and non-imaged areas are equal, but not to each other, then their projection corresponds to the geometry of a binary zone plate. The discrepancy between using the circular annuli conceived by Moore and the zone plate lies in the fact that the Moore model is formed by projecting the ring pattern formed by incremental sectioning of a spherical thin shell, while the true zone plate geometry is obtained by projecting incremental sections of a paraboidal thin shell.

This leads to some further interesting points. The Moore moiré pattern (and hence computer simulation) does not produce circular image planes, since it is an orthographic projection, although the disparity does not become too obvious until the angle subtended to the centre is large (see chapter 5). If the real field-ion projection is approximately stereographic, then the image of each plane is a set of concentric circles. The overlap of a true zone plate with a grid does produce perfectly circular moiré zone plates (see chapter 2). However, even if the two colour technique is used the model proposed by Moore (and computer simulation) does not produce a true field-ion pattern because the focal lengths (plane prominences) are not correct relative to each other.

In order to simulate the image properly, a zone plate would have to be produced by means of a stereographic projection of a sectioned sphere (see chapter 3), and this should then be overlapped with a lattice grid also projected stereographically.

4.8. Discussion

The moiré analysis has shown that the moiré pattern resulting from the overlap of a number of systems of circles on a hemispherical surface, does consist of further systems of circles. However, the correspondences with the geometrical equations of section 4.3, which are pointed out at the ends of sections 4.4.1, 4.4.2. and 4.4.3., show that in all cases these moire circles are identical, both in location and in equivalent interplanar spacing, to those predicted by the lattice geometry.

Thus while the terraced structure of the surface of a field-ion emitter may indeed by interpreted as a moiré effect, no spurious facets are produced here. The same is true in the field-ion image since (a) there is a one to one correspondence between imaged atoms and image points, and (b) the generalised moiré treatment described in section 4.4.3. has already covered all possible moiré effects.

Therefore the suggestion made by Oster which was referred to in section 4.1 does not after all give rise to concern.

It is possible to consider chapter 3 that the fundamental reason for the identity between the geometric and the moiré approaches, is that the crystal lattice may itself be considered as a moiré pattern. Both treatments derive from considering the effect of the crystal planes intersecting a hemispherical surface.

Strictly the above analysis is referred to a simple cubic lattice. For other cubic lattices there will be a restriction on the values that h, k and l may take

(Moore and Ranganathan (1967)). For the f.c.c. lattice h, k and l must have the same parity (hence for example (200) rather than (100)), and for the b.c.c. lattice h + k + l must be even (hence, for example (420) rather than (210)). The analysis could readily be extended to other lattice types, such as hexagonal.

The moiré analysis itself leads to several new results in the interpretation of field-ion micrographs. This is because, for the first time, the position and appearance of a number of planes can be related to each other via the moiré mathematics. The phase information is particularly valuable in this respect, in providing information on the emitter shape. A new accurate method of determining the local radius of measurements is described the theory for which is a direct result of the moiré analysis.

A significant result of this work is that it has been proved possible to consider the formation of moiré patterns in three dimensions. It has been demonstrated that, while the detailed surface structure of a field-ion emitter may be considered as a moiré pattern, this does not imply the existence of any spurious imaging effects.

Finally, an alternative moiré interpretation of field-ion microscopy is briefly considered. In this case the moiré pattern simulates the interaction between the crystal lattice and a spherical section through it. This analogue is thought to be particularly useful as a teaching aid.

TABLE 4.1

Various local radius of curvature measurements on the micrograph of iridium (figure 4.9)

REGION	DRECHSLER AND WOLF Å	DRECHSLER AND WOLF AVERAGE Å	ACCURATE MOIRÉ Å	APPROX. MOIRÉ Å
002 - 113 at 115			695	
002 - 115	890	650		
113 - 115	417			
204 to 002 at 206			595	600
204 - 206	553	585		
002 - 206	618			
002 to 206 at 208			743	
002 - 208	708	772		
206 - 208	837			
204 to 202 at 406			582	
204 - 406	502	512		
202 - 406	522			

CHAPTER FIVE

LOCAL MAGNIFICATION IN FIELD-ION IMAGES

5.1. Introduction

The field-ion microscope is capable of resolving the position of a single atom. This resolution is achieved by means of a magnification typically of the order of 10^6 times. However, the magnification is not constant over the various crystallographic regions of the micrograph, for example the prominence of crystallographically equivalent planes situated at different angles to the specimen axis is often different. These variations are attributable to differences in local magnification both as a function of angle and of specimen radius. Clearly a knowledge of how local magnification varies from region to region is important in the interpretation of micrographs, particularly when attempting to estimate the size of precipitate particles and voids. It is also important when considering the general topography of the emitter especially when investigating the propagation of, for example, micro-crystals on the emitter surface, generated by vapour deposition.

A simple theory of magnification in field-ion images (Müller (1965)), assuming a simple gnomonic projection (as in the field emission microscope), would suggest that the only parameters involved are the tip to screen distance, T, and the specimen radius R and the magnification is simply given by T/R. Drechsler and Wolf (1958) measured the magnification in certain regions of tungsten micrographs and discovered variations

which they ascribed to changes in the local radius of curvature of the specimen. Brandon (1964) showed indirectly that magnification was also a function of the projection relationship (N) and the angle subtended by a plane to the specimen axis (θ). In fact, local magnification can be expressed as a function of the following local parameters:-

$$M = f(T,R,N,\theta) \qquad \ldots\ldots(5.1)$$

It is the purpose of this chapter to formulate an approximate expression for the local magnification taking into account all of these parameters.

A sensitive technique will be described whereby the local magnification may be measured. This technique relies heavily on the optical analogue theory of field-ion microscopy previously derived in chapter 3. Each field-ion plane is used to diffract coherent light to a focus in much the same way as a binary zone plate. The focal length of each plane is proportional to the square of the local magnification. Finally, a preliminary investigation into the projection relationship that exists in field-ion microscopy is reported.

5.2. The field-ion microscope projection

The field-ion microscope operates in a fashion similar to that illustrated in figure 5.1. The imaging ions leave the ionisation zone a few Ångstroms above the specimen surface in an approximately radial manner, the trajectory then flattens out as it nears the screen. The trajectory is largely determined by the electric field distribution between the specimen and the screen. Hence by extrapolating the straight line which intersects the

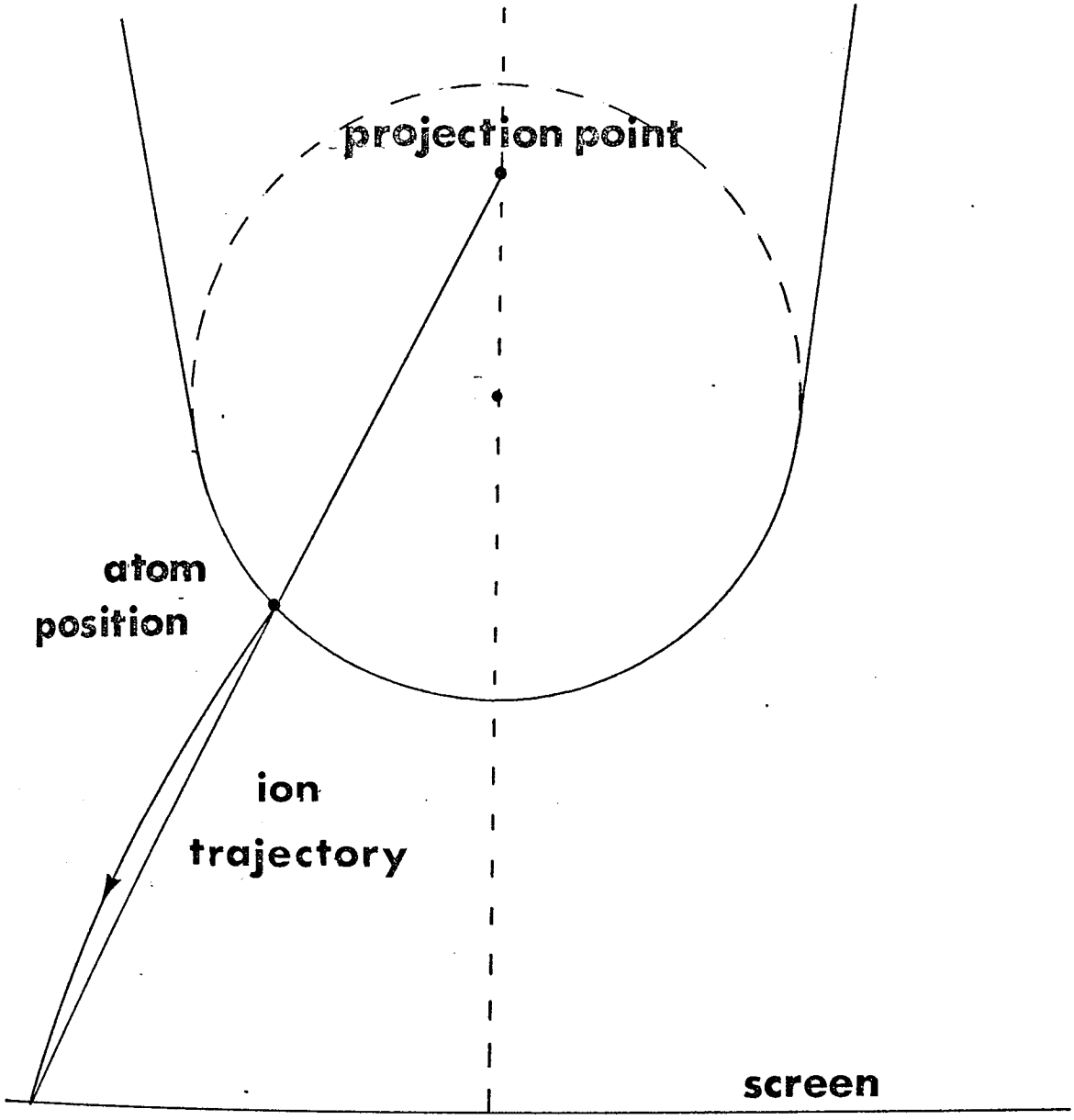

Figure 5.1. Illustrating the trajectory of an imaging gas ion and the concept of an apparent projection point.

image point and the corresponding atom on the specimen surface into the specimen (see figure 5.1), so that the produced line intersects the specimen axis, this intersection is defined as the projection point. In the case of the specimen axis perpendicular to the image plane (phosphor screen), this axis is also the projection axis. Brandon (1964) has used this approach to point projection in an attempt to define a single projection point. Unfortunately, due to the non-uniformity of the specimen topography, the field-ion microscope does not possess a common projection point.

The projection commonly used in the interpretation of field-ion micrographs is the stereographic projection (Brenner (1962)). This has been used with some success, particularly in the analysis of planar defects (for example, Bowkett and Smith (1970)). The orthographic projection has also been used (Good and Müller (1956)), but this projection involves unit magnification and is therefore very unsuitable. A different approach has been taken by Newman, Sanwald and Hren (1967) and Fortes (1971(b)), who use an experimentally derived relationship not involving a specific projection.

Brandon (1964) considered the image to be formed on a plane tangential to the specimen apex (illustrated for convenience on figure 5.2), and parallel to the image plane. This may be termed the tangent plane QQ'. The model assumes a uniform hemispherical specimen envelope of constant radius R and takes no account of the specimen to screen distance, T. Using this model, a point P' on the specimen surface subtending an angle θ to the

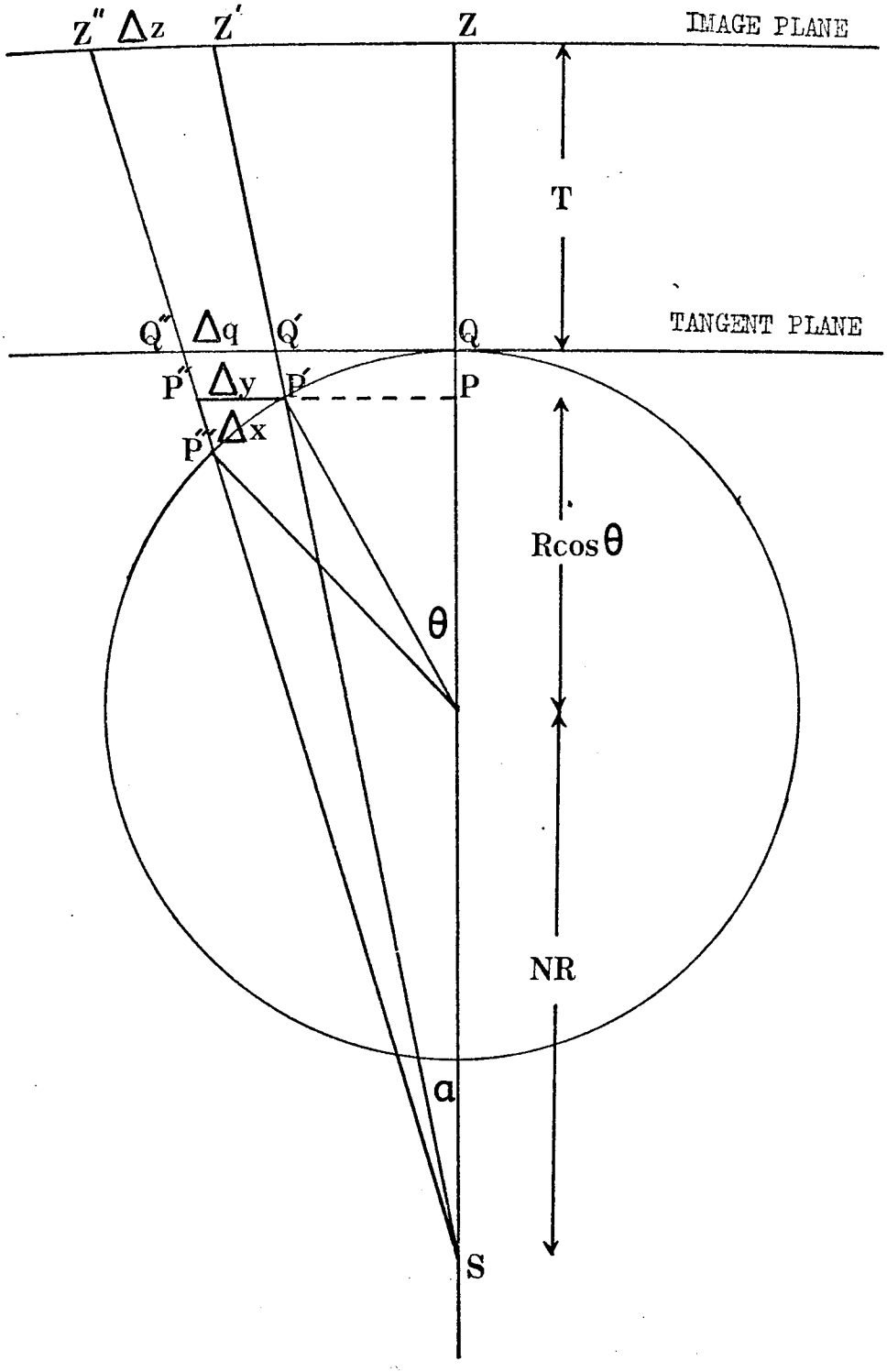

Figure 5.2. The model proposed to account for the magnification in field-ion microscope images. Brandon (1964) proposed a similar model which assumed that the specimen surface has an approximately hemispherical surface. In the present treatment it is assumed that <u>locally</u>, the specimen surface is hemispherical.

projection axis can be projected into the tangent plane at Q'. Thus for instance, projecting from O corresponds to the standard gnomonic (radial) projection (N=0) and a projection from O' would be a stereographic projection (N=1). Brandon used this model to calculate the distance d of a plane from the centre of the micrograph in terms of the radius of the projection sphere R, the angle subtended by the plane to the specimen axis θ and the projection point a distance NR from O and obtained the expression:-

$$d = \frac{R(1+N)\sin\theta}{N + \cos\theta} \qquad \ldots\ldots(5.2)$$

Hence for the gnomonic projection (N=0), $d = R\tan\theta$ and for the stereographic projection (N=1), $d = 2R\tan\frac{1}{2}\theta$. By measuring distances between planes subtending angles θ to the specimen axis on micrographs of tungsten using equation (5.2), Brandon deduced that the projection point was best approximated to the condition N=2, i.e. between stereographic and orthographic. Brandon also pointed out that at large angles the expression became a poor approximation and also warned that differing microscope geometries may produce different results. Equation (5.2) refers to magnification over real sections of the surface. Hence it is affected by variations in the local radius of curvature. A local magnification expression would not be affected to the same degree as the hemispherical approximation is good over local points on the specimen surface. Also, if this approach is used to find magnification, the distance on the micrograph actually magnified does not refer to actual distances such as say the arc P'Q in figure 5.2, but to

distance PP', the exposed ledge width. An analysis in section 5.3.5. will show that the two are not equivalent. Moreover, any realistic attempt to obtain an expression for local magnification must also include the tip to screen distance as a parameter.

5.3. Local magnification

A similar model is proposed to that of Brandon (1964) in order to obtain an expression for the local magnification. In this case, however, it is assumed that each point on the specimen surface possesses its own projection point and projection axis. The local shape of the specimen at each point is considered to be hemispherical.

For convenience, consider that the magnification takes place over three stages (see figure 5.2). Initially, an element of the surface Δx is projected into a plane parallel to the tangent plane, inclined at an angle, θ , to Δx and becomes Δy. Then Δy is projected into the tangent plane and is magnified to become Δq. The final stage involves the projection of Δq into the image plane and now corresponds to a distance Δz. The magnification of this system is $\Delta z/\Delta x$ and this may be expressed in terms of the three stage process as:-

$$M = \frac{\Delta z}{\Delta x} = \frac{\Delta z}{\Delta q} \times \frac{\Delta q}{\Delta y} \times \frac{\Delta y}{\Delta x} \qquad .....(5.3)$$

5.3.1. Magnification from the specimen surface to the tangent plane

Let us consider the first two stages in the magnification process. Consider once more the tangent plane QQ'. A small surface element Δx, which subtends a small

angle, $\Delta\theta$, at the centre of curvature O, of the projection sphere, is projected from a point S on the specimen axis. The surface element Δx subtends an angle, θ, with the specimen axis. The line PP' is constructed perpendicular to the axis, intersects Δx and is then produced to P". Let the small distance, P'P" be Δy and let its magnified image on the tangent plane, Q'Q" be Δq:-

$$\text{Then} \quad \frac{\Delta q}{\Delta x} = \frac{\Delta q}{\Delta y} \times \frac{\Delta y}{\Delta x} \qquad \ldots\ldots(5.4)$$

From similar triangles:

$$\frac{\Delta q}{\Delta y} = \frac{Q'Q''}{PP''} = \frac{Q'S}{P'S} = \frac{N+1}{(N+\cos\theta)} \qquad \ldots\ldots(5.5)$$

Let α be the angle subtended by Δx to the projection axis, then:

$$\tan\alpha = \frac{\sin\theta}{(N+\cos\theta)} \qquad \ldots\ldots(5.6)$$

By applying the sine rule to the triangle P P"P''' we find:

$$\frac{\Delta x}{\sin(90-\alpha)} = \frac{\Delta y}{\sin(90-\theta-\alpha)} \qquad \ldots\ldots(5.7)$$

$$\text{Thus} \quad \frac{\Delta y}{\Delta x} = \cos\theta + \sin\theta\tan\alpha \qquad \ldots\ldots(5.8)$$

Hence by substituting equations (5.5) and (5.8) into equation (5.4) we find:-

$$\frac{\Delta q}{\Delta x} = \frac{N+1}{(N+\cos\theta)}(\cos\theta + \sin\theta\tan\alpha) \qquad \ldots\ldots(5.9)$$

Substituting for $\tan\alpha$ and rearranging:-

$$\frac{\Delta q}{\Delta x} = \frac{(N+1)(N\cos\theta + 1)}{(N+\cos\theta)^2} \qquad \ldots\ldots(5.10)$$

5.3.2. Magnification from the tangent plane into the image plane

Now consider the projection of Δq into the image plane situated a distance T from the tangent plane. The magnification at this stage is essentially linear and can be found by considering the similar triangles

SQ'Q" and SZ'Z".

Hence $\frac{\Delta z}{\Delta q} = \frac{Z'S}{Q'S}$ .....(5.11)

However, the triangles ZZ'S and QQ'S are also similar, therefore $\frac{\Delta z}{\Delta q} = \frac{ZS}{QS} = \frac{T + R(1+N)}{R(1+N)}$ .....(5.12)

For the projections that are likely to be important for field-ion microscopy, i.e. N = 1,2, or 3 and as a typical value of T is 5cm. and a typical value of R, 500Å, $T \gg R(1+N)$.

Hence $\frac{\Delta z}{\Delta q} = \frac{T}{R(1+N)}$ .....(5.13)

5.3.3. Total local magnification

By combining the magnification factors from the three stages considered above into equation (5.3), the total magnification is given by the expression:-

$$M = \frac{T}{R}\left[\frac{N\cos\theta + 1}{(N+\cos\theta)^2}\right] \qquad .....(5.14)$$

Substituting for N, for the various values corresponding to the commonly used projections we obtain:-

Gnomonic (N=0) $M = \frac{T}{R}\frac{1}{\cos^2\theta}$ .....(5.15)

Stereographic (N=1) $M = \frac{T}{R}\left[\frac{1}{1+\cos\theta}\right]$ .....(5.16)

Brandon (1964) (N=2) $M = \frac{T}{R}\left[\frac{2\cos\theta+1}{(2+\cos\theta)^2}\right]$ .....(5.17)

These functions are illustrated in figure 5.3. This diagram shows that for the gnomonic (N=0) projection magnification increases rapidly with θ. The stereographic projection (N=1) also shows an increase in magnification as a function of θ, but the rate of increase is not as sharp as in the gnomonic case. The projection suggested by Brandon (1964) (N=2) is associated with a relatively constant magnification term which decreases slowly with θ.

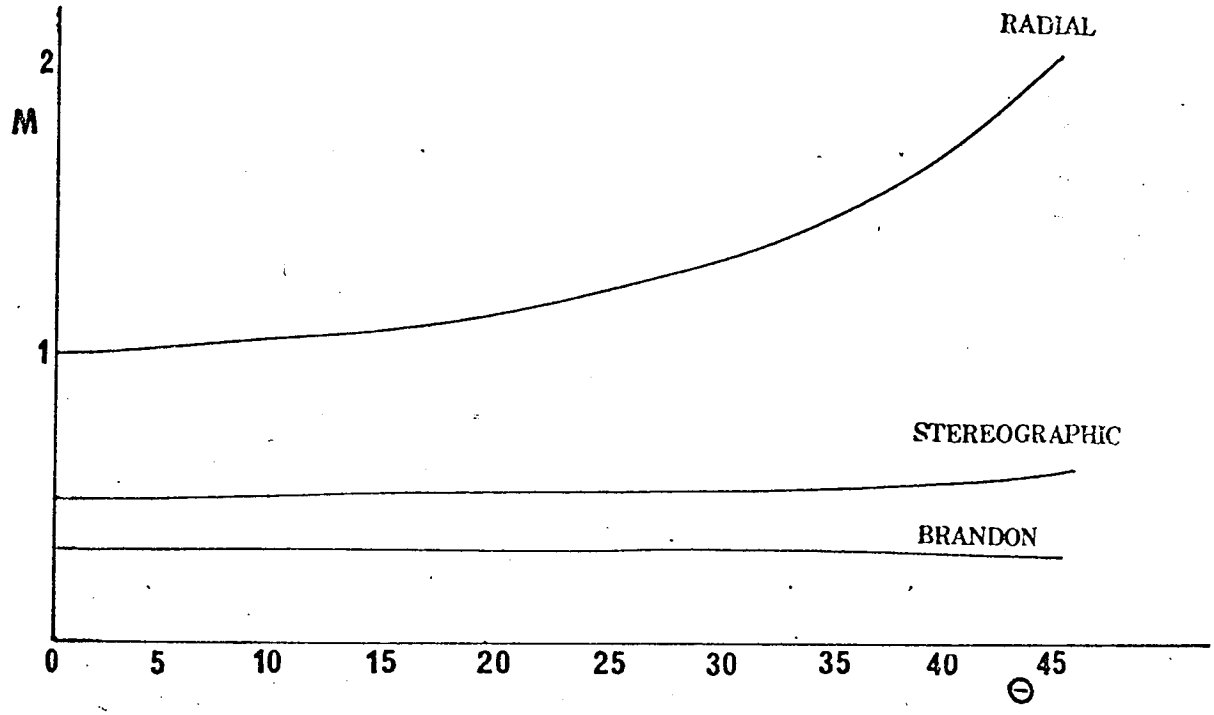

Figure 5.3 The local magnification functions of θ, the angle subtended by a point on the emitter to the specimen axis for each of the following projections :- (a) radial, (b) stereographic and (c) Brandon (1964).

5.3.4. The actual length of a finite surface sector

In the analysis of particle sizes and voids which possess a finite size and which can be defined by the angle subtended at O, (see figure 5.2), integration of expression 5.14 between the appropriate angular limits (θ_1 and θ_2) gives a more accurate result. However, if angular limits are difficult to specify, but the angle subtended by the centre of the particle or void to the specimen axis is known, then the magnification can still be found to a first approximation using equation 5.14 (provided that the angle subtended by the sector in question is not too large $\sim < 10^0$).

The length of an elemental surface sector dx subtending an angle $d\theta$ at the centre of curvature is simply determined by the equation:-

$$dx = Rd\theta \qquad .....(5.18)$$

The corresponding length in the image dz is related to dx and the magnification by:-

$$dz = Mdx \qquad .....(5.19)$$

Therefore $dz = MRd\theta$ .....(5.20)

Hence a finite length z in the image is found by performing the integral between θ_1 and θ_2.

$$z = \int_{\theta_1}^{\theta_2} M\,R\,d\theta \qquad .....(5.21)$$

Substituting for M from equation 5.14:-

$$z = T \int_{\theta_1}^{\theta_2} \frac{N \cos\theta + 1}{(N + \cos\theta)^2}\, d\theta \qquad .....(5.22)$$

The general solution for which is given by:-

$$z = T\left[\left(\frac{N \sin\theta}{(N^2-1)(N+\cos\theta)}\right)_{\theta_1}^{\theta_2} - \frac{1}{N^2-1}\int_{\theta_1}^{\theta_2}\frac{d\theta}{N+\cos\theta} + \frac{\sin\theta}{(1+N^2)(N+\cos\theta)} - \frac{N}{1-N^2}\int_{\theta_1}^{\theta_2}\frac{d\theta}{N+\cos\theta}\right] \quad \ldots\ldots(5.23)$$

The solution of the integral $\int_{\theta_1}^{\theta_2}\frac{d\theta}{N+\cos\theta}$ can take several forms which are determined by the value taken by N,

i.e.

$$\text{if } N^2 > 1 \quad = \left[\frac{2}{\sqrt{(1-N^2)}}\,\frac{\tan^{-1}(N-1)\tan\theta/2}{\sqrt{(N^2-1)}}\right]_{\theta_1}^{\theta_2}$$

$$\text{for } 1 > N^2 \quad = \left[\frac{1}{\sqrt{(1-N^2)}}\log\frac{[(1-N)\tan\theta/2+\sqrt{(1-N^2)}]}{[(1-N)\tan\theta/2-\sqrt{(1-N^2)}]}\right]_{\theta_1}^{\theta_2}$$

If $1 > N^2$, $\left|(1-N)\tan\theta/2\right| < \sqrt{(1-N^2)}$

$$= \left[\frac{2}{\sqrt{(1-N^2)}}\tanh^{-1}\frac{(1-N)\tan\theta/2}{\sqrt{(1-N^2)}}\right]_{\theta_1}^{\theta_2}$$

and finally for $1 > N^2$, $\left|(1-N)\tan\theta/2\right| > \sqrt{(1-N^2)}$

$$= \left[\frac{2}{\sqrt{(1-N^2)}}\,\text{ctnh}^{-1}\frac{(1-N)\tan\theta/2}{\sqrt{(1-N^2)}}\right]_{\theta_1}^{\theta_2}$$

Although the general solution to equation (5.22) is quite complex, more simple solutions are available for specific projections. For example for the gnomonic projection we have:-

$$z = T\int_{\theta_1}^{\theta_2}\cos^{-2}\theta\ d\theta = T\left[\tan\theta\right]_{\theta_1}^{\theta_2} \quad \ldots\ldots(5.24)$$

and for stereographic projection:-

$$z = T\int_{\theta_1}^{\theta_2}(1+\cos\theta)^{-1}\,d\theta = T\left[\tan\theta/2\right]_{\theta_1}^{\theta_2} \quad \ldots\ldots(5.25)$$

Thus in principle, providing the tip to screen distance is known and z measurable, the actual size of a defect can be determined directly from the micrograph. Thus it should be possible to improve on the computer programme technique of measuring particle sizes devised by Youle et al (1972). In this analysis (in common with all other computer simulation work), they assume an orthographic projection and take no account of real angular magnification. Thus if equation (5.25) was incorporated into their programme an improvement in the accuracy of their measurements would result.

If equation (5.24) and (5.25) are compared with the result obtained by Brandon, which is a special case where $\theta_1 = 0^o$ and $\theta_2 = \theta_2$, then by multiplying the result by 2R/T (Brandon did not consider the magnification between tangent plane and image plane), we obtain values identical i.e. for N = 0, $z = R \tan \theta_2$ and for N = 1, $z = 2R \tan \theta_{2/2}$

5.3.5. Local magnification of exposed ledge widths

In some instances in field-ion microscopy, it is necessary to know the local magnification of a ledge width rather than over a sector of curved surface. In this case, the magnification term turns out to be different to the case considered above. Consider once again the simple magnification model, this time illustrated in figure 5.4. This time, we consider the magnification of a small element of the ledge width P'P", Δx, magnified first into the tangent plane and then into the image plane - a two stage process. The width of the element in the tangent plane is Δq and in the image plane it is Δz.

Thus the total local magnification $M = \Delta z / \Delta x$ which

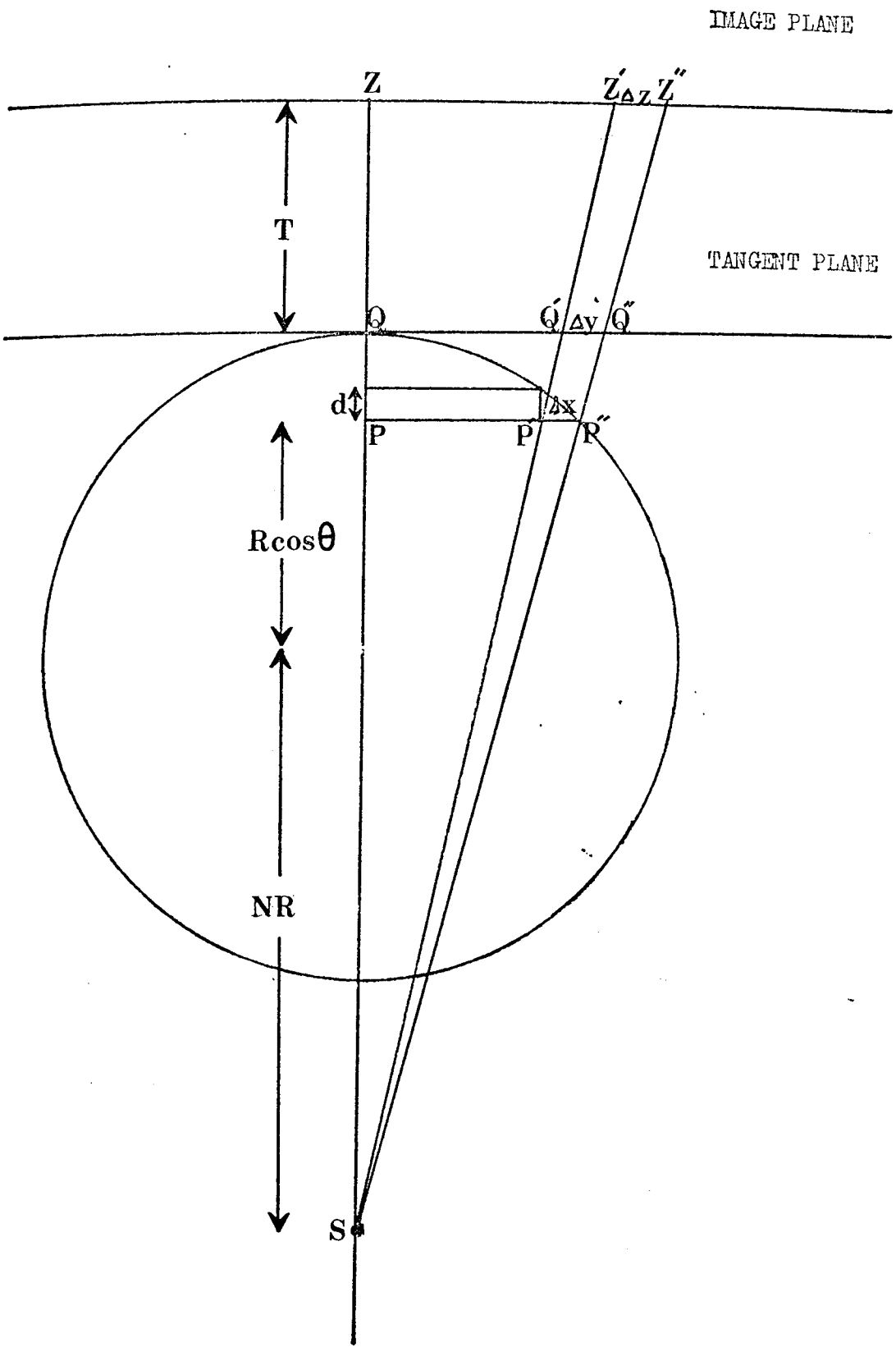

Figure 5.4. The model proposed to account for exposed ledge width Magnification.

may be also expressed as:-

$$M = \frac{\Delta z}{\Delta q} \times \frac{\Delta q}{\Delta x} \qquad \ldots\ldots(5.26)$$

In this very simple case however, the magnification can be determined directly by considering similar triangles.

Hence: $$\frac{\Delta z}{\Delta x} = \frac{Z'S}{P'S} = \frac{ZS}{PS} = \frac{T + R(1+N)}{R\cos\theta + NR} \qquad \ldots\ldots(5.27)$$

but $T \gg R(1+N)$, hence:

$$M = \frac{T}{R} \left(\frac{1}{N + \cos\theta}\right) \qquad \ldots\ldots(5.28)$$

This function is illustrated in figure 5.5 for various values of N. Once again, the gnomonic projection displays the sharpest dependance on θ. Comparison of figures 5.3 and 5.5 reveals that for all other parameters being equal, the magnification of an exposed ledge width is different to the magnification of a surface sector. Hence, care must be taken when specifying the area on the specimen surface in which the particular defect may lie.

5.4. Methods of measuring local magnification

In certain crystallographic regions of the image, the field-ion microscope is capable of resolving each atom. In these planes then, it is possible to measure the magnification directly by measuring the atom separation in the image and calculating the corresponding distance on the specimen surface. Although this method of determining the magnification does give the required local magnification, it is only applicable to a small number of crystallographic planes such as the $\{111\}$ planes in tungsten and some net plane ring edges which are also fully resolved.

Drechsler and Wolf (1958) suggested a method of determining magnification by calculating the distance

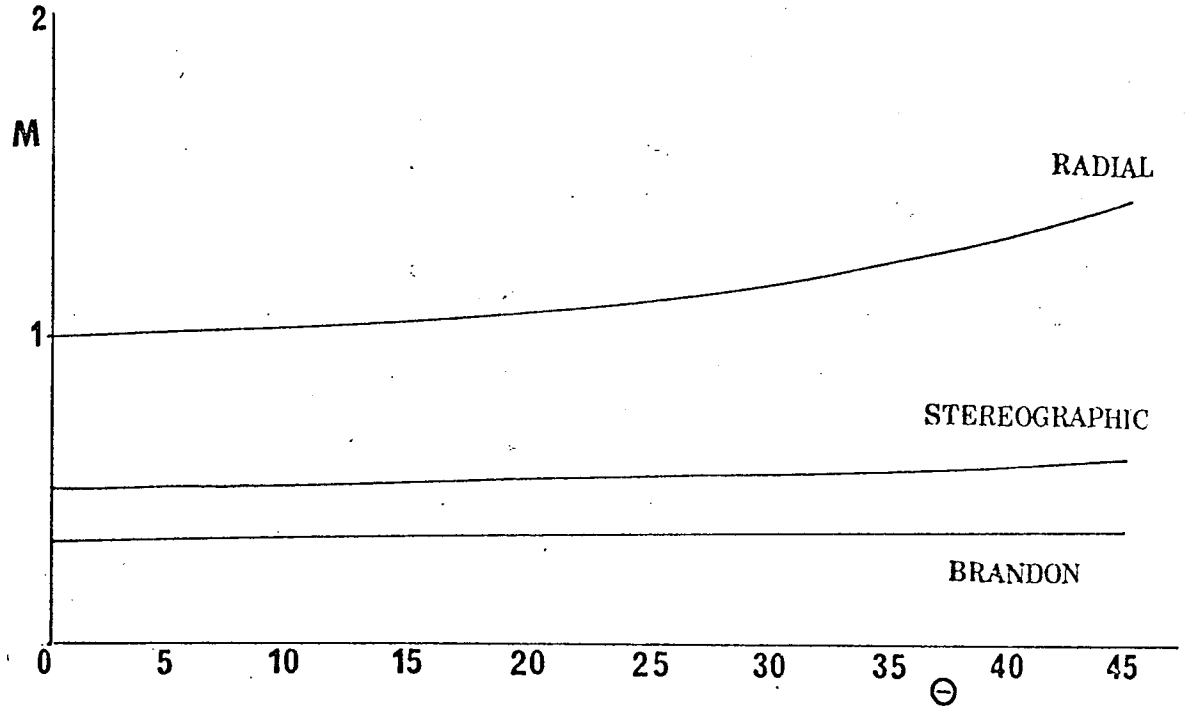

Figure 5.5 The exposed ledge width local magnification functions of θ for the radial, stereographic and Brandon (1964) projections.

between the centres of two adjacent crystallographic planes and then measuring the corresponding distance in the image. In this way, they were able to show that the magnification was not constant. They attributed the variations to changes in the local radius of curvature of the specimen.

An optical method of obtaining the local magnification is described in the next section.

5.5. Focusing field-ion micrographs

The optical analogue that may be drawn between the appearance of a field-ion plane and a binary zone plate has already been discussed in detail in chapter 3. In this section it is intended to briefly discuss how the focal length of a single $\{hkl\}$ field-ion plane may be used to measure local magnification. The technique of measuring the focal length of a field-ion plane is also discussed. An example of how this method may be used to discover the projection point for each $\{hkl\}$ plane is then presented.

5.5.1. Theory

The focal length of a zone plate is directly proportional to the square of the radius r of the concentric circles which make up the zone plate. The same is true for a field-ion plane on the specimen surface, but in the image this ring structure is magnified by a factor M, hence the focal length f is proportional to $(Mr)^2$. As we have shown above the local magnification is not constant and is a function of both θ, and the projection N.

It has been shown in chapter 3 that the focal length

of an axially situated plane on the specimen surface is given by:-

$$f = \frac{2Rd}{\lambda} \qquad \ldots\ldots(5.29)$$

In the image, this value must be multiplied by the square of the magnification factor, M.

$$\text{hence } f = \frac{2Rd}{\lambda} \times M^2 \qquad \ldots\ldots(5.30)$$

Thus as d and λ are known, and f and R can be measured, the local magnification M can be calculated. For the general case of a plane situated at an angle θ, to the specimen axis, using the general equation (5.14) for the magnification, we obtain the following expression for the focal length:-

$$f = \frac{2T^2 d}{\lambda R}\left[\frac{N\cos\theta + 1}{(N + \cos\theta)^2}\right]^2 \qquad \ldots\ldots(5.31)$$

Thus as the focal length, f, can be measured, and for a given $\{hkl\}$ plane, θ, is known the only unknown is N. Hence the projection relationship of each plane in the image can be determined.

5.5.2. Experimental technique

The apparatus required to obtain the focal length of a field-ion plane consists essentially of a helium-neon gas laser which provides a coherent light source of wavelength 6238Å, a collimating system and an optical bench. A photograph of the apparatus complete with a mounted field-ion microscope image is shown in figure 5.6. The collimating system consists of a variable slit aperture, a convex lens and a condenser lens. The maximum focal length of any plane in the image was determined by the length of the optical bench (1 metre). This is done by selecting the most prominent plane, (usually (011) in the

Figure 5.6 The experimental arrangement used for measuring the focal length of field-ion planes.

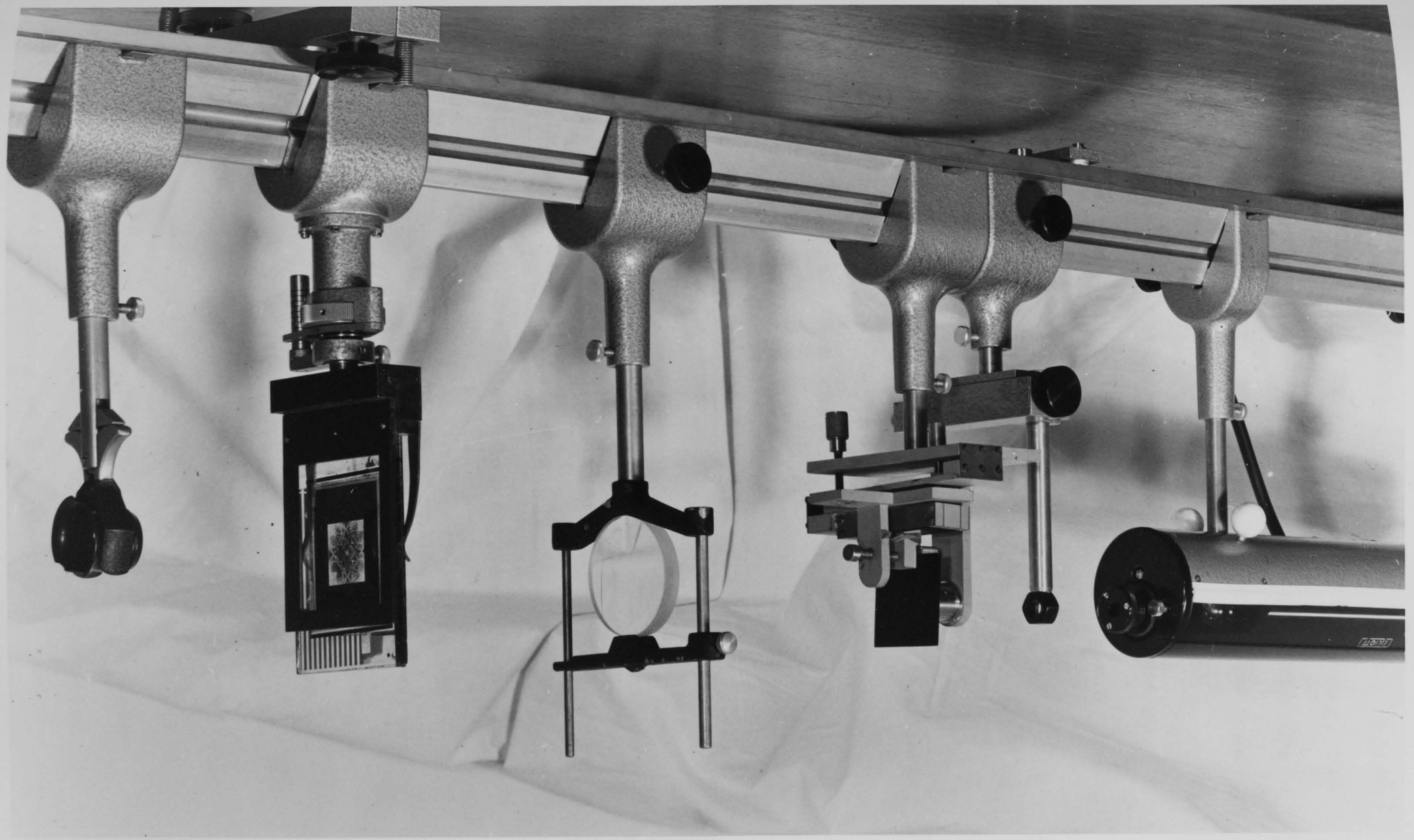

case of tungsten) and plotting the square of the radius of each ring r_n^2 versus n - the number of the ring. The gradient of the approximately straight line gives the square of maximum radius that the first ring can take (it compensates for any field evaporation or phase of the first ring) and the focal length is given simply by r_1^2/λ. The photographically reduced negative was then mounted in optically flat glass. The focal length measurement was taken by focussing an objective lens on the negative noting the value on a vernier scale and then by varying the position of the objective the focus of each $\{hkl\}$ plane in the image was found and the corresponding position on the vernier scale noted. The difference between the two readings gave the value of the focal length. As the focus of field-ion planes possess some spherical aberration, it was sometimes difficult to find the exact position of the circle of least confusion, but in general focal lengths could be measured to within about 5% accuracy.

The quality of the focus was, in general, a good indication of the regularity of the field-ion plane, the plane would have to possess perfectly concentric circles for the image focus not to possess elongation in any direction. Figure 5.7 shows a sequence of photographs of the focus produced by the (002) plane of iridium shown in figure 5.8(a). The photographs were taken at the circle of least confusion (figure 5.7(b)) and to either side of this position. It can be seen that the focus not only contains spherical aberration, but also possesses a degree of astigmatism.

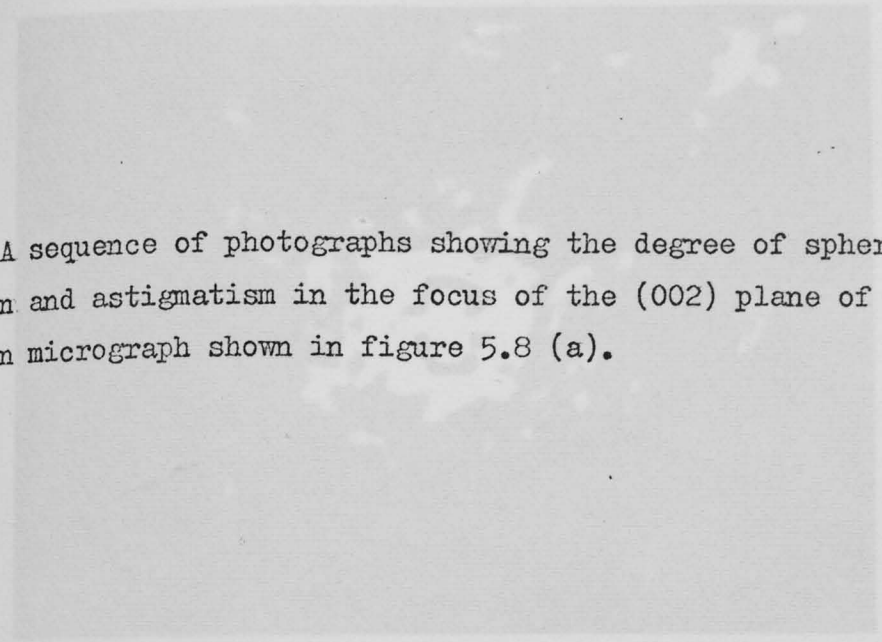

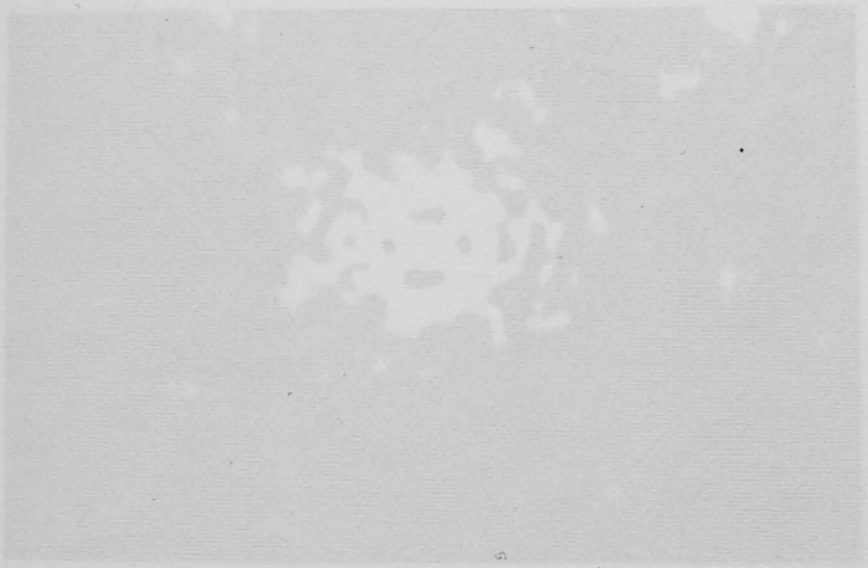

Figure 5.7 A sequence of photographs showing the degree of spherical aberation and astigmatism in the focus of the (002) plane of the field ion micrograph shown in figure 5.8 (a).

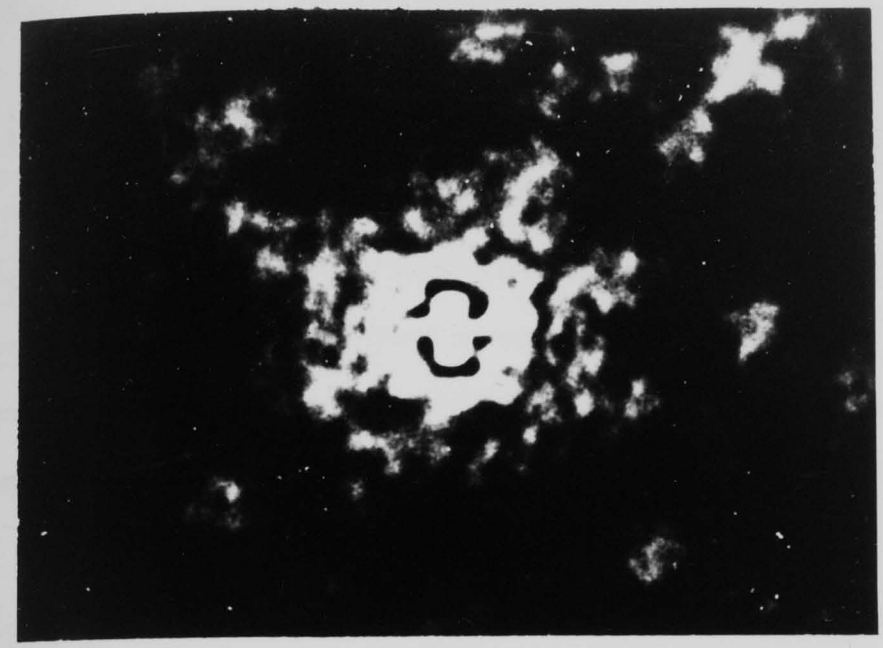

(a)

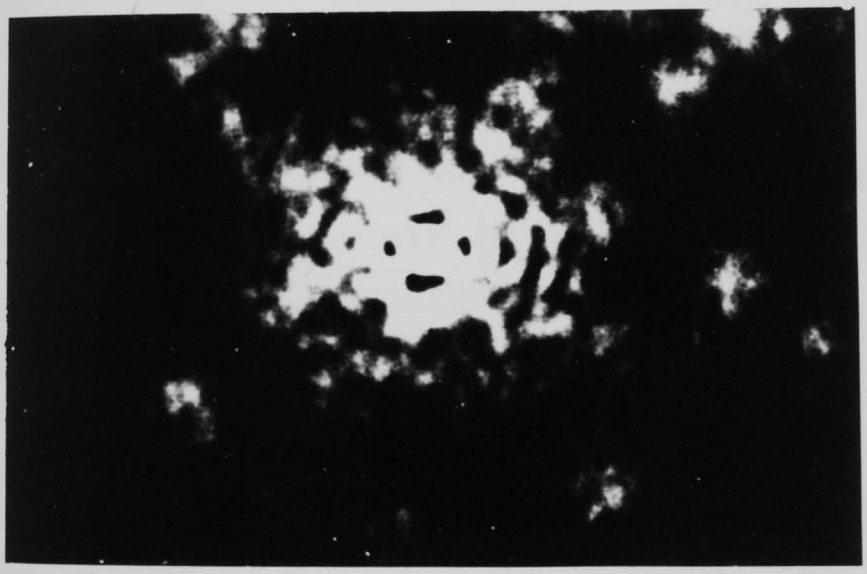

(b)

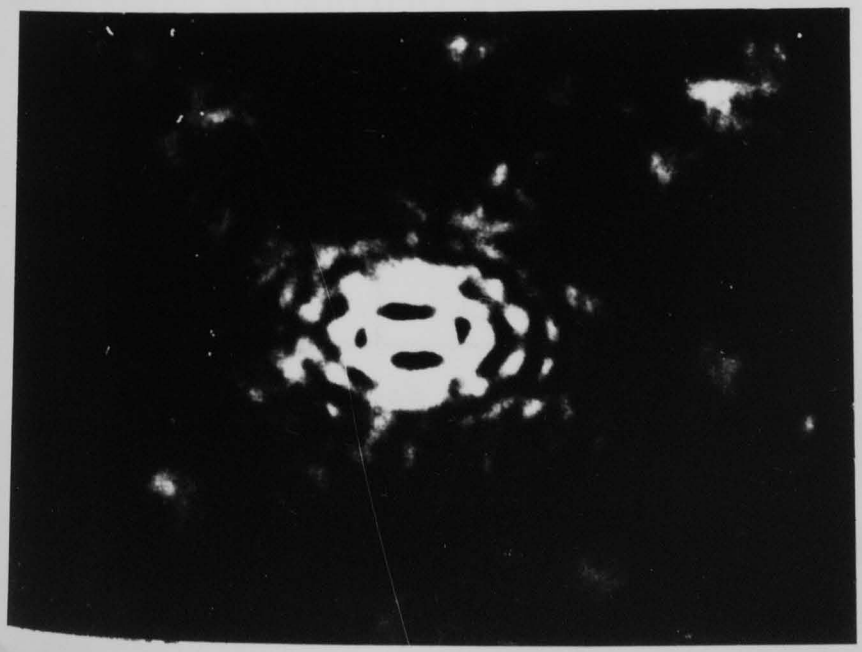

(c)

5.5.3. Projection information

A preliminary investigation into obtaining information regarding the projection operating in the field-ion microscope has been carried out. The variation of magnification with θ was found by normalising against the focal length of the apex plane where $\theta = 0^{o}$. The focal length of say the (002) plane in iridium (see figure 5.8(a)) would have only a small θ component. Thus, if the focal length of the plane situated at the apex is measured using the technique described above, the focal lengths of all $\{hkl\}$ planes situated at various angles θ, to the specimen axis can be calculated using equation(5.31) using no angular magnification component. This would then be the idealised focal length. Then the focal lengths of all $\{hkl\}$ planes could be measured and by plotting $\frac{f \text{ measured}}{f \text{ ideal}}$ versus θ, the resultant scatter gives the angular function of magnification. In order to compare these results, the various M^2 function of the commonly used projections are plotted on the same graph. These functions for the gnomonic, stereographic and orthographic projections are listed below:-

Projection	N	$M(\theta)^2$
Gnomonic	0	$\cos^{-4}\theta$
Stereographic	1	$\frac{4}{(1+\cos\theta)^2}$
Orthographic	α	$\cos^2\theta$

Results were taken from several different micrographs obtained on different microscopes, to discover if varying microscope and specimen geometry played any part. Typical results of these experiments are shown in figures 5.8(a) and (b), and 5.9(a) and (b). Figure 5.8(a) is a micrograph

of iridium and figure 5.8(b) is the corresponding projection plot for a number of planes. Figure 5.9(a) is a micrograph of platinum and figure 5.9(b) is the corresponding projection plot. The scatter of points in figure 5.8(b) shows a general trend and corresponds to a projection between stereographic and orthographic, whereas figure 5.9(b) shows an approximate relationship with a projection between gnomonic and stereographic. What is clear is that each {hkl} plane has a different operating projection. The scatter of points also appears to change with the specimen environment.

Work is now in progress on micrographs for which the tip to screen distance, T, has been measured, the local radius of curvature can be calculated and hence by using the focussing technique absolute measurements of local magnification can be made. Hence, if the absolute values of the local magnification about each {hkl} region are known, the absolute value of N, the projection relationship, can be found for each region of the specimen surface.

5.6 Discussion

In this chapter, we have attempted to formulate a general equation for local magnification in the field-ion microscope image. The detailed applications of the theory are presently receiving attention and occur in the determination of actual sizes and shapes of particles, voids and the width of planer defects such as twin slices. In this way, it is now possible to consider that defects that display a non-uniform shape in the image, may in fact have a uniform geometry, but

Figure 5.8 (a) A field-ion micrograph of iridium (courtesy G. K. L. Cranstoun)

(b) A projection plot for a number of planes appearing in the micrograph above.

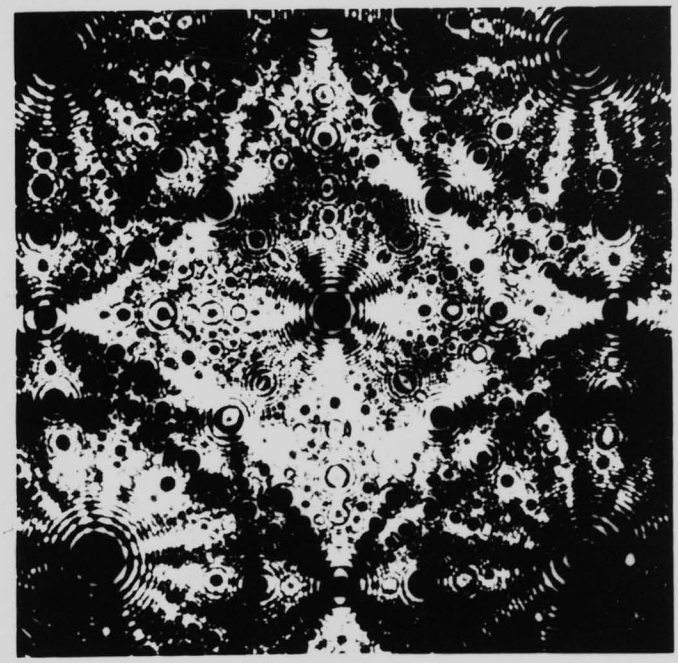

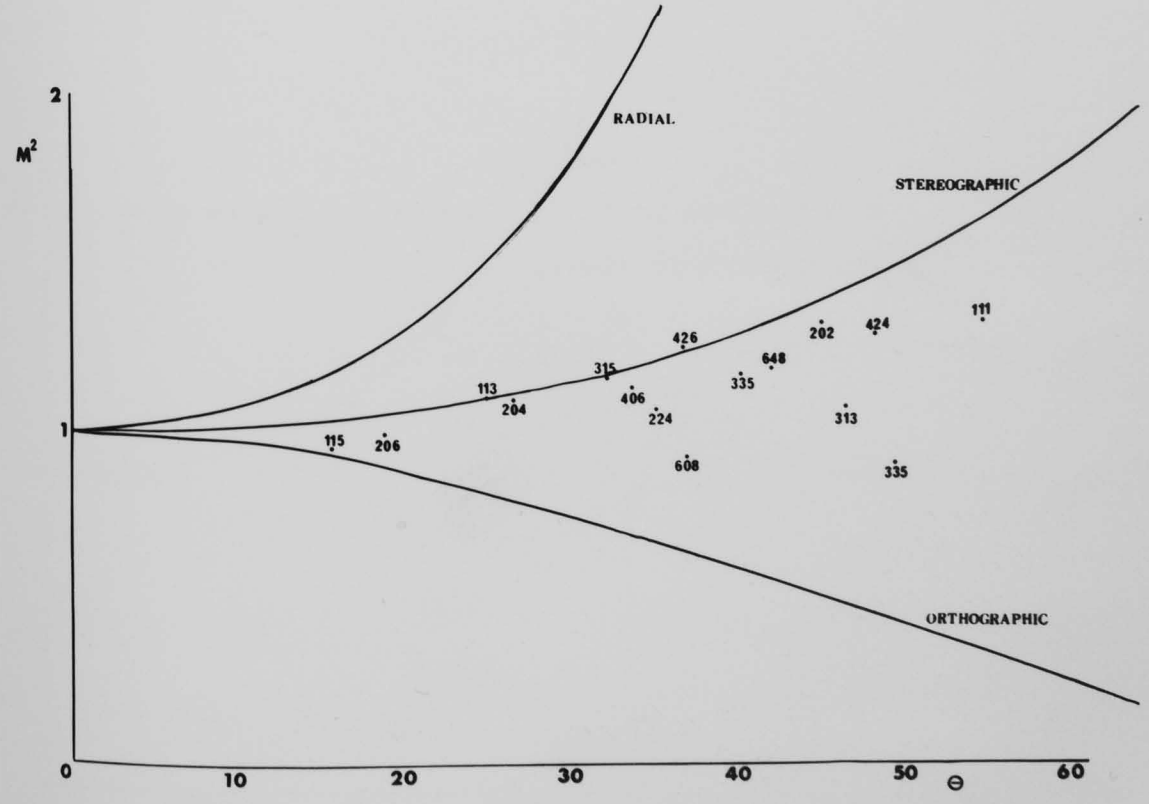
2
M²
1
RADIAL
STEREOGRAPHIC
ORTHOGRAPHIC
111
424
202
426
648
315
335
113
204
406
224
313
115
206
608
335
0
10
20
30
40
50
60
θ

Figure 5,9 (a) A field-ion micrograph of platinum (courtesy E.W.Müller)

(b) A projection plot for a number of planes appearing in the micrograph above.

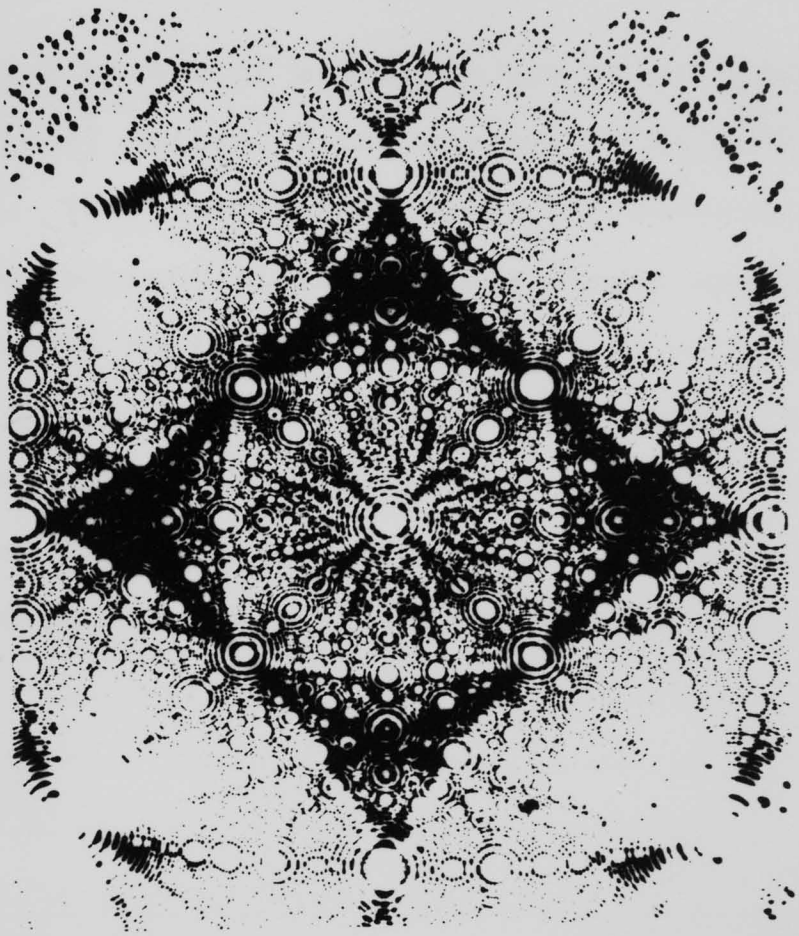

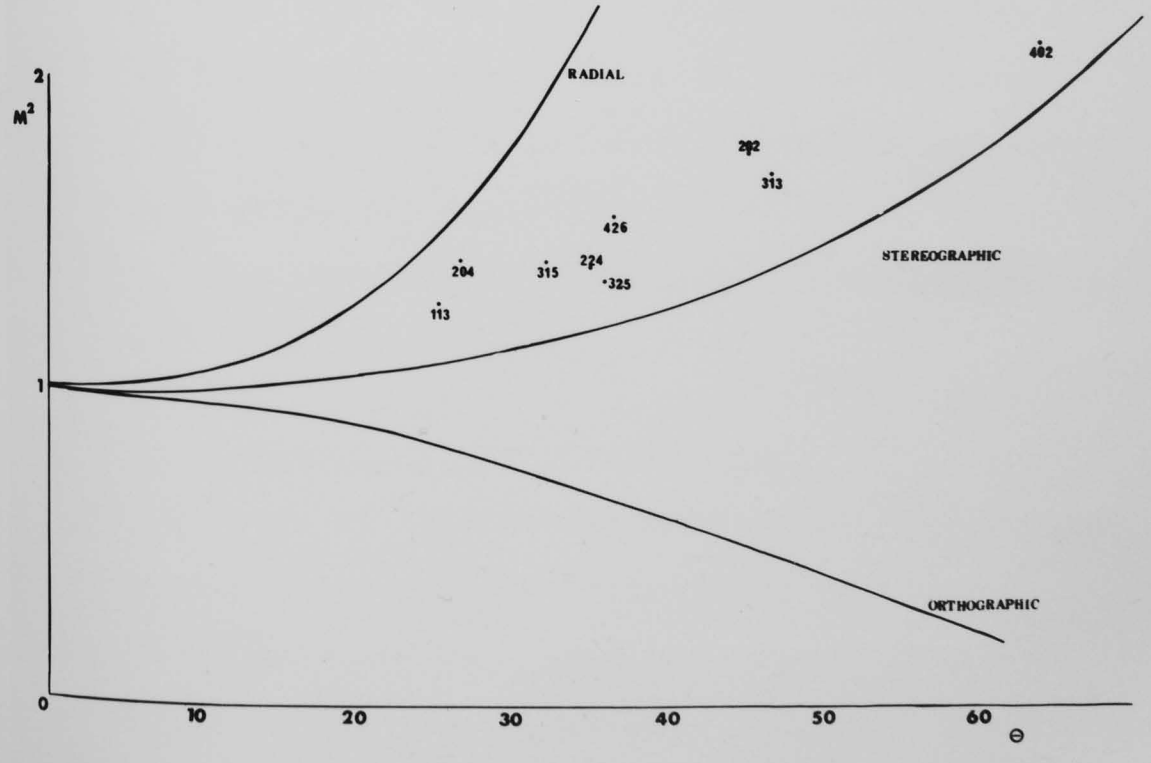
2
M²
1
0
RADIAL
STEREOGRAPHIC
ORTHOGRAPHIC
402
202
313
426
204
315
224
325
113
10
20
30
40
50
60
θ

whose apparent shape is distorted in the image forming process.

A novel method of measuring the local magnification over any {hkl} region of the micrograph is also described. The technique involves the focussing of collimated coherent light and is a direct application of the optical analogue models discussed in chapter 3. Preliminary results concerning the determination of the field-ion microscope projection are also presented. It is hoped that work now in progress will shed some light on this rather complex problem.

CHAPTER SIX

LOW-ENERGY ION BOMBARDMENT OF METAL SURFACES

6.1 Introduction

Up to this point we have considered only the characterisation of an atomically clean, field-ion microscope specimen surface. The attainment of clean, well defined structures using field-ion microscopy is simple and is achieved by merely field evaporating surface atomic layer. Moreover the surface remains clean while the high electric field is applied because contaminant atoms are ionised and repelled before they are able to adsorb on the imaging surface. Unfortunately, this method of cleaning is impracticable for macroscopic samples. An important and highly effective method of contamination removal used extensively in other surface research techniques consists of cycles of alternate ion bombardment and annealing. The investigation of the effects of this technique provides the basis for this chapter. This study involves a large number of variables and hence the work presented here is essentially of a preliminary nature and is primarily intended to assess those areas where the field-ion microscope is likely to provide useful information, difficult or impossible to obtain with other techniques.

6.2 The objectives of the present study

The purpose of this investigation into the process of low-energy inert gas ion bombardment of tungsten is primarily to dicover the nature and extent of damage introduced into the target lattice. For many surface research techniques such as low-energy electron diffraction

(L.E.E.D), Auger electron spectoscopy (A.E.S) and photoelectron spectroscopy (E.S.C.A.) the surface properties of the sample dominate results and therefore an atomically clean surface is a necessity. The most common method of accomplishing this condition is by means of ion bombardment and/or heating (Farnsworth et al (1958)).† The process of ion bombardment removal of surface atoms by a gradual process of erosion is a phenomenon known as sputtering. However, although such surfaces may be chemically clean as monitored by A.E.S. for example, their exact topography is undefined and may exert a considerable influence on the subsequent experiments. In particular it is known that ion bombardment causes considerable surface and subsurface damage, not all of which may be removed by the annealing processes that are feasible. This aspect of ion bombardment induced lattice damage is not only important to surface study techniques where electrons and X-rays are used, but is also crucial to the technique of ion scattering spectroscopy which employs low-energy ions as the primary excitation agent. Further, the revival of interest in a fusion nuclear power programme makes the study of the interaction of particle beams with refractory b.c.c. metals very important as these materials are strong candidates as first wall materials for fusion reactors and as fuel cladding material for fast breeder reactors.

Although there is little doubt that the study of the depth and precise nature of the damage is important

† A review of most cleaning techniques has been made by Roberts (1963) and includes a section on ion bombardment.

very little work has been done because a precise description of these events occurs at the atomic level and hence their nature is as yet imperfectly understood.

Depth of damage measurements have been obtained by MacDonald and Hameman (1966) for low-energy argon ion bombardment in germanium using a very indirect method. Ibrahim and Bashara (1972(a) and 1972(b)) have attempted to characterise lattice damage occurring in silicon using ellipsometry and Bellina and Farnsworth (1971) have attempted the same in tungsten and molybdenum using LEED. However, none of these techniques possess a sensitivity comparable to that of the field-ion microscope i.e. on the atomic scale.

Many of the previous investigations of low-energy ion bombardment using the field-ion microscope have not considered subsurface events, but have been confined to the surface only. Thus, many of these studies have not been able to distinguish between bombardment events and contamination adsorption effects.

In the present investigation an ion flux sufficient to cause considerable surface and subsurface damage has been used. Precautions have been taken against possible contamination and by utilising the ability of the field-ion microscope to examine the specimen substructure by controlled field-evaporation, a layer by layer account of the damage caused to a tungsten emitter has been obtained. Experiments have been conducted on tungsten targets using, helium, neon, argon and xenon ions in the energy regime (100-1000)eV. An attempt has been

made to correlate these results with information found using the techniques mentioned above and also the gas release experiments carried out by the research groups of Kornelsen and Carter.

6.3. Processes involved in low-energy radiation damage

In this section, a brief outline will be given of some of the processes involved when a low-energy ion is incident on the crystal lattice. More detailed accounts are available, for example, the books of Thompson (1969), Carter and Colligan (1968) and Nelson (1968). Review articles are also available, including Grant and Carter (1967), Dearnaley (1969) and Venables (1970).

For ion energies below 1 keV it is generally assumed that the collision events are two body events and that the colliding atoms can be treated as hard spheres. The hard sphere approximation breaks down at higher energies and various other parameters must be taken into account (Lindhard, Scharff and Schiott (1963)). Hagstrum (1954) has shown that an ion incident on a metal surface is neutralised by an Auger emission process. Hence all the collisions are considered to be between an incident atom and the substrate lattice atoms.

6.3.1. The production of defects

Low-energy radiation damage in the crystal lattice can be described in terms of some simple models and these may be used to calculate the amount of damage caused during the attenuation of the incident ion energy. When the incident atom initially makes contact with the

substrate surface, it dissipates a fraction of its energy in what is termed the primary collision event. This event causes a secondary cascade of atomic collisions which may cause the displacement of some of the surrounding atoms. At low incident ion energies, this primary event may take place at or near the surface and may cause the ejection of some surface atoms. This phenomenon is known as sputtering. Alternatively, the primary energy may be transferred hundreds of Ångstroms from the position of the primary event by means of collision sequences. Some of these basic processes are illustrated in figure 6.1.

The most simple damage mechanism between an energetic atom and the crystal lattice is the displacement of an atom from a normal lattice site into an interstitial position, hence forming a Frenkel pair. A certain energy is required for the formation of Frenkel pair and it is termed the displacement energy E_d and is usually of the order of 25eV. Usually the recoiling primary atom possesses sufficient energy to cause a cascade of secondary displacements, but if the energy of the particle falls below $2E_d$, then the primary atom may simply replace the displaced atom producing no net displacement. Therefore the mean number of Frenkel pairs produced per incident ion $\gamma(E)$ increases from zero at $E=E_d$ to unity at $E=2E_d$. Kinchin and Pease (1955) proposed a simple model of atomic displacements assuming hard sphere collisions and showed that:

$$\gamma(E) = \frac{E}{2E_d} \quad \text{for } E \geq 2E_d \qquad \ldots\ldots(6.1)$$

Snyder and Neufield (1955) then corrected for the energy E_d which is transferred to the lattice at each

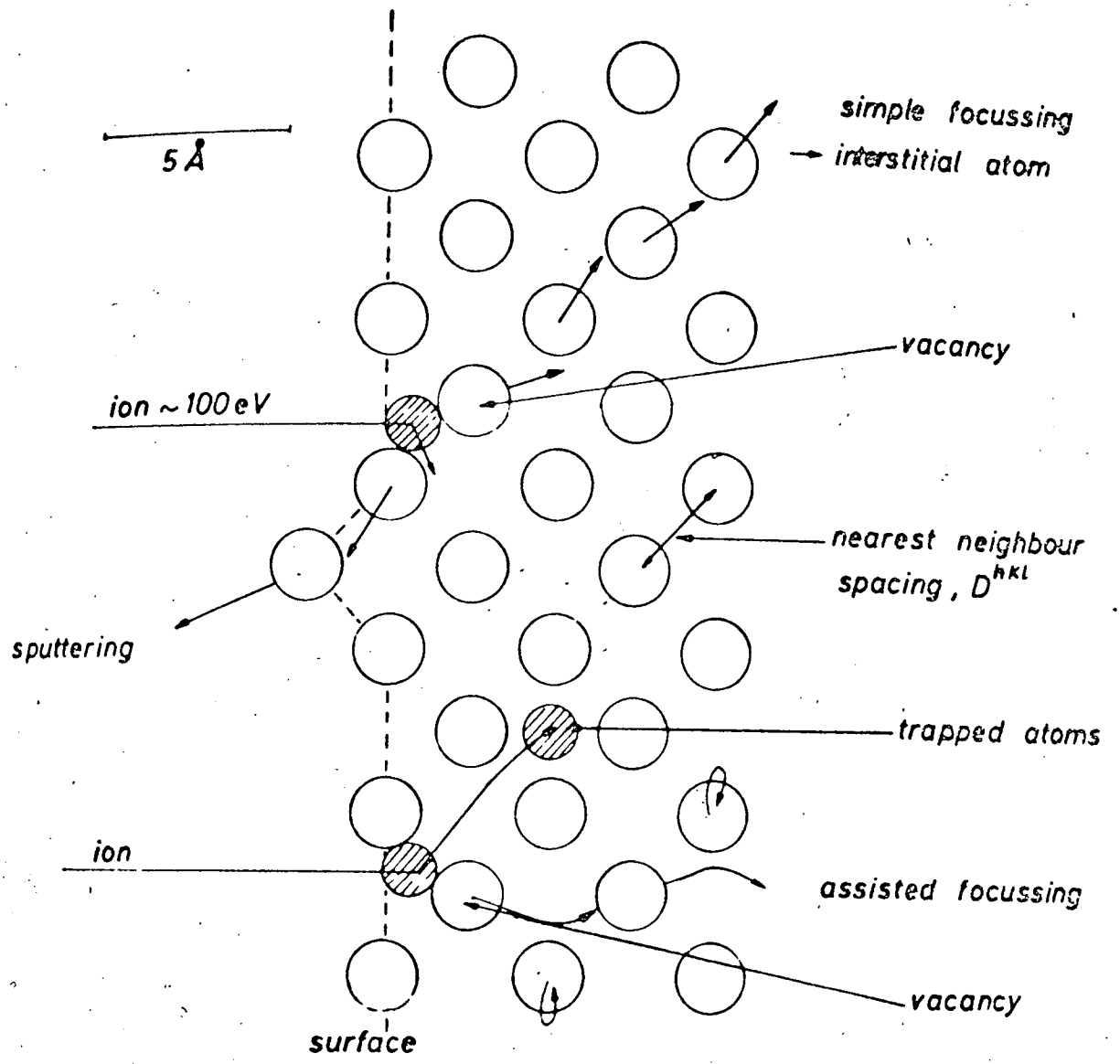

Figure 6.1 Atomic scale collision processes occurring in low-energy ion bombardment. (Venables (1970)).

displacement and by considering the relative number of replacement and displacement collisions found:

$$\gamma(E) = 0.35 \frac{E}{E_d} \qquad \ldots\ldots(6.2)$$

These equations assume that the mass of the incident atom M_1 and the mass of the substrate atom M_2 are equal. If this is not the case then the energy actually transferred E_T to the lattice must replace the incident ion energy E.

Thus: $$E_T = \frac{4M_1M_2}{(M_1+M_2)^2} E \qquad \ldots\ldots(6.3)$$

6.3.2. Factors affecting the range and distribution of damage

The Kinchin and Pease theory outlined above takes no account of the crystallinity of the bombarded substrate. Once the high degree of order exhibited by the lattice is considered, effects emerge that are highly significant to the range and distribution of damage. These effects are known as channelling and the focussed collision sequence.

Robinson and Oen (1963), using computer simulations, found that incident atoms should penetrate along the open channels found between close packed rows of atoms. Hence because <110> rows are closest packed, the <110> channels would be most favourable. Figure 6.2 is a view along such a channel with the incident atom penetrating deep into the crystal. Nelson and Thompson (1963) demonstrated the effect by firing a 75keV proton beam at a gold crystal 3500Å in thickness, and by rotating the crystal found the transmitted current increased whenever there was incidence along the <110> direction.

Figure 6.2 An illustration of the channelling process in crystals.

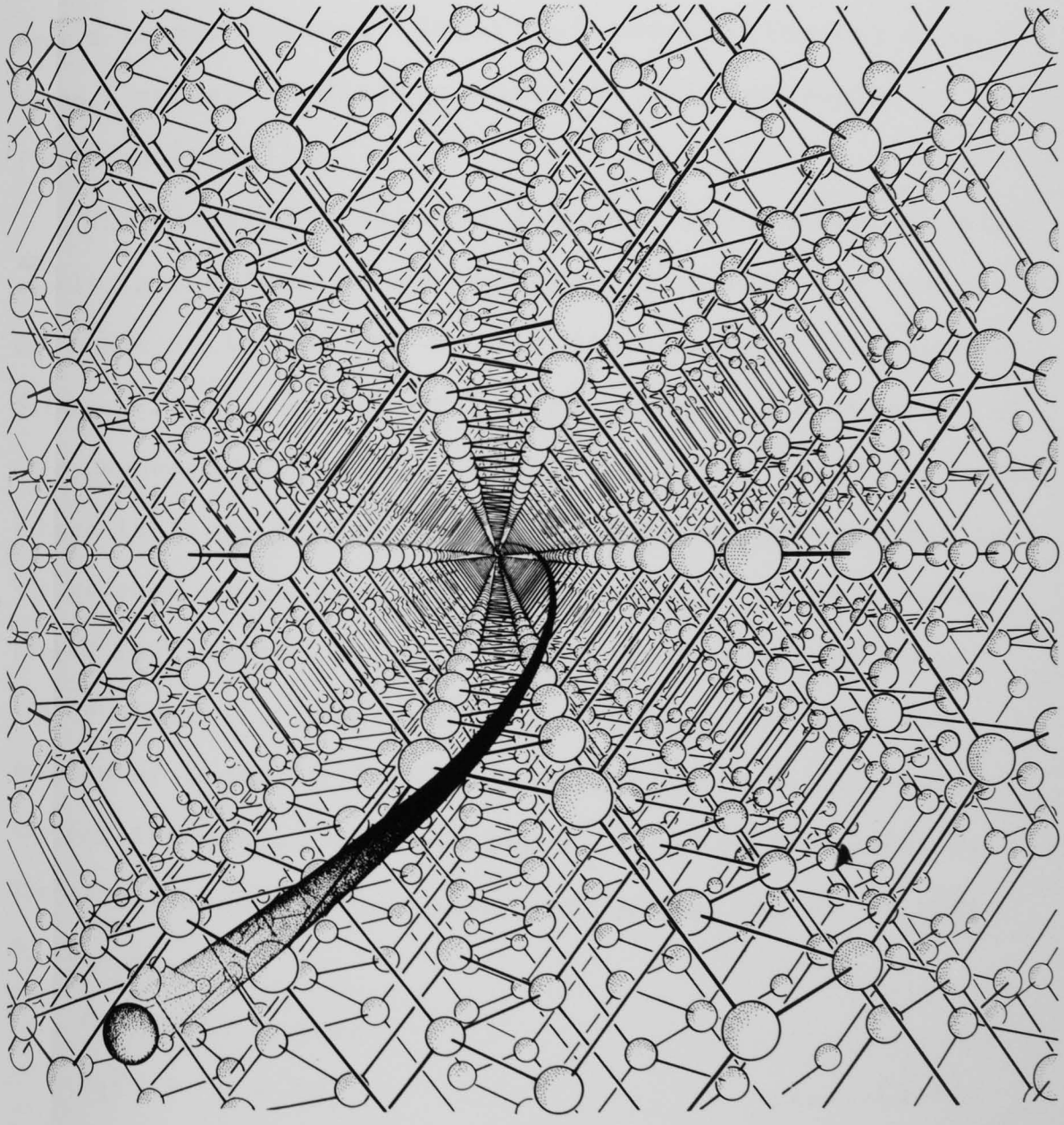

Although channelling occurs most favourably along the <110> direction, it can also occur in any of the low index directions. Channelling reduces the average number of displaced atoms, for while the atom is channelled it is unable to cause atomic displacements. However, long range channelling does spread the damage over a larger volume. Imperfect channelling may also cause a number of displacements to a large depth (Thompson (1969)).

The focussed collision sequence phenomenon may also result in the long range transfer of energy and matter and hence influence the atomic displacement distribution. Silsbee (1957), was the first to predict the presence of this phenomenon. At low energies the radius of the hard sphere is large and momentum may only be transferred to the nearest neighbour. In the situation where a close packed row exists, a chain of collisions may be propagated along it. Consider the collision between two spheres of radius R (see figure 6.3), with a separation D, the collision occurs when atom A_1 reaches the point P. The second atom A_2 then moves off along PA_2 at an angle θ_2 to A_1A_2.

For small angles:-

$$A_1P = D - 2R \qquad \ldots\ldots(6.4)$$

and $$\theta_1 (D-2R)\theta_1 = -2R\theta_2 \qquad \ldots\ldots(6.5)$$

defining a focussing parameter f where $f = -(\theta_2/\theta_1)$

$$f = \frac{D}{2R} - 1 \qquad \ldots\ldots(6.6)$$

Therefore $D > 4R$ for $f > 1$ and $|\theta_1| < |\theta_2|$

$D < 4R$ for $f < 1$ and $|\theta_1| > |\theta_2|$

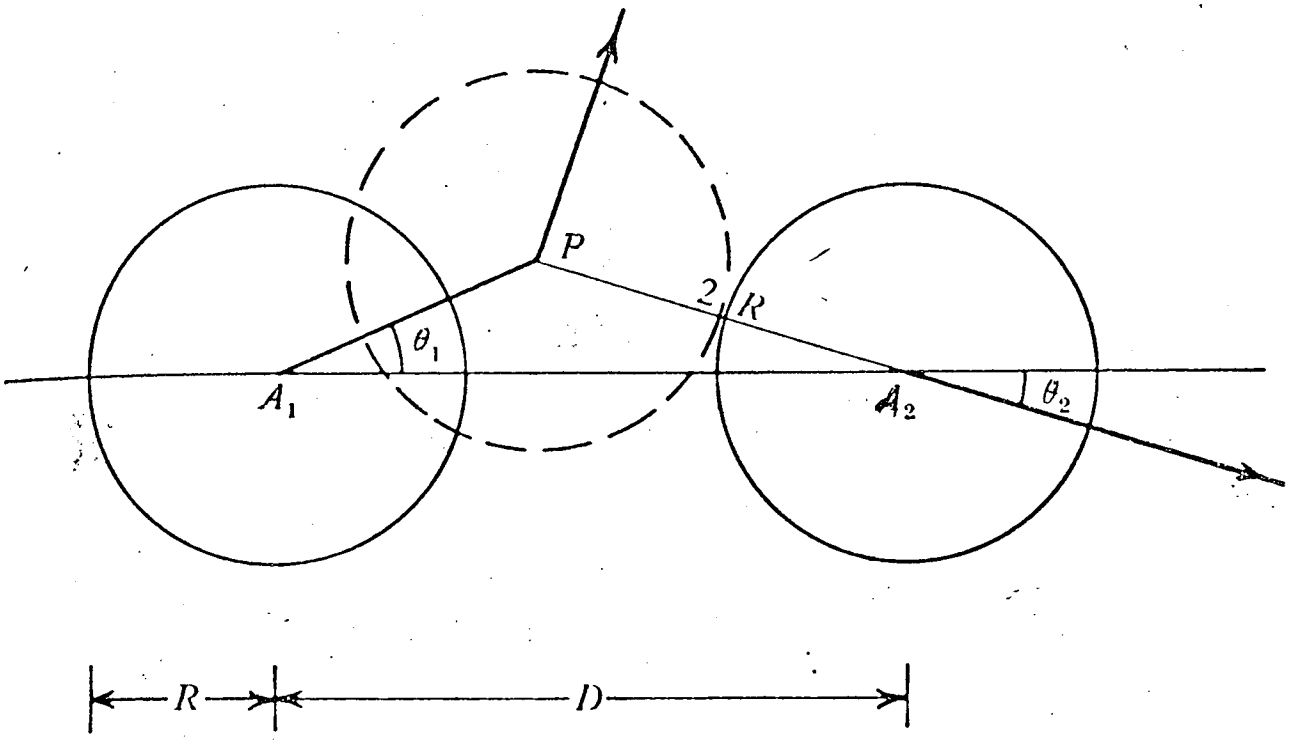

Figure 6.3 The simple focussing process (Thompson (1969)).

If there is an equally spaced row of atoms:

$$\theta_n = (-f)^n \theta_1 = (1 - \frac{D}{2R})^n \theta_1 \quad \ldots\ldots(6.7)$$

so that if $D > 4R$ and $f > 1$, θ_n will diverge and eventually an atom will not collide with its neighbour in the row. If $D < 4R$ and $f < 1$, θ_n converges to zero and hence the momentum transfer is perfectly efficient.

The focussed collision sequence is not only able to transfer energy, but also atoms, in replacement collision sequences where an interstitial atom is produced a long way from the primary collision. The collision sequence phenomenon has been investigated by many authors, for example Thompson (1969) and extensive theoretical treatments are available.

Both the focussing energy E_f^{hkl} and the replacement energy E_r^{hkl} determine the range of these sequences. For instance simple focussing along close packed directions takes place for initial energies in the range $E_r^{hkl} < E < E_f^{hkl}$. Assisted focussing also occurs in directions such as <110> for b.c.c. metals. The range of both simple focussing and assisted focussing depends on lattice vibration (and hence temperature) and on the distribution of defects.

6.4 The range of low-energy inert gas ions in tungsten

Ions incident at a metal target surface with low energies (<1keV) are neutralised a short distance (about 5Å) from the metal surface. Thus, entry into the target subsurface must be in the atomic state and hence at these energies electronic stopping effects become negligible.

Some of the ions incident on the target surface may be neutralised, then reflected, or may penetrate and then be reflected by the second atomic layer. The various processes involved in the penetration of low-

energy inert gas ions have been studied using computer techniques. For instance, Erents and Carter (1968), Pryde, Smith and Carter (1971) and Smith and Carter (1972). These investigations have underlined the complexity of the situation, but as a general rule they conclude that the ability of an ion to penetrate into the target sub-surface increases rapidly with increasing ion energy, and also, penetration at a particular energy may vary with the crystallographic plane approached, (Smith and Carter (1972)). In qualitative terms the hard sphere collision diameter decreases logarithmically as the incident ion energy increases, hence the crystal lattice structure will appear more porous with increasing ion energy.

Few theoretical or experimental results are available concerning the range of low-energy ions. Lindhard and Scharff (1961) have used energy transfer considerations employing an interaction potential of the Thomas-Fermi type to derive a relationship for the range, R, in terms of a number of parameters including the respective masses of the incident and target atoms. It was shown that the range was approximately proportional to the incident ion energy E. By using the approximate relationship:-

$$P = 3.06E \qquad .....(6.8)$$

where P is the reduced range and E the reduced energy, Erents (1967) has calculated the average ranges for all the inert gas ions in tungsten. These values are reproduced in table (6.1). It must be remembered that these values were calculated for polycrystalline tungsten and that

TABLE 6.1

The theoretical range of low-energy inert gas ions in tungsten (after Erents (1967)).

Energy	100eV	500eV	1keV	2keV
He^+	98Å	490Å	980Å	1960Å
Ne^+	4.5Å	22.6Å	45.2Å	90.4Å
A^+	1.5Å	7.3Å	14.6Å	29.2Å
Kr^+	C.45Å	2.26Å	4.52Å	9.04Å
Xe^+	C.23Å	1.17Å	2.34Å	4.7Å

the Lindhard and Scharff theory takes no account of the crystalline nature of the target. Hence channelling effects which will tend to elongate the range will not be accounted for. Further, Carter, Grant and Whitton (1968) consider that at low energies, a better interaction potential than that of the Thomas-Fermi type exists in the form of a suitable power potential. Experimental range data found using an electrolytic peeling technique on the depth distribution of embedded radioactive atoms has been found to be much deeper. For example, for 0.5keV Xe^+ bombardment of a (110) single crystal, 99% of the Xe^+ ions came to rest in a tungsten layer approximately 7.5Å deep; the experiments being conducted at room temperature (Kornelsen et al (1964)). These results will be compared with values obtained using the field-ion microscope, later in this chapter.

6.5 Difficulties associated with the investigation of low-energy radiation damage using the field-ion microscope

The field-ion microscope has been used extensively in the investigation of radiation damage. Work prior to 1969 has been reviewed by Ralph (1968) and Ralph and Hudson (1969). Most of these investigations and those made more recently have been made using high energy incident radiation; very little work has been done on low-energy ion bombardment. However the high energy work has revealed many pitfalls and has pointed out the experimental and interpretational difficulties involved especially with regard to the interpretation of point defect contrast.

6.5.1. Experimental difficulties

All the difficulties in radiation damage studies using the field-ion microscope have been linked either directly or indirectly with contamination. This is a serious problem because the field-ion microscope image is sensitive to a single contaminant atom and even at background pressures of 10^{-8} Torr, a monolayer coverage is achieved in approximately 100 seconds, assuming unit sticking probability. Hence pressures better than 10^{-9} Torr are obligatory. These pressures may be obtained using a U.H.V. field-ion microscope of the type described in chapter 1. Few radiation damage investigations have been conducted in such a vacuum and hence confusion has arisen between the contrast exhibited on the surface by contaminant atoms and interstitial atoms. Notable exceptions here however, are the investigations of Scanlan, Styris and Seidman (1971(a)(b)) (and subsequent experiments of the Cornell group†) and Cranstoun, Browning and Pyke (1973). The latter experimental arrangement is the one on which the present study is based.

More often, however, the problem of contamination is overcome by leaving the applied field on the specimen. Hence contaminant atoms are ionised before they reach the specimen just as in the case of the imaging gas. This method does have serious drawbacks. Not only will the applied electric field (whose value changes rapidly from region to region) affect the ion trajectory, but also the negative hydrostatic pressure on the specimen produces a 3% elastic increase in the lattice volume (Rendulic and Müller (1967)). Further, the effect of

† These were high energy experiments and the first 30 atomic layers were disregarded. A review of the work up to 1973 has been made by Seidman (1973).

the applied field on the diffusivity of interstitials particularly at subsurface sites which offer easy relaxation must be considered.

6.5.2. Difficulties in the interpretation of point defects

The power of the field-ion microscope as a technique for atomic structural examination lies in its ability to resolve each atom in the specimen surface. This capability suggests that the technique would be eminently suitable in the study of point defects and hence for a quantitative investigation of radiation damage processes. However, one should always be aware of the high concentration of surface artefacts possibly caused by the rigorous imaging conditions. Although vacant sites may represent genuine vacancies and bright spots indicate the position of interstitials, considerable care must be taken to distinguish between these and artefact point defects. In some cases this is not possible.

Many of the previous investigations of radiation damage (usually high energy) have attempted a semi-quantitative analysis on the atomic scale involving both vacancy and interstitial counting. Considerable effort has been put into the counting of vacancies and in tungsten specimens the {211} plane edges have been considered the most suitable region for such counts. Even so, the number of vacancies counted has been found to be extremely subjective even though the number of artefacts in tungsten is considered to be low (Bowkett and Smith (1970)). The counting of individual vacancies has been shown to be even more unsatisfactory in iridium where large numbers of artefact vacancies are known to

exist. In fact, Fortes and Ralph (1966) found that a neutron dose of 10^{13} n.v.t. produced a vacancy population indistinguishable from the normal residual artefact population. Recent radiation damage studies have been concerned with vacancy clusters whose characterisation is a little less ambiguous (Hudson and Ralph (1972)), Wilson and Seidman (1973). However, the present author feels that even a semi-quantitative analysis of vacancy clusters is too ambitious and that possibly the optimum level is that of the atomic layer and only then under certain stringent conditions.

6.5.2.1. Surface vacancy contrast

Artefact vacancies occur in a variety of situations. The simplest case is the occurance of a phosphor screen dead spot (this has not affected the present study as a channel plate image intensifier has been used). This artefact is not difficult to find as it usually occurs in a non-normal lattice position. Further, it is impervious to field evaporation. However, far more serious artefacts do occur on the specimen surface and Page and Ralph (1973) have followed Balluffi et al (1970) to propose some possible mechanisms of artefact surface vacancy formation in pure metals the most important of these are listed below.

a) the most serious artefact vacancy is that caused by the imaging conditions used in the field-ion microscope. Müller (1970) has calculated that the field stress during helium field-ion microscopy is equivalent to a negative hydrostatic pressure of 10^{11} dynes/cm but considers this value to be insufficient to cause artefact vacancies.

This view is not supported by Page and Ralph (1973) who have produced convincing numerical evidence in support of their argument.

b) the second mechanism is rather uncertain and only seems to occur when helium-neon imaging gas mixtures are used. This phenomenon has been reported by Ast and Seidman (1970) when imaging gold and Nishikawa and Müller (1964) who have suggested that the neon is adsorbed on the specimen surface and hence acts as an intermediate collision partner.

c) the most common mechanism of vacancy artefact formation appears to be that of field induced chemical etching. Surface vacancies have been shown to appear when adsorbates such as nitrogen and water vapour have been removed by field evaporation (Mulson and Müller (1963)). This mechanism may be avoided provided that the experiments are conducted in situ in a U.H.V. field-ion microscope ensuring that the specimen is thoroughly outgassed. However, Turner et al (1973) using the FIM atom-probe have discovered that small amounts of hydrogen are responsible for producing vacancy artefacts, even in UHV conditions.

Several other mechanisms have been considered, one particularly novel approach was that of Müller (1968) who suggested the possibility of radiation damage occurring when negative ions are attracted to the specimen, the negative ions being released by the imaging device when hit by image gas ions. However, this mode of surface vacancy artefact formation is not considered to be very important.

6.5.2.2. Interstitial contrast

The point imperfection in which an atom occupies an abnormal lattice position is termed an interstitial. In ion bombardment two types of interstitial may be encountered.

1) The first type involves the repositioning of a normal substrate lattice atom due to an atomic collision event, this is termed a self interstitial atom (S.I.A.).

2) Secondly, an inert gas atom may be trapped in a vacant lattice site or an interstitial position and in each case may cause sufficient local lattice distortion to produce S.I.A.s in the surrounding lattice.

In the field-ion microscope image, the interstitial atom is generally characterised by a bright spot (Müller (1960)). Sinha and Müller (1964) were responsible for the conventional view that an extra bright spot was caused by an S.I.A. positioned one atomic layer beneath the surface. This interpretation has since been adopted by many authors, for instance, Bowkett and Ralph (1969) and Attardo and Galligan (1966). However, in what is part of the most detailed, rigorous and expensive programme to investigate the precise nature of S.I.A. contrast in field-ion microscope images, Seidman and Lie (1972) have reviewed and extended the existing ideas on interstitial contrast. In this investigation these authors have concluded that an extra bright spot may be caused by an S.I.A. several atomic layers beneath the surface. Further, the S.I.A. need not be characterised by an extra bright spot, but in certain situations

may also be characterised by a bright spot in a normal lattice position. Also, following Brandon (1968) they proposed that S.I.A.s may be preferentially field evaporated leaving vacant lattice site contrast.

Several other effects cause the interpretation of the position and the nature of interstitials, in field-ion microscope specimens, to be approached with caution. Firstly, there exists the zone decoration phenomenon. In tungsten this effect is manifested on the <100> zone by single or multiple rows of bright atom spots marking the edges of {110} net plane edges. These spots are wide and bright, adjacent to the {110} plane, but gradually dim and show normal contrast between the {021} and {031} planes. The precise nature of this contrast is still unknown but Müller (1964) has suggested that these atoms are bound at reduced co-ordination sites and are stabilised against field evaporation by an increased polarisation. On a freshly field evaporated surface it is not too difficult to pick out the zone decoration atoms however, on an ion bombarded surface such as that shown in figure 6.4 they can easily be confused with the bright spot contrast associated with interstitial atoms.

Bright spot contrast may also be exhibited by impurities in the substrate lattice. For instance, Fortes (1968) found a considerable number of bright spots exhibited in iridium which they assigned to an oxygen impurity content. A trapped inert gas atom in tungsten should not produce any contrast itself and on exposure to the surface should be preferentially field

Figure 6.4 An example of a tungsten surface bombarded with 200eV neon ions. The zone decoration bright spots cannot be distinguished from the bright spots introduced by bombardment.

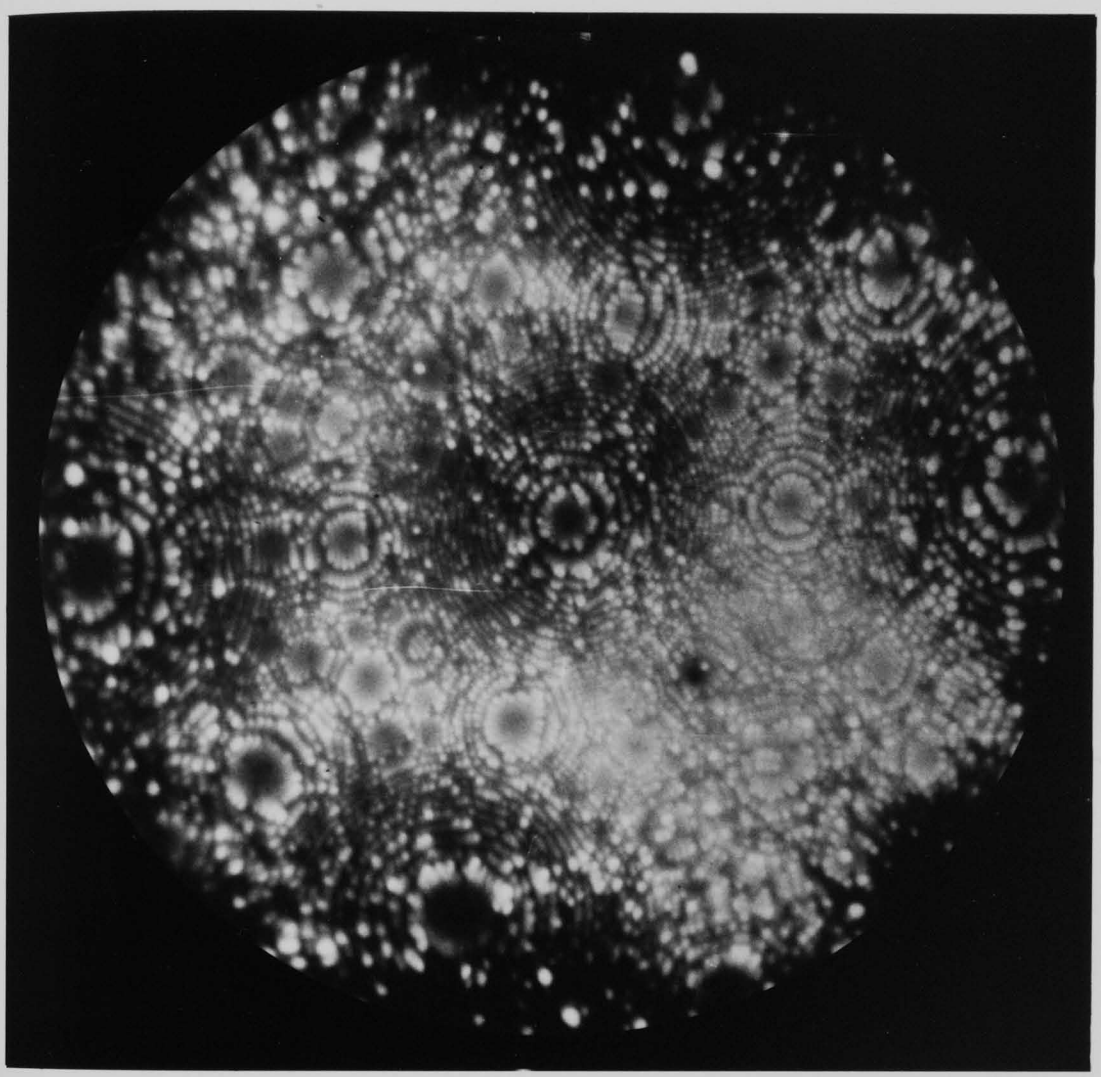

evaporated (Southworth and Ralph (1969)). The theory of Southworth and Ralph would also suggest that in low index plane regions S.I.A.s may be directly imaged provided that they are protected from the field by a large step height and hence do not protrude through the thin shell in the model proposed by Moore (1962).

Another factor which contributes to this rather unsatisfactory picture is the affect of the applied electric field on the interstitial atom. Van Oostrom (1970(b)) and Buswell (1971) have shown that the interaction of the electric field with contaminant can cause surface artefact interstitials, an even more important effect has been found by Sinha and Müller (1964) who found that a proportion of interstitials migrate to the surface under the influence of the electric field. Scanlan, Styris and Seidman (1971(a),(b)) however, have performed control experiments which suggest that this effect is unimportant.

All the above factors reduce confidence in any radiation damage concerned with specific atomic events. Statistically however, meaningful results may be obtained on the scale of an atomic layer provided that the number of interstitials introduced into the lattice is a realistic figure and hence cannot be confused with the resident artefact population.

6.6 Previous field-ion microscope investigations of low-energy ion bombardment

These investigations may be subdivided into two sections according to the experimental arrangement used.

6.6.1 Cathode sputtering

This is the easiest, but least controlled method of ion bombarding field-ion microscope specimens in situ. All that is required is the specimen is used as a field electron emitter in a suitable pressure of the chosen gas. Ions are formed by electron bombardment and are attracted to the specimen which is held at a negative potential, typically of the order of 1-3kV. The ion energy is inhomogenous and depends on the point in space where the ion is formed. The impact direction is another unknown. Investigations utilising this type of ion source have been reported by Müller (1960) and Dranova and Mikhailovski (1970); Vernickel (1966) has used the field emission microscope to study ion bombardment effects induced in this manner. Both Müller (1960) and Dranova and Mikhailovski (1970) observed the formation of dislocations in this way, Müller (1960) has termed these defects "shallow dislocation loops", because they penetrated only 10 to 20 atomic layers. An example of a tungsten specimen bombarded with low-energy He^+ ions displaying contrast typical of these shallow dislocation loops is illustrated in figure 6.5.

The author has conducted several cathode sputtering experiments with a number of gases. Figure 6.6 shows an evaporation sequence caused by argon cathode sputtering with the specimen held at about -0.5kV for ten minutes.

Figure 6.5 'Shallow dislocation loops', interstitials and vacancies caused by helium ion cathode sputtering (Müller (1970)).

1̄10
121
111
011
112
1̄01

Figure 6.6 Examples of the damage caused by cathode sputtering.

(a) A field-ion micrograph of tungsten featuring a grain boundary prior to cathode sputtering with argon ions.
(b) The same tungsten surface after bombardment. The surface is extensively damaged. Note the dark line contrast features.
(c) After the removal of part of a (011) atomic plane by field evaporation; the surface damage is still severe.
(d) Shows the damage at a depth of one (011) plane beneath that depicted in (c). The low index planes are now clearly discernible.
(e) Another (011) atomic layer has been removed.
(f) Depicts the situation after a total of four (011) planes had been field evaporated. A number of 'bright spots' are still evident.

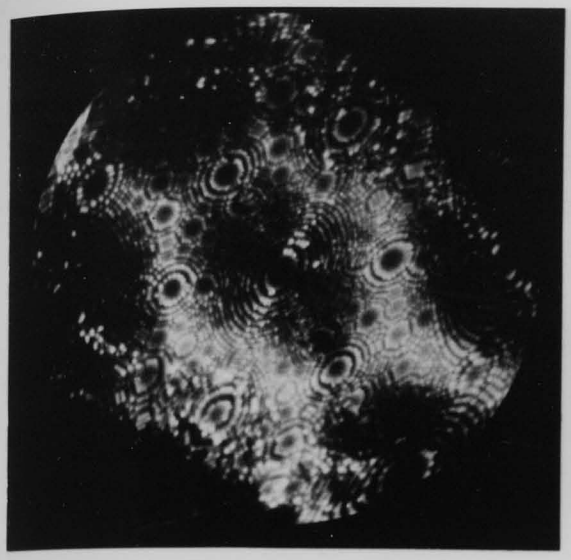

A

B

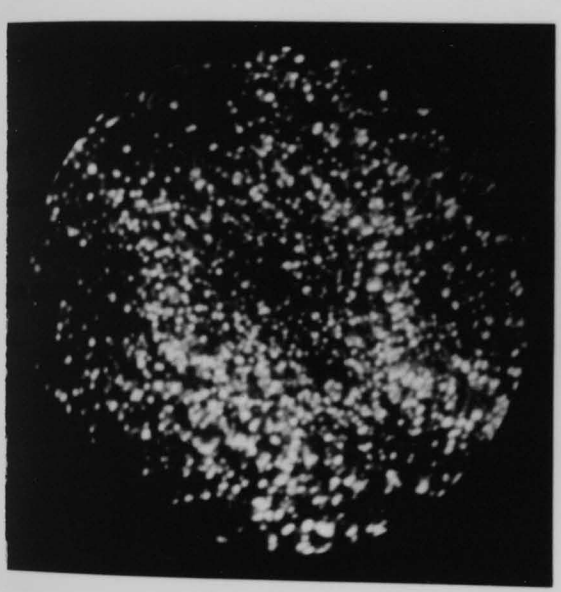

C

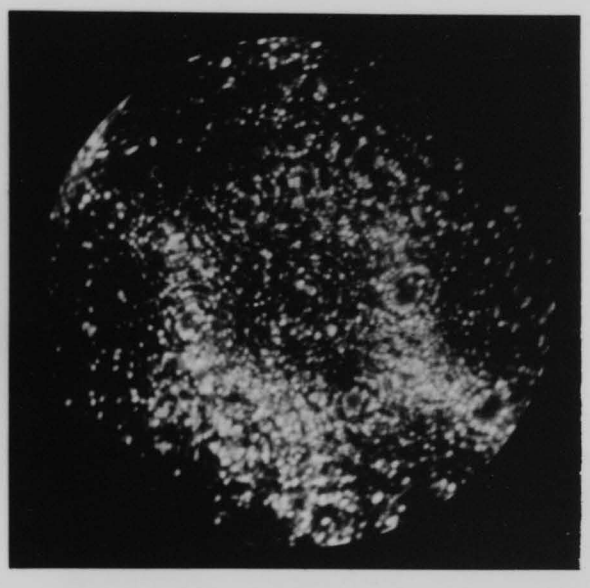

D

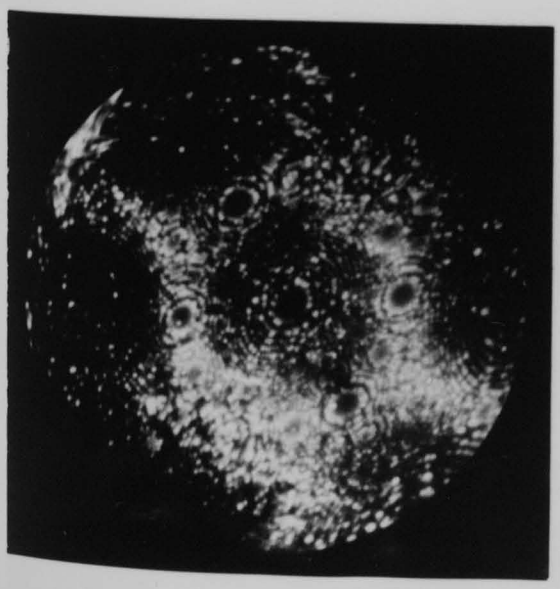

E

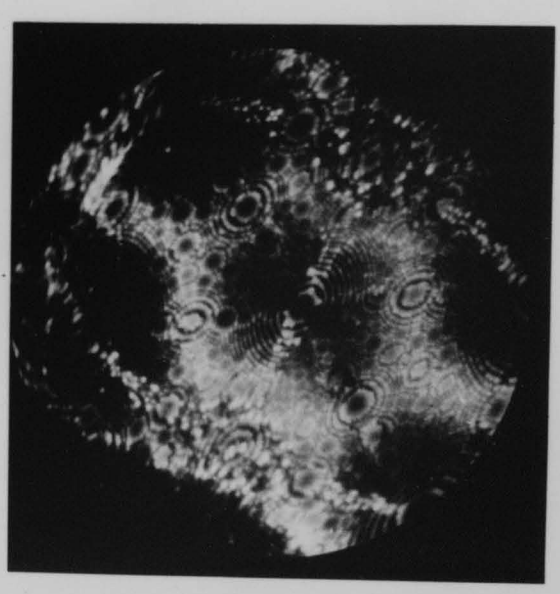

F

Compared with results presented later in the chapter, the depth of damage caused by this type of ion bombardment was shallow, possibly due to a different impact direction.

6.6.2. Experiments utilising an ion gun

The first low-energy experiments of this type were devised by Brandon et al (1963) and Wald (1963) who studied the effect of low-energy (<100eV) argon atoms incident on a tungsten specimens in order to elucidate threshold displacement energies. One possible explanation for their anomalously high preliminary value of 70eV is that as they were operating with "field— on" condtions, it is possible that many of the incident atoms of energy <70eV were ionised before ever reaching the specimen.

Bennette et al (1966) used an axially mounted ion gun to xenon ion bombard tungsten specimens at 77°K with incident ion energies in the range 100eV to 1300eV. These authors came up with the interesting observation that at low energies, more atoms were displacedon the side of the specimen away from the ion beam, than on the side upon which the ion beam was incident. They ascribed this phenomenon to focussed collision sequences running through the <111> direction. The effect was not observed at the higher incident ion energies ($\sim$1300eV). Although this study was conducted using "field-off" conditions in a nominally U.H.V. environment, control experiments revealed the presence of considerable contamination. Controlled field evaporation revealed that the depth of damage caused

by 1300eV Xe^+ ions was about 6 (110) layers and that at 100eV only a single (110) atomic layer was affected.

More recently, Gregov and Lawson (1972) used a similar kind of arrangement to investigate the effects of low-energy (150-450)eV Ar^+ bombardment of tungsten. Their investigation was centred on the production and subsequent interpretation of surface point defects. These experiments were also conducted with "field-off" conditions in a U.H.V. microscope. However, their ion gun delivered only $\sim 10^{-9}$ amps ion current on the specimen and hence they had to wait a considerable length of time for any effect to occur, thus increasing the likelihood of contamination difficulties, (which they indicate existed). Unlike the findings of Bennette et al (1966), these authors found that at low energies the defect density was higher on the side of the specimen closest to the source.

Finally, Cranstoun, Browning and Pyke (1973) have devised an in-situ ion source device which operates similarly to a Bayard-Alpert ionisation gauge. A review of this particular study will not be made here, but references will be found in the subsequent text dealing with a similar experimental arrangement.

6.7 Experimental details

All of the low-energy ion bombardment experiments to be described subsequently were carried out, in situ, in the stainless steel, U.H.V. field-ion microscope which was described in chapter 1. In view of the experience gained by previous experimenters, particular care was taken with contamination and a systematic

procedure was developed to optimise the cleanliness of the specimens and the system. In this way real effects could be distinguished from contamination effects as control experiments showed the latter to be negligible.

All the micrographs presented in this chapter were taken using a Nikon F camera at mark f4 using Kodak Tri-X film. The use of a channel plate intensifying device meant that exposure times were typically 10-12 seconds, using an imaging gas pressure of about 2×10^{-4} Torr. Helium field-ion microscopy was generally used, but helium - 10% neon mixtures were found to be best for high radius specimens as it produced a more even image contrast. Occasionally, neon field-ion microscopy was used, especially when details of the specimen surface were required at comparatively low applied electric fields.

In this section, the ion source is described and information regarding its construction and operating characteristics is provided. In addition, the method designed to reduce the risk of contamination is presented and results of a typical control experiment presented.

6.7.1. The ion source

The ion source employed was similar to that used to sputter clean LEED specimens by Farnsworth et al (1958). This arrangement has been subsequently modified by Cranstoun, Browning and Pyke (1973) for use in an all glass field-ion microscope. Minor development of the source has been necessary to enable this source to be used in the stainless steel field-ion microscope.

6.7.1.1. Description of the ion source

Reference to figure 6.7 will show that the source is basically a Bayard-Alpert ion gauge construction and consists of a filament and a cylindrical grid; the field-ion microscope specimen itself acts as the ion collector. Electrons are generated by thermionic emission from the hot filament and are accelerated towards the grid which is held at a positive potential. The source is filled with the appropriate inert gas, by leaking clean, gettered gas into the system, to a pressure of about 1×10^{-4} Torr. Ions are formed by electron bombardment within the grid region and these are then accelerated to the specimen which is held at earth or a small negative potential with respect to the grid. The ion current at these pressures was typically in the order of 1μA. The ion energy could be varied by changing the potential difference between the grid and the specimen and the ion flux was changed by increasing or decreasing the pressure of inert gas in the system.

Ion sources based on this principle, but incorporating an extractor plate replacing the collector have been reported by many authors (for instance Khan and Schroeer (1971) and Leffel (1970)). It is clear from these authors that this type of ion source can be used to supply ions of up to at least 3keV energy. The present study was only concerned with ion energies in the range (100eV-1000eV). The energy spread of ions using this source is of course very wide, but a significant proportion of the ions have an ion energy

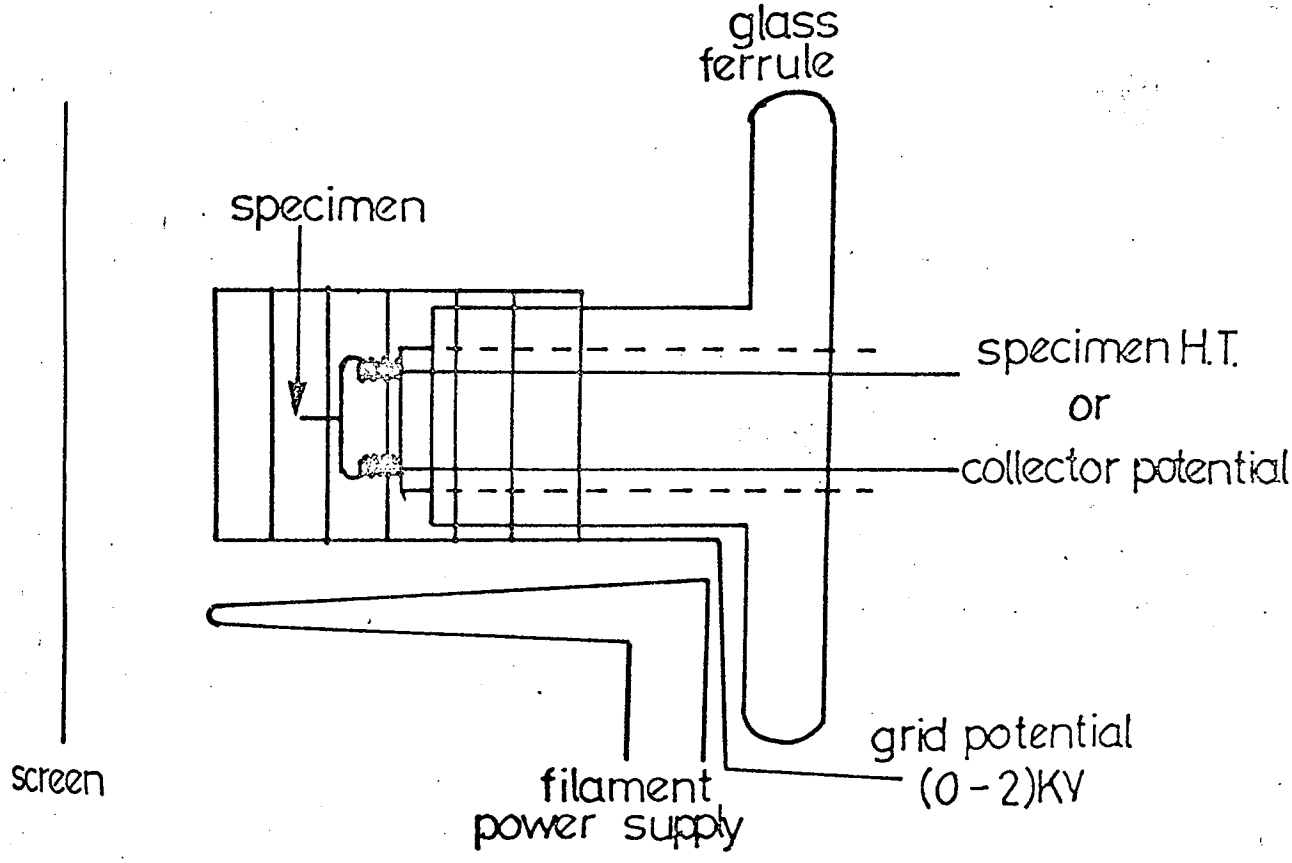

Figure 6.7 A schematic diagram of the ion source.

comparable with that generated by the maximum potential difference between grid and specimen. Hence effects occurring at this high energy edge to the spectrum could be followed. The presence of multiply charged species cannot be discounted, but the proportion of these is felt to be small.

6.7.1.2. Construction of the ion source

Three objectives were in mind when constructing the ion source. The Birmingham U.H.V. field-ion microscope was multifunctional and hence the first requirement was that the ion source must be demountable and as a corollary must be robust. Moreover, in keeping with the U.H.V. environment, the ion source must be clean and able to be outgassed.

6.7.1.2.(a) The grid assembly

The grid assembly consisted of a cylindrical spiral of 0.2mm tungsten wire which was constructed around a 0.25mm Ni frame. All the joints were spot welded. The dimensions of the grid were such that it encompassed the specimen and its associated temperature control wires, and was of a diameter sufficient to clear the heating loop and also not to interfere with the field-ion image. Hence the grid was about 2.5cm in diameter and was approximately 4cm long. Electrical contact with the grid was made via an insulated Ni loop which skirted the specimen holder and which was subsequently joined to a tungsten rod seated into a glass to metal seal. Considerable care was taken to electrically insulate the grid from the microscope and a glass mounting ferrule of the appropriate dimensions was used

in this capacity (see figure 6.7). The glass ferrule made a good sliding fit with the copper cylinder (15mm diameter) which held the specimen iocating pins. The grid was also a good sliding fit with the outside diameter of the ferrule.

In order to remove any small asperities that could cause electrical breakdown and also to prepare the grid for its U.H.V. environment, it was initially electropolished in a strong NaoH solution. Subsequent outgassing was conducted in a similar manner to out-gassing an ionisation gauge, by electron bombardment using the V.I.G.10 ionisation gauge control unit.

6.7.1.2.(b) The filament assembly

The filament was intended to supply electrons to the region within the grid and was simply a V.I.G.10 ion gauge filament (Vacuum Generators Ltd.). It was demountable, although for the period during which the experiments were conducted, it remained a permanent fixture. The filament was mounted via a $1\frac{3}{4}$" ODFC flange on a EFT5 electrical feedthrough. Two stainless steel filament holders were made comprising at one end of a 2BA threaded cylinder to facilitate mounting on the electrical feedthrough and a grub screw arrangement on the other to hold the filament. In this way the filament was mounted 1cm from the grid assembly. This facilitated both the action of the ion source and the insertion and removal of the specimen holder.

6.7.1.3. The electrical circuit

The electrical circuit is illustrated in figure 6.8. Its main features are:-

(a) The grid was supplied using a 15mA, (0-5)kV V.G.MK1, power supply (Vacuum Generators (Electronics) Limited). This power supply was tunable to .1V and has 0.005% drift and 0.25% accuracy. The grid current was adequately measured using an avometer.

(b) The filament was supplied by an Edwards model 1 ion gauge control unit and apart from the heating current was floated at -68V. The power supply enabled a variable grid current to be obtained.

(c) The specimen was connected to earth using the same Edwards ion gauge power supply. The ion current was measured using either a Keithley 602 picoammeter or a Systron donner 7004 multimeter.

6.7.1.4. Operating characteristics of the ion source

The behaviour of the ion source to gas pressure was investigated so that at any given gas pressure, the ion current could be predicted. Hence both the grid current and the ion current were plotted versus varying values of gas pressure, for each of the inert gases used in the study. Figure 6.9 shows the behaviour of the ion current with argon gas pressure monitored at room temperature. The ion current is seen to rise rapidly especially in the pressure region about 10^{-4} Torr, to a value of about $5\frac{1}{2}\mu A$ at 5×10^{-4} Torr. Similar results for He, Ne and Xe were recorded, and the values of ion current at 5×10^{-4} Torr pressure were 3.62μA, 4.26μA and over 10μA respectively.

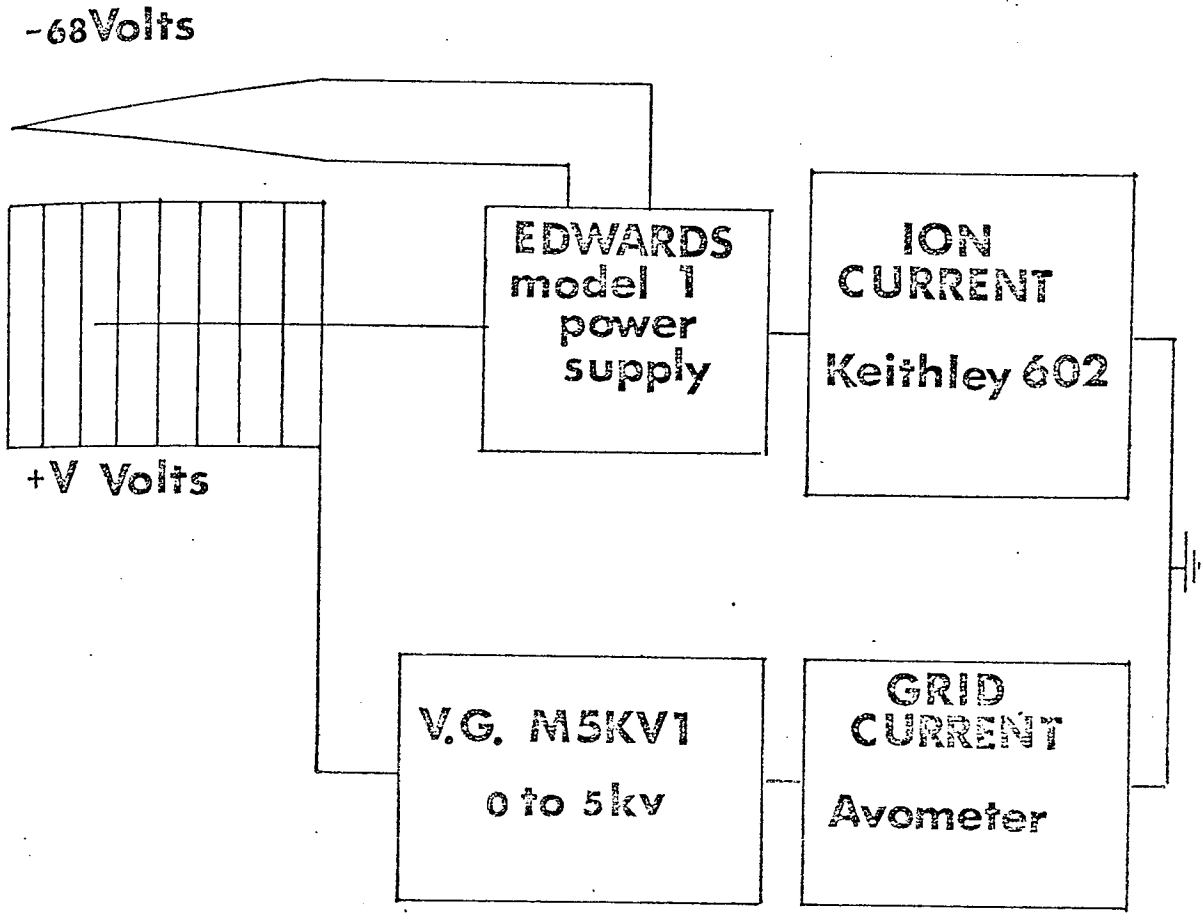

Figure 6.8 A block diagram of the ion source electrical circuit.

Figure 6.9 Operating characteristics of the ion source. The ion current (μA) as a function of argon gas pressure (Torr).

Figure 6.10 The grid current (mA) as a function of gas pressure (Torr).

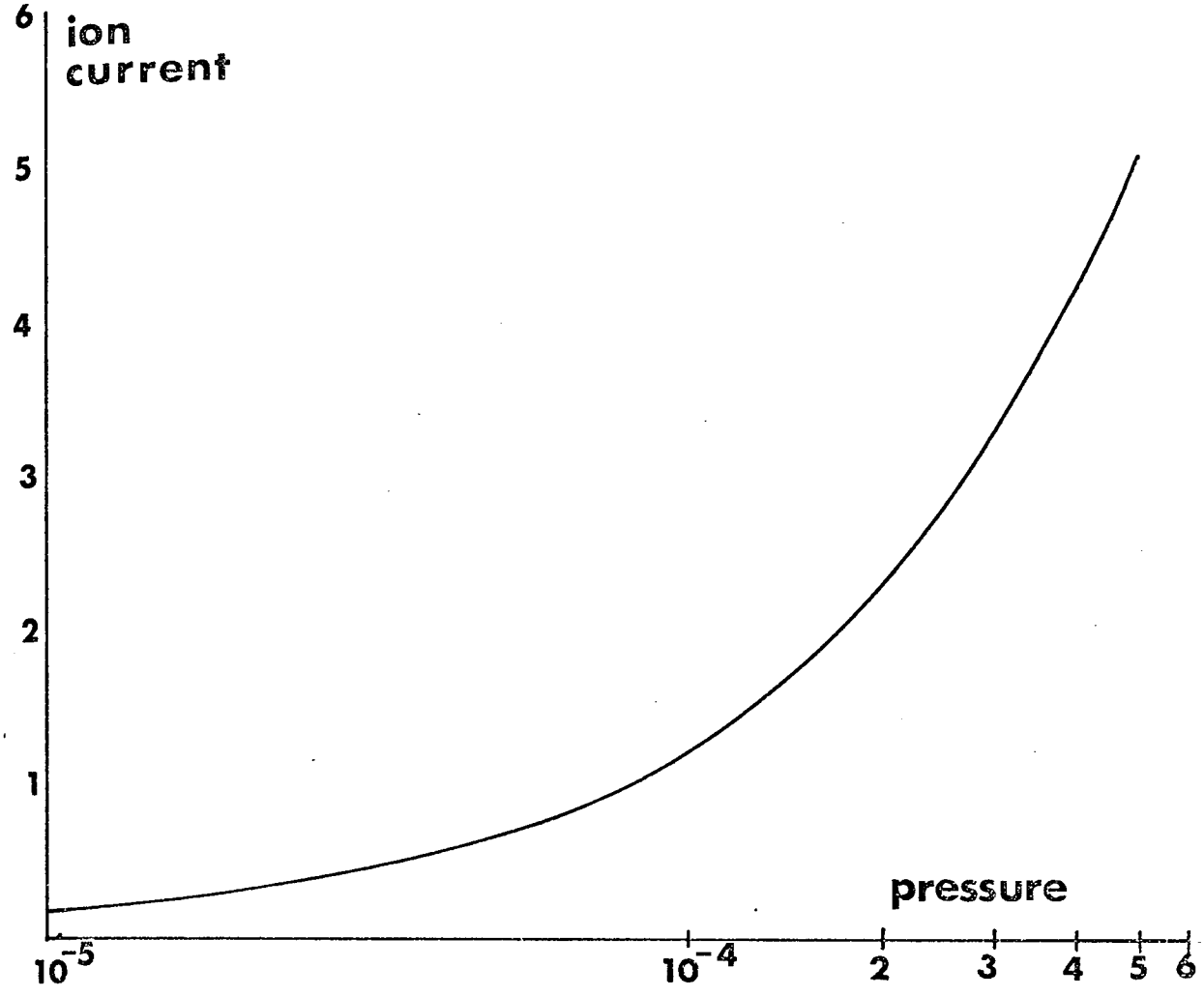
6
ion
current
5
4
3
2
1
pressure
10^{-5}
10^{-4}
2
3
4
5
6

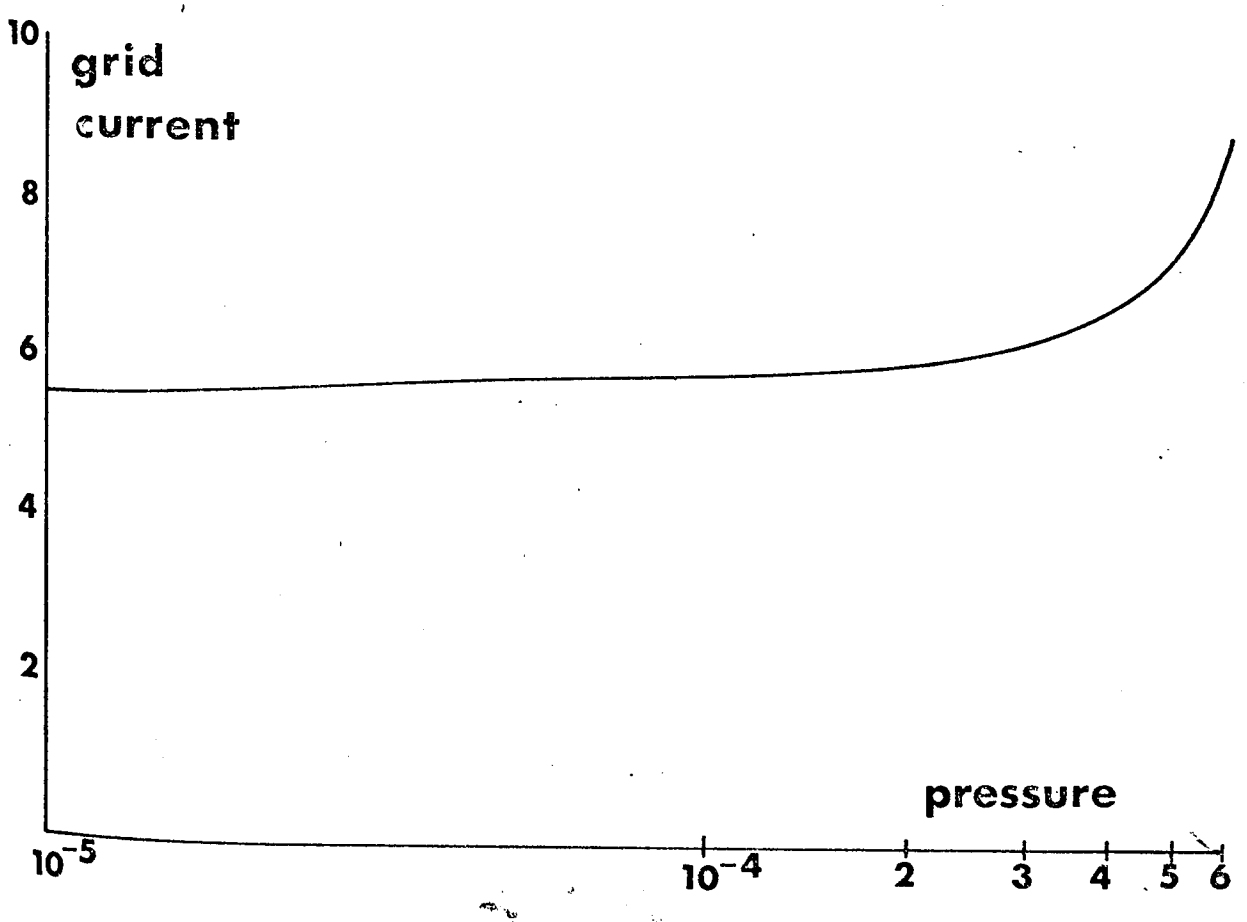
10
grid
current
8
6
4
2
pressure
10^{-5}
10^{-4}
2
3
4
5
6

The variation of grid current with gas pressure was also investigated and figure 6.10 illustrates the results for argon gas. The grid current is seen to be quite steady at about 6mA, but increases rapidly at a pressure value of about 2×10^{-4} Torr to reach about $8\frac{1}{2}$mA at a pressure of 6×10^{-4} Torr. Once again similar results were obtained with the inert gases He, Ne and Xe.

6.7.2. Experimental procedure

Previous sections in this chapter have attempted to underline contamination problems in the field-ion microscope. Although fractions of a monolayer coverage may not make subsequent ion bombardment experiments invalid, because the microscope is sensitive to a single atom of contaminant, interpretation of results is made difficult. Hence, with these factors in mind, a careful experimental procedure was fixed to control background contamination, subsequent control experiments confirmed the success of these precautions.

6.7.2.1. Vacuum technique

Experiments were always conducted in a vacuum of better than 1×10^{-9} Torr. The routine background pressure of the microscope after bakeout was usually about 5×10^{-10} Torr. The specimen was always thoroughly outgassed before and after bakeout using the temperature controller described in Appendix (I). Outgassing of the ion source filament and grid was achieved before any experiment. A titanium sublimation pump was activated in order to remove any active gases in the system and only when this well gettered U.H.V. environment was obtained was an experiment started.

6.7.2.2. Standard ion bombardment experimental procedure

With U.H.V. conditions obtained, the ion species and ion energy were selected and the following routine was then followed.

(a) The first experimental requirement was that of a reference specimen surface. To achieve this, the following routine was carried out. The ion pump was valved off, (see the diagram of the field-ion microscope pumping system in chapter 1) and the diffusion pump was left to pump the system. Prior to the entry of imaging gas, the T.S.P. was fired. Then the grade X imaging gas (usually helium) was leaked into the system through the T.S.P. to remove any active gases.

(b) The specimen was imaged and micrographs obtained of the clean, well-defined field evaporated end form.

(c) Leaving the positive applied electric field on the specimen (hence preventing the adsorption of any active gases in the system), the supply of imaging gas was terminated. When the pressure had fallen to approximately 1×10^{-9} Torr, the T.S.P. was reactivated and the chosen bombarding species (also gradeX) was admitted to the system to the required pressure.

(d) The positive applied field on the specimen was then removed and the ion source activated immediately for the time period required (usually 10 minutes).

(e) The specimen was then re-imaged.

6.7.2.3. Control experiments

Control experiments were conducted with each ion species to gauge the success of the methodology employed above. Typical results of these are figures 6.11(a),(b) (c) and (d). Figure 6.11(a) shows the tungsten field ion microscope surface at stage (b), the central (110) plane is at maximum size. One or two bright spots are evident on close examination of the micrograph, but the surface is essentially clean. The specimen was imaged in helium gas at an applied potential of 8.5kV. The requirements of stage (c) were then followed and a pressure of $9x10^{-10}$ Torr was achieved (compared with the background pressure of $7x10^{-10}$ Torr) before the positive H.T. was disconnected from the specimen. Then neon gas was leaked into the system to a pressure of $1x10^{-4}$ Torr and left in the system for ten minutes following the requirements of stage (d). Upon re-imaging (stage e) in helium figure 6.11(b) depicts the surface at 7.5kV and figure 6.11(c) at BIV (8.5kV), although new bright spots possibly corresponding to adsorbed contaminant atoms can be seen, these amount to less than one hundreth of a monolayer. Subsequent ion bombardment experiments will show that the specimen surface is severely damaged and that the amount of contamination depicted in figures 6.11(b) and 6.11(c) is negligible.

Subsequent removal of one (011) atomic layer reveals a contaminant free surface comparable to the reference surface (figure 6.11(d)). From these results and results obtained with each of the ion species used, it could

Figure 6.11 Contamination control experiments.

(a) The uncontaminated tungsten reference surface prior to exposure to 1×10^{-4} Torr of neon for ten minutes.
(b) The same surface after exposure to the gas at zero applied field. Few extra bright spots are discernible. This image corresponded to an applied specimen potential of 7.5 kV.
(c) The same surface as (b) but at a specimen potential of 8.5 kV.
(d) After removal of one (011) atomic layer.

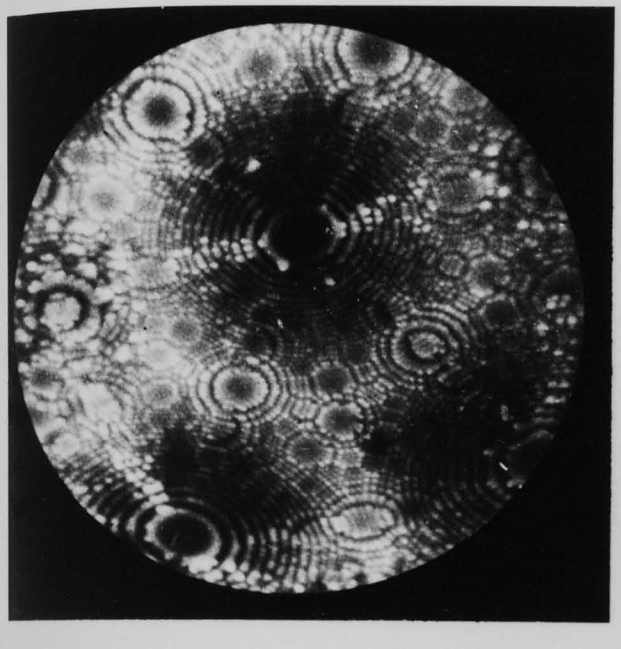

A

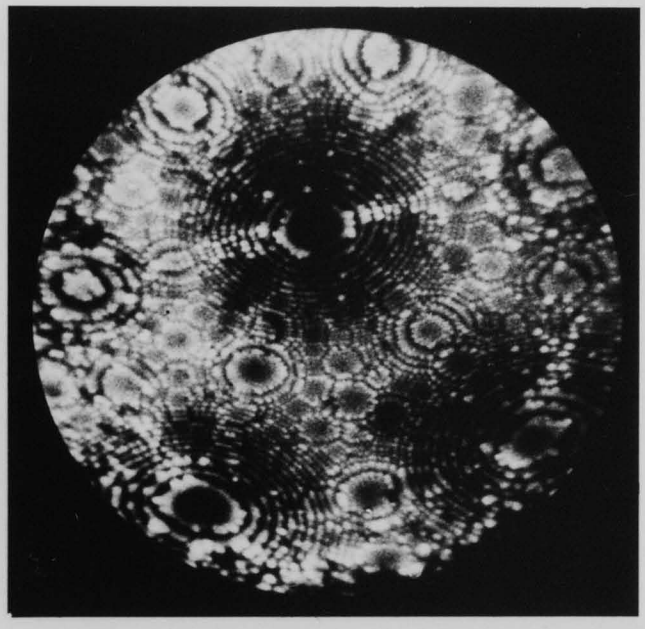

B

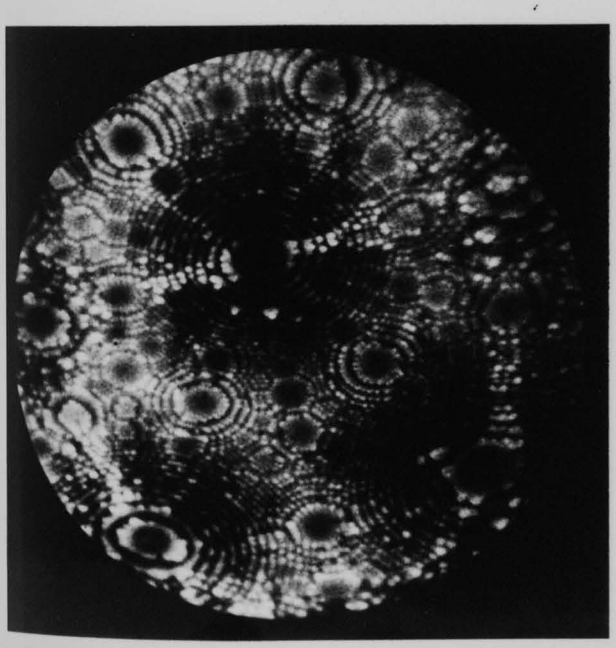

C

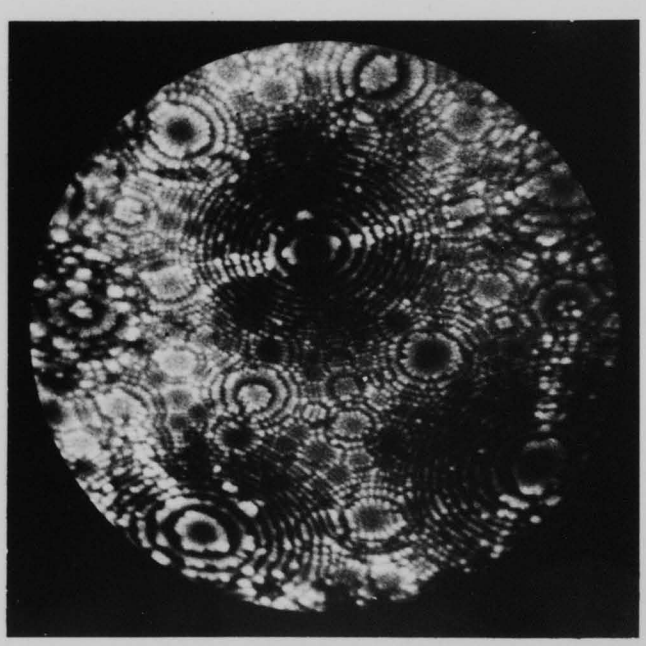

D

be assumed that the surface re-arrangement evident after a bombardment sequence was certainly a real affect and not a result of contamination.

6.8 Results

In this section the results of the various ion bombardment experiments on (011) orientated tungsten are presented. The experiments were conducted using four inert gas species (Xe, Ar, Ne and He) and the results are arranged in order of decreasing atomic weight. In each case an experiment at a particular energy value is discussed in detail. Ion energies of 132eV, 332eV, 532eV, 732eV and 932eV were used for each ion species and occasionally additional experiments were carried out at other ion energy values. All the experiments were performed using an ion current (received by the specimen and its supports) of 1.2μA for a period of ten minutes. This corresponds to an ion current density in the order of $1\mu A/cm^2$. This value was chosen as the most appropriate after a trial series of experiments had indicated that this ion flux was the most suitable. For xenon ion bombardment this value was sufficient to severely damage the first surface layer, but not to the extent that it was completely unrecognisable when field evaporating. Hence, the number of atomic layers removed by field evaporation could still be monitored.

Imaging of the specimen after each bombardment sequence was conducted at a temperature of 78°K (liquid nitrogen).

The routine devised to minimise contamination effects (described in the previous section), was followed at all times. Further, at the start of each ion bombardment experiment it was ensured that the (011) plane on the specimen surface was at maximum size, i.e. its phase factor was zero. Following bombardment, the specimen substructure was carefully revealed usually by removing half (011) atomic plane layers, by field evaporation. Sometimes at features of special interest an atom by atom profile was obtained. Micrographs were taken at each stage.

6.8.1. Xenon ion bombardment

From table 6.2 it can be seen that xenon is the heaviest of the inert gases used in this study and perhaps more significantly, it is the largest. Xenon ion bombardment damage was particularly characterised by the large amount of surface disorder produced. In fact, at all ion energies the first atomic layer was rendered almost amorphous - an effect reported to occur in silicon by Davidson (1972). The distribution of damage appears to follow an exponential type of decay. While the surface atomic layer was almost amorphous, crystallinity was largely restored in the second atomic layer. Defects could always be found at a depth greater than that defined as a mean depth of damage.

The type of damage found usually consisted of large numbers of interstitial atoms and vacancies possibly associated with Frenkel pair production caused by atomic collision events. Scanlan, Styris and Seidman (1971(a),(b)) have shown that at 78°K long

range migration of tungsten self-interstitial atoms certainly takes place unless trapped at impurity sites. Also there was evidence for a large number of interstitial atoms unassociated with vacancy contrast, particularly at large depths beneath the initially bombarded surface. These defects may be interpreted as a result of embedded xenon ions, indeed Surmeijer, Boers and Begemann (1970) have suggested that during sputtering, surface layers actually become an alloy containing 10-30% inert gas particles. Also xenon was particularly prone to show the dark line contrast feature first observed by Cranstoun, Browning and Pyke (1973). Figure 6.12(a) depicts a typical example of this contrast effect. This micrograph was taken after 932eV xenon ion bombardment and shows the surface after three (011) layers had been removed. The contrast does not appear to be developed by a line defect nor is it appearance convincingly planar. Other examples of this type of defect occurring at various ion energies of inert gas ion bombardment are illustrated in figures 6.13(a),(b),(c) and (d).

The defects usually appeared in the first four atomic layers beneath the bombarded surface and were commonly associated with a disordered surface. It was noticed that the contrast was more prevalent at higher energies, but was also manifested at low energies. The contrast shown in figure 6.12(a) shows the bright-dark contrast usually associated with slip (Page and Ralph (1970)), although this is not always a feature. Certainly, the defect is not extensive; figure 6.12(b), shows the same surface

Figure 6.12 (a) An example of a dark line contrast feature found after one (011) atomic layer had been removed from a tungsten surface bombarded with 932 eV xenon ions.

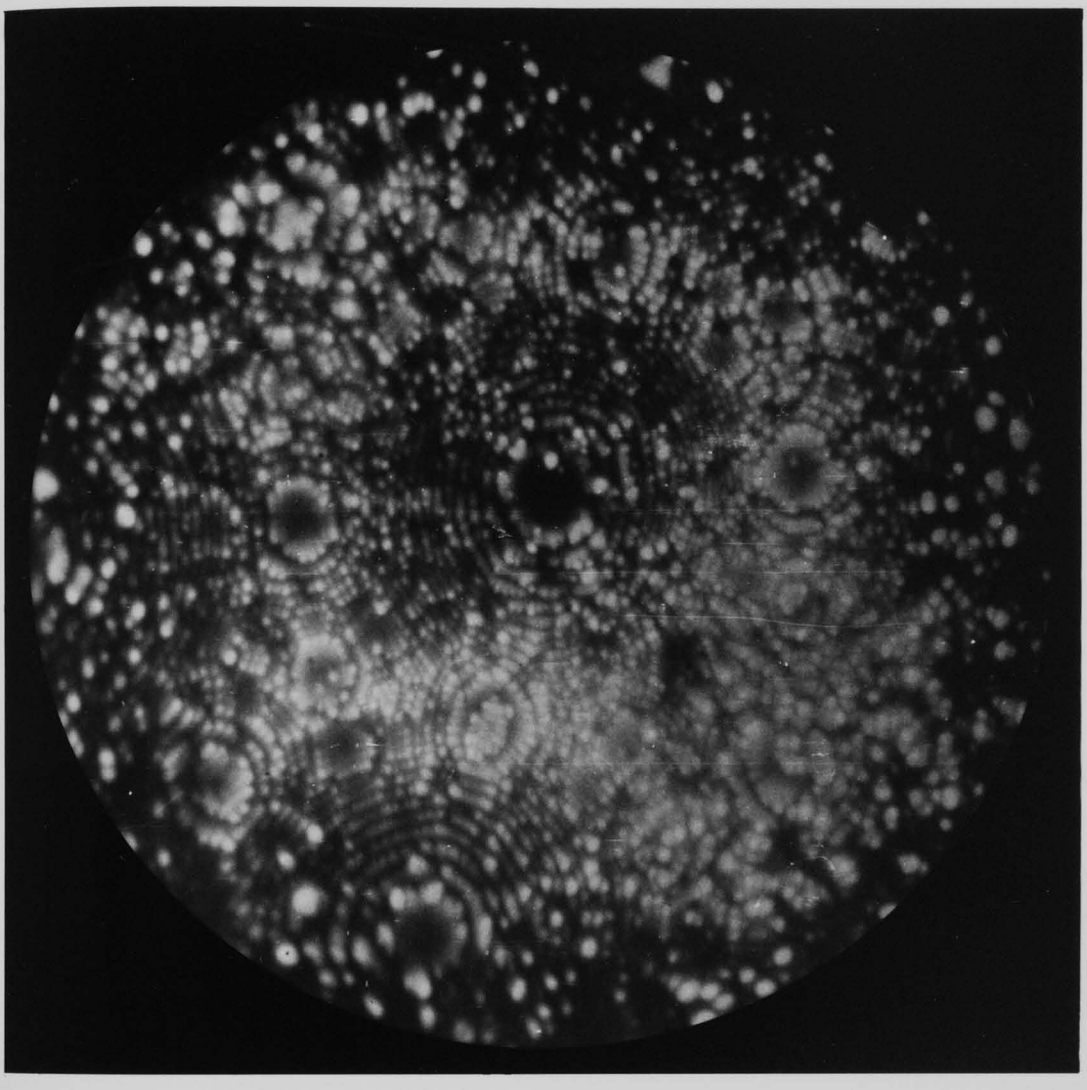

Figure 6.12 (b) The same tungsten emitter as that shown in (a), but about $\frac{1}{5}$ (011) layer had been removed.

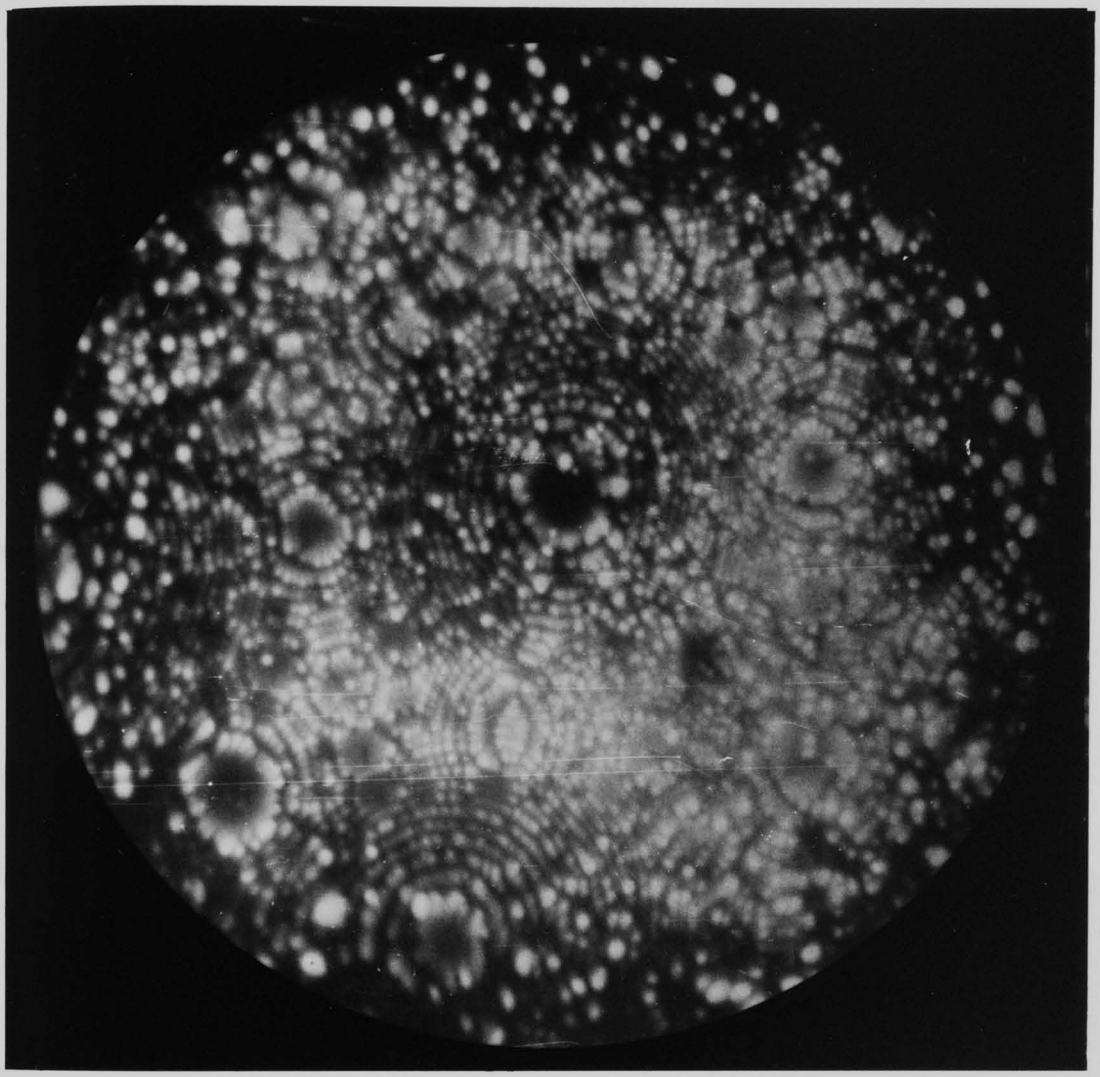

after about 1/5th of a (110) plane had been field evaporated. The contrast is now not visible. All these points tend to suggest that these are slip traces. Unfortunately these defects were almost always associated with severe lattice distortions and in the particular case of xenon ion bombardment a unambiguous planar trace was never obtained. Allied to this is the very unsatisfactory state of planar trace analysis of field-ion microscope images (Fortes (1971(b)), no positive identification of possible slip planes can be obtained. However, Cranstoun, Browning and Pyke (1973) have attempted an analysis of these features produced by argon ion bombardment and have concluded that although a significant proportion correspond to known slip planes, some of the traces cannot correspond to any of the known operative slip planes in tungsten. A fuller discussion will be delayed until section 6.8.2. where an unambiguous planar trace was obtained after argon ion bombardment.

Examination of the (121) plane rings in figure 6.13(b) also reveals the occurence of a vacancy cluster about 25Å diameter. Xenon ion bombardment, in particular, was responsible for the production of this particular type of defect particularly at the higher energies.

The results of a particular experiment will now be discussed in detail, showing the state of the lattice at different levels in the sub-structure. In the case of xenon we shall choose a 732eV bombardment sequence. Figure 6.14(a)- this figure illustrates the undamaged tungsten reference surface of radius, R=520Å, prior to

Figure 6.13 Examples of dark line contrast defects, (some of the more notable traces have been arrowed).

(a) $4\frac{1}{2}$ (011) planes had been removed after 932 argon ion bombardment.
(b) $1\frac{1}{2}$ (011) planes had been removed after 600eV neon ion bombardment.
(c) $2\frac{1}{2}$ (011) planes had been removed after 332eV neon ion bombardment.
(d) $3\frac{1}{2}$ (011) planes had been removed after 932eV xenon ion bombardment.

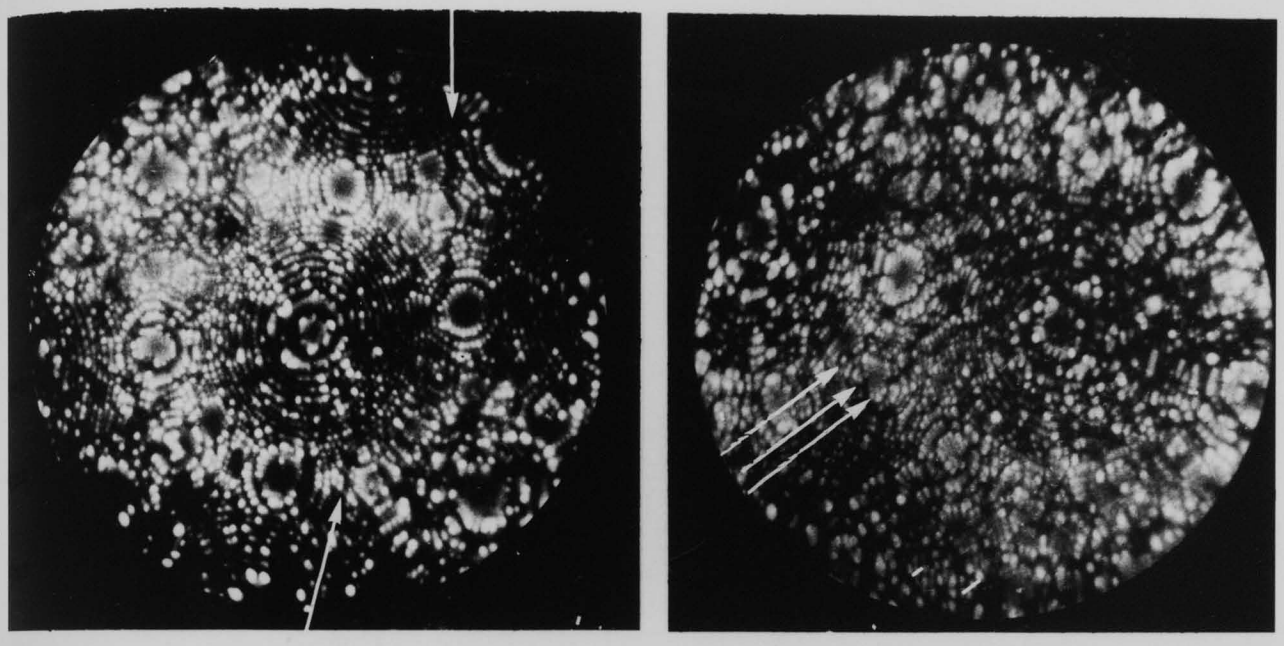

(a) (b)

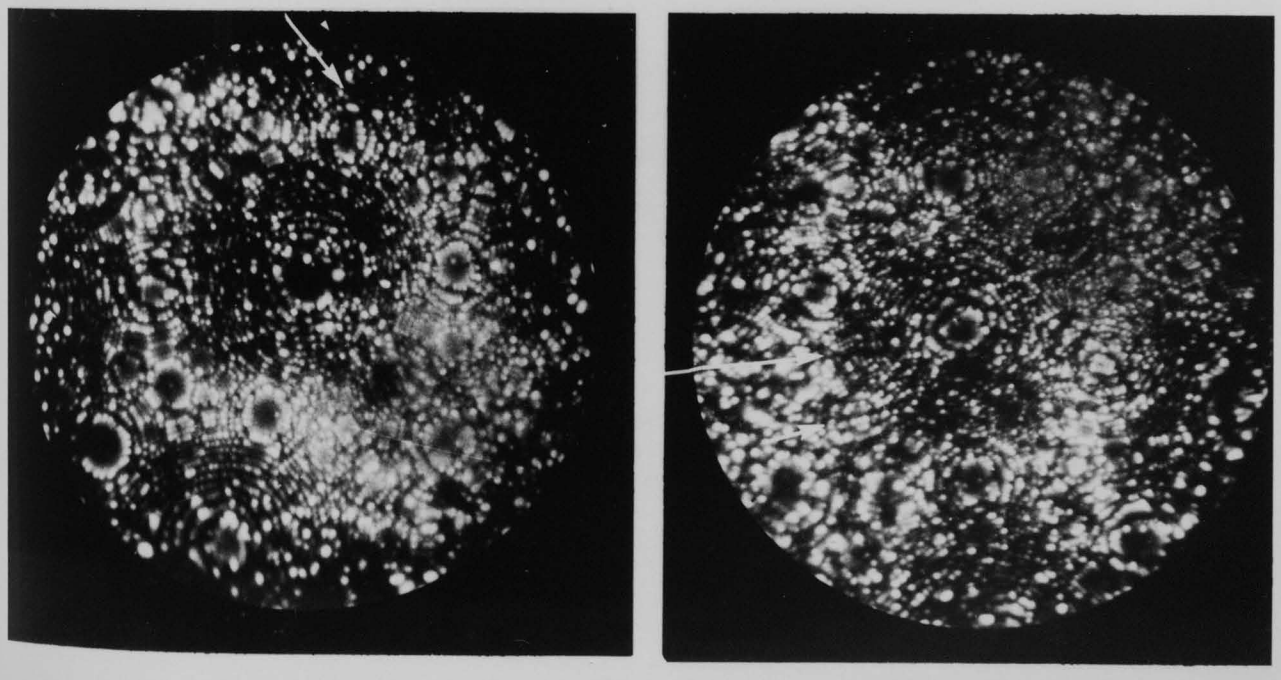

(c) (d)

ion bombardment. The central (011) plane is at maximum size (little remains from the previous atomic layer). This micrograph was taken with 8.7kV applied to the specimen and imaged in 2×10^{-4} Torr of helium. The (013) plane is unfortunately masked by the channel plate 'dead spot', this feature is common to all the micrographs in this sequence.

Figure 6.14(b) - This figure depicts the surface after xenon ion bombardment (ion energy equal to 732eV) following the procedure outlined in section 6.72. Consistent with other xenon ion bombardment experiments the surface displays no crystallinity with what at first sight appears to be a random array of spots. Closer inspection not only reveals the dark streak contrast first pointed out by Cranstoun, Browning and Pyke (1973) but also depicts straight lines of bright spots. However, because the image is in a rather disordered state these may simply be the result of a fortuitous integration by the eye. Lines of interstitials have been observed in a number of specimens after irradiation. One possible explanation is that they may be associated with some form of focussed collision sequence - a tracking phenomenon. Another interpretation may be that these atoms have been arranged in a fashion similar to the one dimensional clusters of atoms that Tice and Bassett (1973) have found when investigating vapour deposition of material onto field-ion specimens. Although no crystallinity is observable on figure 6.14(b), on slow field evaporation, the collapsing rings were distinguishable.

Figure 6.14(c) - Figure 6.14(c) illustrates the lattice damage after the top (011) layer had been removed. The damage is extensive and takes the form of numerous interstitials and vacancies. Several vacancy and interstitial clusters also appear to exist. A possible dark line contrast feature is also evident and intersects the (112) plane. However, the crystallography of the image is largely restored.

Figure 6.14(d) - At this stage two (011) layers have been removed. There is a marked reduction in the number of bright spots and vacancies, but there appears to be an increased number of the dark line contrast feature defects. A notable example splits the ($\bar{1}$12) plane, although they exist in most regions of the image particularly in the region between the ($\bar{1}$21) and (121) planes.

Figure 6.14(e) - This micrograph depicts the surface after a total of five (011) planes have been removed. The surface is now far more ordered. Interstitial contrast is still evident especially around the (011) plane edges and vacancy contrast is particularly rife in the (211) type plane edges. One notable aspect occurs if figure 6.14(e) is compared with figure 6.14(a) the reference surface. In particular, compare the width of the zone decoration metastable sites, the zone decoration appears to be much wider in the case of figure 6.14(e). Possible explanations of this may be that this region contains sites of reduced threshold displacement energy or it may just be that those sites which are on (011) plane edges are protected from the

Figure 6.14 A tungsten emitter bombarded with 732 eV xenon ions.

(a) The undamaged reference surface.
(b) The same surface after ion bombardment.
(c) After one (011) atomic layers had been removed.
(d) After two (011) atomic layers had been removed.
(e) After five (011) atomic layers had been removed.
(f) After seven (011) atomic layers had been removed.

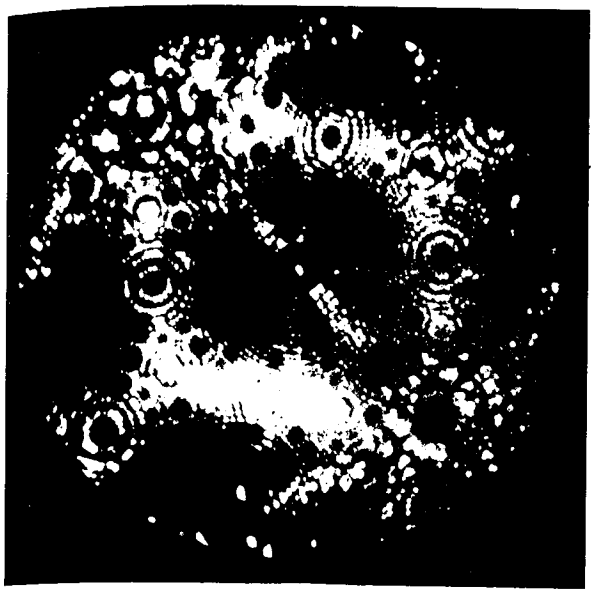

A

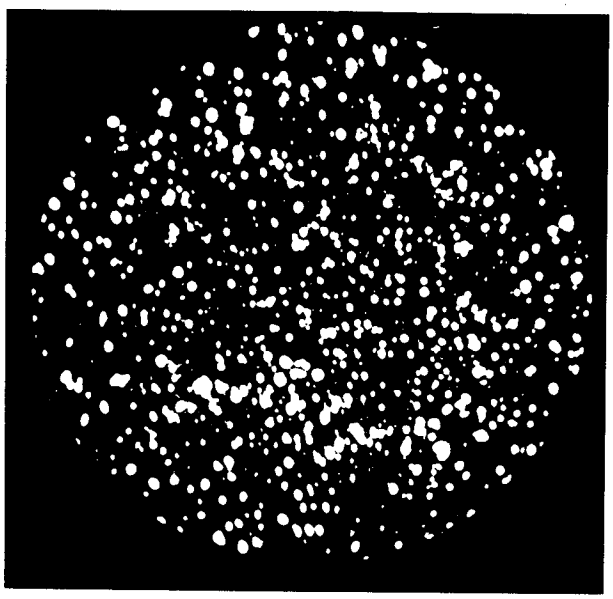

B

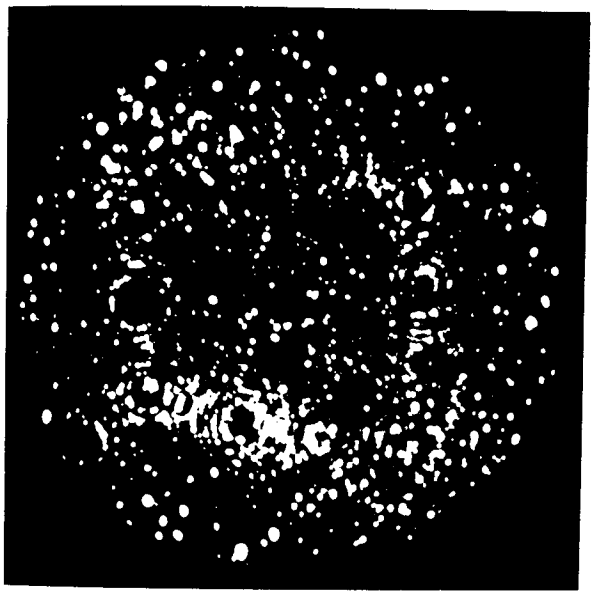

C

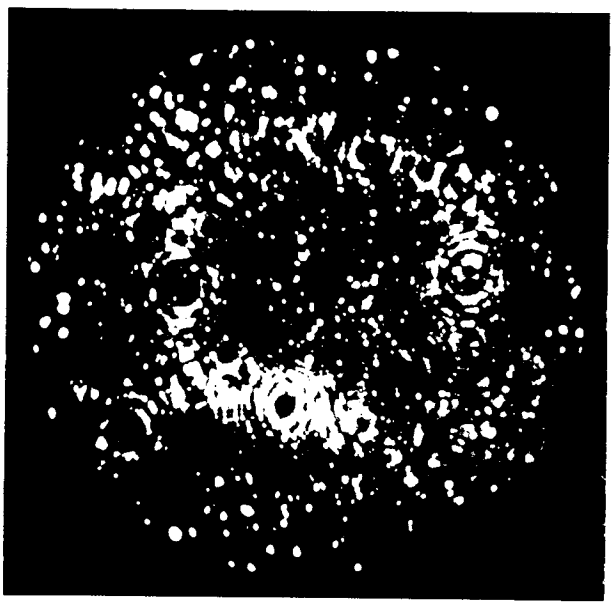

D

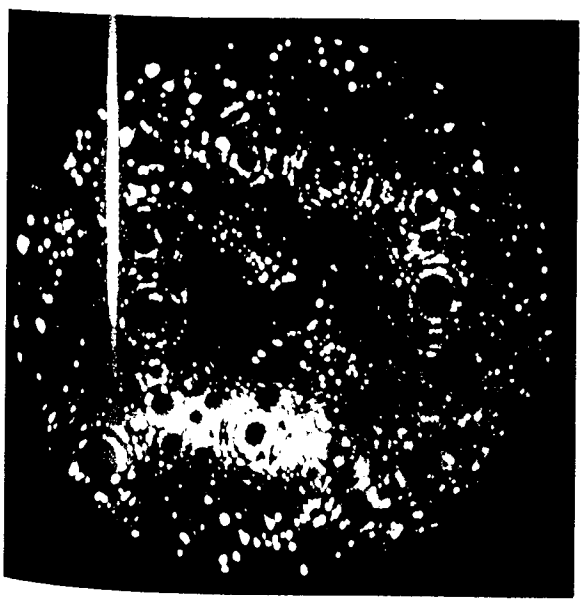

E

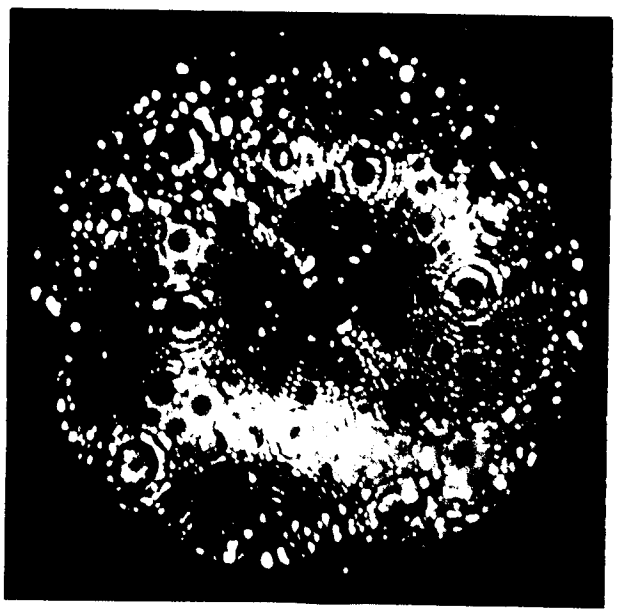

F

field and hence interstitials sitting within a (011) ledge will image whereas this is not the case with interstitials sitting within ledges of planes of smaller step height. Note the absence of any dark line contrast feature.

Figure 6.14(f) - At this point, a total of seven (011) planes had been removed. Very little damage now remains although a number of bright spots do occur in the (011) plane rings. This surface, however, conforms to an arbitrary definition relating to the depth of damage which is explained later, but merely corresponds to the surface containing less than five bright spots in a $(\bar{1}12)$-$(\bar{1}21)$-(011) region. Hence the depth of damage of 732eV Xe^+ ions is about seven (011) layers.

It is interesting to note that in figures 6.14(e) and (f) although there is a considerable number of "bright spots", there are surprisingly few vacant sites. This mitigates against the interpretation of the "bright spots" as self interstitials (i.e. tungsten atoms) formed by an atomic collision. Indeed, this evidence suggests that at these depths the "bright spot" corresponds to a xenon interstitial position although clearly there is no way in which the two species can properly be distinguished, except by field-ion atom probe work.

Figure 6.14(g) - Not all the damage was removed at a depth of seven (011) layers. Figure 6.14(g) shows the surface after twelve (011) layers had been removed. The damage is light (a few interstitials) and these

Figure 6.14 (g) After twelve (011) layers had been removed.

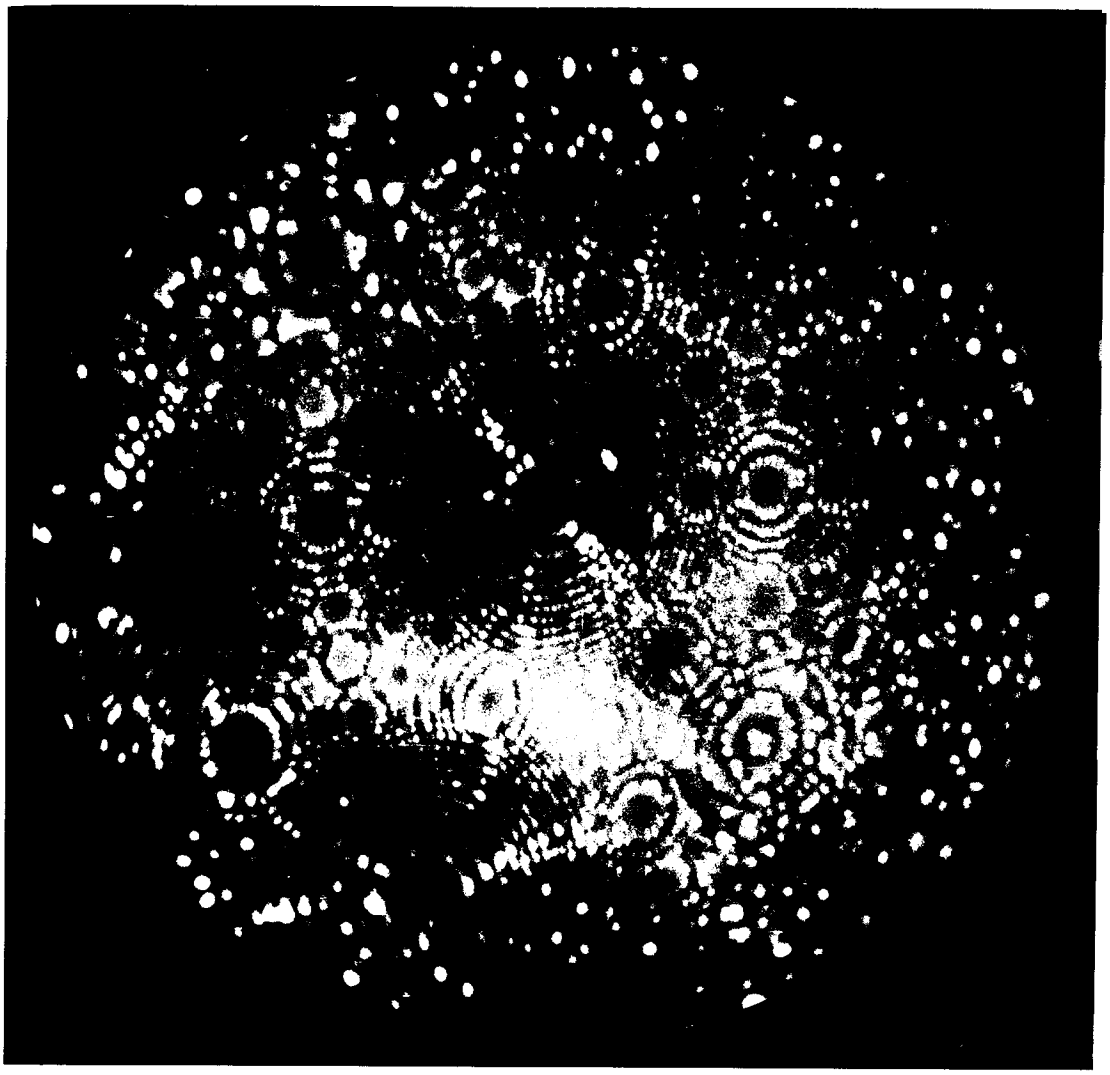

cannot be claimed to have been unambiguously the result of ion bombardment, although interstitials did exist up to this point. It is possible that a replacement sequence or some diffusion process caused the transport of the interstitials, but channelling of Xe is thought to be unlikely.

One surprising feature of xenon ion bombardment of tungsten at low energies was that the depth of damage as defined above at an ion energy of 132eV was four (110) layers. This is certainly not in line with the Lindhard and Scharff theory. A plot of depth of damage for xenon and other ions versus ion energy is plotted in figure 6.21 and from this it can be seen that an approximately linear relationship results. This point will be discussed in more detail in section 6.8.5.

6.8.2. Argon ion bombardment

Argon has an atomic weight of 39.95 a.m.u. and is light compared with xenon (atomic weight 131.30 a.m.u.). In an argon-tungsten collision, equation (6.3) shows that about 58% of the incident argon ion energy is transmitted to the tungsten atom, compared with 99% for xenon.

Argon ion bombardment was carried out at various energies (132eV, 232eV, 332eV, 532eV, 732eV and 932eV) and once again high surface layer damage was characteristic (though not as severe as xenon). Once again the same type of defect distribution was found and although the amount of subsurface damage is comparable to that of xenon, the depth of damage was greater. These points are illustrated in figure 6.15 which contains a sequence of micrographs taken as successive surface atomic layers

Figure 6.15 A sequence of helium field-ion micrographs taken before and after bombardment with 732 eV argon ions.

(a) The tungsten reference surface.

(b) The same tungsten surface after irradiation.

(c) The damage at a depth of $3\frac{1}{2}$ (011) atomic layers.

(d) The damage at a depth of $7\frac{1}{2}$ (011) atomic layers.

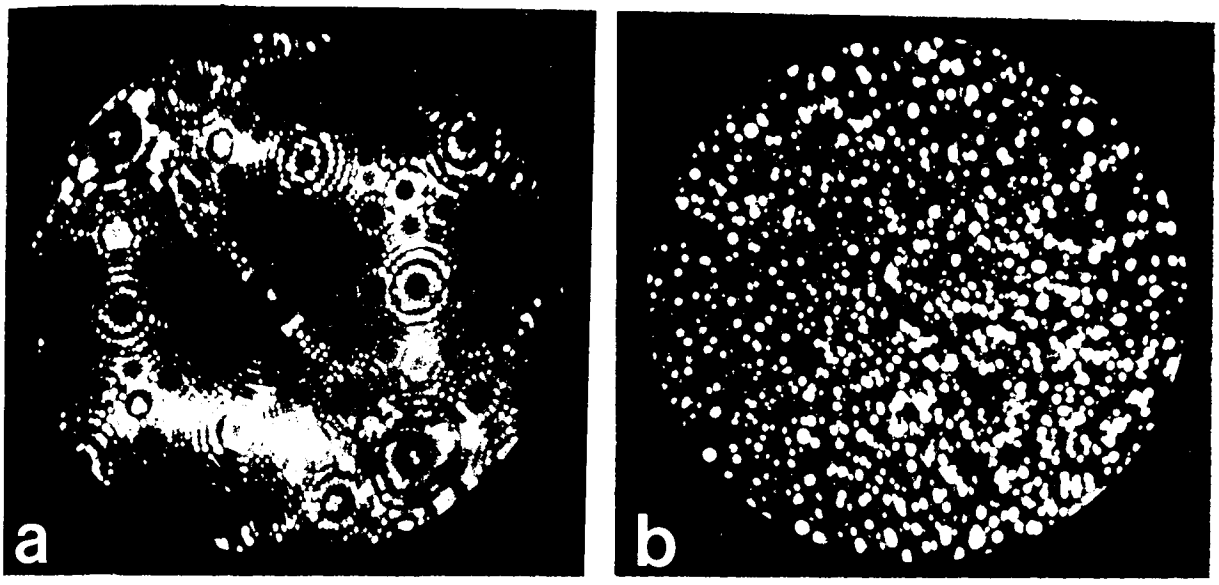
a
b

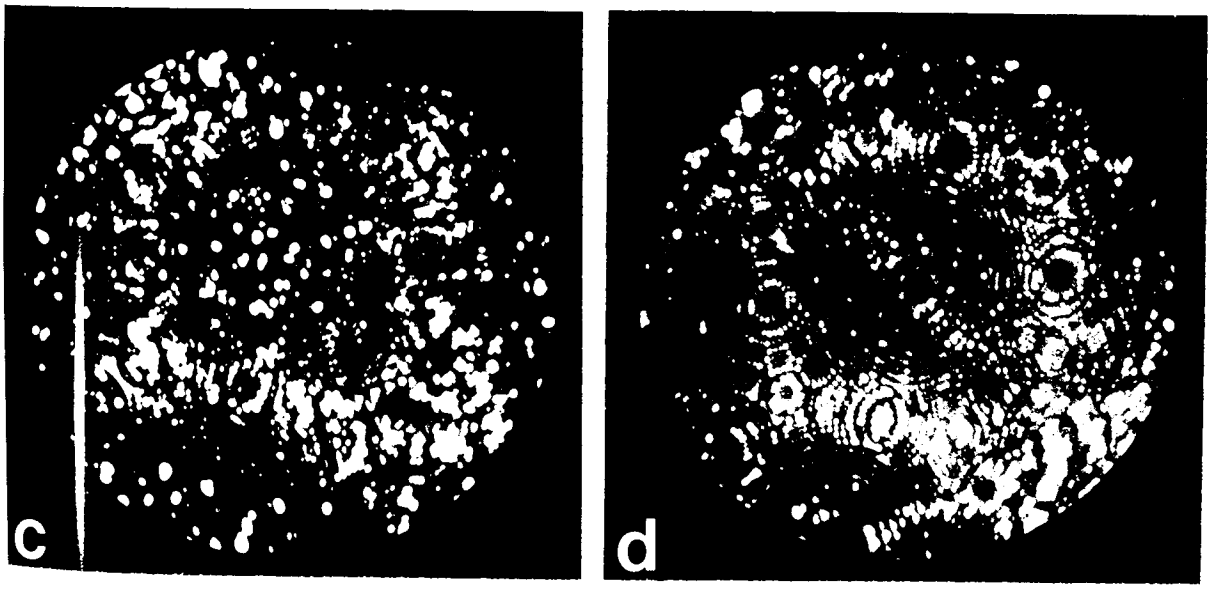
c
d

were removed after irradiation with 732eV argon ions. All the types of damage found in the xenon ion bombardment experiments were found including interstitials, vacancies and vacancy clusters. The dark line contrast features were also observed after each experiment particularly at depths up to three or four (011) layers. They were again specially abundant after higher ion energy experiments had been performed. Figure 6.15(d) reveals the depth of penetration of argon, for instance after $7\frac{1}{2}$ (011) layers had been removed, defect contrast was still evident, this micrograph should be compared with figure 6.14(e) which depicts a tungsten surface irradiated with 732eV xenon ions after 7 (011) layers had been removed. The component of embedded argon to self interstitial among the "bright spot" population is likely to be higher for argon than xenon as there is a possibility of argon transmitting its energy to a greater depth. Indeed Smith (1971) investigating argon ion bombardment surface cleaning processes on Ta and W using AES found evidence of a large amount of impregnated argon and the sticking probability is quite high - particularly at the higher energies (Kornelsen (1964) (see figure 6.30). Once again a plot of depth of damage versus incident ion energy reveals an approximately linear relationship. The depth of damage at low incident ion energies was surprising; four (011) atomic layers of damage at an incident ion energy of 132eV.

One distinct defect feature occurred at 132eV argon ion bombardment and this is illustrated in

figure 6.16(a). The defect first appeared after 2 (011) planes had been removed and it was completely removed by the time 4 (011) layers had been removed. Figure 6.16(a) shows the defect at the stage when 3 (011) layers had been field evaporated. The defect is planar in nature and can be seen to intersect the (121) plane, the first or second (011) ring and then moves out of the field of view near to the (112) plane. Hence we can state that the defect is not extensive and that it is most certainly planar. Page and Ralph (1970) have previously analysed a field-ion microscope observation of slip in iridium and indicated that a bright to dark contrast effect should occur to each side of the trace because the slipped portion would partially shield the unslipped crystal from the electric field. This analysis was carried out on a high radius specimen whereas the tungsten specimen illustrated in figure 6.16(a) has a radius of only $\sim$200Å. This may account for the absence of this contrast effect. However, the ring matching across the trace strongly resembles the ring matching exhibited by the observation of Page and Ralph.

The three primary modes of slip in tungsten have been found to be (110) <111>, (112) <111> and (123) <111> (Taylor (1966), Argon and Maloof (1966)). There is evidence that slip in tungsten is temperature dependent. Argon and Maloof (1966) investigating the plastic deformation of high purity tungsten crystals in the temperature range 77°K to 450°K found traces corresponding to slip on {110} and {112} planes. In the high temperature range, Taylor (1966) found indications

Figure 6.16 (a) The appearance of a planar defect in a tungsten emitter bombarded with 132 eV argon ions. This micrograph shows the extent of the damage after three (011) layers had been removed from the reference surface.

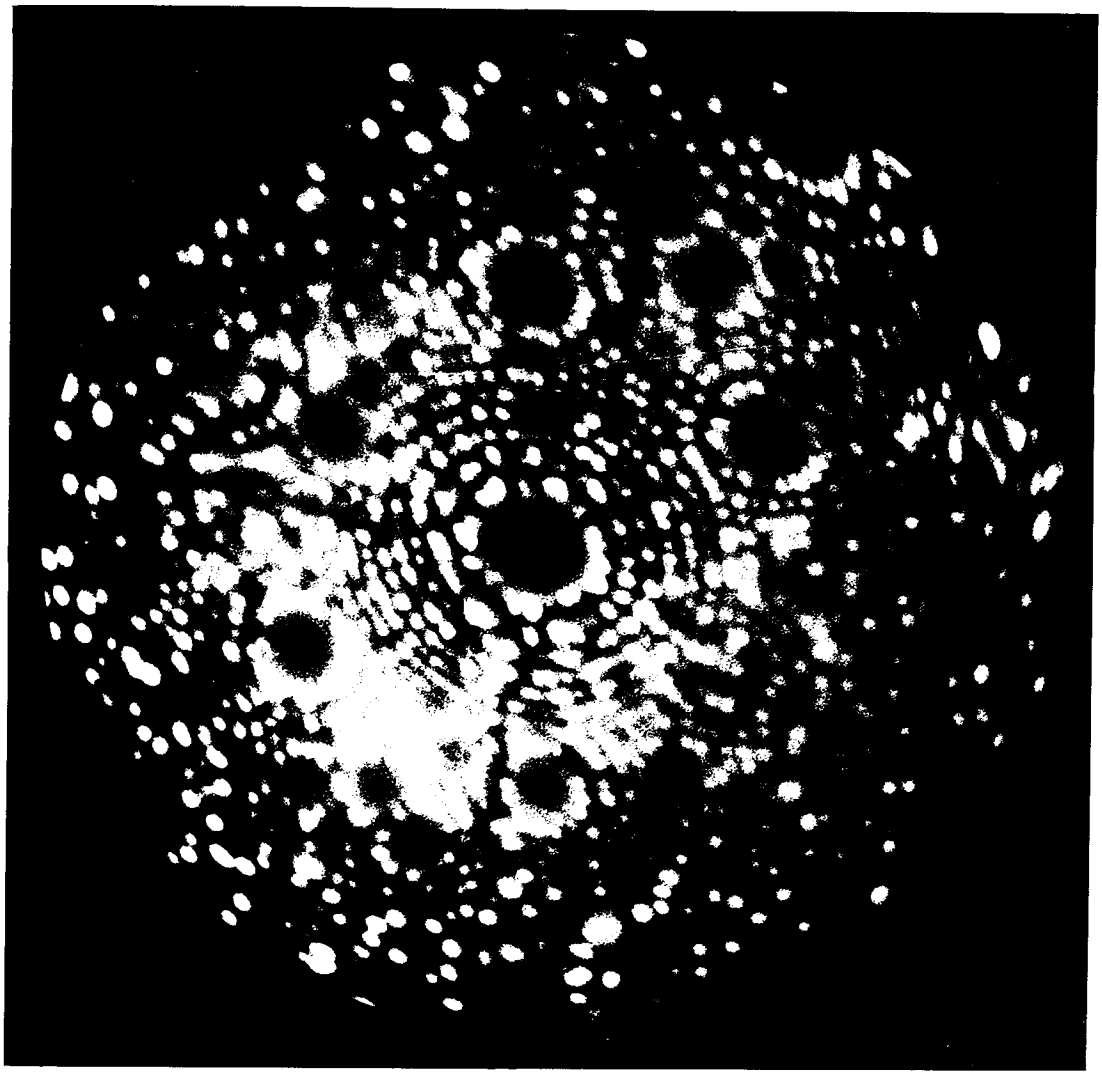

Figure 6.16 (b) The same tungsten specimen as (a), but one (011) layer has been removed from the surface. It is probable that the planar defect shown in (a) was slip.

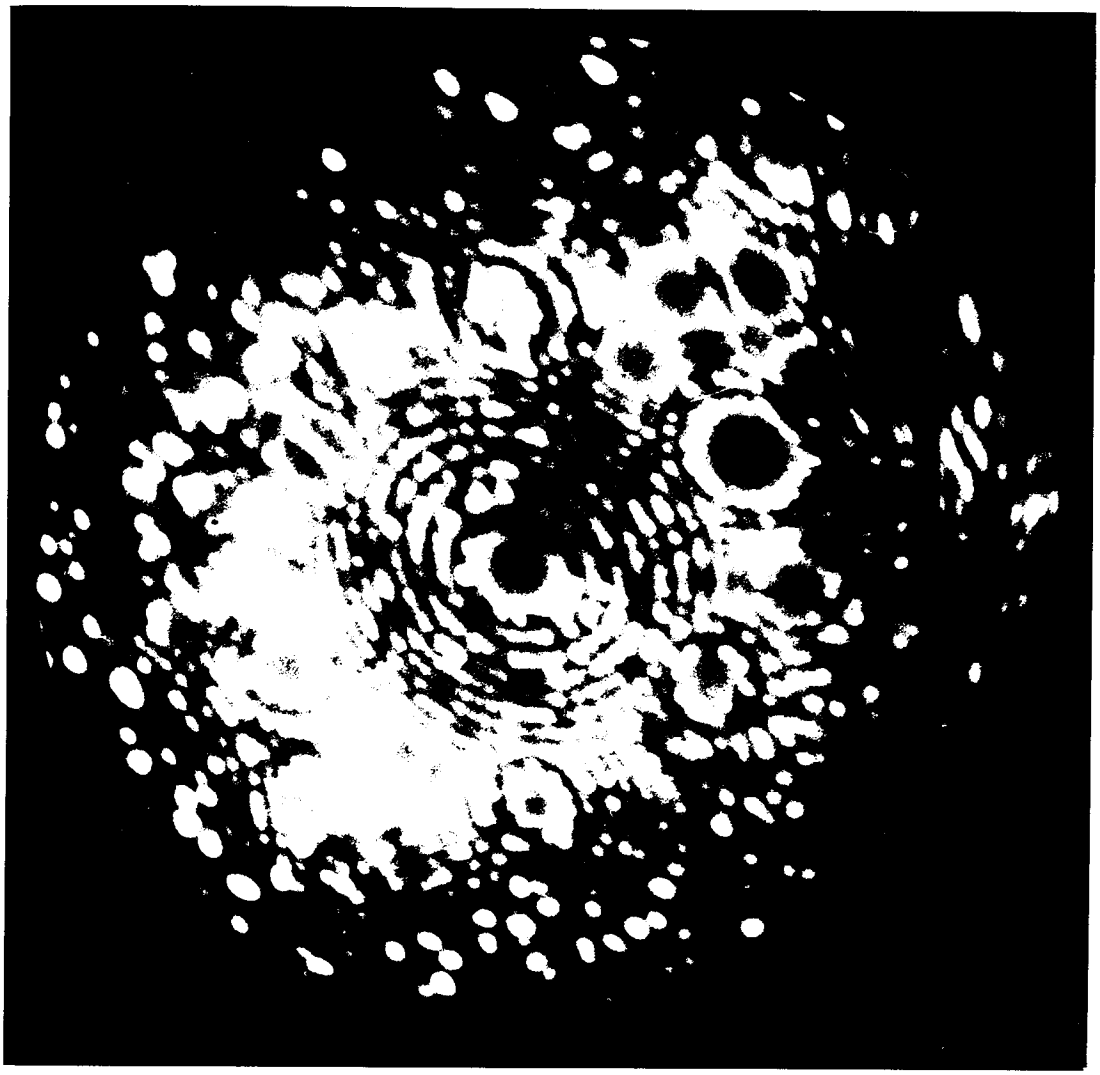

of slip occurring on a third plane {123} <111> which became operative between room temperature and 1645°K. This experimental evidence is contrary to the predictions made by Andrade and Chow (1940) who believe that slip in b.c.c. metals occurs only on {123} <111> above approximately half the homologous temperature.

Field-ion microscope observations of slip in tungsten have been rare. Müller (1960) slipped field-ion specimens by exposing them to a high electric field at elevated temperatures and claimed that the highly complex contrast that resulted was attributable to slip on {110} and {112} planes. Also, the author observed slip to occur on a tungsten tricrystal after field evaporation of a few atomic planes, the field stress was thought to play a considerable part in this observation. Work is at present in progress in a study of the deformation crystallography of b.c.c. metals using the field-ion microscope by G. G. Summers (1973).

If the defect shown in figure 6.16(a) is slip then from the evidence sited above it most likely occurred on the {110} or {112} planes. The trace is inadequate for performing a rigorous stereographic analysis, but a crude analysis indicated that the {110} plane was most likely. Certainly, more traces and traces occurring on high radius specimens are required before it can be properly claimed that slip occurs under these conditions. The existance of the high stress caused by the applied imaging field is felt to be an important factor.

6.8.3 Neon ion bombardment

Neon has an atomic weight of 20.18 a.m.u. and in an atomic collision with tungsten transfers about 36% of its energy (table 6.2). However, it is a much smaller atom thatn argon or xenon and hence from the Lindhard and Scharff theory would be expected to penetrate and cause damage deeper into the crystal. This has certainly been found to be the case.

In comparison with xenon and argon ion bombardment experiments, the surface layer was much less disordered and the crystallinity of the specimen was usually apparent after the removal of only half a (011) atomic layer. For example figure 6.17 shows a sequence of micrographs taken as successive atomic layers had been field evaporated from a tungsten surface (figure 6.17(a)) previously subjected to 332eV neon ion bombardment. Figure 6.17(b) shows the state of the ion bombarded surface while figure 6.17(c) is the same specimen after only half a (011) layer had been removed. Although this surface is extensively disordered the low index planes may certainly be identified. Also in this particular experiment, planes exhibiting spiral contrast normally indicative of the intersection of a dislocation (Bowkett and Smith (1970)) were observed. For instance, figure 6.17(e) features spiral contrast on the (011) plane, typical of a perfect dislocation. Six (011) layers had been removed at this point. Figure 6.17(f) depicts the same specimen after $7\frac{1}{2}$ layers had been removed, a typical dissociated dislocation contrast is shown in the ($\bar{1}$12) plane. Both of these defects were extensive, but not

Figure 6.17 The effect of bombarding a tungsten emitter with 332 eV neon ions. A sequence of micrographs is presented as successive atomic layers are removed by field evaporation.

(a) The undamaged reference surface.
(b) The same surface after ion bombardment.
(c) After $\frac{1}{2}$ a (011) atomic layer had been removed.
(d) After 4 (011) atomic layers had been removed.
(e) After 6 (011) atomic layers had been removed.
(f) After $7\frac{1}{2}$ (011) atomic layers had been removed.

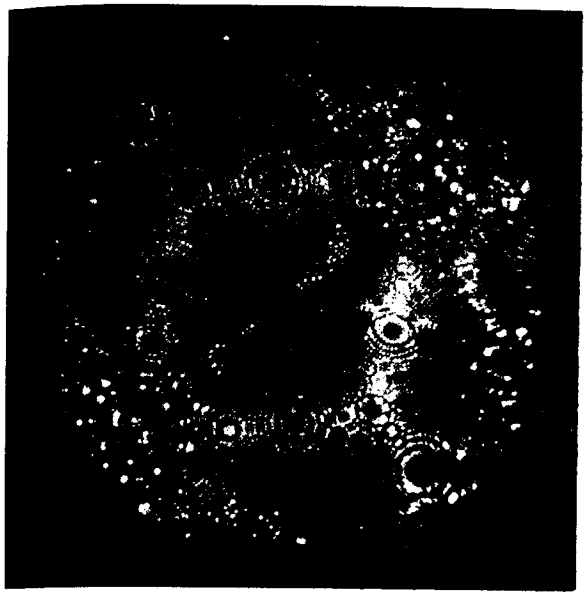

A

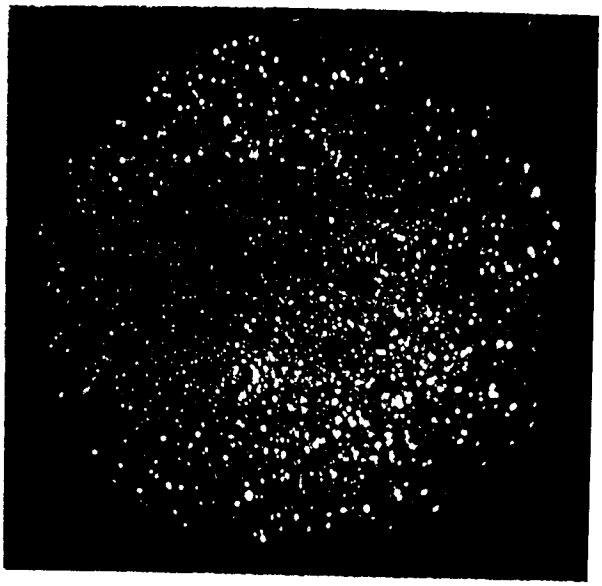

B

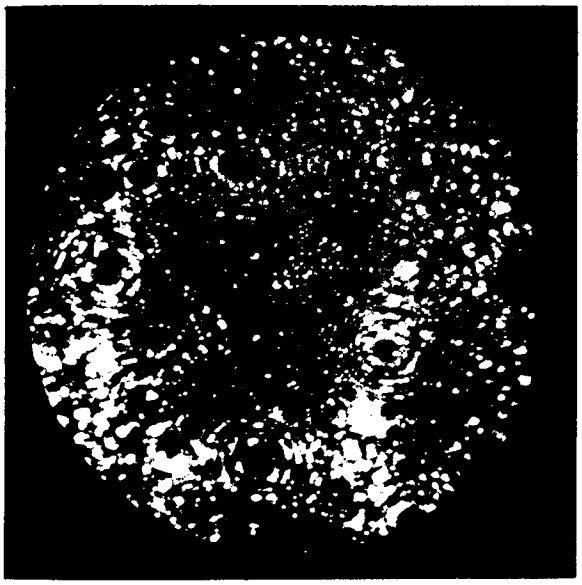

C

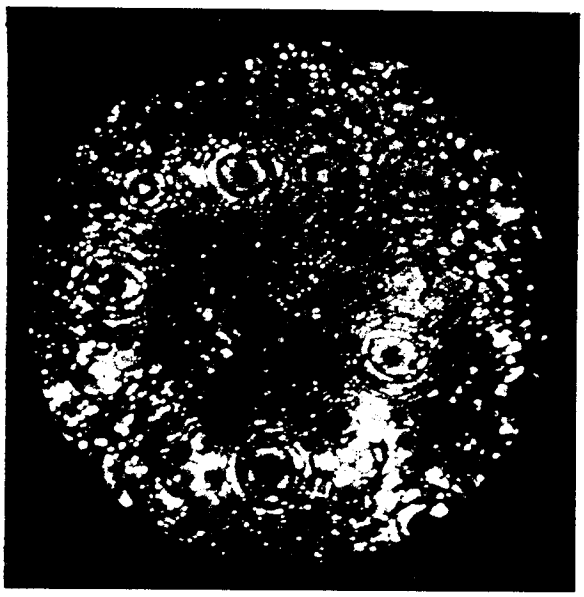

D

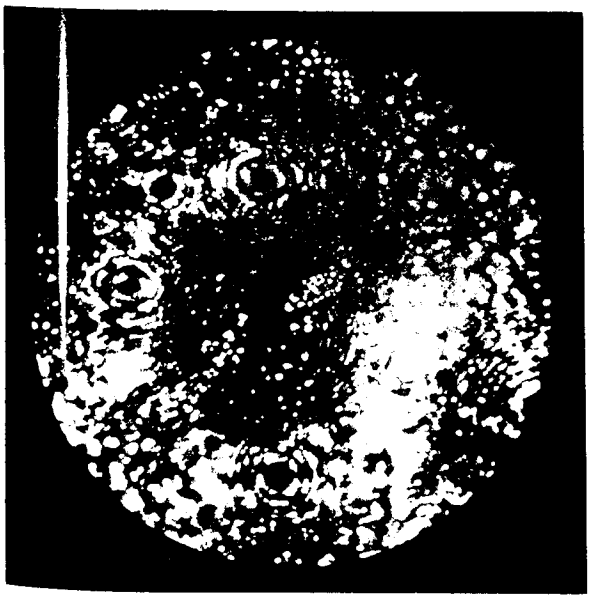

E

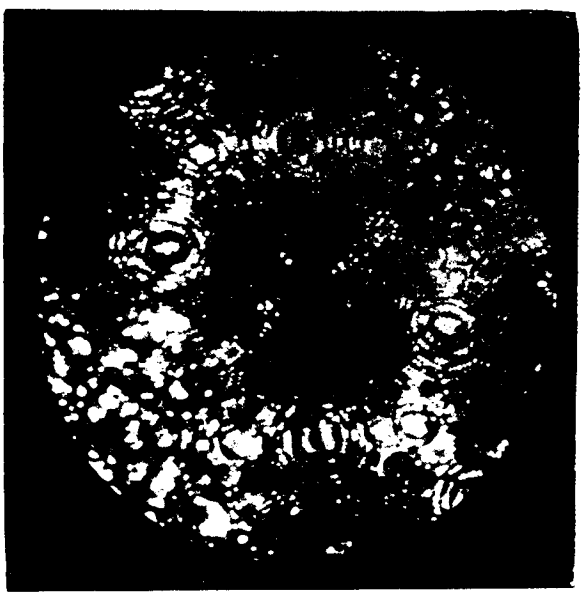

F

in the normal sense; they were evident for 20 (011) atomic layers or so (about 45Å) and correspond to the shallow dislocation loops reported by Müller (1970) found in his cathode sputtering experiments. Rajo and Bru (1972) have found a similar phenomenon to occur in f.c.c. metals (Au, Ag and Cu). Using electron microscope techniques they found that small dislocation loops (interstitial in character) were associated with 5 keV argon ion bombardment in a localised damage layer only 70Å thick.

As with xenon and argon, the usual defects found after neon ion bombardment were vacancies, interstitials, vacancy and interstitial clusters and the dark line contrast defects. The extent of the damage caused was less than that caused by either xenon or argon, but defects could be traced to a greater depth. The same type of defect distribution with atomic layers removed was found, but due to the more gradual tail off the depth of damage could not be specified with the usual certainty. In fact 932eV bombardment caused little damage beyond a depth of 8 (011) layers, but this damage was sufficient to count to a depth of 21 layers within the arbitrary definition of 5 "bright spots" within the ($\{211\}$ - $\{112\}$ - $\{011\}$) region.

6.8.4. Helium ion bombardment

The helium atom has an atomic weight of 4 a.m.u. and a mean atomic diameter of 2.30Å. In a helium-tungsten atomic collision, equation (6.3) predicts that only 8% of the incident ion energy will be transmitted (see table 6.2). The range of helium in

tungsten is high because of its very small atomic diameter enabling channelling to occur easily, thus making any comparison between the depths of damage caused by helium and the other inert gas ions rather tenuous.

Although it is thought that the large inert gas atoms come to rest substitionally (Domeij (1966)) and hence would distort the surrounding lattice to give "bright spot" contrast this is not the case with helium. It has been shown (Erents, Farrell and Carter (1968) Kornelsen (1970)) that lattice defects act as trapping sites for helium at low temperatures ($\lesssim 300^{\circ}K$ in tungsten). Otherwise the helium undergoes rapid interstitial diffusion and escapes through the surface. This mechanism and the relatively small size of the helium atom may explain the comparitively small numbers of "bright spots" found after helium ion bombardment. Kornelsen (1972) has produced evidence to suggest that these sites are point defects rather than extended defects, and that the vacant site is the most probable site for helium trapping.

By and large, point defect damage could be found on the surface for all the ion energies used (132eV, 332eV, 532eV, 732eV and 932eV). Although the extent of this damage was not comparable to that caused by the heavier inert gas ions, considerable damage was caused to the first two atomic layers. For example, figure 6.18(a) depicts the state of the specimen surface bombarded with 732eV helium ions, after one (011) layer has been removed. Considerable interstitial contrast

Figure 6.18 (a) An example of the effect of 732 eV helium ion bombardment. This surface depicts the damage after one (011) layer had been removed from the bombarded surface.

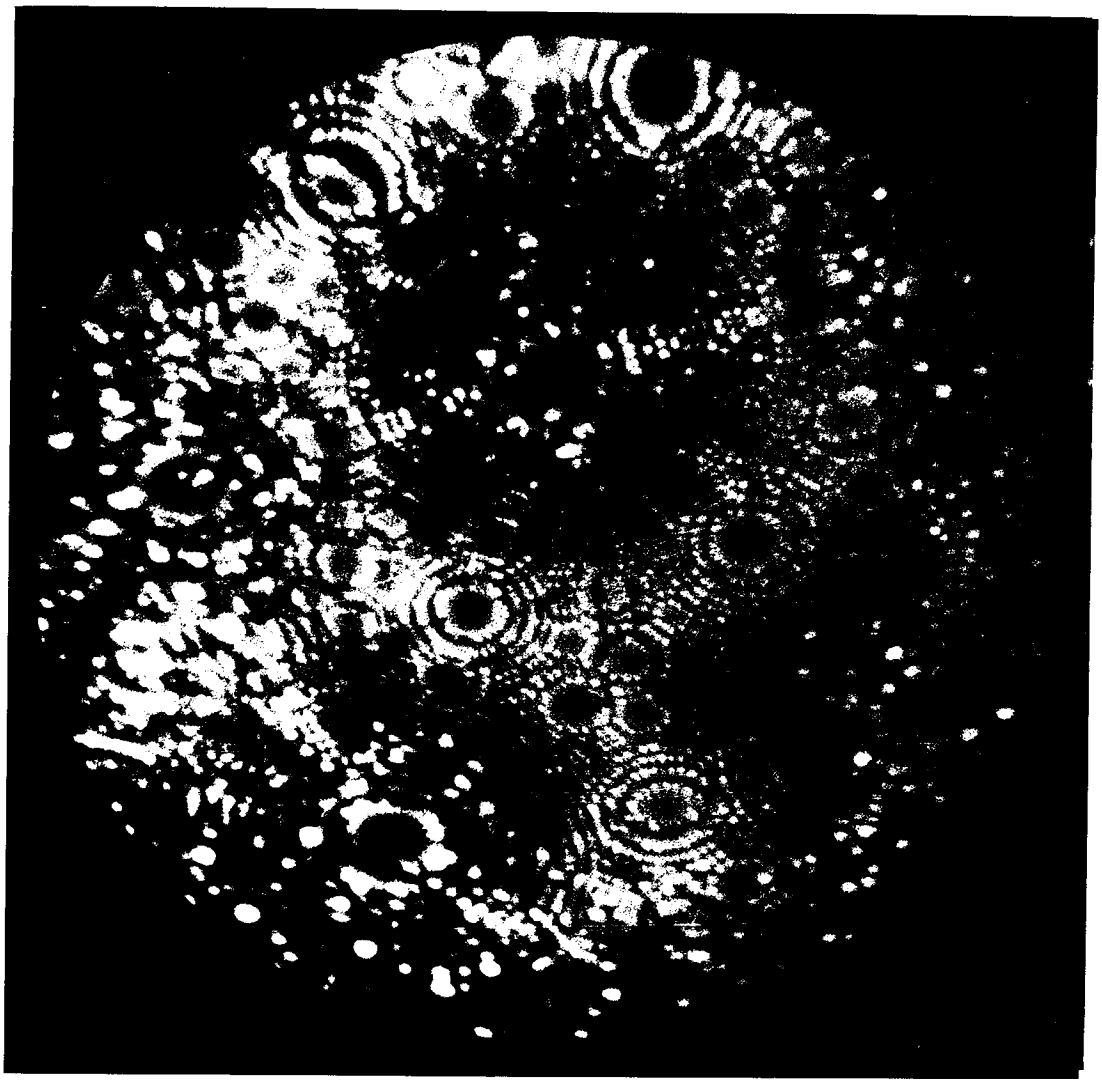

is exhibited especially in the (011) plane ledges. Figure 6.18(b) shows the same specimen after 20 layers had been removed, there are still a number of bright spots in the (011) plane regions. Although one might be tempted to put this feature down to channelling events, it is also possible that some diffusion process is responsible.

In general, contrary to anticipation, surface damage was found to decrease with increasing ion energy, although it must be stated that this effect was small.

An unexpected and colossal damage feature occurred during an experiment involving bombardment with 132eV helium ions. As the maximum transmitted energy can only be about 11eV, nominally below the usually accepted threshold displacement energy, the mode of production of the defect defies interpretation. Figure 6.19(a) shows the largely defect free surface prior to bombardment. The bombardment procedure followed that laid down in section 6.72 and the pressure of helium required to produce an ion current of 1.2μA was 2×10^{-3} Torr. As the image of the bombarded surface appeared, clusters of atoms were observed to form 'star' shaped clusters. Examples of this effect are shown in figure 6.19(b) at this stage less than two (011) planes have been removed. The star shaped features are arrowed. Further removal of surface layers revealed spiral contrast on the (011) plane and evidence of planar defects (arrowed). Figure 6.19(c) illustrates these features and depicts the surface after the removal of five (011) layers. The effect becomes even more recognisable as more surface

Figure 6.18 (b) After the removal of 20 atomic layers.

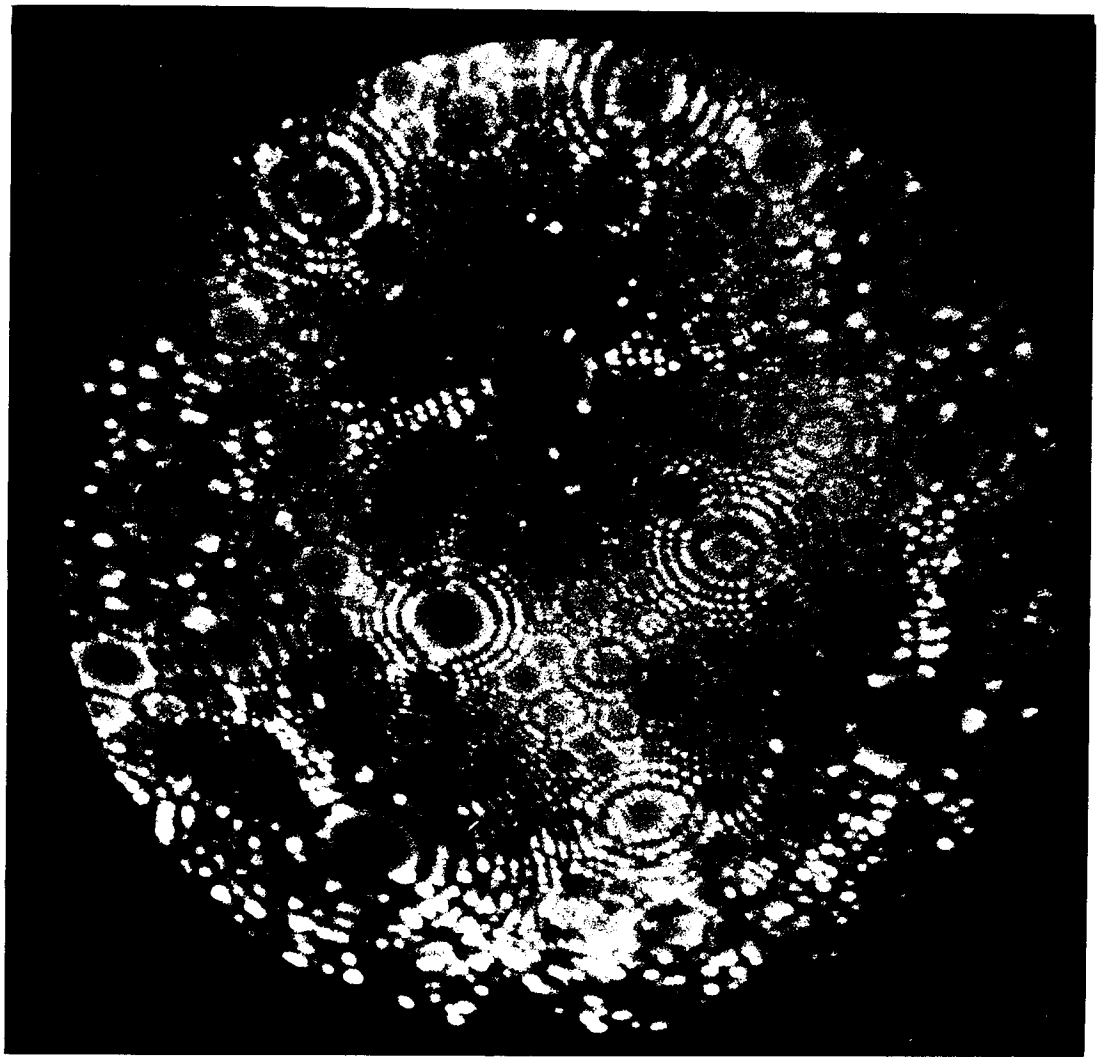

layers are removed. For example, figure 6.19(d) is a micrograph taken after the removal of eight (011) surface layers. As the surface layers were removed, the extent of damage was reduced and figure 6.19(e) shows the defective surface after thirteen (011) layers had been removed. More than one planar trace is incident at the surface making a detailed analysis unworthwhile, however, the contrast displayed by the groups of atoms in "star" configurations are similar to those characterised by Fortes and Ralph (1969) as dislocation loops. The removal of 25 (011) layers resulted in the micrograph shown in figure 6.19(f). Most of the defect contrast has been removed and there are certainly no planar defects crossing the image. Hence the defect produced during (or after) the bombardment occupied a region very close to the surface. Although there can be little doubt that the applied field stress must have had a part to play in the formation of the defect, it is unlikely that this was the only factor. Some extensive damage must have been caused by the bombarding helium ions, but a defect on this scale could never be attributed to field stress alone.

6.8.5 The depth of damage

The mean range of the various inert gas ions in solids was discussed in section 6.4. Kornelsen (1970) believes that lattice damage extends over a depth comparable with the ion penetration depth. This prediction would seem to be supported by the work of Sigmund and Sanders (1968) who found that the two were approximately the same (usually the calculated depth

Figure 6.19 Damage caused to a tungsten emitter bombarded with 132 eV helium ions.

(a) The defect free surface prior to ion bombardment.
(b) The damage at a depth of 2 (011) atomic layers.
(c) The damage at a depth of 5 (011) atomic layers.
(d) The damage at a depth of 8 (011) atomic layers.
(e) The damage at a depth of 13 (011) atomic layers.
(f) The damage at a depth of 28 (011) atomic layers.

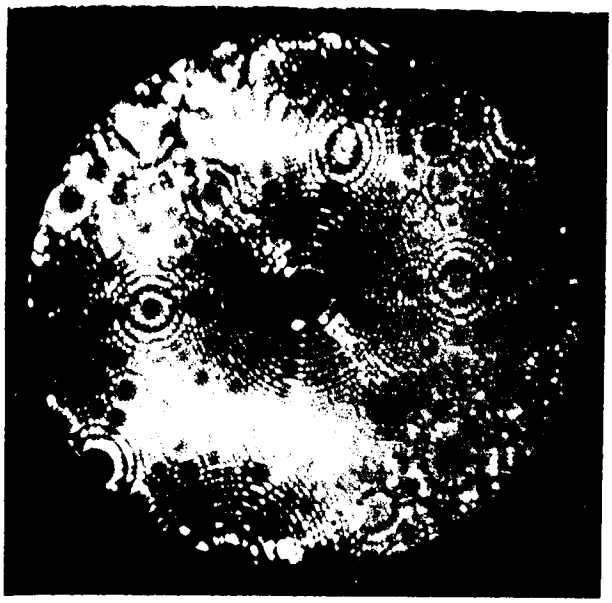

A

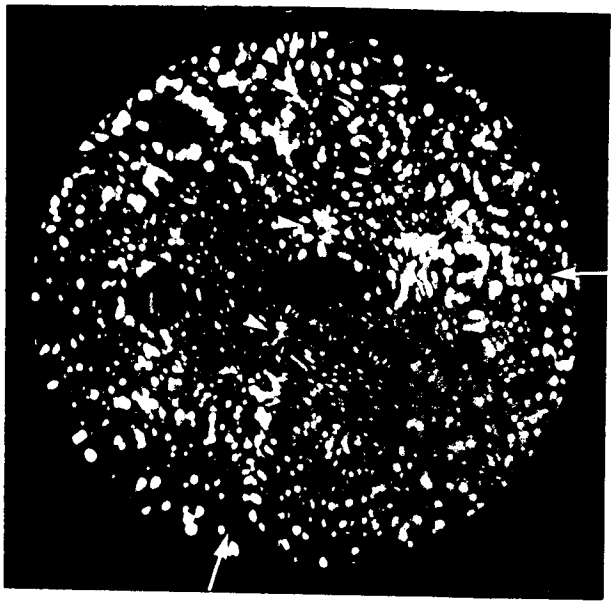

B

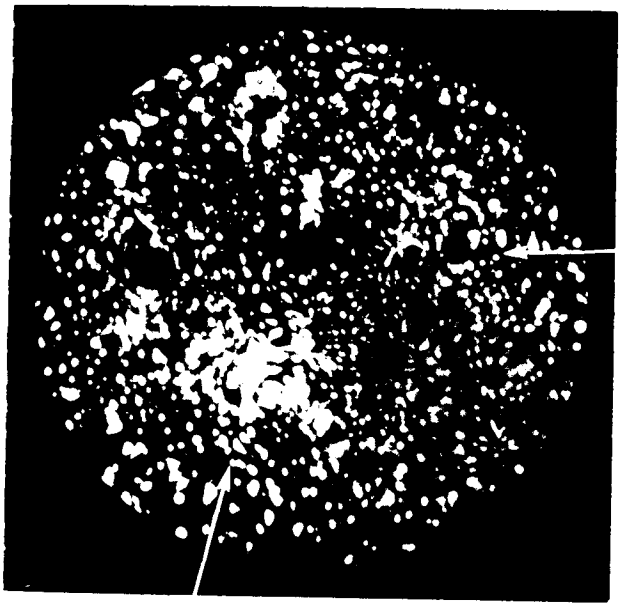

C

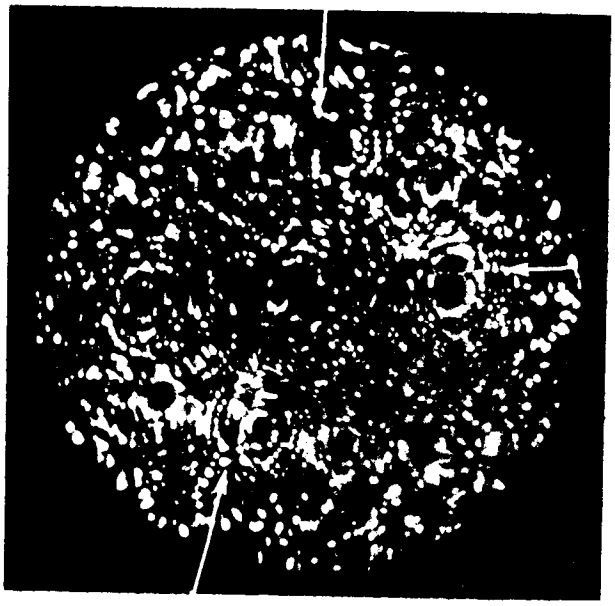

D

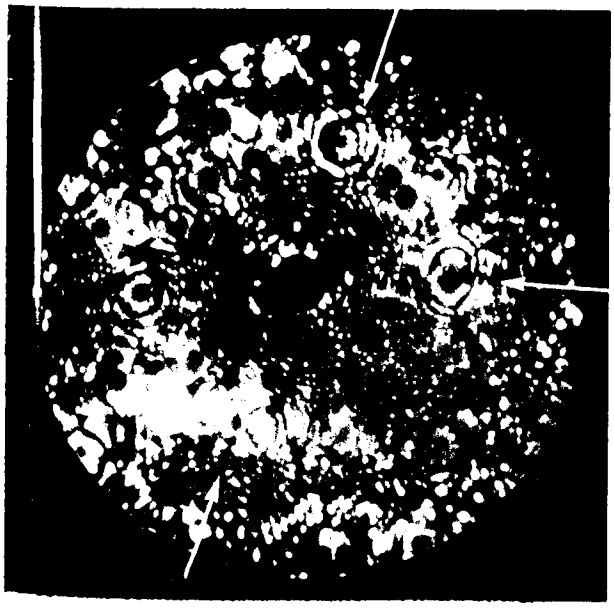

E

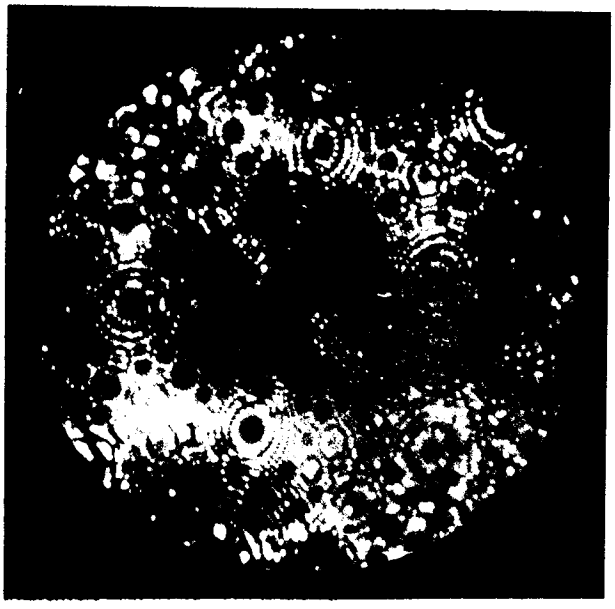

F

of damage was less than the range), in amorphous germanium at high energies, but the approximation was better at the lower energies. Data concerning the depth of damage is very important in gas release studies, where considerable work has been done, because it is now known that vacancies induced into the metal subsruface act as trapping sites for the incoming ions (Erents and Carter (1967)).

Apart from the electrolytic peeling technique used by Kornelsen (1964), a method exists based on the differences in sputtering yield for a given energy, between material previously damaged by a higher energy bombardment and material previously undamaged. This technique has been used by MacDonald and Haneman (1966) to find the depth of damage caused by low-energy ions in germanium. Both these methods are indirect and involve difficult calibration procedures. The field-ion microscope however, possesses the capability of field evaporation which enables the controlled removal of surface atomic layers to reveal the quality of the subsurface structure. Hence provided that the radius of the specimen is greater than the depth of damage; the depth of damage can be specified.

One difficulty involved in the use of the field-ion microscope is the definition of the depth of damage. In this study, for convenience, each micrograph corresponding to the successive removal of surface layers was examined and the critereon used to asses the depth was that in the region ((121)-(011)-(112)) less than five "bright spots" must be evident. The value of 5 interstitials was taken so that there could be no

confusion with bright spots associated with impurities or the normal equilibrium concentration of "bright spots". In all experiments, it is certain that the damage was caused at depths much greater than that recorded, but it is felt that this approach would lead to the most unambiguous results. For example, using this critereon, in the case of 800eV xenon ion bombardment, the surface layer corresponding to figure 6.14(e) would be used to define the depth of damage (7(011) layers).

In this way it was possible to record a depth of damage for each ion species (except helium) at each incident ion energy. The depth of damage was then plotted versus ion energy and the results are presented in figure 6.20. Plotted in figure 6.21 are the range calculations of the appropriate ions in tungsten of Erents (1967) (see section 6.4). Figure 6.21 shows that neon is capable of creating damage at a greater depth than argon and xenon in that order. This is in the same order as that predicted by Erents (1967) using the Lindhard and Scharff (1961) theory. The actual discrepancy in the range values is large, but may in part be due to the difference in definition with regard to the depth of damage or penetration.

Using equation (6.3) and atomic weights in table 6.2 energy transfer Q(E) in an atomic collision between an ion of mass M_1 and a tungsten atom of mass M_2, then the proportion of incident ion energy E_i transferred for each ion species was calculated as follows:-

Xenon	Q(E)	=	0.993Ei
Argon	Q(E)	=	0.587Ei
Neon	Q(E)	=	0.356Ei
Helium	Q(E)	=	0.083Ei

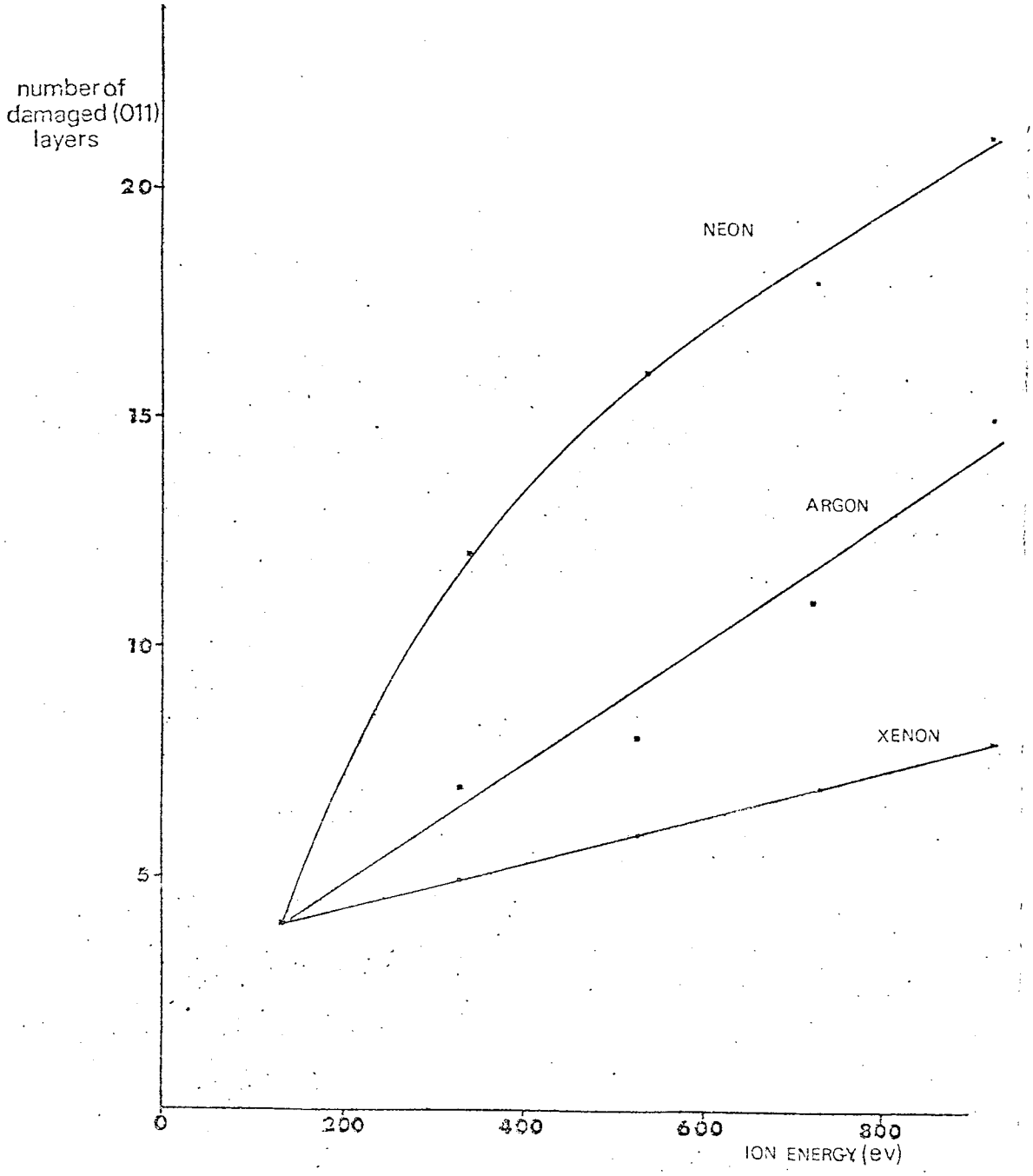

Figure 6.20 The depth of damage for various inert gas ions in tungsten as a function of incident ion energy.

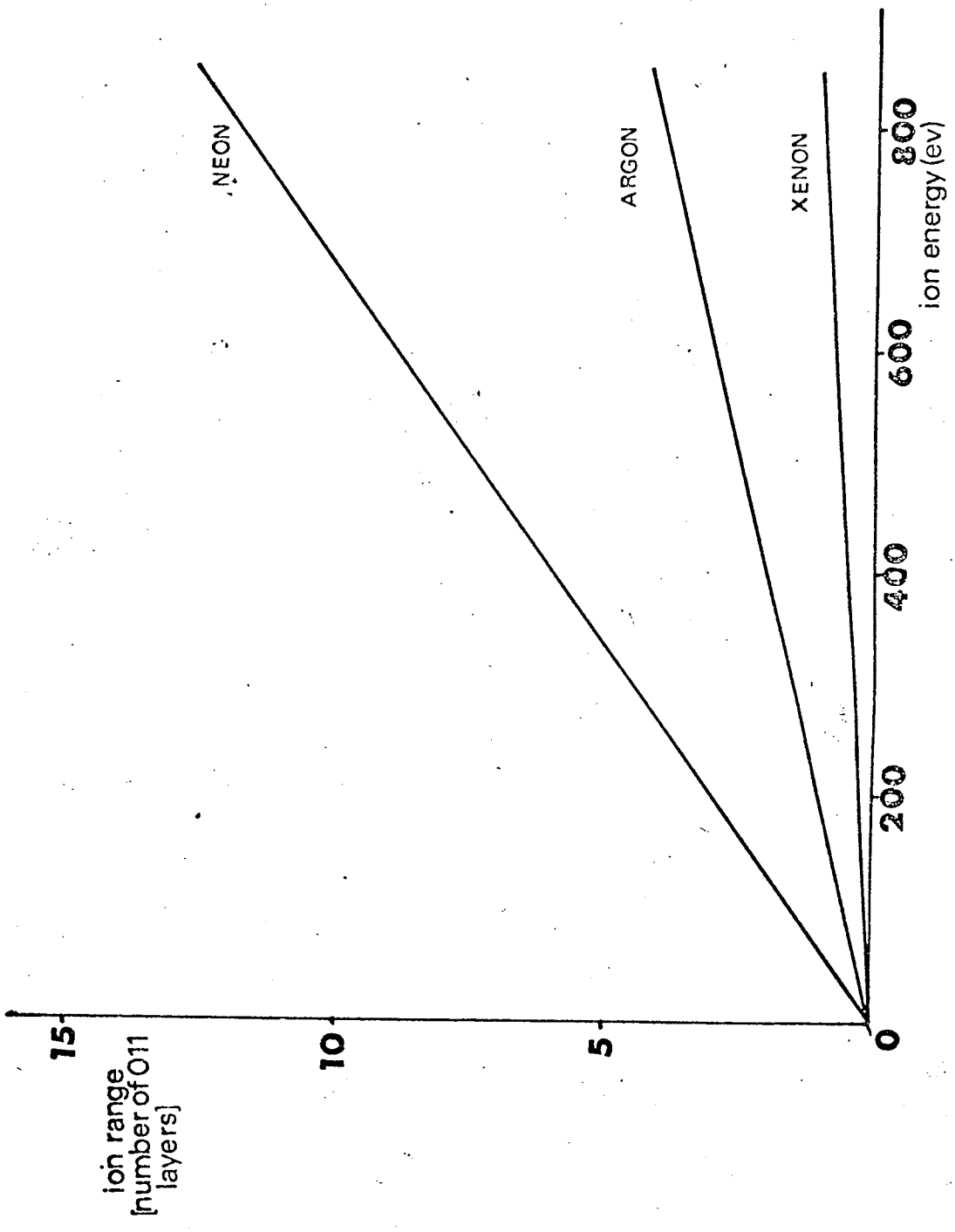

Figure 6.21 The theoretical range of low energy inert gas ions in tungsten.

Using these values, the Q(E) corresponding to the various ion energies used have been calculated and are presented in table 6.2. Note in particular the small amount of energy transmitted in a helium-tungsten collision. An helium ion of incident ion energy 132eV will transmit a maximum of only 11eV to the tungsten atom. This could provide a very sensitive method of determining surface damage thresholds.

These values of Q(E) have then been plotted versus the depth of damage caused in figure 6.22. Comparison between figures 6.20 and 6.22 reveals a much greater rate of increase in depth of damage per unit rise in energy if the Q(E) value is taken. The results for xenon ion bombardment differ slightly from those of Kornelsen et al (1964) for 500eV ions. Kornelsen found that virtually all the damage was confined to a layer 7.5Å thick. However, interpretation from figure 6.21 suggests that 6 (011) atomic layers would be affected, that is, about 13Å.

6.8.6 The threshold energy for the production of surface damage

The threshold displacement energy has been defined as the minimum energy required to produce a stable Frenkel pair. The value of the threshold displacement energy will vary according to the crystallographic plane examined and hence an averaging quantity, the mean displacement energy has been invoked. Kornelsen (1970) has used a value of 40eV for tungsten found by Neely et al (1968) employing electron radiation techniques. Several other values exist for the mean threshold displacement energy. Kornelsen (1970) has recognised however, that

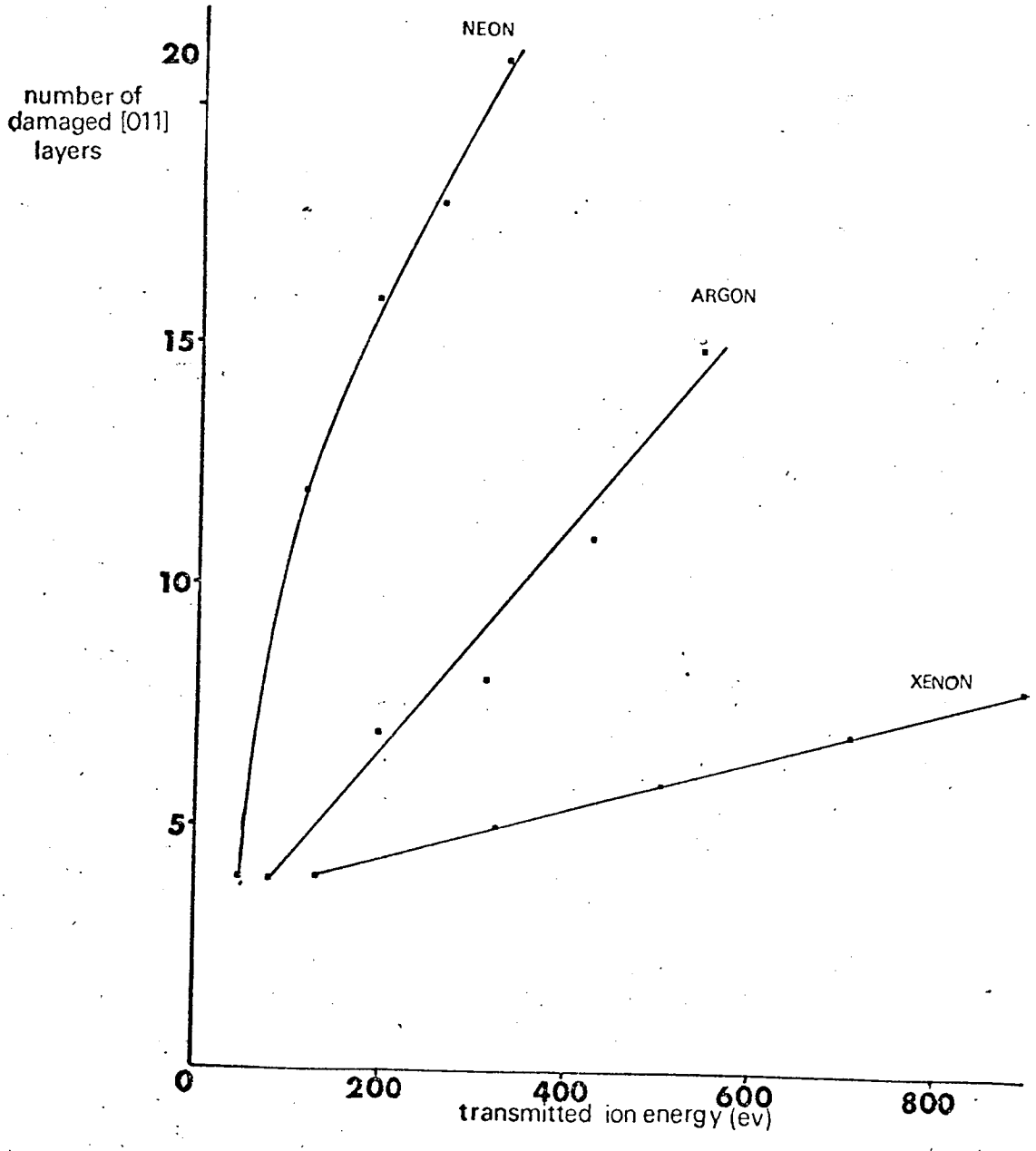

Figure 6.22 The depth of damage of neon, argon and xenon ions in tungsten, taking into account equation (6.3).

the surface threshold displacement energy will be much less. Certainly, the present experiments showed that subsurface damage occurs when 332eV helium ions are used. The equivalent maximum transmitted energy for this value is about 28eV. Figure 6.23 depicts the second layer of a tungsten specimen after bombardment. Interstitial and vacancy contrast is clearly present. Also an experiment with 132eV helium ions was associated with the most colossal damage pattern. Although a rigorous systematic experiment is required to find the threshold displacement energy, present results do indicate that 40eV (for the surface at least) is too high.

6.9. Annealing

The importance of ion bombardment in the production of atomically clean surfaces for surfaces study techniques (Farnsworth et al (1958), (Hüfner, Cohen and Wertheim (1972)), and the associated annealing in vacuum makes the study of surface thermal re-arrangement of clean, undamaged and ion bombardment induced damage very important. A pilot investigation is described here involving the observation of both heating effects on clean, field evaporated field-ion microscope specimens and the annealing of argon ion bombarded surfaces.

6.9.1. Thermal surface atom re-arrangement of undamaged tungsten surfaces

In this section the effects of subjecting a field-ion emitter to temperatures in the range 690°K to 1390°K are described. Previous field-ion microscope investigations of the effect of elevated temperatures have

Figure 6.23 A tungsten surface bombarded with 332 eV helium ions.

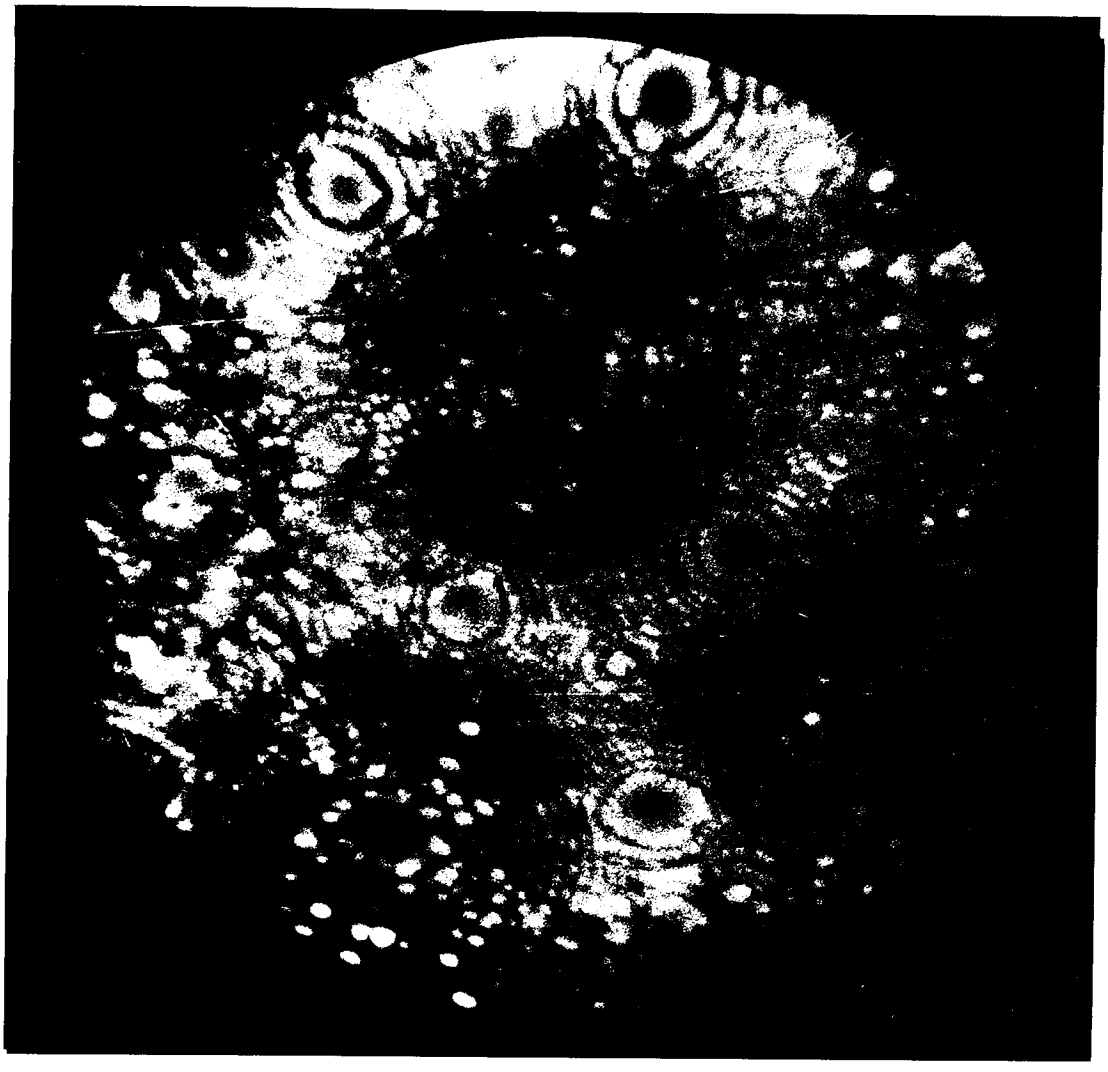

been conducted by Bassett (1963), (1965), (1968) on tungsten and Brenner (1964) on iridium. Recently, Sugata and Tamaki (1972) have studied the effect of 'flashing' tungsten and molybdenum emitters to high temperatures (>2200°K). Experimental conditions were largely governed by the discovery by Brenner (1964) and Bassett (1968) that sub-monolayers of contaminant oxygen can alter the shape and appearance of a thermally treated emitter. Hence U.H.V. field-ion microscopy was obligatory and pressures of better than $1x10^{-9}$ Torr were used, consistent with the vacuum precautions previously outlined in section 6.72. Helium field-ion images with the emitter cooled to 78°K were used. The familiar atomically smooth and almost perfectly ordered tungsten surface was obtained by field evaporation prior to any heat treatment. The emitters were heated electrically at zero applied electric field, using the specimen temperature controller described in Appendix (I). Temperatures were measured directly from this device and checked using an optical pyrometer.

The lowest temperature at which meaningful surface atom movement took place was 690°K in agreement with the results of Bassett (1963). Figure 6.24(a) depicts the clean field evaporated surface prior to heat treatment and figure 6.24(b) shows the effect of heating to a temperature of 690°K for ten minutes and subsequent rapid cooling to 78°K. Bassett (1963) found, (using a high radius emitter), that surface atom movement was crystallographically specific; proposing that atom movement started in the {111} planes at 690°K and in the

Figure 6.24 The surface re-arrangement of atoms due to heat treatment only.

(a) The tungsten reference surface prior to heat treatment.

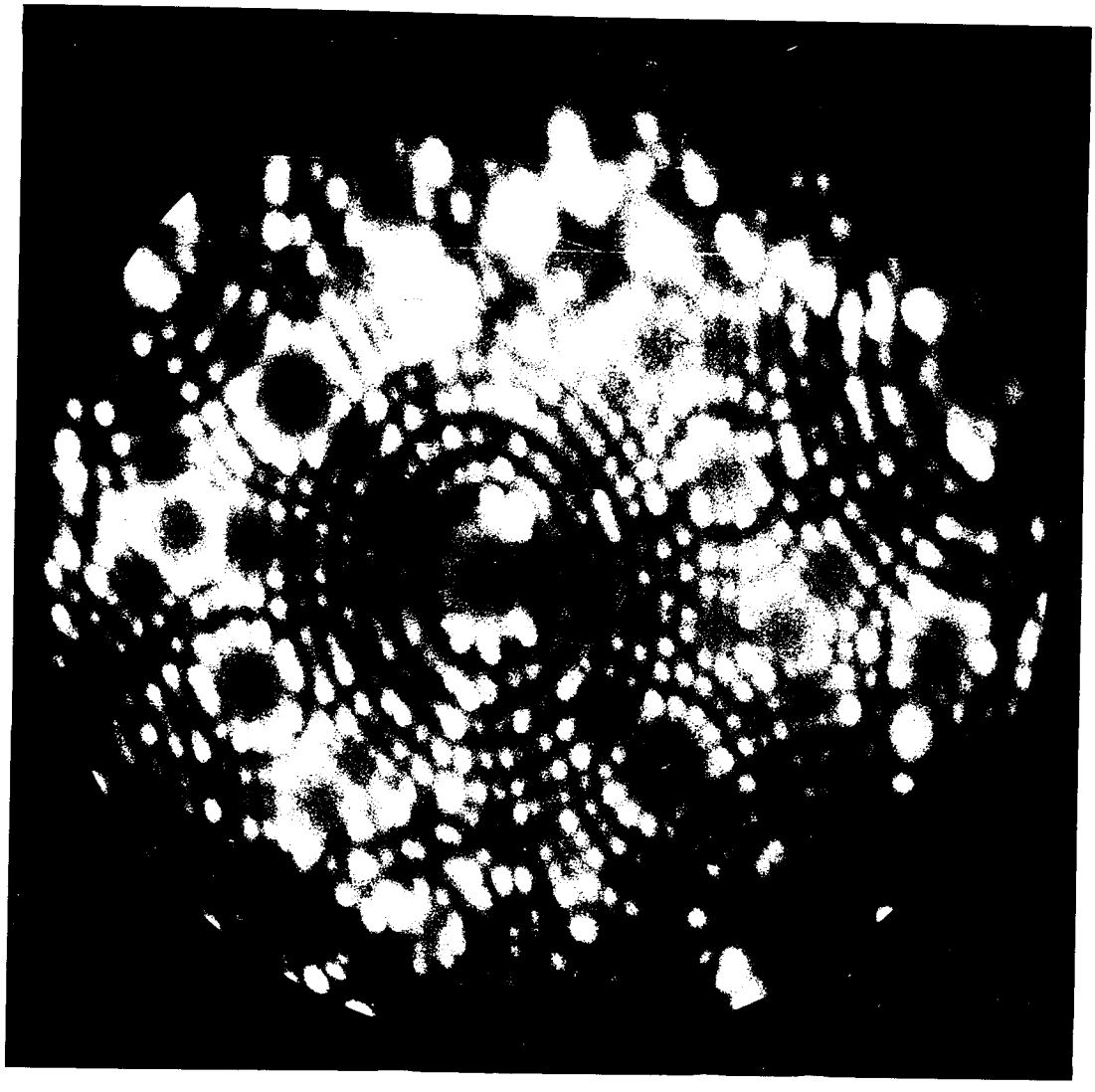

Figure 6.24 (b) The effect of heating to 690° K for ten minutes.

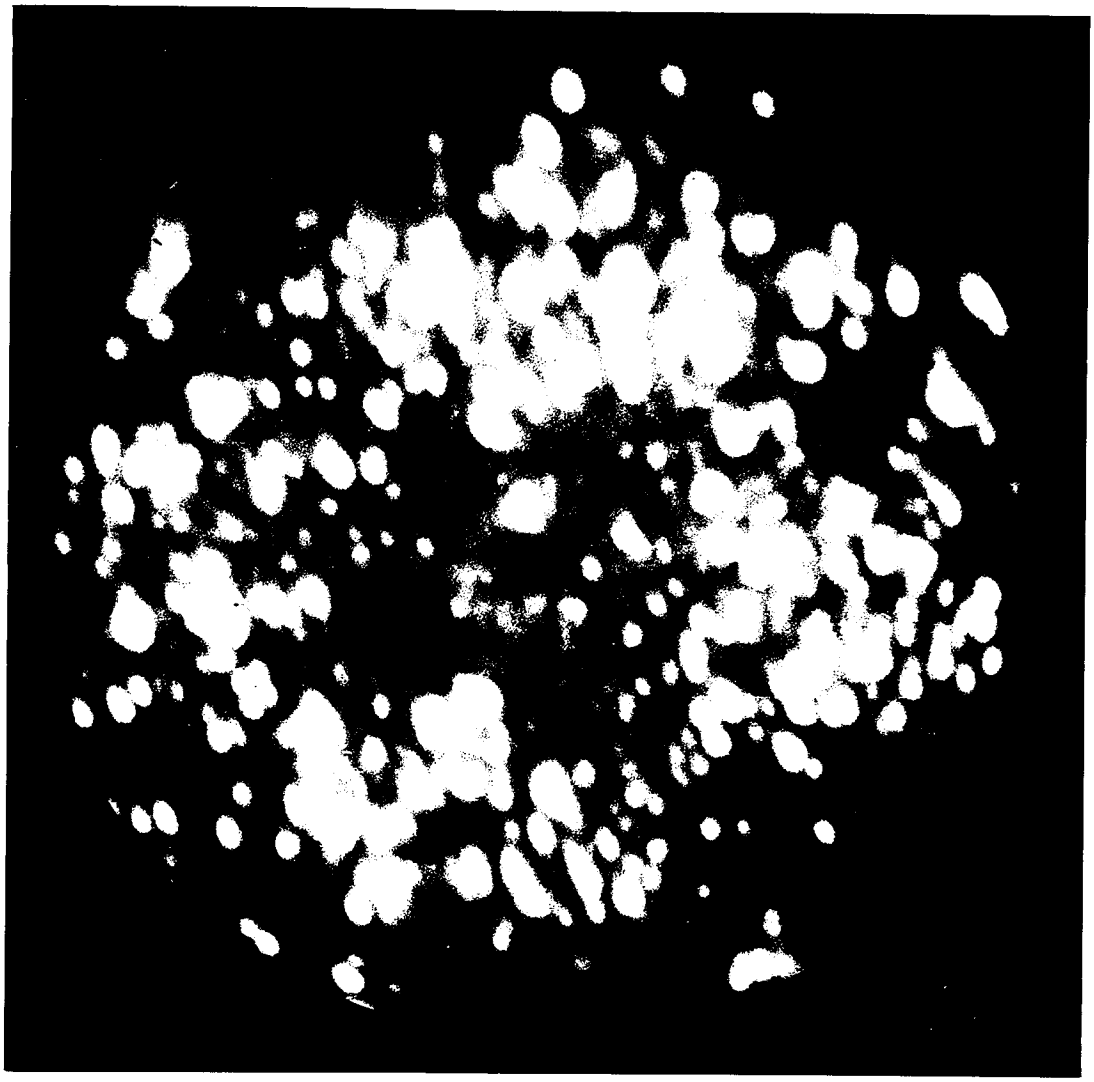

{001} planes at 740°K. Later, evidence by Bassett (1965) showed that atoms in kink sites are mobile on the {011} terraces at 500°K, with similar displacements occurring along the edges of the {111} and {001} terraces at 600°K and 700°K respectively.

Figures 6.25(a),(b),(c) and (d) depict the thermal end form as the temperature is raised to 1090°K, 1140°K, 1290°K and 1390°K respectively. These micrographs show that the tungsten surface is relatively disordered and that only the most densely packed crystal planes such as {110}, {211} and {100} are well developed and atomically smooth. The degree of faceting increasing with temperature. At these high temperatures surface diffusion causes a steady increase in emitter radius, since the surface energy is reduced. Thus as the temperature treatment of the specimens featured in figures 6.25(a) to 6.25(e) is raised, so is the specimen radius of curvature and hence also the applied voltage necessary to image the surface. This sequence of micrographs also illustrates the gradual development of atomically flat facets on the {211} {100} and {110} type planes. The possibility of some oxygen contamination from the shank is not discounted.

A field evaporation sequence through a thermally faceted image to the field evaporated end form is illustrated in figure 6.26(a),(b),(c),(d),(e) and (f). Upon applying the specimen imaging potential, the first detail to emerge is depicted in figure 6.26(a), where the low radius {111} planes appear first. On increasing the applied voltage the familiar faceted image gradually emerges and is fully formed as depicted in figure 6.26(c).

Figure 6.25 A tungsten emitter subjected to 2 minute heat treatments at the following temperatures:-

(a) 1090°K

(b) 1140°K

(c) 1290°K

(d) 1390°K

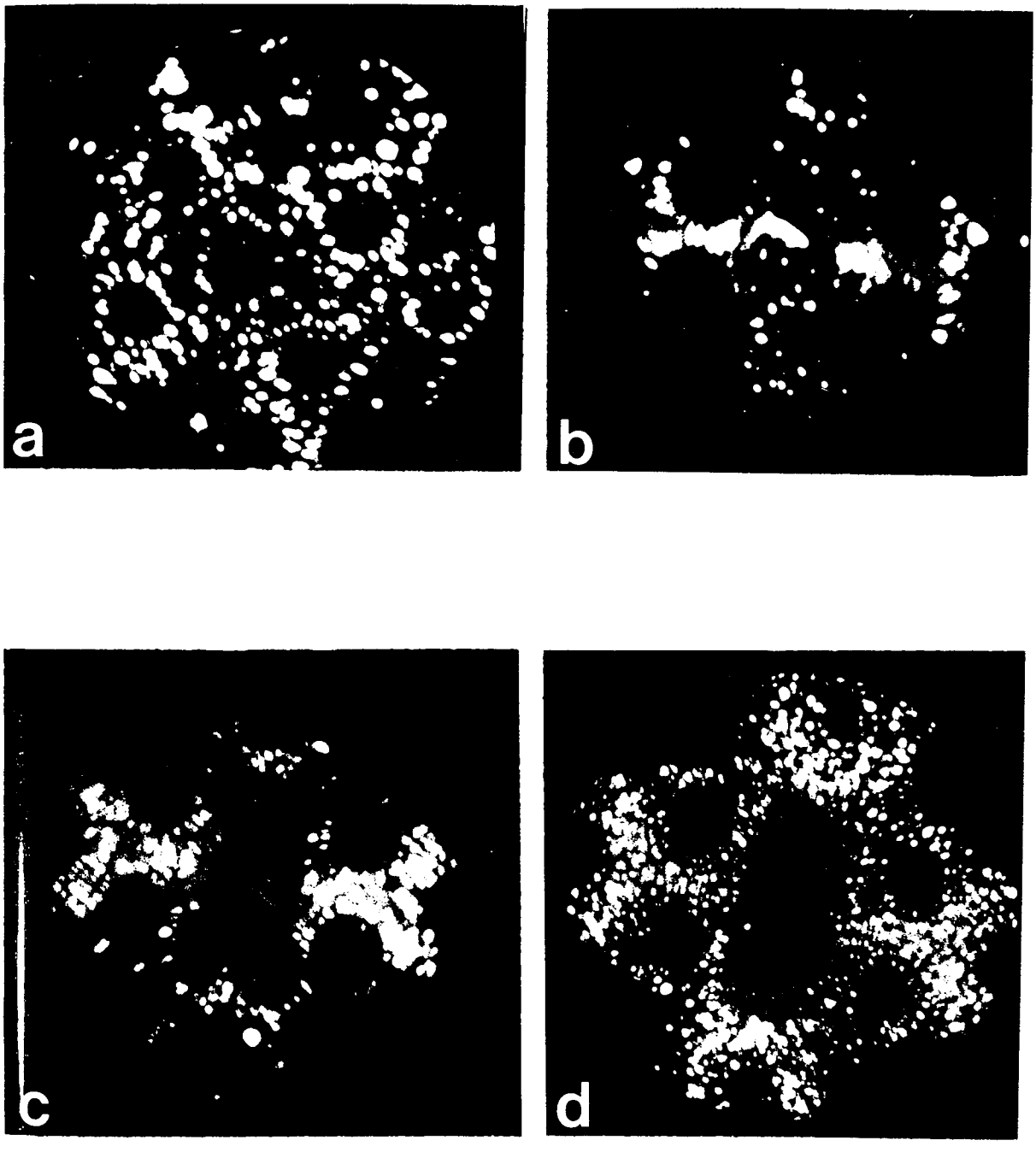
a
b
c
d

Figure 6. 26 A field-evaporation sequence through a thermally faceted end form.

A

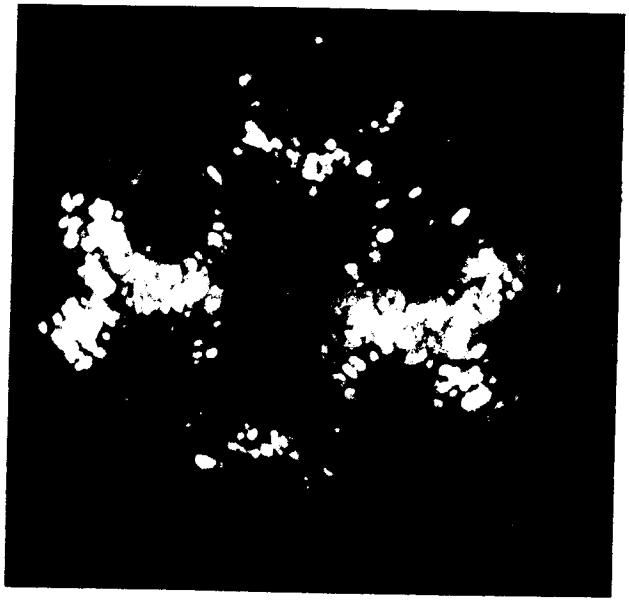

B

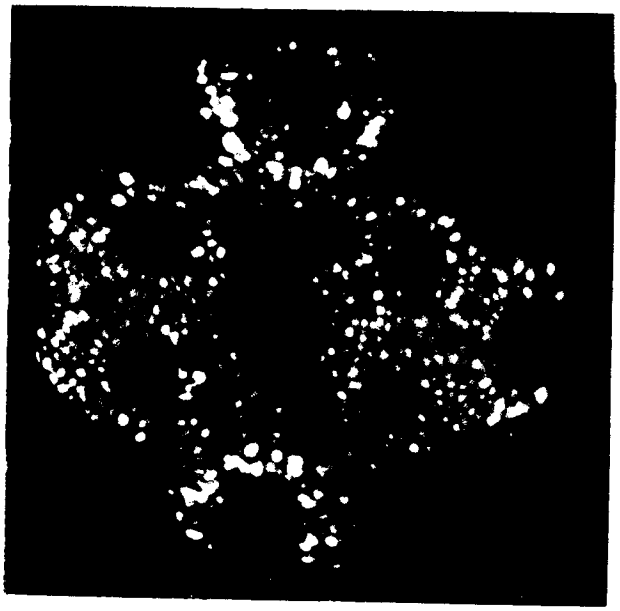

C

D

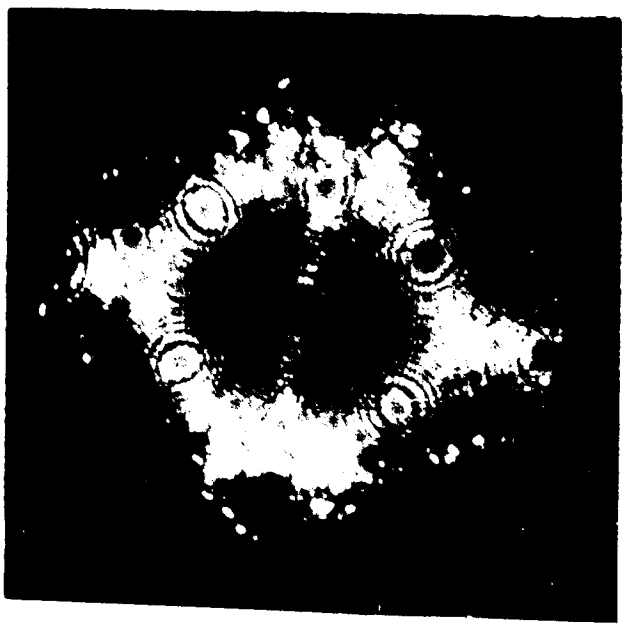

Removal of a total of four (011) atomic layers follows before the familiar field evaporated end form is re-attained. It should be noted that even after $1\frac{1}{2}$(011) planes had been removed, considerable surface disorder was still evident.

6.9.2. Thermal re-arrangement of ion bombardment induced damaged surfaces

From the results described in the previous section it is clear that surface atom re-arrangement is not appreciable under 690°K. Moreover, two minute elevated temperature treatments of about 1090°K were required to promote sufficient thermal re-arrangement consistent with avoidance of emitter blunting.

Several annealing experiments were conducted on specimens subjected to 532eV argon ion bombardment for ten minutes using 1.2×10^{-4} Torr of argon (background pressure 8×10^{-10} Torr) at an ion current of about $1.2 \mu A/cm^2$. Reference to figure 6.20 reveals that about 9 (011) atomic layers would be affected by lattice damage. Annealing at temperatures <970°K did not completely remove surface damage except in the {111} regions. To illustrate this point figure 6.27(b) shows a tungsten surface ion bombarded under the conditions described above and subsequently annealed for two minutes at 970°K. The {111} regions display considerable structure while the remainder of the image is disordered. The undamaged reference surface is depicted in figure 6.27(a). Annealing at 1030°K for two minutes and removal of the thermal facets was found to produce a specimen surface comparable to that of the reference surface. Removal of successive

Figure 6.27 The surface re-arrangement of atoms after annealing ion bombardment induced pressure.

(a) The undamaged reference surface.

Figure 6.27 (b) After bombardment with 532 eV argon ions and subsequent annealing at 970° K. Note the structure in the {111} regions.

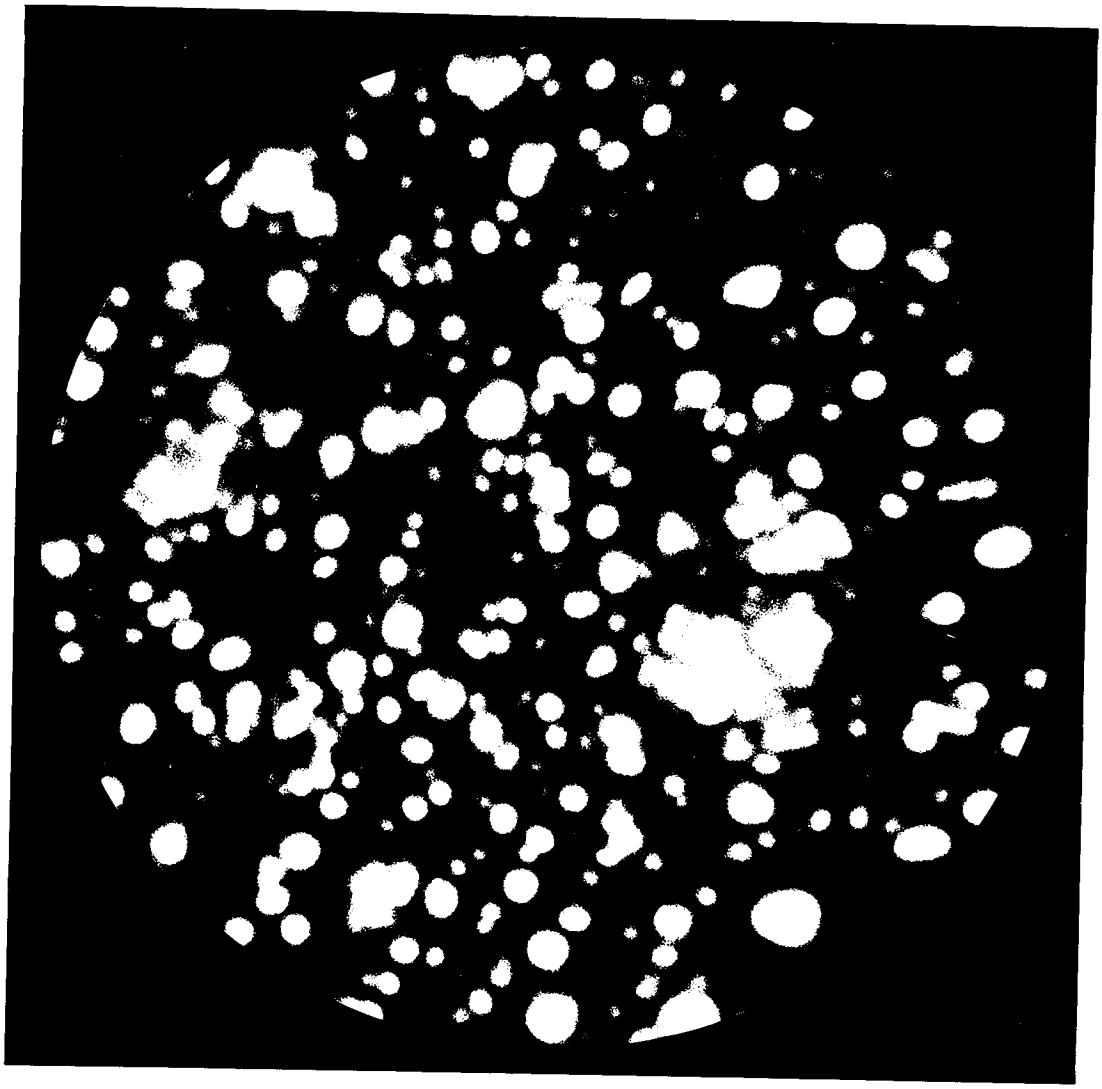

atomic layers confirmed that little apparent subsurface lattice damage remained.

An example of the annealing of gross damage is illustrated in figure 6.28. The highly defective image shown in figure 6.28(a) was caused by sputter sharpening a field emitter which had been blunted by heating to 1570°K. The blunted emitter itself provided field emitted electrons which produced argon ions by impact with argon atoms at a pressure of 1×10^{-4} Torr. The argon ions then sputter sharpen the emitter which is held at a negative potential of about 1kV to 3kV. This method is similar to that used by Janssen and Jones (1971) who sharpened field emitters by cathode sputtering with neon ions (resharpening of field emitters is discussed in chapter 7). After annealing for two minutes at 1090°K much of the order had been restored (viz. figure 6.28(b)). Heat treatment at 1090°K for a further two minutes and the removal of one (011) atomic layer produced the ordered image shown in figure 6.28(c).

Although the present study suggests that annealing at about 1100°K is usually adequate to remove normal ion bombardment induced damage (such as point defects) and gross topographical distortions; it may be that higher temperatures are required to remove more extensive lattice defects. Indeed, Cranstoun, Browning and Pyke (1973) found that similar temperatures were insufficient to remove considerable structural damage. Also, Navinšek, Marinkovic, Osredkar and Carter (1970) attempting to correlate thermal desorption processes with annealing stages found with tungsten transmission electron micro-

Figure 6. 28 The annealing of gross topographical damage.

(a) A 10 kV helium field-ion micrograph illustrating the gross topographical damage caused by argon ion cathode sputtering to a tungsten emitter.

(b) The same surface after annealing at 1100°K for 3 minutes.

(c) After a further 3 minutes, the image is now symmetrical and no significant amount of lattice damage remains. One (110) atomic layer had been removed from the surface illustrated in (b).

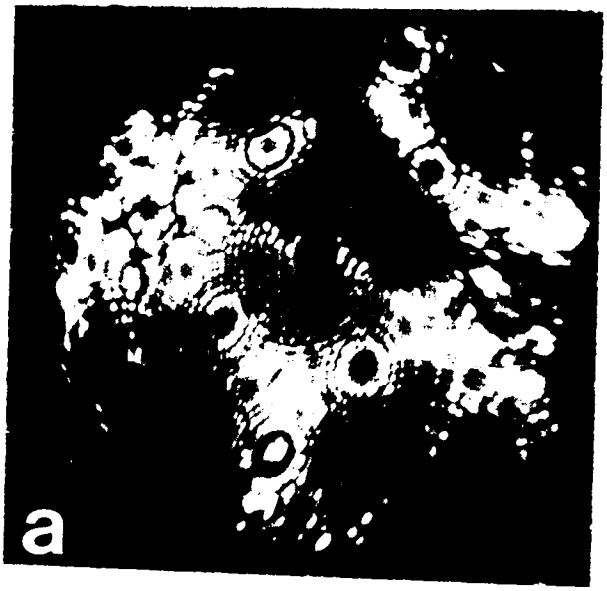
a

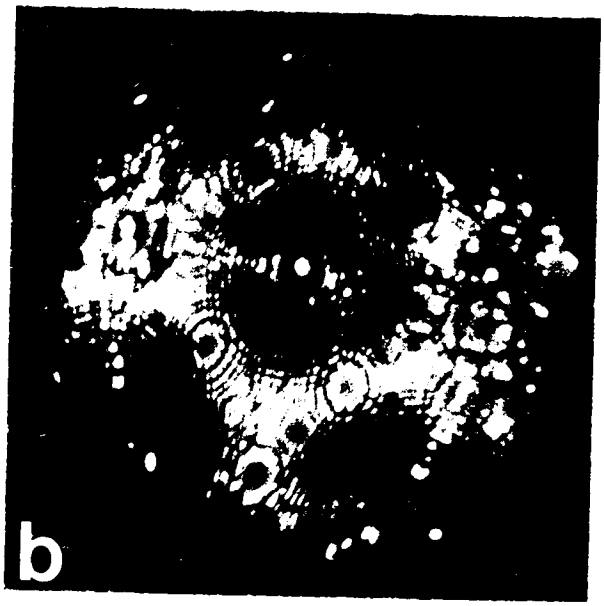
b

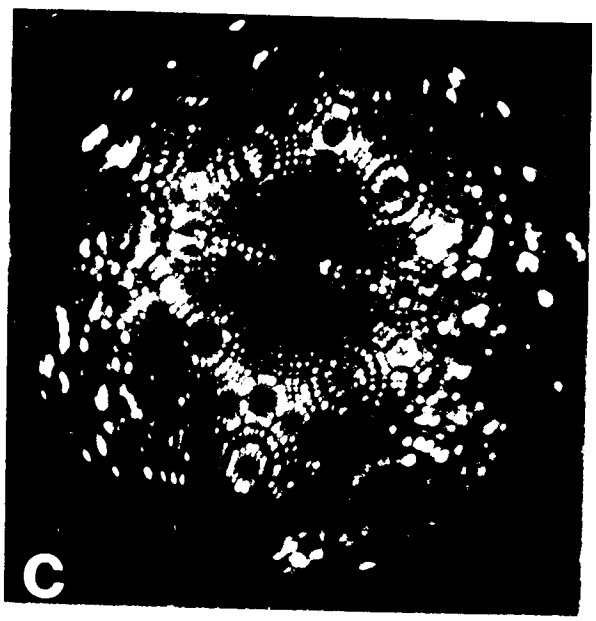
c

scope foils bombarded with 4keV argon ions that although most of the damage annealed at about 1470°K, complete annealing does not take place until 1770°K.

6.10 Discussion

The low-energy inert gas ion bombardment of tungsten has revealed new information with regard to the nature and extent of the resulting lattice damage. It is clear that several mechanisms are possible when a low energy ion is incident on a solid surface. In general the incoming atom penetrates the surface and collides with a number of substrate atoms and then either comes to rest within the lattice or leaves the substrate with a fraction of its incident ion energy. Radiation damage may be caused to the lattice in a number of ways.

a) Some of the incident atoms may become embedded in the substrate lattice. Atoms that come to rest as interstitials may perturb the surrounding lattice atoms whilst those trapped in vacancies will not perturb the lattice to the same extent.

b) The incident atom may produce Frenkel pairs by collision with lattice atoms hence producing both vacancies and self-interstitials.

c) Atoms on the surface may receive sufficient energy, either directly or indirectly from the incident atom, to leave the surface. This process, known as sputtering, would produce surface vacancies.

Evidence has been obtained for all three mechanisms. Certainly, all experiments showed surface vacancies subsurface vacancies and interstitials to exist. No distinction could be made from the field-ion microscope

images about the precise nature of these interstitials. However all "bright spots" must be associated in one way or another with displaced or interstitial tungsten atoms. That is, the "bright spot" contrast either shows the existance of a true S.I.A. formed by atomic collision or it may show the disturbance of the surrounding lattice caused by an embedded inert gas atom. The "bright spot" contrast should not be associated with tungsten interstitial atoms as these are mobile at temperatures as low as 28°K (Scanlan, Styris and Seidman (1971(a),(b)), unless it is trapped by impurity. An inert gas atom could not be directly imaged in the same way as an S.I.A. might be, for instance, sitting within a ledge site protected from the electric field. Once exposed to the surface, theory predicts that the inert gas atom would be field evaporated due to the absence of any bonding term, (Southworth and Ralph (1969)). Thermal desorption studies have shown that the trapping efficiences for inert gases in polycrystalline tungsten (at room temperature) increases rapidly with incident ion energy (Kornelsen (1964)), as shown in figure 6.29. Further, the trapping probability increases with decreasing atomic weight of the ion species. For the heavier gas atoms the trapping sites are likely to be either substitutional or interstitial, but helium undergoes rapid interstitial diffusion at room temperature and can hence escape through the surface (Kornelsen (1970)), unless it encounters a lattice defect which acts as a trapping centre (Erents and Carter (1967)). These trapping centres are usually generated artifically by pre-bombarding with heavy inert gas ions. This may

help to explain the small number of "bright spots" found in the field-ion microscope experiments for helium compared with xenon, argon and neon. There is also evidence which supports the suggestion of Farrell and Grant (1970) that low energy helium ion bombardment can produce its own trapping sites. Combined with its rapid diffusivity, helium is a very small atom and hence even if it were trapped in the same way as the other inert gases, its size would mitigate against "bright spot" contrast being formed by surrounding lattice distortion.

The formation of more extensive lattice damage has been observed commonly in the shape of vacancy and interstitial clusters. The occurrence of dislocations and slip have also been noted. The formation of more extensive defects may have been of the form described by Hermanne and Art (1970). The part played by applying the high electric field to the specimens when imaging is an unknown quantity. Unfortunately, the unambiguous characterisation of these defects was not possible as they usually occurred in the presence of a large number of point defects making the general image quality inadequate. The one property that typifies all these defects, although extensive, was that they did not expand into the crystal more than 80Å. Hence the close proximity of the surface is another parameter to be considered especially with regard to the formation of surface slip steps.

The distribution of damage as revealed by the layer by layer field evaporation sequences was similar for each of the three heavier species (Xe, Ar, Ne) and took

the form of a roughly exponential decrease of the damage with depth at all ion energies agreeing with the range measurements of MacDonald and Haneman (1966) in the same energy range. (Also, previous experiments had revealed that different ion fluxes still produce the same sort of distribution).

The depth of damage measurements for xenon, argon and neon confirm that the size of the bombarding ion is crucial. General observations were that the range increased with ion energy and decreased with the atomic weight of the bombarding species. Measurement of the range of low-energy helium ions was not possible partly because of the small amount of damage produced (and hence easily confused with artefacts) and also because as Kornelsen (1970) observes; helium ions injected at a few hundred eV are trapped at depths exceeding 1μ, which is greater than the usual radius of a field-ion emitter. The depth of damage versus ion energy plots produced linear functions for xenon and argon (neon gave a non-linear function, but this may be merely a result of our arbitrary definition of range), similar to that found by MacDonald and Haneman (1966). These measurements also confirm the findings of Farnsworth and Hayek (1967) using L.E.E.D to study the effects of ion bombardment on single crystal tungsten. They found a larger decrease in the diffracted peak intensity for light ions compared with the heavier ions. This evidence suggests that the size of the ion is the determining factor rather than momentum, that is, the larger ions cause less damage due to their smaller penetration.

As far as the cleaning properties of ion bombardment are concerned, it is common practice especially in Auger electron spectroscopy to employ approximately 500eV argon ions to sputter clean specimen surfaces (for instance Dooley and Haas (1970)). Inexplicably, other inert gases are rarely considered. The requirements of the bombarding ion species are that it sputters as much material as possible consistent with an acceptable minimum of associated lattice damage. In the case of tungsten, sputtering yield data, table 6.2 shows that 500eV argon ions possess a sputtering yield of 0.62 atoms/ion and figure 6.20 reveals that about 13 (011) layers are affected by lattice damage. However, if we now look at the corresponding figures for xenon at the same ion energy we find that it has a sputtering yield of 1.18 atoms/ion, but causes only six (011) layers of damage. Hence in comparison with argon, xenon produces almost twice the sputtering for half the depth of damage. It would thus seem pertinent to point out that the use of 500eV Xe ions would produce more optimum cleaning results. Another bonus is that xenon has the lowest trapping coefficient (Kornelsen (1964)) (figure 6.29) and hence reduces the amount of inert gas contaminant.

Of course, for materials other than tungsten the picture changes somewhat, because for lighter materials other inert gases may possess better sputtering yields viz for beryllium, argon has a sputtering yield of 0.80 atoms/ion whilst for xenon it is 0.42 atoms/ion for 600eV ion energies. In this case argon would give the

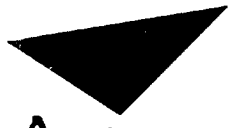

Aston University

Content has been removed for copyright reasons

Figure 6.29 The trapping probability of inert gas ions in polycrystalline tungsten. (Kornelsen (1964)).

optimum results. As a general rule equation (6.3) controls the efficiency of the process and the closer the atomic weight of the inert gas atom and the substrate (be it metal atom, oxide or other contaminant) the more optimum are the conditions for sputtering. Ideally, the published sputtering yields should be consulted. To conclude, the premise that xenon should not be used because it causes too much damage (Cranstoun, Browning and Pyke (1973)) appears to be false.

TABLE 6.2

	HELIUM	NEON	ARGON	XENON
Atomic number	2	10	18	54
Atomic weight a.m.u.	4.003	20.183	39.948	131.30
Mean atomic diameter	2.30Å	-	2.90Å	3.70Å
First ionisation potential	24.46eV	21.47eV	15.68eV	12.08eV
Sputtering yield on Tungsten at 600eV (atoms/ion)	0.008	0.32	0.62	1.18
Maximum percentage of incident ion energy transferred to a W atom upon collision	8%	36%	59%	99%

CHAPTER 7

THE PREPARATION AND RESHARPENING OF FIELD-ION EMITTERS BY ION ETCHING

7.1 Introduction

The use of sputtering in profile etching and the micromachining of solids has already been successfully exploited in many areas of research. For instance, glass has been machined by Bayly and Townsend (1972) and optically polished by Pearson and Harsell (1972). The technique is also being applied to the surface modification of microelectronic materials and to the drilling of such materials as diamond and steel (Carter and Colligon (1968)).

Heitel and Meyeroff (1965) have used sputter etching to prepare thin metal foils suitable for the transmission electron microscope (T.E.M.); the range of materials has since been extended and Barber (1970) has managed to produce satisfactory foils of glasses, minerals and ceramics.

The methods usually employed in the preparation of field-ion microscope specimens are chemical etching and electropolishing and are similar to those used to prepare T.E.M. specimens of the same material. A comprehensive review of these methods and their disadvantages is available (Müller and Tsong (1969)). Barber (1970) has pointed out that ion etching techniques may reveal features hitherto unobtainable by conventional chemical etching or electropolishing methods. For instance, it is known that these latter methods may preferentially leach out some microstructures

occurring in certain multiphase systems. However, the major advantage of the ion etching technique is its applicability to all materials.

In the preparation of thin foil T.E.M. specimens a proviso must first be met, that is, a thick foil must first be obtained. A similar condition exists in the ion etching method of emitter preparation. In this case, the starting material should conform to a general conical shape. This can usually be obtained using an electropolishing or chemical etching technique.

It has been found during the present study that ion etching of suitably shaped specimens consistently produces low radius emitters even with more difficult materials such as cadmium sulphide. The technique has also proved ideal for the resharpening of blunt or "flashed" emitters, providing that their conical shape has been retained.

This method of specimen preparation also possesses the advantage that it does not contaminate, but rather, contaminant layers such as metal oxide films are removed from the emitter surface by sputtering to provide a clean specimen. The only contamination that remains is that due to the atmosphere upon transferring the emitter from the etching device to the microscope. This is a particular advantage in U.H.V. field-ion microscopy.

The application of ion beam etching to the preparation of field electron emitters and field-ion microscope specimens will be especially useful for materials for which adequate polishing solutions may be unknown.

7.2 Experimental details

The ion source used in the tip sharpening experiments was developed by Fitch et al (1970). The electrostatic (or twin anode) ion source, which operates as a cold cathode device has already been shown to be suitable for sputter-ion etching of metallic and non-metallic materials for electron microscopy (Fitch and Rushton (1971)) and is now commercially available. The high vacuum system used in this study was supplied by Edwards High Vacuum International and is not unlike the I.B.M.A. 1 system which is manufactured specifically for the production of thin foils. A simple conversion could make this system also suitable for emitter profile etching.

7.2.1. The electrostatic ion source

The electrostatic ion gun is illustrated schematically in figure (7.1). The gun consists essentially of two 1.5mm diameter tungsten rods surrounded by a stainless steel cathode of 3.75cm diameter. End plates are used to enclose the ends of the cathode and argon is injected into the ion gun through a gas inlet pipe in the cathode wall. The anodes are maintained at a positive potential Vt, with respect to the earthed cathode. The electrostatic field produced within the ion gun induces any electrons present to follow oscillatory trajectories between the anodes along the general direction of the y axis of the ion gun and the discharge current is measured at the cathode. Positive ions formed at the discharge are allowed to emerge through an aperture in the cathode.

The device operates at a low pressure of argon without recourse to a magnetic field, neither does it require a differential pumping system. The ions emerge through the cathode aperture as an intense collimated beam obviating the need for focussing electrodes.

7.2.2. Experimental arrangement

The pre-etched or blunt emitter is placed at a distance of 2cm from the aperture in the ion gun cathode from which the positive ions emerge. The longitudinal axis of the emitter is positioned in a direction parallel to the x-axis of the ion gun (see figure 7.1). The emitter is rotated about this axis at approximately 5rpm in order to obtain an even etch and also to prevent the development of topographical irregularities such as cones (for example, Stewart and Thompson (1969)).

The ion gun assembly was operated in a stainless steel, oil diffusion pumped vacuum system with a typical background pressure of $1x10^{-6}$ Torr; the argon gas pressure in the vicinity of the emitter being maintained at about $1x10^{-4}$ Torr.

7.3 Results

Field-ion emitters of refractory metals have been resharpened using ion beam etching. The technique has also been shown to work in the preparation of non-metallic emitters. In the case of the refractory metal specimens, a blunt field-ion emitter imaging at over 30kV (outside the useful range for field-ion microscopy) was inspected in the scanning electron microscope (S.E.M.), resharpened using the ion etch technique and re-examined in the S.E.M.

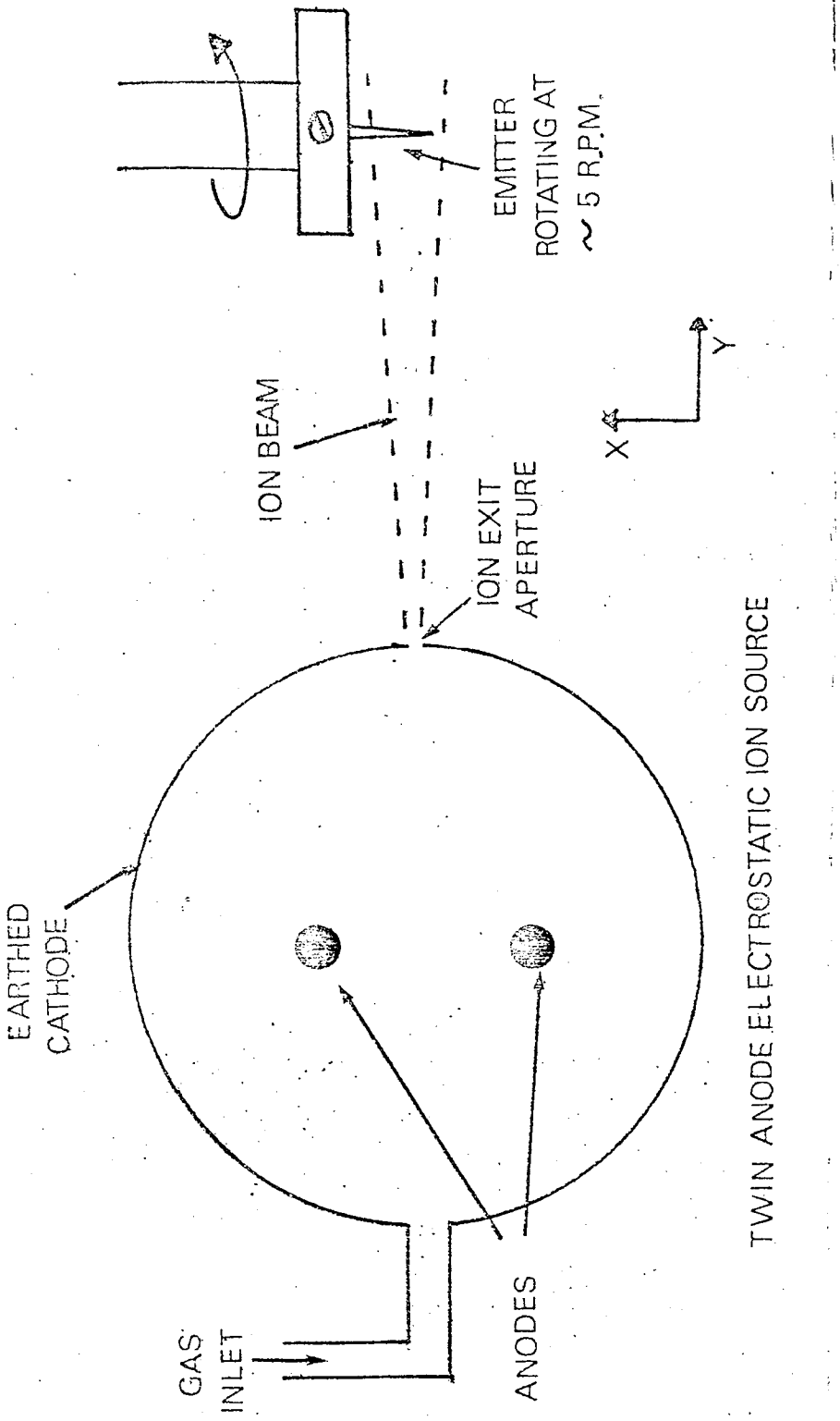

Figure 7.1 A schematic diagram of the ion etching apparatus.

7.3.1. Metal emitter resharpening

The two metals chosen were tungsten and iridium; b.c.c. and f.c.c. crystal structure respectively. Specimens were mounted in a duralumin device suitable both for S.E.M. and the ion source assembly. The specimen shown in figure 7.2(a) is iridium and had 'flashed' in the field-ion microscope, the result was a high radius emitter (about 10,000Å), still retaining the required conical shape although the shank profile was somewhat irregular. A profile of the same specimen after ion etching for one hour (Vt = 6kV and It = 7.5ma) is shown in figure 7.2(b). The emitter radius has been considerably reduced and is now approximately 2,000Å, also the shank has a much smoother appearance. Figure 7.2(c) shows the profile of the same emitter at the same magnification after a further two hours ion etching, the result is a very sharp emitter. Similar encouraging results have been obtained for iridium specimens that had not flashed, but had merely blunted due to field evaporation. Similar successful experiments were performed using tungsten emitters.

7.3.2. Non-metal emitter preparation

Cadmium sulphide presents a different type of material to that usually encountered in field emission or field-ion microscope studies. It possesses a h.c.p. structure, is a compound and a semiconductor. Although emitters of this material can be obtained by chemical etching, the procedure is difficult and prone to failure.

The CdS emitters used in this investigation were initially pre-etched using a combination of chemical

Figure 7.2 The sharpening of field-ion emitters by ion etching

(a) A scanning electron micrograph of a flashed iridium emitter x 5,000

(b) After ion etching for one hour the emitter radius has been reduced and the shank has a much smoother appearance. x 5,000

(c) After ion etching for 3 hours in total; a very sharp emitter x 5,000

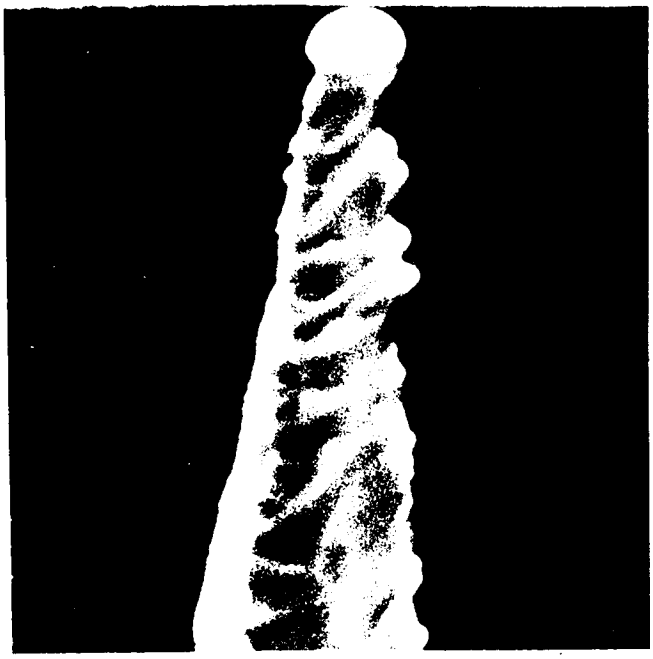

(a)

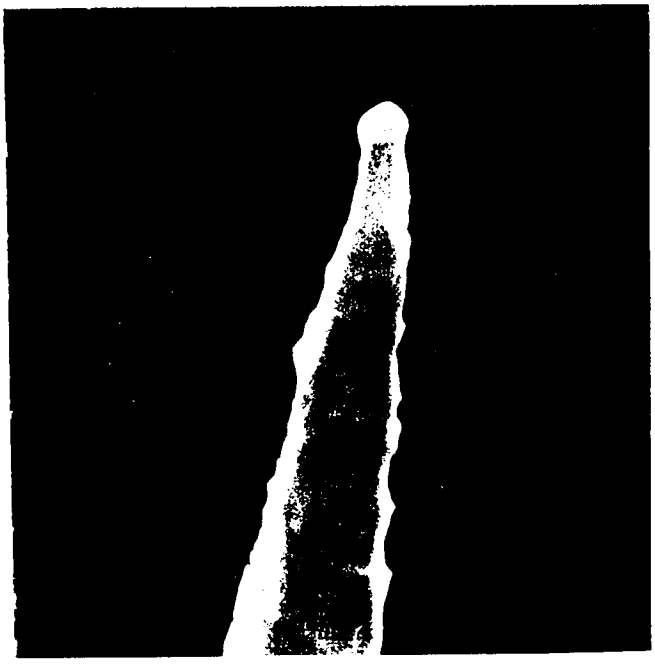

(b)

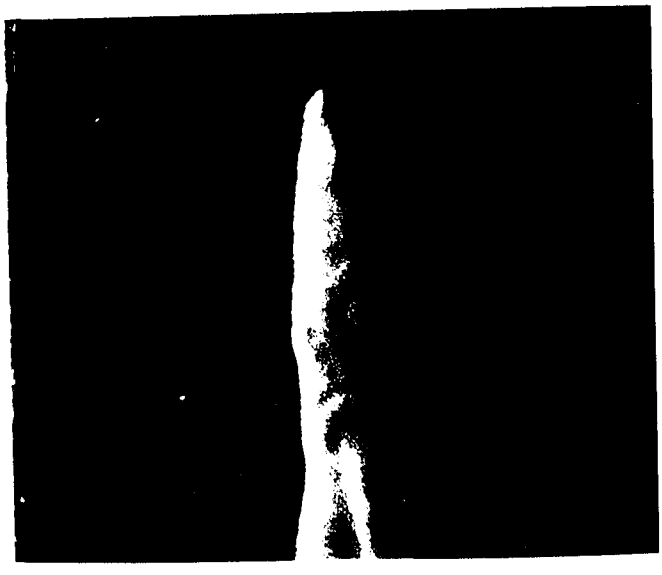

(c)

etchants. The crystals were first etched by rotating them in concentrated hydrochloric acid and then polished in hot phosphoric acid to remove any surface irregularities and so produce a smooth, well defined conical shape (Salmon (1972)). The pre-etched emitter was then ion etched, a typical result of this process is shown in figure (7.3(a)). A smooth, very low radius (about 100Å) emitter has been produced. Figure (7.3(b)) is an end-on view of the same emitter and shows that the emitter is faceted along certain crystal planes rather similar to the faceting shown to occur in tungsten by Janssen and Jones (1971). Another interesting feature are the parallel ridges seen to extend along each faceted face.

7.3.3. Ion etch removal of gross contamination

The technique of sputtering induced removal of contamination from metal (and non-metal) surfaces has been employed in many surface study techniques, (see chapter 6). The method is also useful in field-ion microscopy as it removes gross contamination existing on the shank and hence reduces the need to subject the specimen to in situ transient high temperature treatment which removes contamination, but also blunts the specimen. Figure 7.4(a) shows an area of the shank of an iridium specimen which had been previously electropolished, leaving a heavily contaminated specimen. The shank is encrusted with what is probably an oxide layer. Figure (7.4(b)) shows an area of the shank after ion etching. The specimen is now smooth and uncontaminated and ideal for ultra high vacuum work where high temperature

Figure 7.3 The ion etch sharpening of semiconducting materials.
(a) A scanning electron micrograph of an ion etched cadmium sulphide field emitter. x 15,000
(b) An 'end-on' view of the same emitter. x 19,000

Figure 7.4 The removal of gross contamination by ion etching.
(a) A portion of a contaminated iridium emitter surface. x 5,000
(b) The same region of the shank after ion etching. x 6,500

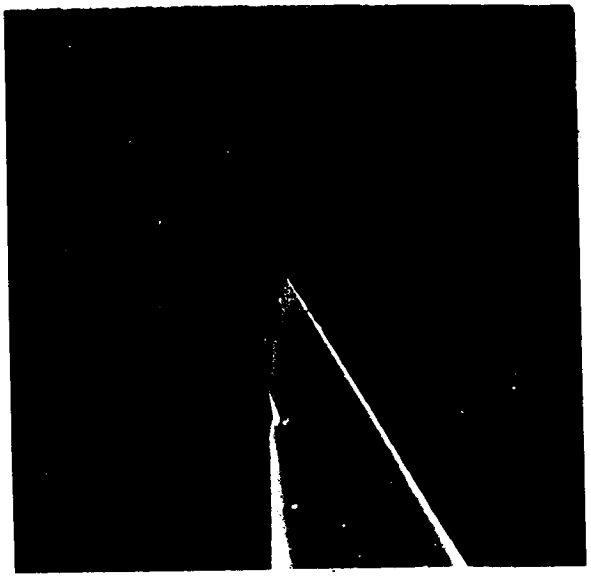

(a)

(b)

(a)

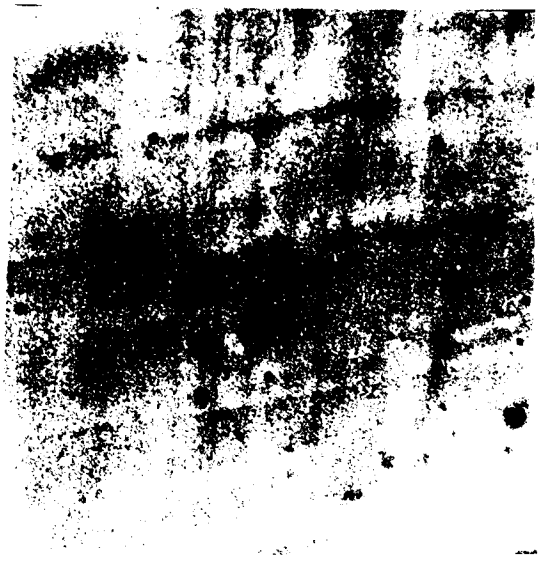

(b)

7.3.4. In situ resharpening of field-ion emitters by cathode sputtering

A convenient method of resharpening field-ion emitters by cathode sputtering has been described by Müller (1937) and more recently by Janssen and Jones (1971). The method used by Janssen and Jones (1971) essentially consists of running a field emission current provided by the specimen into a neon environment of 5×10^{-5} Torr. Positive ions are formed by gas atom collision with field emitted electrons and are then accelerated to the field emitting specimen which is held at a negative potential (typically 1 to 3kV). Material is then sputtered from the emitter by ion impact.

However, these conditions may not be optimum. For instance, the sputtering yield of neon on tungsten is 0.32 atoms/ion whereas the sputtering yield for argon on tungsten is 0.62 atoms/ion (Laegried and Wehner (1961)). Thus experiments were performed using argon as the bombarding species.

An interesting feature of these experiments was that successful sharpening largely depended on the emitter topography. Sharpening rarely occurred if the technique was applied to a field evaporated surface, but success was more likely if a thermally annealed end form was used. For example, figure (7.5(a)) dpeicts a field-ion micrograph of a thermally annealed (011) orientated, tungsten end form, imaging at an applied voltage of 15kV. The polarity of the specimen was then reversed and held in the field emission mode. The specimen was emitting electrons in an argon pressure of

Figure 7.5(a). A thermally annealed tungsten end-form prior to cathode sputtering.

(15kV image).

Figure 7.5(b). A low radius tungsten image after ion etch sharpening (a).

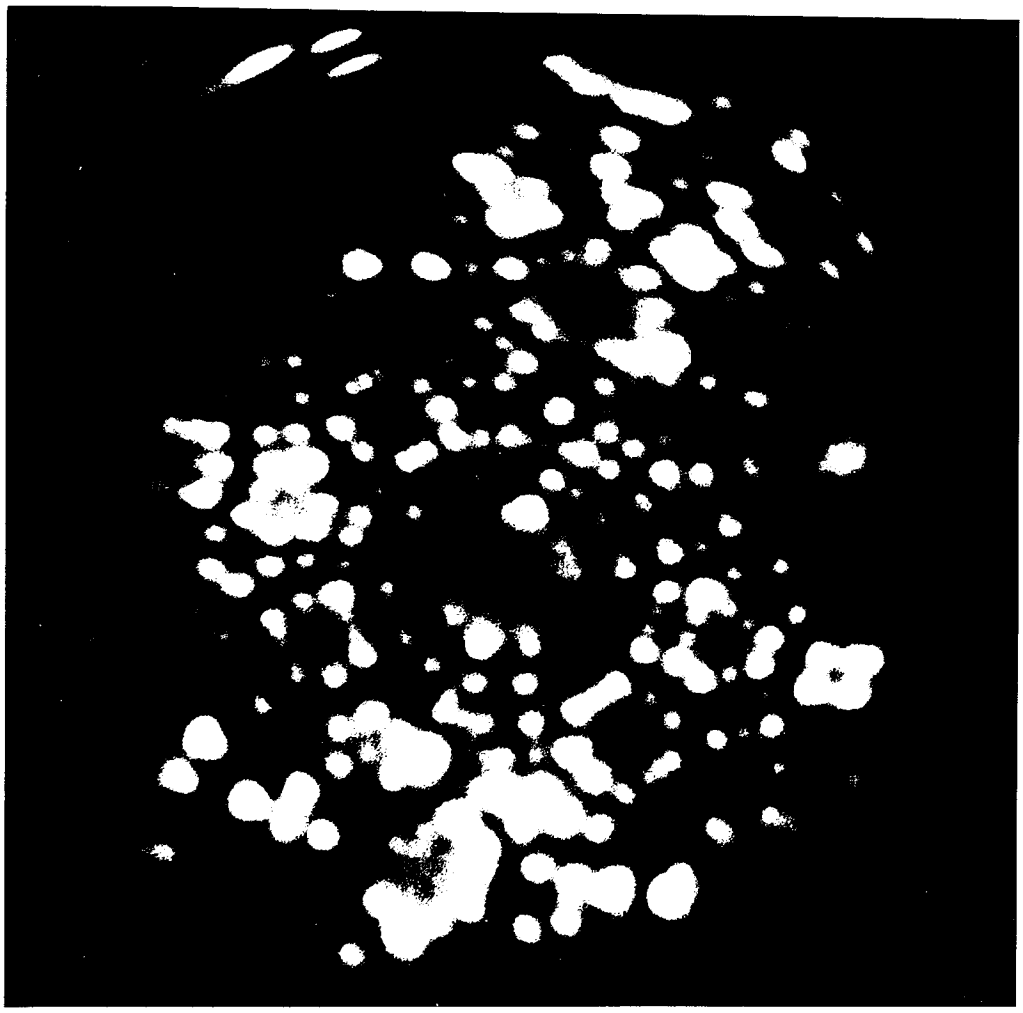

4×10^{-4} Torr for five minutes. Figure 7.5(b) shows the outcome after 4 (011) atomic layers had been removed from the original surface. The specimen radius is now only about 100Å and was imaged at 4kV. Similar experiments using neon confirmed that a thermally annealed topography was required for sharpening to occur. However, the time required to sharpen specimens using neon was considerably longer than the time required using argon. Annealing of damage caused by the technique, without subsequent blunting, took place at about 1100°K (see chapter 6).

Further experiments using the field-ion emitter as a useful reference topography may prove useful in the general elucidation of equilibrium ion etched shapes.

7.4 A simple geometric theory of ion etch sharpening of field-ion emitters

The effects of ion sputtering on the various shapes of the specimen substrate have been investigated in detail and techniques exist to predict the resultant equilibrium profile (Catana, Colligon and Carter (1972), Barber et al (1973)). In order to be able to predict the time and conditions required to resharpen or to prepare an emitter, a simple two-dimensional argument is effective. The argument essentially follows the model proposed by Janssen and Jones (1971) which was invoked to account for tip sharpening caused by cathode sputtering.

The model proposed by Janssen and Jones contained one or two geometric mistakes, but the assumptions made

here are essentially the same. The first assumption is that there exist two independent resolved sputtering rates (one in the axis direction and the other perpendicular to the emitter axis). Secondly, the conical shape of the emitter is not altered so that the cone half angle θ remains constant during sputtering. This would seem to be a fair assumption judging from the evidence found in scanning electron micrographs.

Let the original emitter radius be defined by the distance AO_a (see figure (7.6)), the cone half angle being θ and defined by $A\hat{P}aOa$. The emitter radius after ion etching is ObB and it is important to note that the circles defining the radii in the two cases are not concentric. ObB is produced to meet AP_a produced at A'. The thickness of material removed in the x direction is Δx and Δy is the corresponding thickness removed in the y direction.

Hence from figure (7.6):-

$$\Delta x = x_b + P_aP_b - x_a \qquad .....(7.1)$$

From the similar triangles $P_bB'O_a$ and P_aAO_a

$$\sin\theta = \frac{R_a - AB'}{O_aP_b} = \frac{R_a}{P_aO_a}$$

therefore:-

$$P_bO_a = \frac{R_a - AB'}{\sin\theta} \quad \text{and} \quad P_aO_a = \frac{R_a}{\sin\theta} \qquad .....(7.2)$$

$$\text{But } P_aP_b = P_aO_a - P_bO_a \qquad .....(7.3)$$

Substituting for P_bO_a and P_aO_a

$$P_aP_b = \frac{RR_a}{\sin\theta} - \frac{R_a - AB'}{\sin\theta}$$

$$P_aP_b = \frac{AB'}{\sin\theta} \qquad .....(7.4)$$

Substituting for P_aP_b in equation 7.1:-

$$\Delta x - \frac{AB'}{\sin\theta} = x_b - x_a \qquad .....(7.5)$$

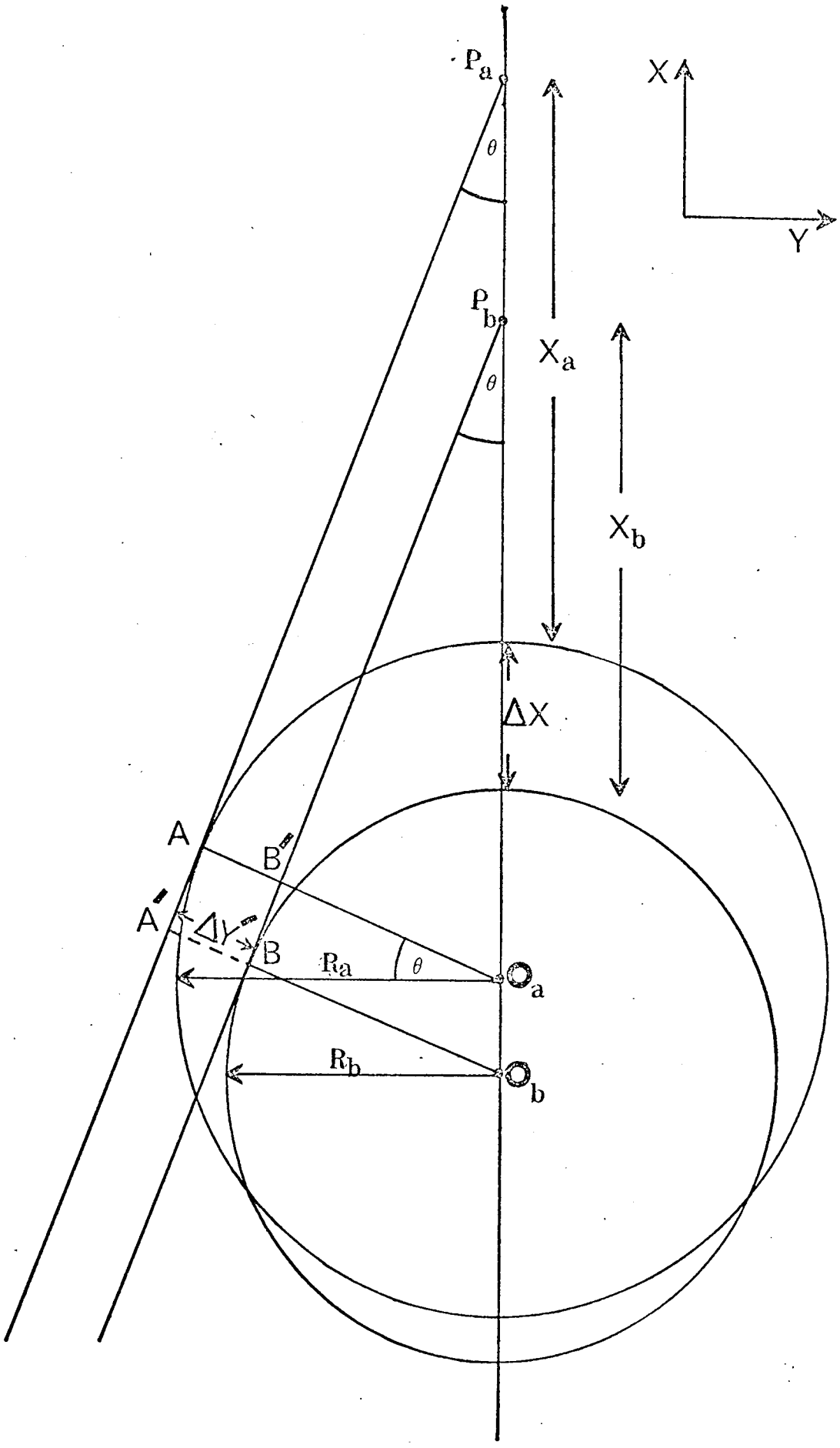

Figure 7.6 The schematic model used to account for the sharpening of field-ion emitters by ion etching.

But $\sin\theta = \frac{R_a}{x_a + R_a} = \frac{R_b}{x_b + R_b}$

Therefore:-

$$x_a = R_a\left(\frac{1}{\sin\theta} - 1\right) \text{ and } x_b = R_b\left(\frac{1}{\sin\theta} - 1\right)$$

Consequently:-

$$x_a - x_b = (R_a - R_b)(\text{cosec}\,\theta - 1) \qquad \ldots\ldots(7.6)$$

Substituting for $X_a - X_b$ in equation (7.5):-

$$\frac{AB'}{\sin\theta} - \Delta x = (R_a - R_b)(\text{cosec}\,\theta - 1)$$

but $AB' = \Delta y \cos\theta$

Hence:-

$$\frac{\Delta y}{\tan\theta} - \Delta x = (R_a - R_b)(\text{cosec}\,\theta - 1)$$

Let $R_a - R_b = \Delta R$ then:-

$$\frac{\Delta y}{\tan\theta} - \Delta x = \Delta R\,(\text{cosec}\,\theta - 1) \qquad \ldots\ldots(7.7)$$

Equation (7.7) predicts that a change in the radius of the emitter ΔR is a function of the thickness removed from the y and x directions and the cone half angle.

From equation (7.7) if θ is constant, differentiate with respect to time t,

Then $\frac{dy}{dt}\tan\theta - \frac{dx}{dt} = \frac{dR}{dt}(\text{cosec}\,\theta - 1)$

But $\frac{dy}{dt}$ is the sputtering rate in the y direction Sy.

Similarly, $\frac{dx}{dt}$ is Sx.

Rearranging:-

$$\frac{\text{cotan}\,\theta - \frac{Sx}{Sy}}{\text{cosec}\,\theta - 1} = \frac{\frac{dR}{dt}}{Sy} \qquad \ldots\ldots(7.8)$$

If the function on the left hand side of equation (7.8) is plotted against θ for various values of the ratio ($p = Sx/Sy$), sharpening occurs even for very large cone half angles (see figure (7.7)). This is not unlike that produced by Janssen and Jones (1971), but the

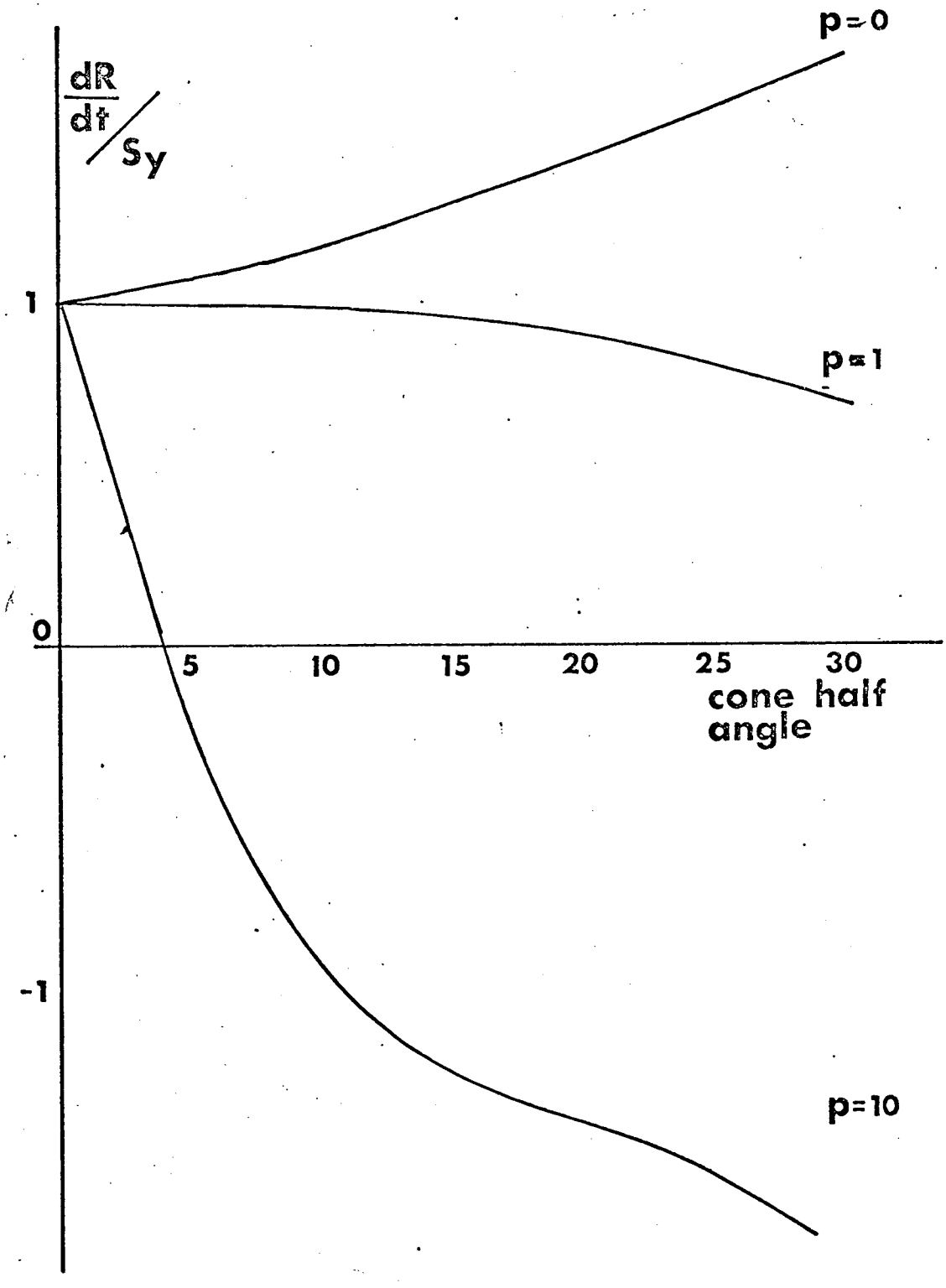

Figure 7.7 The dependance of sharpening on cone angle and sputtering rates.

disparity worsens with increasing θ. However the general conclusions remain the same. The rate at which sharpening occurs is dependant on the value of the ratio Sy/Sx; for sputtering in the y direction (where the x component is effectively zero), the rate of sharpening actually increases with increasing cone half angle. This situation is ideal for non-metals such as cadmium sulphide where the cone half angle obtained by pre-etching is usually found to be much greater than those encountered with metals.

In the experimental arrangement employed, a collimated ion beam is incident along the y direction; figure (7.7) shows that this condition where p = 0, is the most favourable for sharpening to occur. The sputtering yield is also dependent on the angle of incidence of the ion with the material surface. If the cone half angle is constant, then except for the extreme portion of the emitter the sputtering yield as a function of the angle of incidence α should be constant.

In this situation then, Δx in equation (7.7) may be neglected,

$$\text{Hence } \frac{\Delta y}{\tan\theta} = \Delta R \ (\operatorname{cosec}\theta - 1) \qquad \ldots\ldots(7.9)$$

$$\text{and therefore } \Delta y = \Delta R \qquad \ldots\ldots(7.10)$$

That is, the thickness of material eroded from the shank determines the decrease in radius of the emitter. A simple experiment whereby the amount of material eroded from the material surface as a function of time would enable a prediction to be made of the approximate time required to prepare an emitter of a certain radius, given a pre-etched specimen of known radius.

7.5 A calibration of the ion etch process

It is usual practise to prepare metal field-ion specimens from cold drawn 0.01" diameter wire. In order to be able to calibrate the ion etch process, a length of tungsten wire of this diameter was mounted in a SEM field-ion specimen holder, part of the wire was masked using aluminium foil, the remainder remained exposed. The interface between masked and exposed wire was then ion etched for periods of between two and nine hours. The value of the ion current density during these experiments was typically 200$\mu A/cm^2$. The specimens were then examined in the SEM and the decrease in radius Δy of the tungsten wire was plotted versus time.

The amount of material eroded displayed an approximately linear dependence with time. From this information an estimate of the time required to remove a given thickness of material could be found and from equation (7.10) the radius of a pre-etched or blunt specimen could be reduced to a pre-selected value in this estimated time. Erosion rates for other materials could be found by comparing the sputtering yields of tungsten and the new material for argon ion bombardment at the relevant ion energy (about 4keV).

7.6 Discussion and conclusions

One possible undesirable feature of this emitter preparation technique is the radiation damage induced into the crystal lattice. The damage caused by low-energy argon ion bombardment in tungsten field-ion emitters has been investigated by the present author

(in the previous chapter) and also by Cranstoun, Browning and Pyke (1973). This damage not only takes the form of vacancies and interstitials, but more severe damage such as dislocations, and slip bands may also be encountered. An example of an ion etched iridium surface is shown in figure 7.8(b), the defect free surface prior to ion etching is depicted in figure 7.8(a). Spiral contrast, typical of a dislocation, intersects many of the planes including the (002) plane, indicating the existance of a dislocation network. However, evidence from the previous chapter and Janssen and Jones (1971) shows that tungsten may be annealed at about 1100°K without causing the emitter to blunt by surface migration. This lattice damage feature of ion etching presents more serious difficulties in the preparation of alloy field-ion emitters. The contrast exhibited by certain disordered alloys may be indistinguishable from the contrast expected from ion bombarded specimens. Heat treatment is precluded because of the possibility of ordering taking place.

It has been shown that ion etching is a reproducible and predictable method of resharpening and preparing field-ion emitters provided the essential pre-required conical shape is first obtained. This method of specimen preparation, although not as convenient as conventional techniques, does offer several new advantages, not least its universal applicability. Ion etching, besides its usefulness in the preparation of field-ion microscope specimens, may also be useful in the production and more particularly, the resharpening of field-electron emitters. It is conceivable that the present experimental arrangement

Figure 7.8 (a) A helium field-ion micrograph of iridium prior to ion etching (courtesy A. G. Tyson).

(b) After ion etching spiral contrast is exhibited on several planes indicating the formation of dislocations.

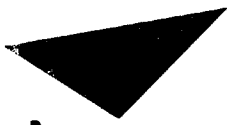

Aston University

Content has been removed for copyright reasons

could be adapted to provide in situ resharpening of field electron sources for the scanning electron microscope and possibly the scanning transmission electron microscope. Furthermore, experimental evidence suggests that the in situ technique of sharpening field-ion emitters is sensitive to the precise topography of the end form and it is suggested that the field-ion specimen surface would provide a convenient reference for the determination of ion etched profiles.

CHAPTER EIGHT

SUMMARY AND SUGGESTIONS FOR FUTURE WORK

8.1 Field-ion Microscopy

A comprehensive review of basic field-ion imaging theory and image interpretation has been provided in chapter 1. Emphasis has been placed on those aspects both technical and geometrical, that subsequently become useful in the characterisation of clean, field evaporated, surfaces. Hence, such aspects as the detailed atomic structure and existing methods of evaluating the local radius of curvature of the emitter are examined in some detail. This provides essential groundwork for the analogue models of field-ion microscopy discussed in chapters 2,3 and 4. Although much of this material is mostly concerned with the emitter itself, the information that it provides together with the review of the basic principles of computer simulation are also relevant to effects which occur in the field-iom image. Finally, chapter 1 provides a brief description of the U.H.V. field-ion microscope used in the investigation of the effects of low-energy ion bombardment and associated annealing procedures (see chapters 6 and 7).

8.2 Optical techniques

Although the optical techniques developed in chapter 2 are primarily intended for subsequent application to various situations in field-ion microscopy, these techniques are important in their own right. Certainly, there are instances other than in field-ion microscopy, where these techniques are directly relevant, for example, synthetic holography.

Initially, the geometric and focussing properties of the various types of zone plate are considered. Emphasis is placed on distinguishing the differences in behaviour exhibited by the Fresnel zone plate and the binary zone plate. This distinction becomes very important when the zone plate analogue of a field-ion plane is investigated. The philosophy of the moiré phenomenon is then considered. A categorisation of the various mathematical methods that exist for the analysis of moiré patterns is presented for the first time. Two specific moire patterns are considered in detail. The first is the moiré pattern formed by overlapping zone plates. Secondly, the moiré pattern formed by superimposing a zone plate and a grid structure is considered. In each case, new information regarding the formation of these moiré patterns is presented.

This work not only provides the groundwork for the moiré interpretation of field-ion microscopy, but these techniques may be used in a variety of physical situations. For example, the electrostatics within the twin anode electrostatic ion source can be understood by overlapping figures simulating the appearance of the equipotentials around each anode considered in isolation.

8.3 Optical analogue interpretation of field-ion micrographs

This thesis represents the first detailed attempt to apply optical analogue techniques to the analysis of field-ion micrographs.

Using techniques developed in chapter 2, it has been shown that an analogue may be derived between the geometry of a single field-ion plane and a binary zone plate. It

is then possible to use the focussing properties of the zone plate to obtain new information from field-ion micrographs. Hence, the local magnification of field-ion images may be obtained when the focal lengths of the field-ion planes are used together with relations derived for local magnification in chapter 5.

Further, the entire emitter surface may be regarded as a moiré pattern formed between overlapping zone plates. The fundamental reason lies in the fact that the crystal lattice itself is an interdependant moiré pattern. The overlapping zone plate treatment also gives rise to several new relationships in the interpretation of field-ion micrographs. This approach also leads to the moiré simulation of field-ion micrographs. Thus, it has been possible to simulate the appearance of micrographs according to various angular and projection relationships by superimposing suitably aberrated zone plates. A detailed mathematical analysis of the atomic structure of the emitter, in chapter 4, has shown that the moiré pattern formed on the emitter surface is identical to that expected on purely crystallographic grounds. This analysis has made it possible, for the first time, to relate the properties of various field-ion planes to one another. The moiré analysis is equally true in the image as it is on the emitter surface as it deals with relationships and not absolute measurements.

Much of the work presented here is of a much wider significance as techniques have been developed in chapters 3 and 4 which enable three dimensional moiré patterns to be analysed. It is likely that the next stage of development of the moiré interpretation of

field-ion microscopy will lie in the simulation and analysis of line and planar crystal defects.

8.4 The investigation into the effects of sputtering

Low-energy ion bombardment is an essential preliminary to much surfaces research as a means of producing a chemically clean surface. It is important to know the nature and distribution of the resultant lattice damage and the extent to which it may be removed by subsequent annealing procedures.

The field-ion microscope has proved to be an ideal technique for investigating such damage as its characterisation lies on the atomic scale. The present study has been concerned with the in situ sputtering of tungsten emitters using helium, neon, argon and xenon ions with energies in the region 100eV to 1keV, together with the effect of annealing.

It has been shown that the surface layers are heavily disordered by bombardment with low-energy neon, argon and xenon ions and that annealing of such disordered surfaces may not recrystallise the surface layers in its entirety to perfection. The depth of damage caused by these low-energy ions has also been determined by removing successive disordered layers by field evaporation until a surface is revealed comparable in perfection to that exhibited by the pre-bombarded images.

Several types of defect have been characterised. It has been shown that bombardment always produces point defects (interstitials and vacancies). Interstitial and vacancy clusters have also occurred in all experiments. More extensive defects have also been observed, including

the occurrence of dislocation loops after helium ion bombardment. All the extensive defects have been characterised by their proximity to the specimen surface, that is, none have extended further than about 80Å into the surface.

Work is planned to perform parallel electron microscopy and high voltage electron microscopy (H.V.E.M.) on ion bombarded field-ion emitters. In this way, it should be possible to identify, in an unambiguous fashion, the more extensive defects, regardless of field-ion image quality. An investigation modelled on gas release experiments is also planned. A mass spectrometer will be fitted to the U.H.V. field-ion microscope so that the re-emission of inert gas can be monitored whilst at the same time characterising the particular defect responsible as the trapping site by observing the field-ion image at the equivalent temperature. In addition, with the provision of a monoenergetic ion source, it should be possible to determine the threshold displacement energies for a variety of substrates and bombarding gas species. Further, experiments using Auger electron spectroscopy should provide more information on optimum cleaning methods discussed in chapter 6.

A parallel study has revealed that ion etching may be a valuable method of producing field-ion microscope specimens. Using a technique similar to that used to prepare transmission electron microscope specimens, field-ion emitters have been produced from materials usually difficult to electropolish. The methodology required for the consistent production of sharp field-ion emitters in this way has been established.

APPENDIX I

A TEMPERATURE CONTROLLER FOR FIELD-ION EMITTERS

A temperature controller using recently available microcircuits has been designed and built to control the temperature of the centre of a filament supporting a field-ion emitter to ± 10°K from 600°K to 2000°K. Filament power requirements have been met within the ranges 0-4 volts at 0-6 amps, or 0-9 volts at 0-10 amps. A wide range of filament characteristics could be accommodated within these limits, although the present unit was designed for 40mm long by 0.25mm dia. tungsten filaments, tapped for 10mm ± 0.5mm with 0.005mm dia. tungsten wire, over the centre section.

In use, the controller was switched to the desired range and the temperature dialled on a ten turn potentiometer. This potentiometer reading was calibrated against an optical pyrometer at suitable points, and agreed well with resistivity measurements on the filament. The temperature overheat was negligible and equilibrium was reached within 5 secs. starting with the filament at 78°K and within 2 seconds the filament was at ambient temperature.

To facilitate capacitative and resistive isolation, from earth, the controller was battery powered. The minimum capacity, determined by the physical size of the case, was less than 40pf. When mounted away from earthed conductor, it was corona free to ± 30kV D.C. or peak A.C. at 50 Hz. With suitable screens, the controller was operated safely while at high voltage, and has survived, due to internal protection, flashovers

between the filament leads and the vacuum chamber.

The device has been successfully utilised in a number of ways in conjunction with a U.H.V. field-ion microscope. For example, the temperature controller has been used successfully to investigate the annealing processes at various temperatures following ion bombardment induced damage in tungsten. The device is also extremely useful for routine outgassing.

REFERENCES

Andrade, E. N., Da, C. and Chow, Y. S. (1940) Proc. Roy Soc. A, 175, 290.

Argon, A. S. and Maloof, S. R. (1966) Acta. Met., 14, 1449.

Ast, D. G. and Seidman, D. N. (1971) Surface Sci., 28, 19.

Attardo, M. J. and Galligan, J. M. (1966) Phys. Stat. Solidi, 16, 449.

Balluffi, R. W., Lie, K. H., Seidman, D. N. and Siegal, R. W. (1970) 'Vacancies and Interstitials in Metals' Eds. Seeger A. et al p.125 (North Holland).

Barber, D. J. (1970) J. Mater. Sci., 5, 1.

Barber, D. J., Frank, F. C., Moss, M., Steeds, J. W. and Tsong, I.S.T. (1973) to be published.

Bassett, D. W. (1963) Nature, 198, 468.

Bassett, D. W. (1965) Proc. Roy. Soc., A286, 191.

Bassett, D. W. (1968) Trans. Faraday Soc., 64, 489.

Bayly, A. R. and Townsend, P. D. (1972) J. Phys. D., 5, L103.

Bellina, J. J. and Farnsworth, H. E. (1972) J. Vac. Sci. and Technol., 9, 616.

Bennette, C. J., Strayer, R. W., Swanson, L. W. and Cooper, E. C. (1966) N.A.S.A. research report CR-54704.

Bowkett, K. M. and Ralph, B. (1969) Proc. Roy. Soc., A312, 51.

Bowkett, K. M. and Smith, D. A. (1970) 'Field-ion Microscopy' (North Holland).

Boyes, E. D. and Southon, M. J. (1972) Vacuum, 22, 447.

Brandon, D. G. (1964) J. Sci. Instrum., 41, 373.

Brandon, D. G. (1968) in 'Field-ion Microscopy' Eds. Hren J.J. and Ranganathan S. p.47 (Plenum Press).

Brandon, D. G. and Perry, A. J. (1967) Phil. Mag., 16, 723.

Brandon, D. G., Wald, M., Southon, M. J. and Ralph, B. (1963) J. Phys. Soc. Japan, 18, 324.

Brenner, S. S. (1962) in 'Metal Surfaces: Structure, Energetics and Kinetics' p.305 (American Society of Metals, Cleveland).

Brenner, S. S. (1964) Surface Sci., 2, 496.

Buswell, J. T. (1971) Phil. Mag., 23, 293.

Carter, G. and Colligon, J. S. (1968) 'Ion bombardment of Solids' (Heineman: London).

Carter, G., Grant, W. A. and Whitton, J. L. (1968) Phil. Mag., 18, 873.

Catana, C., Colligon, J. S. and Carter, G. (1972), J. Mater. Sci., 7, 467.

Chau, H.H.M. (1969(a)) Appl. Opt., 8, 1207.

Chau, H.H.M. (1969(b)) Appl. Opt., 8, 1209.

Chau, H.H.M. (1970) J. Opt. Soc. Am., 60, 255.

Childers, H. M. and Stone, D. E. (1969) Am. J. Phys. 37, 721.

Conger, R. L., Long, L. T. and Parks, J. A. (1968) Appl. Opt. 7, 623.

Cranstoun, G.K.L. (1972) Nature Phys. Sci., 237, 108.

Cranstoun, G.K.L., Browning, D. J. and Pyke, D. R. (1973) Surface Sci., 34, 597.

Cranstoun, G.K.L. and Pyke, D. R. (1971) App. Phys. Lett., 18, 341.

Crawford, R.A.H. (1973) M.Sc. thesis, University of Birmingham.

Davidson, S. M. (1972) J. Mater. Sci., 7, 473.

Dearnaley, G. (1969) Rep. Prog. Phys., 32, 405.

Domeij, B. (1966) Arkiv. Fysik., 32, 179.

Dooley, G. J. and Haas, T. W. (1970) J. Metals, 22, 17.

Dranova, Zh. I and Mikhailovski, I. M. (1970) Sov. Phys-Solid State, 12, 104.

Drechsler, M. and Liepack, H. (1965) Colloq. Inter. C.R.N.S., Nancy, p.49.

Drechsler, M. and Wolf, P. (1958) Proc. 4th Int. Conf. on Electron Microscopy (Springer: Berlin) 1, 835.

Durelli, A. J. and Parks, V. J. (1967) Exptl. Mech., 7, 97.

Durelli, A. J. and Parks, V. J. (1970) 'Moiré analysis of Strain' (Prentice Hall: New Jersey).

Engel, A. and Herziger, G. (1973) Appl. Opt., 12, 471.

Erents, K. (1967) Ph.D. thesis, University of Liverpool.

Erents, K. and Carter, G. (1967) Vacuum, 17, 215.

Erents, K. and Carter, G. (1968) J. Phys. D., 1, 1323.

Erents, K., Farrell, G. and Carter, G. (1968) Proc. of the 4th Int. Vacuum Congress, p.145.

Farnsworth, H. E. and Hayek, K. (1967) Surface Sci., 8, 35.

Farnsworth, H. E., Schlier, R. E., George, T. H. and Burger, R. M. (1958) J. Appl. Phys., 29, 1150.

Farrell, G. and Grant, W. A. (1970) Rad. effects, 3, 249.

Fitch, R. K., Mulvey, T., Thatcher, W. J. and MacIlraith, A. H. (1970) J. Phys. D., 3, 1399.

Fitch, R. K. and Rushton, G. J. (1972) J. Vac. Sci. and Technol., 9, 1.

Forbes, R. G. (1971) Nature Phys. Sci., 230, 165.

Fortes, M. A. (1968) Ph.D. thesis, University of Cambridge.

Fortes, M. A. (1971(a)) Surface Sci., 28, 95.

Fortes, M. A. (1971(b)) Surface Sci., 28, 117.

Fortes, M. A. and Ralph, B. (1966) Phil. Mag., 14, 189.

Fortes, M. A. and Ralph, B. (1967) Acta. Met., 15, 707.

Fortes, M. A. and Ralph, B. (1969) Phil. Mag., 19, 181.

Goldfischer, L. I. (1964) J. Opt. Soc. Am., 54, 845.

Gomer, R. (1961) 'Field Emission and Field Ionisation' (O.U.P.)

Good, R. H. and Müller, E. W. (1956) Handb.d. Phys., 21, 218, (Springer: Berlin)

Grant, W. A. and Carter, G. (1967) Met. and Mater., 1, 176.

Gregov, B. and Lawson, R.P.W. (1972) Can. J. Phys., 50, 791.

Guild, J. (1956) 'The interference systems of crossed diffraction gratings' (Clarendon Press: Oxford).

Hagstrum, H. D. (1954) Phys. Rev., 96, 336.

Heitel, B. and Meyeroff, K. (1965) Z. Physik, 47, 165.

Hermanne, N and Art, A. (1970) Rad. Effects, 5, 203.

Hoppe, W., Katerbrau, K-H., Langer, R., Möllenstedt, G., Speidel, R. and Thon, F. (1969) Siemens Rev., 36, 24.

Horman, M. H. and Chau, H.H.M. (1967) Appl. Opt., 6, 317.

Hren, J. J. and Ranganathan, S. (1968) Eds. 'Field-ion Microscopy' (Plenum: New York).

Hudson, J. A. and Ralph, B. (1972) Phil. Mag., 25, 265.

Hüfner, S., Cohen, R. L. and Wertheim, G. K. (1972) Phys. Scripta., 5, 91.

Ibrahim, M. M. and Bashara, N. M. (1972(a)) Surface Sci., 30, 632.

Ibrahim, M. M. and Bashara, N. M. (1972(b)) Surface Sci., 30, 680.

Ingrham, M. G. and Gomer, R. (1954) J. Chem. Phys., 22, 1279.

Janssen, A. P. and Jones, J. P. (1971) J. Phys. D., 4, 118.

Jason, A. J., Burns, R. P. and Inghram, M. G. (1965) J. Chem. Phys. 43, 3762.

Jenkins, F. A. and White, H. E. (1964) 'Fundamentals of Optics' (McGraw-Hill: New York).

Khan, M. and Schroeer, J. M. (1971) Rev. Sci. Instrum., 42, 1348.

Kinchin, G. H. and Pease, R. S. (1955) Rep. Prog. Phys., 18, 1.

Kornelsen, E. V. (1964) Can. J. Phys., 42, 364.

Kornelsen, E. V. (1970) Can. J. Phys., 48, 2812.

Kornelsen, E. V. (1972) Rad. Effects, 13, 227.

Kornelsen, E. V., Brown, F., Davies, J. A., Domeij, B. and Piercy, G. R. (1964) Phys. Rev., 136, A849.

Laegried, N and Wehner, G. K. (1961) J. Appl. Phys., 32, 365.

Leffel, C. S. (1970) Rev. Sci. Instrum., 41, 285.

Leifer, I., Walls, J. M. and Southworth, H. N. (1973) Opt. Acta., 20, 33.

Leifer, I., Rogers, G. L. and Stephens, N.W.F (1969) Opt. Acta., 16, 535.

Lewis, R. and Gomer, R. (1969) App. Phys. Lett., 15, 384.

Lindhard, J. and Scharff, M. (1961) Phys. Rev., 124, 128.

Lindhard, J., Scharff, M. and Schiott, H. E. (1963) Danske Vid Selsk, Mett-Fys Medd, 33, No. 14.

MacDonald, R. J. and Haneman, D. (1966) J. Appl. Phys. 37, 1609.

McKinstry, D. (1972) Surface Sci., 29, 37.

Möllenstedt, G., Von Grote, K. H. and Jonsson, C. (1963) 'X-ray Optics and X-ray microanalysis' p.73 (Academic Press: New York)

Moore, A.J.W. (1962) J. Phys. Chem. Solids, 23, 907.

Moore, A.J.W. (1967(a)) Phil. Mag., 16, 739.

Moore, A.J.W. (1967(b)) Proc. 14th Field emission symp. Washington D.C.

Moore, A.J.W. and Ranganathan, S. (1967) Phil. Mag., 16, 723.

Moser, J., Bahčevandžijev, S., Janosha, M. and Janičijevič, Lj. (1964) God Zborn PMF Skopje, 15A, 113.

Müller, E. W. (1937) Z. Physik, 116, 604.

Müller, E. W. (1960) Adv. Electron. Electron Phys., 13, 83.

Müller, E. W. (1964) Surface Sci., 2, 484.

Müller, E. W. (1965) Science, 149, 591.

Müller, E. W. (1967) Surface Sci., 8, 462.

Müller, E. W. (1968) in 'Field-ion Microscopy' Eds. Hren J.J. and Ranganathan S. (Plenum Press).

Müller, E. W. (1970) in 'Vacancies and Interstitials in Metals' Eds. A Seeger et al p.557 (North Holland).

Müller, E. W. (1972) J. Less. Comm. Met., 28, 37.

Müller, E. W., McLane, S. B. and Panitz, J. A. (1968) Surface Sci., 17, 430.

Müller, E. W. and Tsong, T. T. (1969) 'Field-ion Microscopy' (Elsevier: New York).

Mulson, J. F. and Müller, E. W. (1963) J. Chem. Phys., 38, 2615.

Navinšek, B., Marinkovic, V., Osredkar, M. and Carter, G. (1970) Rad. Effects, 3, 115.

Neely, H. H., Keefer, D. W. and Sosin, A., (1968) Phys. Stat. Solidi, 28, 675.

Nelson, R. S. (1968) 'The observation of atomic collisions in crystalline solids' (North Holland).

Nelson, R. S. and Thompson, M. W. (1963) Phil. Mag., 8, 1677.

Newman, R. W., Sanwald, R. C. and Hren, J. J. (1967) J. Sci. Instrum., 44, 338.

Nishijima, Y. and Oster, G. (1964) J. Opt. Soc. Am., 54, 1.

Nishikawa, O. and Müller, E. W. (1964) J. Appl. Phys., 35, 2806.

Norden, H. and Bowkett, K. M. (1967) J. Sci. Instrum., 44, 238.

Oster, G. (1964) 'Symposium on Quasi-Optics' p.49 (Polytechnic Press: Brooklyn).

Oster, G. (1967) 'Symposium on Modern Optics' p.541 (Polytechnic Press: Brooklyn).

Oster, G. and Nishijima, Y. (1963) Sci. Am., 208, 54.

Oster, G., Wasserman, M. and Zwerling, C. (1964) J. Opt. Soc. Am., 54, 169.

Page, T. F. and Ralph, B. (1970) Surface Sci., 23, 211.

Page, T. F. and Ralph, B. (1973) Surface Sci., 36, 9.

Pearson, A. D. and Harsell, W. B. (1972) Mat. Res. Bull., 7, 567.

Phillips, F. C. (1962) 'An introduction to crystallography' (Longmans)

Pfeifer, C. D., Ferris, L. D. and Yen, W. M. (1973) J. Opt. Soc. Am., 63, 91.

Pryde, M., Smith, A. G. and Carter, G. (1971) J. Phys.D., 4, 1681.

Rajo, J. M. and Bru, L. (1972) Phil. Mag., 25, 1409.

Ralph, B. (1968) 'Field-ion microscopy' Eds. Hren, J.J. and Ranganathan, S. (Plenum Press

Ralph, B. (1970) Surface Sci., 23, 130.

Ralph, B. and Hudson, J. A. (1969) 'Applications of field-ion microscopy' Eds. Hochman, R.F., Müller, E.W. and Ralph, B. (Georgia Tech. Press: Atlanta).

Lord Rayleigh (1874) Phil. Mag., 47, 81.

Rendulic, K. D. and Müller, E. W. (1967) J. Appl. Phys. 38,2070.

Roberts, R. W. (1963) Brit. J. Appl. Phys., 14, 537.

Robinson, M. T. and Oen, O. S. (1963) Phys. Rev., 132, 2385.

Rogers, G. L. (1950) Nature, 166, 237.

Rogers, G. L. (1959) Proc. Phys. Soc., 73, 142.

Rogers, G. L. (1966) J. Sci. Instrum., 43, 328.

Rogers, G. L. and Leifer, I. (1970) International symposium on the applications of holography, Besançon.

Rosenburg, D. and Wehner, G. K. (1962) J. Appl. Phys., 33, 1842.

Salmon, L.T.J. (1972) Ph.D. thesis, University of Aston in Birmingham.

Sanwald, R. C. and Hren, J. J. (1968)Surface Sci., 9, 257.

Scanlan, R. M., Styris, D. L. and Seidman, D. N. (1971(a)) Phil. Mag., 23, 1439.

Scanlan, R. M., Styris, D. L. and Seidman, D. N. (1971(b)) Phil. Mag., 23, 1459.

Seidman, D. N. (1973) J. Phys. F., 3, 393.

Seidman, D. N. and Lie, K. H. (1972) Acta. Met., 20, 1045.

Shulman, A. R. (1970) 'Optical Data Processing' Chap. 9 (Wiley: New York).

Sigmund, P. and Sanders, J. B. (1968) Proc. Conf. on applications of ion beams to semiconductor technology' (Grenable: C.E.N.)

Silsbee, R. H. (1957) J. Appl. Phys., 28, 1246.

Sinha, M. K. and Müller, E. W. (1964) J. Appl. Phys., 35, 1256.

Smith, A. G. and Carter, G. (1972) Rad. Effects, 12, 63.

Smith, D. A. and Smith, G.D.W. (1970) Phys. Bull., 21, 393.

Smith, G.D.W. (1971) 18th Field Emission Symposium, Eindhoven.

Smith, T. (1971) Surface Sci., 27, 45.

Snyder, W. J. and Neufield, J. S. (1955) Phys. Rev., 99, 1326.

Southworth, H. N. (1970) Contemp. Phys. 11, 209.

Southworth, H. N. and Ralph, B. (1969) J. Microscopy, 90, 167.

Stecher, M. (1964) Am. J. Phys., 32, 247.

Stewart, A.D.G. and Thompson, M. W. (1969) J. Mater. Sci., 4,56.

Stigliani, D. G. and Mittra, R. (1967) J. Opt. Soc. Am., 57, 610

Sugata, E. and Tamaki, S. (1972) J. Electron Mic., 21, 13.

Summers, G. G. (1973) M.Sc. thesis, University of Birmingham.

Surmeijer, E. P. Th. M., Boers, A. L. and Begemann, S. H. (1970) Surface Sci., 20, 424.

Taylor, D. M. (1970) Ph.D. thesis, University of Cambridge.

Taylor, J. L. (1966) Trans. A.I.M.E., 236, 464.

Theocaris, P. S. (1969) 'Moiré Fringes in Strain Analysis' (Pergamon Press).

Thompson, M. W. (1969) 'Defects and Radiation Damage in Metals' (Cambridge Univ. Press).

Tice, D. R. and Bassett, D. W. (1973) 10th Solid State Physics Conference, Manchester.

Tsong, T. T. and Müller, E. W. (1964) J. Chem. Phys., 41, 3279.

Turner, P. J., Cartwright, P., Southon, M. J., Van Oostrom, A. and Manley, B. W. (1969) J. Phy. E., 2, 731.

Turner, P. J., Regan, B. J., Brandon, D. G. and Southon, M. J. (1973) 20th Field Emission Symposium (Penn. State Univ.).

Vali, W. and Gordon, G. L. (1967) Appl. Phys. Lett., 11, 119.

Van Oostrom, A. (1970(a)) Phillips Res. Repts., 25, 87.

Van Oostrom, A. (1970(b)) Appl. Phys. Lett., 17, 206.

Venables, J. A. (1970) 'Atomic collision phenomena in solids' p.132 Eds. Palmer, D.W., Thompson, M.W. and Townsend, P.D. (North Holland).

Vernickel, H. (1966) Z. Natur., 21, 1308.

Vesely, M. and Ehrlich, G. (1973) Surface Sci., 34, 547.

Wald, M. S. (1963) Ph.D. thesis, University of Cambridge.

Waldman, G. S. (1966) J. Opt. Soc. Am., 56, 215.

Walls, J. M., Leifer, I. and Southworth, H. N. (1973) Phil. Mag., 27, 915.

Wilson, K. L. and Seidman, D. N. (1973) Proc. Int. Conf. on 'Defects and Defect clusters in b.c.c. metals and their alloys' N.B.S., Washington D.C.

Youle, A., Davies, D. M., Dury, B.L., Schwartz, D. M. Taylor, D. M. and Ralph, B. (1971) J. Microscopy, 95, 309.

ACKNOWLEDGEMENTS

It is a great pleasure to thank both Professor E. Braun and Dr. H. N. Southworth for their encouragement, advice and assistance during the period of research which culminated in the completion of this thesis.

I would like to express my gratitude to Dr. G. L. Rogers, Dr. N.W.F. Stephens and in particular Dr. I. Leifer for their advice and assistance in developing the optical theory presented in this thesis. I am also indebted on this account to Professor D. F. Lawden for outlining some of the mathematical techniques involved.

I am pleased to acknowledge the co-operation of Dr. G. J. Rushton and Dr. R. K. Fitch over the use of the twin wire electrostatic ion source and to Mr. J. J. Fuggle over the use of the scanning electron microscope. The temperature controller described in the appendix is due to collaboration with Mr. J. M. Pelmore and Mr. C.J.S. Chapman. Useful discussions with Dr. G.K.L. Cranstoun are also gratefully acknowledged.

It is also with great pleasure that I thank those members, past and present, of the surfaces research group of the Department of Physical Metallurgy and Science of Materials, University of Birmingham and those of the field emission group of this department, who have continuously contributed much good advice and discussion.

Finally, my thanks are due to the Science Research Council for a studentship during the tenure of which this work was undertaken.